



AFRL-RQ-WP-TR-2014-0079

NUMERICAL MODELING OF COMPRESSIBLE FLOW AND ITS CONTROL

Jonathan Poggie

**Hypersonic Sciences Branch
High Speed Systems Division**

**MARCH 2014
Interim Report**

Approved for public release; distribution unlimited

**AIR FORCE RESEARCH LABORATORY
AEROSPACE SYSTEMS DIRECTORATE
WRIGHT-PATTERSON AIR FORCE BASE, OH 45433-7542
AIR FORCE MATERIEL COMMAND
UNITED STATES AIR FORCE**

NOTICE AND SIGNATURE PAGE

Using Government drawings, specifications, or other data included in this document for any purpose other than Government procurement does not in any way obligate the U.S. Government. The fact that the Government formulated or supplied the drawings, specifications, or other data does not license the holder or any other person or corporation; or convey any rights or permission to manufacture, use, or sell any patented invention that may relate to them.

This report was cleared for public release by the USAF 88th Air Base Wing (88 ABW) Public Affairs Office (PAO) and is available to the general public, including foreign nationals.

Copies may be obtained from the Defense Technical Information Center (DTIC)
(<http://www.dtic.mil>).

AFRL-RQ-WP-TR-2014-0079 HAS BEEN REVIEWED AND IS APPROVED FOR
PUBLICATION IN ACCORDANCE WITH ASSIGNED DISTRIBUTION STATEMENT.

*//Signature//

JONATHAN POGGIE
Program Manager
Hypersonic Sciences Branch
High Speed Systems Division

//Signature//

RODOLFO BUENTELLO-HERNANDEZ
Branch Chief
Hypersonic Sciences Branch
High Speed Systems Division

//Signature//

THOMAS A. JACKSON
Principal Scientist
High Speed Systems Division
Aerospace Systems Directorate

This report is published in the interest of scientific and technical information exchange, and its publication does not constitute the Government's approval or disapproval of its ideas or findings.

*Disseminated copies will show “//Signature//” stamped or typed above the signature blocks.

REPORT DOCUMENTATION PAGE				Form Approved OMB No. 0704-0188	
<p>The public reporting burden for this collection of information is estimated to average 1 hour per response, including the time for reviewing instructions, searching existing data sources, gathering and maintaining the data needed, and completing and reviewing the collection of information. Send comments regarding this burden estimate or any other aspect of this collection of information, including suggestions for reducing this burden, to Department of Defense, Washington Headquarters Services, Directorate for Information Operations and Reports (0704-0188), 1215 Jefferson Davis Highway, Suite 1204, Arlington, VA 22202-4302. Respondents should be aware that notwithstanding any other provision of law, no person shall be subject to any penalty for failing to comply with a collection of information if it does not display a currently valid OMB control number. PLEASE DO NOT RETURN YOUR FORM TO THE ABOVE ADDRESS.</p>					
1. REPORT DATE (DD-MM-YY) March 2014		2. REPORT TYPE Interim		3. DATES COVERED (From - To) 01 January 2012 – 01 January 2014	
4. TITLE AND SUBTITLE NUMERICAL MODELING OF COMPRESSIBLE FLOW AND ITS CONTROL				5a. CONTRACT NUMBER In-house	
				5b. GRANT NUMBER	
				5c. PROGRAM ELEMENT NUMBER 61102F	
6. AUTHOR(S) Jonathan Poggie				5d. PROJECT NUMBER 3002	
				5e. TASK NUMBER N/A	
				5f. WORK UNIT NUMBER Q05P	
7. PERFORMING ORGANIZATION NAME(S) AND ADDRESS(ES) Hypersonic Sciences Branch (AFRL/RQHF) High Speed Systems Division Air Force Research Laboratory, Aerospace Systems Directorate Wright-Patterson Air Force Base, OH 45433-7542 Air Force Materiel Command United States Air Force				8. PERFORMING ORGANIZATION REPORT NUMBER AFRL-RQ-WP-TR-2014-0079	
9. SPONSORING/MONITORING AGENCY NAME(S) AND ADDRESS(ES) Air Force Research Laboratory Aerospace Systems Directorate Wright-Patterson Air Force Base, OH 45433-7542 Air Force Materiel Command United States Air Force				10. SPONSORING/MONITORING AGENCY ACRONYM(S) AFRL/RQHF	
				11. SPONSORING/MONITORING AGENCY REPORT NUMBER(S) AFRL-RQ-WP-TR-2014-0079	
12. DISTRIBUTION/AVAILABILITY STATEMENT Approved for public release; distribution unlimited.					
13. SUPPLEMENTARY NOTES PA Case Number: 88ABW-2014-1181; Clearance Date: 25 March 2014. This report contains color.					
14. ABSTRACT This report describes work carried out on numerical modeling of high Mach number flows and their control. Two main technical areas were addressed: nanosecond-pulse, dielectric barrier discharge flow control actuators, and large-scale unsteadiness in separated shock-wave/boundary-layer interactions. Numerical simulations of experiments in the Ohio State University Mach 5 tunnel on control of a cylinder flow with a plasma actuator revealed the interaction of the disturbance generated by the actuator with the bow shock, and ruled out sidewall interactions as a major influence on the experiments. High-fidelity fluid simulations of nanosecond-pulse discharges demonstrated the importance of rapid relaxation of excited neutrals and recombination of ions in generating the flow disturbance. Comparisons of fluid simulations with particle-in-cell simulations showed good agreement, confirming the appropriateness of the fluid approach. In a supersonic compression ramp flow, a gliding discharge plasma actuator was found to be very effective in reducing the extent of separation and the low-frequency content of the turbulent fluctuations. This low-frequency content was examined in data from wind tunnel experiments, Hypersonic International Flight Research Experimentation flight test 1 (HiFIRE-1), and large-eddy simulations, and was found to agree with a theory developed by Plotkin that represents the separation bubble as a frequency-selective amplifier. This approach to understanding of the physics of separation unsteadiness, combined with effective flow control actuators, shows promise for mitigating fatigue loading on high Mach number aircraft.					
15. SUBJECT TERMS computational fluid dynamics, CFD, computational, flow control, plasma, algorithms, hypersonics					
16. SECURITY CLASSIFICATION OF:			17. LIMITATION OF ABSTRACT: SAR	18. NUMBER OF PAGES 206	19a. NAME OF RESPONSIBLE PERSON (Monitor) Jonathan Poggie 19b. TELEPHONE NUMBER (Include Area Code) N/A
a. REPORT Unclassified	b. ABSTRACT Unclassified	c. THIS PAGE Unclassified			

Table of Contents

Section	Page
List of Figures	iv
Acknowledgements	v
1. Summary	1
2. Introduction	2
2.1 Background	2
2.2 Program Objectives	5
2.3 Approach	6
2.4 Challenges	6
3. Results and Discussion	7
3.1 Nanosecond-Pulse Dielectric Barrier Discharge Actuators	7
3.2 Shock-Wave/Boundary-Layer Interaction	9
3.3 Transitional/Turbulent Boundary Layers	11
4. Conclusions	13
5. References	14
List of Acronyms, Abbreviations, and Symbols	15
Appendix A - Nanosecond-Pulse Dielectric Barrier Discharge Actuators	16
Appendix B - Shock-Wave/Boundary-Layer Interaction	50
Appendix C - Transitional/Turbulent Boundary Layers	158

List of Figures

Figure	Page
Figure 1: Simulation of Nanosecond-Pulse Dielectric Barrier Discharge	7
Figure 2: Wall Pressure Fluctuation Spectra, with Comparison to Plotkin Model	10
Figure 3: Large-Eddy Simulation of Mach 2.9 Turbulent Boundary Layer	12

Acknowledgements

Work at AFRL under this project was sponsored in part by grants from the Air Force Office of Scientific Research (monitored by F. Fahroo, AFOSR/RTA, and J. Schmisser, AFOSR/RTE), and by grants of High Performance Computing (HPC) time from the Air Force Research Laboratory (AFRL), Army Research Laboratory (ARL), and the U.S. Army Engineer Research and Development Center (ERDC) DoD Supercomputing Resource Centers (DSRC).

The author would like to acknowledge helpful discussions of this ongoing work with D. Gaitonde, D. Rizzetta, M. Visbal, and M. White. G. Candler provided the hypersonic computational fluid dynamics code US3D for use in this project.

1 Summary

This report describes work carried out on numerical modeling of high Mach number flows and their control. Three main technical areas were addressed: nanosecond-pulse, dielectric barrier discharge flow control actuators, large-scale unsteadiness in separated shock-wave/boundary-layer interactions, and transitional/turbulent boundary layer flows.

High-fidelity fluid simulations of nanosecond-pulse discharges demonstrated the importance of rapid relaxation of excited neutrals and recombination of ions in generating the flow disturbance. Comparisons of fluid simulations with particle-in-cell simulations showed good agreement, confirming the appropriateness of the fluid approach.

In a supersonic compression ramp flow, a gliding discharge plasma actuator was found to be very effective in reducing the extent of separation and the low-frequency content of the turbulent fluctuations. This low-frequency content was examined in data from wind tunnel experiments, the HIFiRE-1 flight test, and large-eddy simulations, and was found to agree with a theory developed by Plotkin that represents the separation bubble as a frequency-selective amplifier. This approach to understanding of the physics of separation unsteadiness, combined with effective flow control actuators, shows promise for mitigating fatigue loading on high Mach number aircraft. Further, large-eddy simulations (LES) were found to be more appropriate for predicting separated, compressible flows than conventional, Reynolds-averaged Navier-Stokes models, in particular because these simulations capture the large-scale unsteadiness.

Additional calculations were carried out on transitional and turbulent boundary layer flows. Preliminary direct numerical simulations were carried out for the HIFiRE-1 boundary layer trip, and the effect of Reynolds number on the trip wake pattern was explored. A verification and validation project was undertaken for high-fidelity, implicit LES. In the first step of the project, results obtained with different computer codes and numerical approaches were compared to experimental measurements of turbulent boundary layer flows.

2 Introduction

Hypersonic flight is an enabling factor for long-range strike and reconnaissance in contested airspace. A particularly difficult and important scientific challenge in hypersonics is predicting and controlling the interaction of a shock wave and a turbulent boundary layer. Shock-wave/boundary-layer interactions occur in both internal flows (such as engine flow-paths) and external flows (such as fin-body junctures). They are associated with large-scale unsteadiness, extreme thermomechanical loads, and engine operability problems. The work reported here has focused on predicting heating and large-scale unsteadiness, and using plasma-based control schemes to mitigate their deleterious effects.

2.1 Background

Research efforts under this project have focused on high-speed flow and its control with plasma actuators. The physical models and numerical methods are described here.

2.1.1 Plasma Modeling

A reduced plasma kinetic model (23 species and 50 processes) was developed by carrying out a sensitivity analysis of a zero-dimensional plasma computation with an extended chemical kinetic model (46 species and 395 processes). The reduced model included the following species: molecular nitrogen and oxygen, atomic nitrogen and oxygen, ozone, nitric oxide, electrons, three species of ions, five electronically excited neutral species, and eight vibrationally excited neutrals. The reaction mechanism includes electron impact reactions, reactions with neutral radicals, quenching reactions and other transitions, charge exchange reactions, and electron-ion recombination.

Rather than use the traditional drift-diffusion (one-moment) model for charged particle motion, we chose to employ the more complex five-moment model in order capture nonlocal effects, and to directly address the transfer of momentum and energy between the charged particles and neutrals. For the neutral species, a diffusion equation formulation was used, and a mass-averaged formulation was used for the gas as whole.

The formulation allows for the interaction of the discharge with the bulk gas flow through both a body force and heating. The energy delivered to the bulk gas by the electric field is initially apportioned between internal energy, thermal energy, and kinetic energy. The portion that goes into internal energy is set by the chemical kinetic model, which also allows for chemical energy to thermalize over time.

A separate temperature was computed for each charged species, but a single translational temperature was assigned to all neutral species. The neutral translational temperature was determined by subtracting the flow kinetic energy and charged particle thermal energy from the total energy, and then solving the resulting expression for neutral gas energy for the translational temperature.

In the diffusive fluxes for the overall gas, a number of terms were retained involving the diffusion velocity that are often neglected in the mass-averaged formulation. In particular, the electron heat conduction and energy convected by the electron diffusion flux make significant contributions to the total energy balance near the edge of the cathode sheath.

Inelastic and elastic momentum and energy exchange were incorporated as source terms in the species conservation equations. The Poisson equation was employed to compute the electric potential.

The calculations were carried out using the Air Force Research Laboratory computer code HOPS (Higher Order Plasma Solver), which includes several physical models and numerical schemes. Here, the physical model described above was solved using an implicit, second-order, upwind formulation. The equations were solved in nondimensional form.

Time integration of the conservation equations was carried out using a second-order implicit scheme, based on a three-point backward difference of the time terms. The formulation is similar to the standard technique of Beam and Warming, but is adapted to a multi-fluid formulation with different models for particle motion. The solution was time accurate, with all equations advanced with the same time step.

Approximate factoring and quasi-Newton subiterations were employed. The implicit terms were linearized in the standard thin layer manner. The implicit terms were evaluated with second-order spatial accuracy, yielding a block tridiagonal system of equations for each factor. The species were loosely coupled, limiting the rank of the flux Jacobian matrices to the order of the moment model (one for the diffusion equation formulation, five for the charged particles and overall conservation equations). The resulting equations were solved using a standard block tridiagonal solver, and the change in the solution vector of conserved variables was driven to zero by the subiteration procedure at each time step. Three applications of the flow solver per time-step were employed for the present work.

For the charged particles and the bulk gas, the Roe scheme was employed for the inviscid fluxes. For the diffusion model, a simple upwinding scheme was employed, based on the convection velocity. In both formulations, stability was enforced using the minmod limiter in the MUSCL formalism.

The Poisson equation was solved at the end of each subiteration in the implicit time-marching scheme. (This procedure yields a stable time step that is comparable to that obtained using methods based on the linearization of the right-hand-side of the Poisson equation.) The formulation of the implicit scheme was analogous to that used for the conservation equations, with linearization of the implicit terms, approximate factoring, and an iterative procedure that drives the change in the solution to zero. The spatial derivatives were evaluated using second-order central differences, and the system was solved using a standard tridiagonal algorithm.

2.1.2 Fluid Modeling

For the work reported here, simulations were carried out with three, independently implemented computer codes (US3D, FDL3DI, and HOPS). The baseline numerical scheme for all three

solvers included nominally sixth-order accurate spatial differencing, and implicit, second-order accurate time integration. All three codes include the option of switching to a lower-order, upwind scheme in the vicinity of a shock.

The US3D code is an unstructured, finite volume solver developed by G. Candler's group at the University of Minnesota. The code solves the compressible Navier-Stokes equations using a cell-centered, finite-volume formulation. For the calculations of both the inviscid and viscous fluxes, gradients of flow variables are computed using a weighted least squares method.

In the present work, the inviscid fluxes were evaluated using the low-dissipation, kinetic energy preserving scheme of Subbareddy and Candler. In this formulation, the inviscid fluxes F are computed as the combination of a nondissipative symmetric component F_s and an upwinded dissipative component F_d multiplied by a shock detecting switch α :

$$F = F_s + \alpha F_d \quad (1)$$

The parameter $\alpha \in [0, 1]$ is chosen so that the dissipative portion of the flux evaluation is only used in regions near discontinuities. The present work employed the Ducros switch:

$$\alpha = \frac{(\nabla \cdot \vec{u})^2}{(\nabla \cdot \vec{u})^2 + \|\vec{\omega}\|^2} \quad (2)$$

where \vec{u} and $\vec{\omega}$ are the velocity and vorticity vectors, respectively.

Spatial derivatives of the inviscid fluxes were evaluated using a sixth-order accurate, gradient-based interpolation scheme with the following form:

$$\phi_{i+\frac{1}{2}} = \frac{\phi_i + \phi_{i+1}}{2} + \frac{8(\delta\phi_i + \delta\phi_{i+1})}{15} - \frac{\delta\phi_{i+1} + \delta\phi_{i+2}}{45} \quad (3)$$

Here $\delta\phi_i$ is the scalar (dot) product of the gradient of ϕ in Cell i and the vector from the center of Cell i to the center of Face $i+1/2$. The viscous fluxes were evaluated using a second-order accurate central difference scheme. The current computations were carried out using the perfect gas assumption. Second-order accurate, implicit time integration was employed.

Two codes developed at AFRL were also used in this study. The FDL3DI code was named for the Flight Dynamics Laboratory, a precursor organization to AFRL. This code is a high-order accurate, structured-grid, finite-difference solver for the perfect-gas, compressible-flow Navier-Stokes equations. The HOPS code (see Section 2.1.1) includes several physical models, but here it is employed as a single-fluid gasdynamics code. Employed in this way, the two codes represent independent implementations of essentially the same numerical approach.

Time integration of the conservation equations was carried out in the baseline approach using a second-order implicit scheme, based on a three-point backward difference of the time terms. The general formulation is similar to the standard technique of Beam and Warming. Approximate factoring and quasi-Newton subiterations were employed, with three applications of the flow

solver per time step. The implicit terms were evaluated using the scalar pentadiagonal formulation of Pulliam and Chaussee. For comparison, a fourth-order, explicit Runge-Kutta method was employed for some of the calculations.

The baseline spatial differencing scheme was based on compact differencing and filtering. In one dimension, the finite difference approximation to the first derivative ϕ'_i at Node i is evaluated by solving a tridiagonal system of the form:

$$\alpha\phi'_{i-1} + \phi'_i + \alpha\phi'_{i+1} = a\frac{\phi_{i+1} - \phi_{i-1}}{2} + b\frac{\phi_{i+2} - \phi_{i-2}}{4} \quad (4)$$

where α , a , and b are constants chosen to give a certain order of accuracy and set of spectral properties for the scheme.

Numerical stability was enforced using a low-pass, Padé-type, nondispersive spatial filter. The filtering approach replaces the computed value ϕ_i at a particular node with a filtered value $\bar{\phi}_i$:

$$\alpha_f\bar{\phi}_{i-1} + \bar{\phi}_i + \alpha_f\bar{\phi}_{i+1} = \sum_{n=0}^N \frac{a_n}{2} (\phi_{i+n} + \phi_{i-n}) \quad (5)$$

where the constants α_f , a_0 , ... a_N are chosen to give appropriate filter properties. The filter was applied to the solution vector, sequentially, in each of the three computational directions, following each sub-iteration for implicit time integration, or each time-step for explicit integration. The order of the filtering operation was permuted at each time step.

The hybrid compact-Roe shock capturing scheme of Visbal and Gaitonde was employed for flows containing strong shocks. The metrics were evaluated using the method of Thomas and Lombard.

2.2 Program Objectives

The main technical objectives of this program were to develop techniques for the prediction and control of supersonic flows in a range up to Mach 6. This regime is important for the development of Air Force systems with short response time and high survivability. The low supersonic regime is relevant for internal flows in scramjet engines, whereas the higher Mach number range is relevant for external flow over a vehicle.

Particular attention has been given to heat transfer and large-scale unsteadiness in separated, turbulent flow. Work on flow control has focused on actuators based on electrical discharges. These devices are an appealing flow control option for the high-speed regime because of their low profile, rapid actuation, and ability to operate in hostile environments.

2.3 Approach

The technical approach for the efforts on plasma modeling has been to attempt to improve the accuracy of predictions through more complex physical models. There are two main differences between the present approach and other recent studies of nanosecond pulse discharges in air. First, the present model emphasizes the chemical kinetics of energy storage and thermalization. Second, in place of a traditional drift-diffusion model under the local field approximation, a more detailed model of the charged particle motion was employed here to try to capture some of the nonlocal effects, and to directly address the transfer of momentum and energy between the charged particles and neutrals.

For modeling neutral gas flows, the technical approach has emphasized turbulence and transition without the use of explicit models. In particular, direct numerical simulation was applied to laminar-turbulent transition, and implicit large-eddy simulation was applied to turbulent flows. In the latter approach, the effect of unresolved turbulent scales is replicated using the filtering effect of the numerical scheme.

The personnel involved in this work were Dr. Nicholas Bisek, Dr. Roger Kimmel, and Dr. Jonathan Poggie of AFRL/RQHF, Dr. Donald Rizzetta of AFRL/RQVC, Dr. Scott Stanfield of Spectral Energies LLC, Dr. Joel Gronvall and Dr. Timothy Leger of Ohio Aerospace Institute, Dr. Ricky Tang of Universal Technology Corporation, Dr. Alexandre Likhanskii of Tech-X Corporation, and Prof. Igor Adamovich and Dr. Munetake Nishihara of The Ohio State University.

2.4 Challenges

The primary challenge to computational simulation of air vehicles in the hypersonic regime are the disparate length and time scales present in problem. Scales range from the molecular, to the component level, and to the flight profile. These disparate scales make the problems very stiff, and motivate the development of new, more efficient numerical algorithms to attack these problems.

3 Results and Discussion

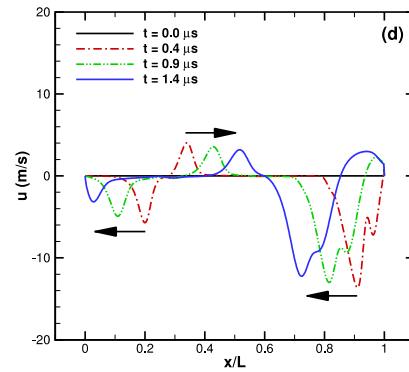
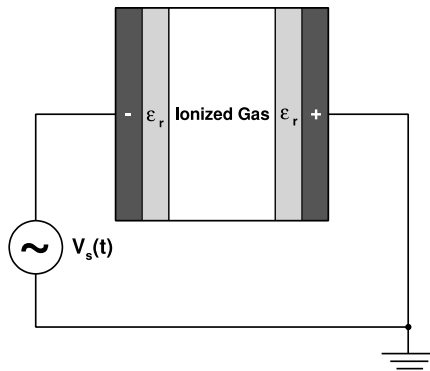
The following subsections review the work that was done under this project to explore high-speed flow and its control. Additional details can be found in publications reproduced in Appendices A through C. The work can be divided into three main categories: nanosecond-pulse dielectric barrier discharge actuators (Section 3.1 and Appendix A), shock-wave/boundary-layer interaction (Section 3.2 and Appendix B), and transitional/turbulent boundary layers (Section 3.1 and Appendix C).

In 2012, work was carried out on plasma-based flow control of separated shock-wave/boundary-layer interactions (Ref. [1], Appendix B). Work in 2013 focused on fluid simulation of nanosecond-pulse dielectric barrier discharges (Ref. [2], Appendix A), control of shock-wave/boundary-layer interaction (Ref. [3], Appendix B), kinetic modeling of discharges (Ref. [4], Appendix A), and large-scale separation unsteadiness (Ref. [5], Appendix B). Work in 2014 addressed turbulent boundary layer flows (Ref. [6], Appendix C), laminar-turbulent transition (Ref. [7], Appendix C), and Reynolds-averaged Navier-Stokes Simulations (Ref. [8], Appendix B).

3.1 Nanosecond-Pulse Dielectric Barrier Discharge Actuators

Repetitive, pulsed discharges are a well-known and appealing method for plasma generation. Such discharges are efficient generators of both ions and electronically excited species because of their high instantaneous reduced electric field. In aerospace applications, nanosecond-pulse discharges have been employed as flow control actuators, as a source of ionization for nonequilibrium magnetohydrodynamic devices, and as a means for enhancing ignition and combustion.

In a nanosecond-pulse discharge, the input energy in the electrical circuit is ultimately converted into heat and gas motion. Motivated by potential uses in flow control applications, we are interested in the details of the physics of this process. In recent work, we have developed both fluid (Ref. [2]) and kinetic models (Ref. [4]) of these discharges.



(a) Diagram of computational domain.

(b) Bulk gas velocity profiles.

Figure 1: Simulation of Nanosecond-Pulse Dielectric Barrier Discharge

3.1.1 Multi-Fluid Modeling

As detailed in Ref. [2], a physics-based model was developed for nanosecond-pulse discharges, including realistic air kinetics, electron energy transport, and compressible bulk gas flow. A reduced plasma kinetic model (23 species and 50 processes) was developed to capture the dominant species and reactions for energy storage and thermalization in the discharge. The kinetic model included electronically and vibrationally excited species, and several species of ions and ground state neutrals. The governing equations included the Poisson equation for the electric potential, diffusion equations for each neutral species, conservation equations for each charged species, and mass-averaged conservation equations for the bulk gas flow.

The results of calculations with this model highlighted the path of energy transfer in the discharge. At breakdown, the input electrical energy was transformed over a timescale on the order of 1 ns into chemical energy of ions, dissociation products, and vibrationally and electronically excited particles. About 30 percent of this energy was subsequently thermalized over a timescale of 10 μ s. Since the thermalization time scale was faster than the acoustic time scale, the heat release led to the formation of weak shock waves originating near the sheath edge, consistent with experimental observations.

Figure 1 shows sample results from this work. The configuration is shown on the left. The right electrode was grounded, and the left electrode was driven with a 27 kV amplitude, 12 ns duration negative Gaussian pulse. The air pressure was about 5 kPa, the discharge gap was 2 mm, and 1-mm-thick dielectric coatings covered the electrodes. The discharge leads to rapid heating at the sheath edges and the formation of shock waves. These waves can be seen in the bulk gas velocity profiles shown in the right figure. The gas velocity is sufficiently large to create a disturbance for flow control.

Despite the simplifications employed in the calculations, the computed translational temperature rise (40 K) and nitrogen vibrational temperature rise (370 K) were of the same order of magnitude as those measured experimentally (50 K and 500 K, respectively). The results illustrate how input electrical energy is rapidly transformed (over roughly 1 ns) at breakdown into ionization products, dissociation products, and electronically excited particles, and how thermalization occurs over a relatively longer time-scale (roughly 10 μ s). The quenching of electronically excited states and electron-ion recombination make roughly equal contributions to the thermalization of stored chemical energy.

This work represents a first step towards detailed fluid modeling of the nanosecond-pulse dielectric barrier discharge actuator. This type of actuator shows promise for high-speed flow control, and accurate numerical modeling will contribute the optimization of these devices. In ongoing work, we are extending the model to multiple dimensions, which should allow a more realistic representation of the electric field and better quantitative comparison with experiment.

3.1.2 Kinetic Modeling

Dielectric barrier discharge plasma (DBD) actuators have demonstrated high potential for active flow control for both subsonic and supersonic applications. However, both experimental and numerical studies showed that the performance of dielectric barrier discharge plasma actuators is

rather sensitive to the dielectric barrier discharge parameters, such as driving voltage and position of the actuators on the aerodynamic body. In order to transition research and development efforts to implementation onto aircraft, it is important to gain confidence in both experimental and simulation results for DBD laboratory studies.

Reference [4] explored the accuracy of simulations. A detail analysis was carried out of the most commonly used physical model (the drift-diffusion approximation) for physical accuracy, numerical convergence, and capabilities for high performance simulations. Detailed comparison was made between the results of drift-diffusion and particle-in-cell simulations, using the Tech-X code Vorpil. Grid resolutions requirements for a converged solution were addressed, along with scaling on multiple processors.

The simulations showed good agreement between kinetic and fluid approaches for key dielectric barrier discharge characteristics, such as streamer thickness, streamer height above dielectric surface, and generated electric fields. The main difference between particle-in-cell and fluid simulations was in the electron number density distribution within a streamer: it is rather grainy for the particle-in-cell approach and smooth for the fluid approach. We observed that maximum electric fields, generated at the streamer head, are in the range of 5×10^7 to 7×10^7 V/m. We also observed a large region between streamer body and dielectric surface, where the vertical component of electric field may reach up to 10^8 V/m.

3.2 Shock-Wave/Boundary-Layer Interaction

Shock-wave/boundary-layer interactions, or (more broadly) inviscid-viscous interactions, are at the heart of many of the design difficulties associated with flight at high Mach number. They occur wherever the vehicle shape deviates from a simple, smooth surface. Such flows are typically characterized by flow separation, large-scale unsteadiness, and extremely high heat transfer rates. They are the source of much of the aero-thermo-acoustic load that a high-speed vehicle must resist.

In recent work, we have addressed several aspects of the prediction of shock-wave/boundary-layer interaction. We have explored the limitations of conventional turbulence models in predicting heat transfer rates in strongly-perturbed, separated flow. We have also investigated large-scale unsteadiness in these interactions, both from the standpoint of prediction and control.

3.2.1 Reynolds-Averaged Navier-Stokes Modeling

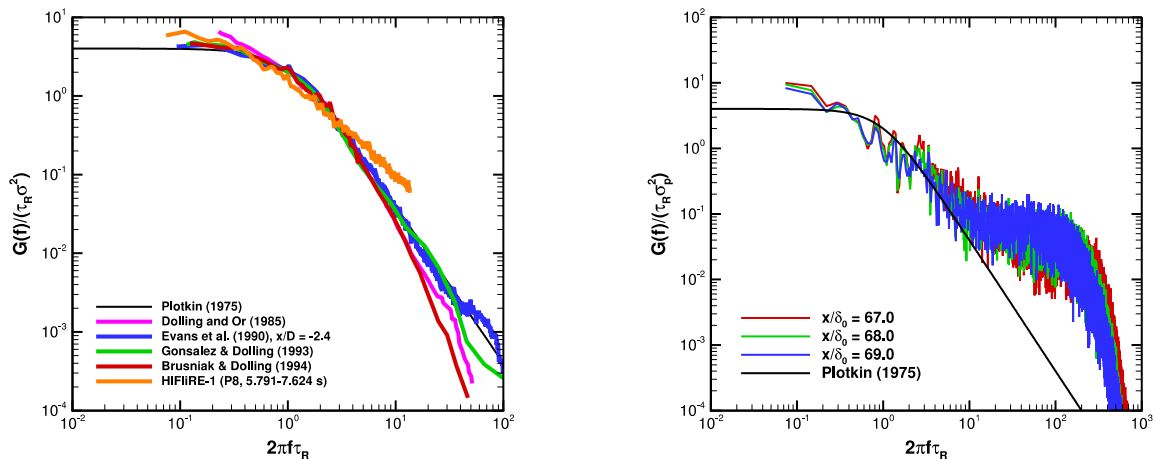
The investigation described in Ref. [8] was conducted to evaluate the error involved in predicting aerothermodynamic loads (surface pressure, skin friction, and heat transfer) using a Reynolds-averaged Navier-Stokes solver. Numerical simulations of shock-wave/turbulent boundary-layer Interaction at Mach 5 were performed, and compared with vetted experimental data. These simulations included three, two-dimensional impinging shock interactions and two, three-dimensional swept interactions. The impinging shock cases involved different levels of interaction intensity, which resulted in attached flow, incipient separation, and fully separated flows. Comparisons between the numerical results and experimental data for each case were used to evaluate the error in predicting the associated aero-thermodynamic loads. The results show

that wall pressure is accurately predicted, skin friction is under-predicted, and heat transfer is over-predicted. However, the trends in skin friction and heat transfer were captured by the RANS simulations. Overall, RANS simulations were judged to give adequate predictions of qualitative flow structure, but to be deficient for quantitative predictions of wall fluxes.

3.2.2 Plasma Control

In the study described in Ref. [1], the Navier-Stokes equations were solved using a high-fidelity, time-implicit numerical scheme, and an implicit large-eddy simulation approach, to investigate plasma based flow control for supersonic flow over a compression ramp. The configuration included a flat-plate region to develop an equilibrium turbulent boundary layer at Mach 2.25, which was validated against a set of experimental measurements. The fully turbulent boundary-layer flow interacted with a 24 deg ramp, and produced an unsteady shock-induced separation. A control strategy to suppress the separation through a magnetically-driven gliding-arc actuator was explored. The size, strength, and placement of the actuator were determined from the results of recent experiments. Three control scenarios were examined: steady control, pulsing with a 50% duty cycle, and control with realistic Joule heating. The results showed that the control mechanism is very effective at reducing the mean separation length for all three situations. The case without pulsing and Joule heating was the most effective, with a reduction in the separation length of more than 75%. Control was also found to significantly reduce the low-frequency content of the turbulent kinetic energy spectrum.

In the follow-on study described in Ref. [3], additional high-order, implicit large-eddy simulations were performed for the 24 deg compression ramp flow. As found previously, the interaction between the turbulent flow and the corner led to a low-frequency, unsteady, shock-induced separation. The model magnetically-driven plasma-based flow controller was applied to the flow to minimize the separated region and its adverse effects. The controller consisted of two streamwise separated segments pulsed 180 deg out of phase at a 50-percent duty-cycle. The results show that this controller configuration was very effective at reducing the separation while only using 80 percent of the power of the configuration in our previous study.



(a) Measured in wind tunnel and flight test.

(b) Computed in large-eddy simulation.

Figure 2: Wall Pressure Fluctuation Spectra, with Comparison to Plotkin Model

3.2.3 Large-Scale Unsteadiness

Large-scale separation unsteadiness is of particular concern in flight applications because the associated wall pressure fluctuations have significant energy content between 10 and 1,000 Hz, which encompasses the range of typical resonant frequencies of flat panels on high Mach number aircraft. Correlations for the form of the wall pressure fluctuation spectra are of interest for design against fatigue loading. Further, reduced-order models of the separation unsteadiness can assist in design decisions, and aid the development of feedback flow control systems. In the work described in Ref. [5], we attempted to quantify some the universal features of the separation unsteadiness by examining data from wind tunnel experiments, flight test experiments, and well-resolved large-eddy simulation.

Spectra of wall pressure fluctuations caused by separation shock unsteadiness were compared for data obtained from wind tunnel experiments, the HiFiRE-1 flight test, and large-eddy simulations. The results (Figure 2) were found to be in generally good agreement, despite varying Mach number and two orders of magnitude difference in Reynolds number. Relatively good agreement was also obtained between these spectra and the predictions of a theory developed by Plotkin, which depicts the separation shock unsteadiness as linearly damped Brownian motion. Further, the predictions of this theory are qualitatively consistent with the results of experiments in which the shock motion was synchronized to controlled perturbations. The results presented here support the idea that separation unsteadiness has common features across a broad range of compressible flows.

3.3 Transitional/Turbulent Boundary Layers

Boundary layer heat transfer rates can be almost an order of magnitude higher in turbulent flow than in laminar flow. Further, our research on separation unsteadiness indicates that the separation bubble acts as an amplifier of the large-scale disturbances in the incoming turbulent flow. To examine these issues, we have carried out high-fidelity boundary layer simulations in two recent studies.

3.3.1 Laminar-Turbulent Transition

Reference [7] describes a computational study of the effects of a discrete roughness element on a high-speed boundary layer flow. Four cases were studied, with one set based on the flow conditions during the ascent phase of HiFiRE-1. The work included a two-dimensional stability analysis of the cone geometry without roughness, and four high-fidelity simulations with the diamond-shaped roughness element. Reynolds number effects on the wake pattern were compared, and a preliminary comparison was carried out between second-order accurate and sixth-order accurate computational results.

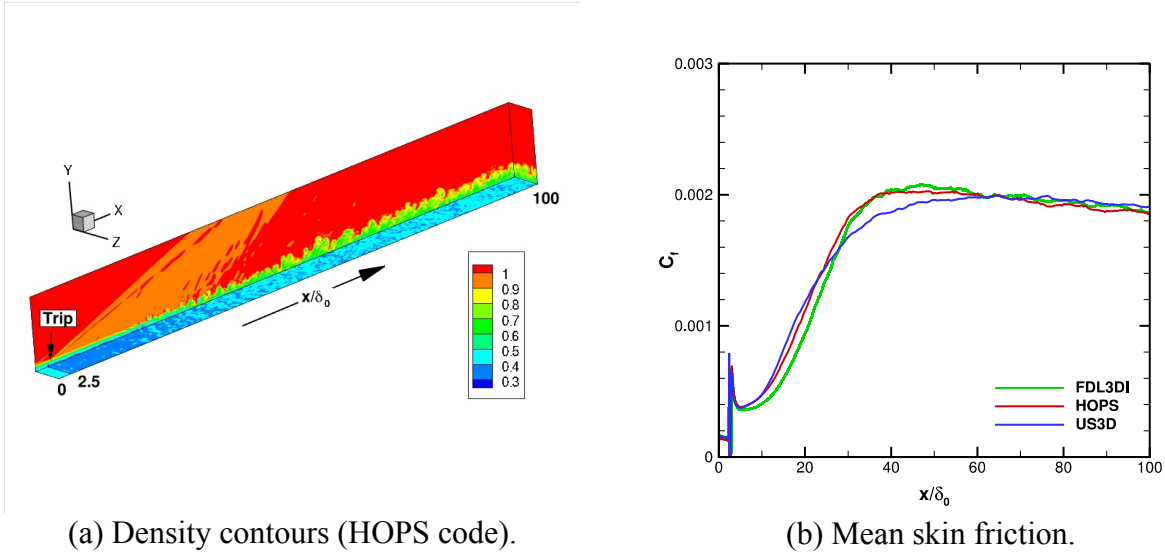


Figure 3: Large-Eddy Simulation of Mach 2.9 Turbulent Boundary Layer

3.3.2 Turbulent Boundary Layer Flow

For the work described in Ref. [6], high-fidelity, implicit LES of a Mach 2.9 turbulent boundary layer flow were carried out using three different computational fluid dynamics codes. The three codes (FDL3DI, HOPS, and US3D) employed the same formal order of spatial and temporal accuracy. The aim of the work was to compare code performance and accuracy, and to identify best practices for large-eddy simulations with the three codes. The simulations were carried out using the same boundary conditions, body force trip mechanism, grids, and time-step. Additional calculations were carried out to compare the results obtained with different numerical algorithms, and to explore correlations characterizing large-scale structures in the flow turbulence.

All three codes were able to produce plausible turbulent boundary layers, and showed good agreement in the region where the boundary layer was well developed (Figure 3). The details of the transition process, however, varied with the numerical method and the details of its execution. In particular, coarser grids and more dissipative numerical schemes led to delayed transition to turbulence in the calculations. The body force trip method was employed successfully in each case, and should be suitable for general application. Many of the features of the large-scale structures were found to match between computation and experiment, but additional work is warranted to explore the use of such comparisons to validate LES codes.

4 Conclusions

Several projects were carried out to explore the modeling of high Mach number flows and their control. The research addressed plasma flow control actuators, large-scale unsteadiness, and turbulent heating rates.

High-fidelity simulations of plasma actuators were carried out with multi-fluid models and particle-in-cell models. Comparison of these methods showed good agreement, confirming the usefulness of the fluid approach. These methods were applied to simulations of nanosecond-pulse discharges, and the results demonstrated the importance of rapid relaxation of excited neutrals and recombination of ions in generating the flow disturbances that are used for control. Additional calculations were carried out using reduced-order discharge models identified the possibility of mitigating the effects of large-scale unsteadiness with these devices.

Large-scale unsteadiness was examined in data from wind tunnel experiments, the HIFiRE-1 flight test, and large-eddy simulations, and was found to agree with a theory developed by Plotkin that represents the separation bubble as a frequency-selective amplifier. Large-eddy simulations were found to be more appropriate for predicting separated, compressible flows than conventional, Reynolds-averaged Navier-Stokes models, because these simulations capture the large-scale unsteadiness.

As a first step in a verification and validation project, three computer codes used in the AFRL Computational Sciences Center were compared for high-fidelity, implicit LES of a supersonic turbulent boundary layer flow. Relatively good agreement was obtained between the predictions of the codes and the results of wind tunnel experiments. Additional direct numerical simulations (DNS) were carried out with one of the codes for the HIFiRE-1 boundary layer trip, and again good results were obtained. High-fidelity simulations (LES and DNS) show promise as engineering tools for the prediction of heating rates in transitional and turbulent flows.

5. References

- [1] N.J. Bisek, D.P. Rizzetta, and J. Poggie, "Exploration of Plasma Flow Control for Supersonic Turbulent Flow over a Compression Ramp," AIAA Paper 2012-2700, American Institute of Aeronautics and Astronautics, June 2012.
- [2] J. Poggie, N.J. Bisek, I.V. Adamovich, and M. Nishihara, "Numerical Simulation of a Nanosecond Pulse Discharge in Mach 5 Flow, AIAA Paper 2013-0458, American Institute of Aeronautics and Astronautics, January 2013.
- [3] N.J. Bisek and J. Poggie, "Large-Eddy Simulations of Separated Supersonic Flow with Plasma Control," AIAA Paper 2013-0528, American Institute of Aeronautics and Astronautics, January 2013.
- [4] A. Likhanskii and J. Poggie, "On the Validation of Fluid Plasma Model for Pulse DBD Actuator Simulations against Full Kinetic Approach," AIAA Paper 2013-2494, American Institute of Aeronautics and Astronautics, June 2013.
- [5] J. Poggie, N.J. Bisek, R.L. Kimmel, and S.A. Stanfield, "Spectral Characteristics of Separation Shock Unsteadiness," AIAA Paper 2013-3203, American Institute of Aeronautics and Astronautics, June 2013.
- [6] J. Poggie, N.J. Bisek, T. Leger, and R. Tang, "Implicit Large-Eddy Simulation of a Supersonic Turbulent Boundary Layer: Code Comparison," AIAA Paper 2014-0423, American Institute of Aeronautics and Astronautics, January 2014.
- [7] J.E. Gronvall, N.J. Bisek, and J. Poggie, "High Fidelity Computational Study of the HIFiRE-1 Boundary Layer Trip," AIAA Paper 2014-0433, American Institute of Aeronautics and Astronautics, January 2014.
- [8] T. Leger and J. Poggie, "Computational Analysis of Shock Wave Turbulent Boundary Layer Interaction," AIAA Paper 2014-0951, American Institute of Aeronautics and Astronautics, January 2014.

List of Acronyms, Abbreviations, and Symbols

Acronym/ Abbreviation	Description
AFOSR	Air Force Office of Scientific Research
AFOSR/RTE	Energy, Power, and Propulsion Department
AFOSR/RTA	Dynamical Systems and Control Department
AFRL	Air Force Research Laboratory
AFRL/RQ	Aerospace Systems Directorate
AFRL/RQHF	Hypersonic Sciences Branch
AFRL/RQVC	Aerospace Vehicles Design & Analysis Branch
ARL	Army Research Laboratory
DBD	Dielectric barrier discharge
DNS	Direct numerical simulation
DoD	Department of Defense
DSMC	Direct simulation Monte Carlo
DSRC	DoD Supercomputing Resource Center
ERDC	US Army Engineer Research and Development Center
FDL3DI	AFRL computational fluid dynamics code
HIFiRE	Hypersonic International Flight Research Experimentation Program
HOPS	Higher-Order Plasma Solver, AFRL computer code
HPC	High-performance computing
LES	Large-eddy simulation
nsDBD	Nanosecond-pulse, dielectric barrier discharge
RANS	Reynolds-averaged Navier-Stokes simulation
US3D	Computational fluid dynamics code from University of Minnesota

Symbols		Subscript	Description
C_f	Skin friction coefficient	d	Dissipative component
f	Frequency	i	Grid index
F	Inviscid flux term	n	Grid index
G	One-sided power spectral density	p	Pressure
L	Reference length scale	s	Symmetric component
t	Time		
u	Velocity		
V_s	Input voltage		
x	Streamwise coordinate		
α	Numerical parameter		
δ_0	Reference boundary layer thickness		
ϵ_r	Relative permittivity		
σ	Standard deviation		
τ_R	Separation time scale		
ϕ	Generic dependent variable		
ω	Vorticity		

Appendix A

Nanosecond-Pulse Dielectric Barrier Discharge Actuators

Numerical Simulation of a Nanosecond Pulse Discharge in Mach 5 Flow

Jonathan Poggie* and Nicholas J. Bisek†

Air Force Research Laboratory, Wright-Patterson AFB, Ohio 45433-7512 USA

Igor V. Adamovich‡ and Munetake Nishihara§

The Ohio State University, Columbus, Ohio 43210 USA

A physics-based model was developed for nanosecond-pulse discharges, including realistic air kinetics, electron energy transport, and compressible bulk gas flow. A reduced plasma kinetic model (23 species and 50 processes) was developed to capture the dominant species and reactions for energy storage and thermalization in the discharge. The kinetic model included electronically and vibrationally excited species, and several species of ions and ground state neutrals. The governing equations included the Poisson equation for the electric potential, diffusion equations for each neutral species, conservation equations for each charged species, and mass-averaged conservation equations for the bulk gas flow. The results of calculations with this model highlighted the path of energy transfer in the discharge. At breakdown, the input electrical energy was transformed over a timescale on the order of 1 ns into chemical energy of ions, dissociation products, and vibrationally and electronically excited particles. About 30% of this energy was subsequently thermalized over a timescale of 10 μ s. Since the thermalization time scale was faster than the acoustic time scale, the heat release led to the formation of weak shock waves originating near the sheath edge, consistent with experimental observations.

I. Introduction

In a nanosecond-pulse discharge, the input energy in the electrical circuit is ultimately converted into heat and gas motion. Motivated by potential uses in flow control applications, we are interested in the details of the physics of this process.

Repetitive, pulsed discharges are a well-known and appealing method for plasma generation.¹⁻³ Such discharges are efficient generators of both ions and electronically excited species because of their high instantaneous reduced electric field.⁴ In aerospace applications, nanosecond-pulse discharges have been employed as flow control actuators,⁵⁻⁸ as a source of ionization for nonequilibrium magnetohydrodynamic devices,^{9,10} and as a means for enhancing ignition and combustion.^{11,12}

The generation of shock waves by volumetric heat release in pulsed discharges was observed and explained in the 1970s in the context of gas laser technology.^{13,14} Early computations by Aleksandrov et al.¹⁴ assumed that all the power dissipated in the discharge immediately went into heating the neutral gas. Popov,¹⁵ however, has proposed a two-stage heating mechanism in which product species and electronically excited species are generated by electron impact, and then the stored chemical energy is converted to thermal energy through quenching and recombination reactions. (Reports on other investigations of kinetic mechanisms can be found in Refs. 16-18.) Two-dimensional calculations have been carried out recently by Unfer and Boeuf,¹⁹ assuming instant thermalization of 30% of the dissipated power that goes into electronic excitation.

In recent experiments by Nishihara et al.,²⁰ control of a Mach 5 cylinder flow was demonstrated using a pulsed surface dielectric barrier discharge. The hollow cylinder model was made of fused quartz. A thin

*Senior Aerospace Engineer, Hypersonic Sciences Branch. Associate Fellow AIAA.

†Research Aerospace Engineer, Hypersonic Sciences Branch. Member AIAA.

‡Professor, Department of Mechanical Engineering. Associate Fellow AIAA.

§Postdoctoral Researcher, Department of Mechanical Engineering. Member AIAA.

copper exposed electrode was affixed to the surface of the cylinder, with a second copper electrode mounted inside. A combination of positive and negative polarity pulses applied to the two electrodes produced a potential difference of about 27 kV, lasting on the order of 5 ns (pulse full-width at half maximum). The effects of the energy release in the resulting discharge were captured using phase-locked schlieren imaging. A weak shock wave was seen to form near the edge of the exposed electrode, and propagate upstream in the shock-layer flow over a time scale on the order of microseconds. When the perturbation reached the bow shock, its shape was altered, and the standoff increased by up to 25%.

We have begun to formulate a high-fidelity physical model of the energy transfer process in the pulsed surface dielectric barrier discharge. For simplicity, we have focused in the present work on a planar geometry; experimental evidence shows that a nearly one-dimensional discharge can occur at relatively low pressures.²¹ Using coupled modeling of the plasma and compressible flow in a one-dimensional geometry for conditions representative of the stagnation region of the Mach 5 cylinder flow experiments, we are studying the dominant physical effects, including energy thermalization kinetics and compression wave formation and propagation.

To this end, a reduced plasma kinetic model (23 species and 50 processes) was developed first by carrying out a sensitivity analysis of a zero-dimensional plasma computation with an extended chemical kinetic model (46 species and 395 processes).²² Transient, one-dimensional discharge computations were then carried out using the reduced kinetic model, incorporating conservation equations for each species, a self-consistent computation of the electric potential using the Poisson equation, and a mass-averaged gas dynamic formulation for the bulk gas motion. This paper presents the major results of these calculations, for conditions corresponding to the cylinder flow experiments.

II. Physical Model

This section presents the chemical kinetics model and the conservation laws governing each species, the bulk gas, and the electrodynamics. There are two main differences between the present approach and other recent studies of nanosecond pulse discharges in air.^{19,23–26} First, the present model emphasizes the chemical kinetics of energy storage and thermalization. Second, in place of a traditional drift-diffusion model under the local field approximation, a more detailed model of the charged particle motion was employed here to try to capture some of the nonlocal effects, and to directly address the transfer of momentum and energy between the charged particles and neutrals.

A. Reduced Kinetic Model

A reduced chemical kinetics model²² was developed to identify the dominant species and reactions affecting the energy balance and the rate of thermalization in the discharge, and to minimize the computational cost of the transient, one-dimensional calculations that will be presented here. To obtain the reduced kinetic model, we applied a sensitivity analysis to a detailed, transient, zero-dimensional air plasma model used in previous work.²⁷ The full air plasma model was based on the model developed by Kossyi et al.²⁸ The main criterion for the sensitivity analysis was the effect of individual processes on the time-dependent energy fraction thermalized after the discharge pulse. The species included in the model are given in Table 1 and the reaction mechanism is listed in Table 2.

The reduced model includes the following species: molecular nitrogen and oxygen, atomic nitrogen and oxygen, ozone, nitric oxide, electrons, three species of ions, five electronically excited neutral species, and eight vibrationally excited neutrals. The reaction mechanism includes electron impact reactions (Reactions 1-10 and 43-50), reactions with neutral radicals (Reactions 11-17), quenching reactions and other transitions (Reactions 18-32), charge exchange reactions (Reactions 33-34), and electron-ion recombination (Reactions 35-42). Rate coefficient curve fits for most of the reactions are given in Table 2, with the remaining coefficients plotted in Fig. 1.

For the high reduced-electric-fields considered here, the rate of electron impact ionization greatly exceeds the rate of electron attachment, and processes involving negative ions do not affect the energy balance. Thus they are omitted from the model.

Further, the model also omits vibrational relaxation, which would occur over time scales much longer than those considered in the simulations. For example, for a temperature of 300 K and a pressure of 0.05 atm, the characteristic time scale for vibrational-translational relaxation of vibrationally excited nitrogen by oxygen atoms²⁹ is about 200 μ s. The time scales of interest in the present simulations are more than an order of

magnitude shorter than this.

In developing the model, zero-dimensional Boltzmann equation calculations were carried out with a steady, two-term expansion of the electron energy distribution function of the plasma electrons.³⁰ These calculations employed experimental cross sections of electron impact electronic excitation, dissociation, ionization, and dissociative attachment processes.^{31,32} The rate coefficients of the electron impact processes, as functions of the electron temperature T_e , were derived from the point Boltzmann solutions by averaging the cross sections over the electron energy distribution function. The results of these calculations are summarized in Fig. 1.

Extremely high reduced electric fields are present in the cathode sheath. Since the sheath is essentially particle-free, the critical region for accurate modeling of the discharge under the present conditions is actually the vicinity of the cathode sheath edge, where significant ionization is present and the reduced electric field is less than 1000 Td.

As a test of the validity of the model, we computed the Townsend ionization coefficient $\alpha/N = k_i/u_e$ for nitrogen using the point Boltzmann solver, and compared the results to the experimental data of Haydon and Williams.³³ The results are shown in Fig. 2. The solid line represents the results of the Boltzmann calculations, and the symbols indicate the experimental data. Error bars are included on the experimental points, representing a tolerance of three times the experimental standard deviation. Error bars are omitted for those points where the experimental uncertainty is on the order of the symbol size.

For reduced electric fields below about 1000 Td, the calculations and measurements agree within the experimental uncertainty (5%-17%). For fields between 1000 Td and 3000 Td, the Boltzmann solution is about 10% higher than the experimental data. Only above 3000 Td does the error become substantial. Thus the level of uncertainty in the present model is typical of continuum electrical discharge computations. Moreover, in PIC-MCC (particle-in-cell, Monte-Carlo collision) computations of streamers in air, Chanrion and Neubert³⁴ found that the reduced electric field had to exceed 1000 Td for runaway electrons to be observed.

Although fields higher than 1000 Td were observed in the present calculations, those regions were essentially free of charged particles. At the location of peak charged particle number density, the reduced electric field ranged from about 50 Td at 5 kV input amplitude to 130 Td at 27 kV input amplitude. Thus the physical model for ionization at the sheath edge is sufficiently accurate to permit basic parametric studies of the nanosecond-pulse, dielectric barrier discharge.

B. Governing Equations

Rather than use the traditional drift-diffusion (one-moment) model for charged particle motion, here we chose to employ the more complex five-moment model³⁵⁻⁴⁰ in order capture nonlocal effects, and to directly address the transfer of momentum and energy between the charged particles and neutrals.

Mass, momentum, and energy conservation equations were solved for each charged species:

$$\frac{\partial}{\partial t}(m_s n_s) + \nabla \cdot (m_s n_s \mathbf{v}_s) = m_s \omega_s \quad (1)$$

$$\frac{\partial}{\partial t}(m_s n_s \mathbf{v}_s) + \nabla \cdot (m_s n_s \mathbf{v}_s \mathbf{v}_s + p_s \mathbf{I}) = \nabla \cdot \tau_s + q_s n_s \mathbf{E} + \mathbf{A}_s \quad (2)$$

$$\frac{\partial}{\partial t}[m_s n_s \mathcal{E}_s] + \nabla \cdot [m_s n_s \mathbf{v}_s \mathcal{E}_s + p_s \mathbf{v}_s] = \nabla \cdot [\tau_s \cdot \mathbf{v}_s - \mathbf{Q}_s] + q_s n_s \mathbf{v}_s \cdot \mathbf{E} + M_s \quad (3)$$

The mass per particle of each species is denoted as m_s , and the corresponding charge per particle is q_s . The species number density is n_s , the velocity is \mathbf{v}_s , the total energy is $\mathcal{E}_s = \epsilon_s + \frac{1}{2}v_s^2$, the internal energy is ϵ_s , and the pressure is p_s . The electric field is \mathbf{E} . Here ω_s is the rate of production of particles in chemical reactions, \mathbf{A}_s is the momentum exchange in collisions, and M_s is the energy exchange. The species shear stress is τ_s and the species heat flux is \mathbf{Q}_s .

The pressure is found from $p_s = n_s k_B T_s$, where k_B is the Boltzmann constant and T_s is the translational temperature. The internal energy per particle is assumed to have the form $m_s \epsilon_s = \mathcal{H}_s^0 + k_B(T_s - T^0)/(\gamma_s - 1)$, where γ_s is the ratio of specific heats and \mathcal{H}_s^0 is the heat of formation per particle of species- s . Values for the heat of formation of each species are given in Table 1.

For the neutral species, a diffusion equation formulation was used:

$$\frac{\partial n_s}{\partial t} + \nabla \cdot \left(n_s \mathbf{w} - \frac{D_s}{k_B T_n} \nabla p_s \right) = \omega_s \quad (4)$$

Approved for public release; distribution unlimited.

3 of 16

where D_s is the diffusion coefficient and \mathbf{w} is the mass-averaged velocity.

For the gas as a whole, a mass-averaged formulation was employed:

$$\frac{\partial \rho}{\partial t} + \nabla \cdot (\rho \mathbf{w}) = 0 \quad (5)$$

$$\frac{\partial}{\partial t} (\rho \mathbf{w}) + \nabla \cdot (\rho \mathbf{w} \mathbf{w} + p \mathbf{I}) = \nabla \cdot \tau + \zeta \mathbf{E} \quad (6)$$

$$\frac{\partial}{\partial t} (\rho \mathcal{E}) + \nabla \cdot (\rho \mathbf{w} \mathcal{E} + p \mathbf{w}) = \nabla \cdot (\tau \cdot \mathbf{w} - \mathbf{Q}) + \mathbf{E} \cdot \mathbf{j} \quad (7)$$

Here ρ is the overall density, p is the overall pressure, ζ is the space charge, and \mathbf{j} is the electric current. The diffusion velocity for each species is $\mathbf{U}_s = \mathbf{v}_s - \mathbf{w}$, $\rho \mathcal{E} = \rho \epsilon + \frac{1}{2} \rho w^2 + \sum_s \frac{1}{2} m_s n_s U_s^2$ is the total energy of the bulk gas flow, and ϵ is the total internal energy per unit mass.

The formulation allows for the interaction of the discharge with the bulk gas flow through both a body force and heating. Note that the energy delivered to the bulk gas by the electric field is initially apportioned between internal energy, thermal energy, and kinetic energy. The portion that goes into internal energy is set by the chemical kinetic model, which also allows for chemical energy to thermalize over time.

A separate temperature was computed for each charged species, but a single translational temperature was assigned to all neutral species. The neutral translational temperature T_n was determined by subtracting the flow kinetic energy and charged particle thermal energy from the total energy $\rho \mathcal{E}$, then solving the resulting expression for neutral gas energy for the translational temperature.

The diffusive fluxes for the overall gas are:

$$\tau = \sum_s (\tau_s - m_s n_s \mathbf{U}_s \mathbf{U}_s) \quad (8)$$

$$\mathbf{Q} = \sum_s \left[\mathbf{Q}_s + m_s n_s \mathbf{U}_s \left(h_s + \frac{1}{2} U_s^2 \right) - \tau_s \cdot \mathbf{U}_s \right] \quad (9)$$

The summations in (8)-(9) include separate flux terms for each charged species, but the fluxes for the neutral species were combined in a single representative term for air. Note that we have retained a number of terms involving the diffusion velocity that are often neglected in the mass-averaged formulation. In particular, the electron heat conduction and energy convected by the electron diffusion flux make significant contributions to the total energy balance near the edge of the cathode sheath.

The Poisson equation was employed to compute the electric potential:

$$\nabla^2 \phi = -\zeta / \epsilon_0 \quad (10)$$

where ϵ_0 is the permittivity of free space. The electric field was found from $\mathbf{E} = -\nabla \phi$.

C. Closure Models

In the equation set (1)-(3), closure models are needed for the collision source terms, the viscous stress tensor, and the heat flux vector. First we consider the elastic and inelastic components of the momentum exchange term $\mathbf{A}_s = \mathbf{A}_s^E + \mathbf{A}_s^I$ and the energy exchange term $M_s = M_s^E + M_s^I$.

Because the gas is assumed to be weakly ionized, the primary elastic collisions are with neutral particles. The following models are used for the elastic components of the collision source terms^{41,42} for the charged particles:

$$\mathbf{A}_s^E = -n_s m_s \nu_s (\mathbf{v}_s - \mathbf{v}_n) \quad (11)$$

$$M_s^E = -n_s \frac{m_s \nu_s}{m_s + m_n} [3k_B (T_s - T_n) + (\mathbf{v}_s - \mathbf{v}_n) \cdot (m_s \mathbf{v}_s + m_n \mathbf{v}_n)] \quad (12)$$

Here ν_s is the rate of collision with the neutrals, and m_n is an average particle mass for the neutrals. The neutral translational temperature T_n was described earlier, and $\mathbf{v}_n \approx \mathbf{w}$ is the mass-averaged velocity of the neutrals.

Inelastic momentum and energy exchange terms, corresponding to the reaction mechanism listed in Table 2, were also included in the closure model. A reaction- r in the kinetic model can be expressed

symbolically in the form:

$$\sum_{s=1}^N \nu'_{rs} \mathcal{M}_s \rightarrow \sum_{s=1}^N \nu''_{rs} \mathcal{M}_s \quad (13)$$

where ν'_{rs} and ν''_{rs} are the stoichiometric coefficients for the reactants and products and \mathcal{M}_s is the chemical symbol for species- s . Using the law of mass action,⁴³ the rate of production of species- s can be expressed as:

$$\omega_s = \sum_r (\nu''_{rs} - \nu'_{rs}) k_r \prod_{t=1}^N n_t^{\nu'_{rt}} \quad (14)$$

where k_r is the reaction-rate constant.

The form for the inelastic momentum source terms was $\mathbf{A}_s^I = m_s \omega_s \mathbf{v}_s$ for all species, and the energy source term for the ions was $M_s^I = m_s \omega_s \mathcal{E}_s$. A more complex energy exchange term was necessary for the electrons:

$$M_s^I = m_s \omega_s \mathcal{E}_s - \sum_r R_r \Delta H_{rs} \quad (15)$$

Here $R_r = k_r \prod_{s=1}^N n_s^{\nu'_{rs}}$ is the rate of progress of reaction- r and ΔH_{rs} is the corresponding energy loss for species- s . The energy loss includes the cost of heating the electrons to the average electron temperature, and is given for each reaction in Table 3.

For a plasma in a uniform electric field, as considered in the Boltzmann solutions used to establish the rates of the electron impact reactions, overall energy conservation reduces to balance between the work done by the electric field and the energy exchange in collisions. This balance was checked for consistency for both the electron (3) and total (7) energy equations, and an error of no more than a few percent was observed over a range of electron temperatures up to 100 eV.

For the flux terms, it was assumed that the viscous term had a Newtonian form, with Stokes hypothesis applied, and that the heat flux followed Fourier's law:

$$\tau_s = \mu_{vs} \left[(\nabla \mathbf{v}_s) + (\nabla \mathbf{v}_s)^T - \frac{2}{3} \nabla \cdot \mathbf{v}_s \mathbf{I} \right] \quad (16)$$

$$\mathbf{Q}_s = -k_s \nabla T_s \quad (17)$$

where μ_{vs} is the viscosity and k_s is the thermal conductivity for species- s .

D. Transport Properties

The viscosity and thermal conductivity of the neutrals were found from standard correlations for air.⁴⁴ The ion-neutral collision rate was determined as follows:⁴⁵

$$\nu_s/N = \sigma_s \sqrt{\frac{8k_B T_s}{\pi m_s}} + |\mathbf{v}_s - \mathbf{v}_n|^2 \quad (18)$$

where σ_s is an effective collision cross-section and N is the overall number density. The collision cross-sections used for each species are given in Table 1; the values were determined from mobility and diffusion coefficient data in the literature.⁴⁵⁻⁵¹ As discussed previously, the collision rate for the electrons was determined from a point Boltzmann solution as a function of electron temperature $\nu_e/N = f(T_e)$, and is shown in Fig. 1.

The relationship between the collision rate and the transport coefficients is as follows:

$$D_s = \frac{k_B T_s}{m_s \nu_s} \quad (19)$$

$$\mu_{vs} = \frac{2}{3} n_s m_s D_s \quad (20)$$

$$k_s = \frac{5}{2} k_B n_s D_s \quad (21)$$

The forms for the viscosity and thermal conductivity correspond to a Lewis number of unity and a Prandtl number of 2/3. Note that the viscosity and thermal conductivity coefficients are proportional to number density. These transport properties are small for the low charged particle number densities in the cathode sheath, but become significant near the sheath edge.

III. Numerical Implementation

This section describes the numerical algorithm and boundary conditions. In short, an implicit, second-order upwind scheme was employed, along with standard boundary conditions for the dielectric surfaces.

A. Numerical Methods

The calculations were carried out using the Air Force Research Laboratory computer code HOPS (Higher Order Plasma Solver), which includes several physical models and numerical schemes.^{22,52} Here, the physical model consisting of (1)-(7) and (10) was solved using an implicit, second-order, upwind formulation. The equations were solved in a nondimensional form that has been described in previous papers.⁵³

Time integration of the conservation equations (1)-(7) was carried out using a second-order implicit scheme, based on a three-point backward difference of the time terms. The formulation is similar to the standard technique of Beam and Warming,⁵⁴ but is adapted here to a multi-fluid formulation with different models for particle motion. The solution was time accurate, with all equations advanced with the same time step.

Approximate factoring and quasi-Newton subiterations were employed. The implicit terms were linearized in the standard ‘thin layer’ manner. The implicit terms were evaluated with second-order spatial accuracy, yielding a block tridiagonal system of equations for each factor. The species were loosely coupled, limiting the rank of the flux Jacobian matrices to the order of the moment model (one for the diffusion equation formulation, five for the charged particles and overall conservation equations). The resulting equations were solved using a standard block tridiagonal solver, and the change in the solution vector of conserved variables was driven to zero by the subiteration procedure at each time step. Three applications of the flow solver per time-step were employed for the present work.

For the charged particles and the bulk gas, the Roe scheme^{55–57} was employed for the inviscid fluxes. For the diffusion model, a simple upwinding scheme was employed, based on the convection velocity. In both formulations, stability was enforced using the minmod limiter in the MUSCL formalism.⁵⁸

The Poisson equation (10) was solved at the end of each subiteration in the implicit time-marching scheme. (This procedure yields a stable time step that is comparable to that obtained using methods based on the linearization of the right-hand-side of the Poisson equation.⁵⁹) The numerical scheme was adapted from the approach described by Holst.⁶⁰ The formulation of the implicit scheme was analogous to that used for the conservation equations, with linearization of the implicit terms, approximate factoring, and an iterative procedure that drives the change in the solution to zero. The spatial derivatives were evaluated using second-order central differences, and the system was solved using a standard tridiagonal algorithm.

B. Boundary Conditions

A one-dimensional computational domain was employed to represent a double dielectric barrier discharge (Fig. 3). All the boundary conditions were enforced to second-order numerical accuracy. No-slip boundary conditions with a constant temperature wall were employed for the bulk gas. A zero wall-normal derivative was imposed for the neutral species.

Standard boundary conditions were employed for the charged particles. First, provisional conditions at the wall were determined by setting the normal derivative to zero. Then, if the ion flow was away from the boundary, the ion flux was set to zero and the ion temperature was set to the wall temperature. For electron flow from the wall into the domain, the normal component of the electron velocity was set to that required to satisfy secondary emission, and the electron temperature was set to a specified emission temperature (here, 1 eV).

Simplified boundary conditions were employed to model a thin dielectric electrode coating.⁴⁹ The dielectric layer was assumed to be sufficiently thin to be approximated a linear potential profile (uniform electric field \mathbf{E}_d). The electric field inside the dielectric was related to the electric field \mathbf{E} at the surface through the relation $\epsilon_0 \mathbf{E} - \epsilon_r \epsilon_0 \mathbf{E}_d = \sigma \mathbf{n}$, where σ is the surface charge density and \mathbf{n} is the unit normal vector pointing into the computational domain. The surface charge was determined by integrating $\partial\sigma/\partial t = -\mathbf{j} \cdot \mathbf{n}$ for each surface point,⁶¹ using a time-marching scheme analogous to that of the main governing equations.

C. Two-Stage Formulation

For computational efficiency, the calculations were carried out in two stages. The first stage encompassed the first 400 ns of the discharge. For this stage, the full physical model discussed above was employed. Since electromagnetic effects and charged particle motion become negligible after the input pulse dies away (after about 24 ns), in the second stage of the computations (0.4 μ s to 100.4 μ s), the electric field was set to zero and neutrality was enforced by appropriately setting the electron number density. This two-stage approach resulted in a substantial savings in computational cost, and tests comparing this approach to the full formulation showed a negligible difference.

IV. Results

Calculations were carried out for a one-dimensional discharge under conditions representative of the stagnation region of a Mach 5 cylinder flow experiment described in a previous publication.²⁰ The corresponding stagnation conditions were 4.74 kPa (36 Torr) and 310.3 K; for each case in the calculations discussed below, the initial, uniform state of the neutral gas was set to these values.

The configuration considered here is illustrated in Fig. 3. The problem is one-dimensional. In the simulations, the right electrode was grounded, and the left electrode was powered with the input signal $V_s = -V_0 \exp[-(t - t_0)^2/\tau^2]$. For the present calculations, the input signal parameters were $V_0 = 5$ kV to 27 kV, $\tau = 3$ ns, and $t_0 = 12$ ns.

Both electrodes were assumed to be covered with a $d = 1$ mm thick dielectric coating, with a relative dielectric constant of $\epsilon_r = 3.8$, chosen to be representative of fused quartz. The discharge gap (distance between the dielectric surfaces) was taken to be $L = 2$ mm. The secondary emission coefficient was $\gamma_{\text{sem}} = 0.05$.

The initial mole fraction of the electrons and each of the neutral minor species was taken to be 1×10^{-10} . The number densities of the vibrational states of N_2 were set to an equilibrium distribution for the initial temperature. The mole fraction for each ion species was equal, and set so that the space charge was zero. The initial electric field was zero. The ion, electron, and neutral temperatures were set to 310.3 K, and all velocities were set to zero.

For the calculations presented here, a uniform grid of 1001 points across the gap was employed ($\Delta x = 2 \mu\text{m}$). Grid resolution studies presented in a previous paper²² indicate that this level of grid resolution is sufficient for this problem.

The time step for the Stage 1 calculations (see Sec. III.C) was taken to be 0.5 ps for the 5 kV case. The minimum chemical kinetic time scale and dielectric relaxation time scale were both about 20 ps, and the minimum electron diffusion time scale was about 2.5 ps, so the time-evolution of the discharge was well-resolved in the calculations. The corresponding time step for the 10 kV and 20 kV cases was 0.25 ps, and for the 27 kV case it was 0.125 ps. For the Stage 2 calculations, the time step was taken to be 0.5 ns for all cases.

A. Baseline Case

A baseline case with $V_0 = 5$ kV was studied first. The general structure of the discharge is shown in figures 4-5, which show profiles of number density, potential, velocity, and temperature at times corresponding to the peak in the input voltage (12 ns, Fig. 4) and the effective end of the input signal (24 ns, Fig. 5). The cathode sheath is evident at the left in the figures as a region largely free of charged particles. There is a relatively large electric field in the sheath, resulting from the region of space charge at the sheath edge ($x/L \approx 0.3$).

Note that the electron velocity and temperature at the left boundary are set by secondary emission. At the peak of the input signal (12 ns), ion velocities reach $\sim 10^3$ m/s in the sheath, and electron velocities $\sim 10^6$ m/s. Corresponding temperatures reach ~ 1 eV for the ions and 50 eV for the electrons. Although these values are quite high, the charged particle density is extremely low in the left sheath, and there is essentially no conduction current or energy storage there. Despite the high dimensional velocities, it should be noted that the maximum electron Mach number is about 0.7, and the maximum ion Mach number lies in the range of 1.0-1.6.

As the input signal dies away, the discharge enters a dual-cathode regime,⁴ as seen in Fig. 5 at 24 ns. At both boundaries, ions travel toward the wall, and electrons away. At this stage, the space charge in the left sheath has decayed significantly, but the right sheath is quite prominent.

Note the qualitative differences between the left and right sheaths. The left sheath is formed during the input voltage rise by way of an ionization wave propagating into a very weakly pre-ionized plasma. The right sheath forms during the voltage fall, in a region with significant existing ionization. Its characteristics are similar to those of sheaths at a negative electrode in a DC or RF discharge. In particular, there is significant ion current in the right sheath, in contrast to the absence of conduction current in the left sheath.

B. Acoustic Waves

The interaction between the discharge and the bulk gas flow occurs through the source terms in Eqs. (6)-(7). Terms of interest include the body force $\zeta \mathbf{E}$, the rate of work done by the body force $\zeta \mathbf{E} \cdot \mathbf{w}$, and the total electromagnetic power $\mathbf{E} \cdot \mathbf{j}$. Maximum values of these terms occur near the edge of the left sheath at the peak of the input waveform, and near the edge of the right sheath as the input waveform decays. The body force is always directed toward the electrodes, and tends to be stronger for the left sheath. For the $V_0 = 5$ kV input amplitude, the order of magnitude of the terms was as follows: peak body force 10^5 N/m³, rate of work done by body force 10^4 W/m³, and total electromagnetic power 10^{10} W/m³. The corresponding values for $V_0 = 27$ kV were: peak body force 10^7 N/m³, rate of work done by body force 10^7 W/m³, and total electromagnetic power 10^{11} W/m³. (These large values exist only for time scales on the order of the width of the input waveform, and for spatial scales on the order of the discharge volume.) Since the total power is four to six orders of magnitude larger than the rate of work done, acoustic waves that appear in the discharge must primarily be a result of thermal energy release.

The formation of acoustic waves from the heat release is illustrated in Fig. 6, which shows temperature and velocity profiles at several times for the 5 kV and 27 kV cases. In both cases, heating at the cathode sheath edge ($x/L \approx 0.3$) generates waves that propagate away from that location. Similarly, heating near the right boundary creates a wave that travels into the domain.

Focusing on the vicinity of the left sheath edge at $0.4 \mu\text{s}$ for the 5 kV case (red curve in Fig. 6b), we note an asymmetry in the waveform that is probably a result of the left-directed body force. The velocity of the left-running wave is about 60% higher than the that of the right-running wave. The corresponding difference for the 27 kV case (red curve in Fig. 6d) is about 40%. Nonetheless, the body force has a relatively small influence on the formation of the acoustic waves.

The results are qualitatively similar for all the cases examined here, with the wave amplitude and speed increasing with the amplitude of the input signal. The wave speeds are nearly sonic for all cases; the Mach number does not exceed 1.08. (The sound speed is 353 m/s for air at 310.3 K, and the wave speeds lie in the range of 350–380 m/s.) At later stages in the computations (not shown), the waves reflect from the solid boundaries, producing complex wave patterns.

These computational results are consistent with the waves emanating from the cathode and anode in a pulsed CO₂ laser observed by Pugh et al.¹³ using interferometry. Those authors noted both generation of waves by discharge heating and reflection of the resulting waves from solid boundaries. The configuration in the Mach 5 cylinder flow experiments²⁰ was somewhat more complicated, but similar results were obtained. A weak shock formed near the edge of the exposed electrode and propagated into the shock layer flow. The results of the present calculations are qualitatively consistent with those of both experimental studies. Further, wave speeds extracted from the computational results shown in Fig. 6d lie in the range of 350–380 m/s, in general agreement with the value of 375 m/s measured in the Mach 5 cylinder flow experiments.

V. Summary and Conclusions

Numerical calculations were carried out to examine the physics of the operation of a nanosecond-pulse, dielectric barrier discharge in a configuration with planar symmetry. This simplified configuration was chosen as a vehicle to develop a physics-based nanosecond discharge model, including realistic air plasma chemistry and compressible bulk gas flow. Discharge parameters (temperature, pressure, and input waveform) were selected to be representative of recent experiments on bow shock control with a nanosecond discharge in a Mach 5 cylinder flow.

The computational results qualitatively reproduce many of the features observed in the experiments, including the rapid thermalization of the input electrical energy and the consequent formation of weak shock waves. Despite the simplifications employed in the calculations, the computed translational temperature rise (40 K) and nitrogen vibrational temperature rise (370 K) were of the same order of magnitude as those

measured experimentally (50 K and 500 K, respectively). The results illustrate how input electrical energy is rapidly transformed (over roughly 1 ns) at breakdown into ionization products, dissociation products, and electronically excited particles, and how thermalization occurs over a relatively longer time-scale (roughly 10 μ s). The quenching of electronically excited states and electron-ion recombination make roughly equal contributions to the thermalization of stored chemical energy.

This work represents a first step towards detailed modeling of the nanosecond-pulse dielectric barrier discharge actuator. This type of actuator shows promise for high-speed flow control, and accurate numerical modeling will contribute the optimization of these devices. In ongoing work, we are extending the model to multiple dimensions, which should allow a more realistic representation of the electric field and better quantitative comparison with experiment.

Acknowledgments

This project was sponsored in part by the Air Force Office of Scientific Research (monitored by F. Fahroo, AFOSR/RSL), and by a grant of High Performance Computing time from the Air Force Research Laboratory Major Shared Resource Center. Work at The Ohio State University was funded in part by the Chief Scientist Innovative Research Fund (CSIRF) of the Air Force Research Laboratory Air Vehicles Directorate (AFRL/RB). The authors would like to thank M. N. Shneider for helpful discussions. Cleared for public release, distribution unlimited (88ABW-2012-6103).

References

- ¹Lieberman, M. A. and Lichtenberg, A. J., *Principles of Plasma Discharges and Materials Processing*, J. Wiley, New York, 1994.
- ²Vasilyak, L. M., Kostyuchenko, S. V., Kudryavtsev, N. N., and Filyugin, I. V., "Fast Ionisation Waves under Electrical Breakdown Conditions," *Physics-Uspekhi*, Vol. 37, No. 4, 1994, pp. 247–269.
- ³Fridman, A. and Kennedy, L. A., *Plasma Physics and Engineering*, Taylor and Francis, New York, 2004.
- ⁴Macheret, S. O., Shneider, M. N., and Miles, R. B., "Modeling of Air Plasma Generation by Repetitive High-Voltage Nanosecond Pulses," *IEEE Transactions on Plasma Science*, Vol. 30, No. 3, 2002, pp. 1301–1314.
- ⁵Opaitis, D. F., Likhanskii, A. V., Neretti, G., Zaidi, S., Shneider, M. N., Miles, R. B., and Macheret, S. O., "Experimental Investigation of Dielectric Barrier Discharge Plasma Actuators Driven by Repetitive High-Voltage Nanosecond Pulses with DC or Low Frequency Sinusoidal Bias," *Journal of Applied Physics*, Vol. 104, 2008, pp. 043304.
- ⁶Roupassov, D. V., Nikipelov, A. A., Nudnova, M. M., and Starikovskii, A. Y., "Flow Separation Control by Plasma Actuator with Nanosecond Pulsed-Periodic Discharge," *AIAA Journal*, Vol. 47, No. 1, 2009, pp. 168–185.
- ⁷(Udagawa), K. T., Zuzeev, Y., Lempert, W. R., and Adamovich, I. V., "Characterization of a Surface Dielectric Barrier Discharge Plasma Sustained by Repetitive Nanosecond Pulses," *Plasma Sources Science and Technology*, Vol. 20, 2011, pp. 055009.
- ⁸Little, J., Takashima, K., Nishihara, M., Adamovich, I., and Samimy, M., "Separation Control with Nanosecond-Pulse-Driven Dielectric Barrier Discharge Plasma Actuators," *AIAA Journal*, Vol. 50, No. 2, 2012, pp. 350–365.
- ⁹Murray, R. C., Zaidi, S. H., Carraro, M. R., Vasilyak, L. M., Macheret, S. O., Shneider, M. N., and Miles, R. B., "Magnetohydrodynamic Power Generation Using Externally Ionized, Cold, Supersonic Air as Working Fluid," *AIAA Journal*, Vol. 44, No. 1, 2006, pp. 119–127.
- ¹⁰Adamovich, I. V., Lempert, W. R., Nishihara, M., Rich, J. W., and Utkin, Y. G., "Repetitively Pulsed Nonequilibrium Plasmas for Magnetohydrodynamic Flow Control and Plasma-Assisted Combustion," *Journal of Propulsion and Power*, Vol. 24, No. 6, 2008, pp. 1198–1215.
- ¹¹Pancheshnyi, S. V., Lacoste, D. A., Bourdon, A., and Laux, C. O., "Ignition of Propane-Air Mixtures by a Repetitively Pulsed Nanosecond Discharge," *IEEE Transactions on Plasma Science*, Vol. 34, No. 6, 2006, pp. 2478–2487.
- ¹²Sun, W., Uddi, M., Won, S. H., Ombrello, T., Carter, C., and Ju, Y., "Kinetic Effects of Non-Equilibrium Plasma-Assisted Methane Oxidation on Diffusion Flame Extinction Limits," *Combustion and Flame*, Vol. 159, 2012, pp. 221–229.
- ¹³Pugh, E. R., Wallace, J., Jacob, J. H., Northam, D. B., and Daugherty, J. D., "Optical Quality of Pulsed Electron-Beam Sustained Lasers," *Applied Optics*, Vol. 13, No. 11, 1974, pp. 2512–2517.
- ¹⁴Aleksandrov, V. V., Kotlov, V. N., Pustovalov, V. V., Soroka, A. M., and Suchkov, A. F., "Space-Time Evolution of the Cathode Layer in Electron-Beam-Controlled Lasers," *Soviet Journal of Quantum Electronics*, Vol. 8, No. 1, 1978, pp. 59–63.
- ¹⁵Popov, N. A., "Investigation of the Mechanism for Rapid Heating of Nitrogen and Air in Gas Discharges," *Plasma Physics Reports*, Vol. 27, No. 10, 2001, pp. 886–896.
- ¹⁶Flitti, A. and Pancheshnyi, S., "Gas Heating in Fast Pulsed Discharges in N₂-O₂ Mixtures," *The European Physical Journal: Applied Physics*, Vol. 45, 2009, pp. 21001.
- ¹⁷Aleksandrov, N. L., Kindysheva, S. V., Nudnova, M. N., and Starikovskiy, A. Y., "Mechanism of Ultra-Fast Heating in a Non-Equilibrium Weakly Ionized Air Discharge Plasma in High Electric Fields," *Journal of Physics D: Applied Physics*, Vol. 43, 2010, pp. 255201.
- ¹⁸Popov, N., "Fast Gas Heating in a Nitrogen-Oxygen Discharge Plasma: I. Kinetic Mechanism," *Journal of Physics D: Applied Physics*, Vol. 44, 2011, pp. 285201.

- ¹⁹Unfer, T. and Boeuf, J. P., "Modelling of a Nanosecond Surface Discharge Actuator," *Journal of Physics D: Applied Physics*, Vol. 42, 2009, pp. 194017.
- ²⁰Nishihara, M., Takashima, K., Rich, J. W., and Adamovich, I. V., "Mach 5 Bow Shock Control by a Nanosecond Pulse Surface Dielectric Barrier Discharge," *Physics of Fluids*, Vol. 23, 2011, pp. 066101.
- ²¹Kirpichnikov, A. A. and Starikovskii, A. Y., "Nanosecond Pulse Discharge – Always Uniform?" *IEEE Transactions on Plasma Science*, Vol. 36, No. 4, 2008, pp. 898–899.
- ²²Poggie, J., Bisek, N. J., Adamovich, I. V., and Nishihara, M., "Numerical Simulation of Nanosecond-Pulse Electrical Discharges," AIAA Paper 2012-1025, American Institute of Aeronautics and Astronautics, Reston, VA, January 2012.
- ²³Likhanskii, A. V., Shneider, M. N., Macheret, S. O., and Miles, R. B., "Modeling of Dielectric Barrier Discharge Plasma Actuators Driven by Nanosecond Pulses," *Physics of Plasmas*, Vol. 14, 2007, pp. 073501.
- ²⁴Breden, D. and Raja, L. L., "Gas Heating Effects in a Nanosecond-Pulse Streamer Discharge Interacting with a Supersonic O_2-H_2 Flow," *IEEE Transactions on Plasma Science*, Vol. 39, No. 11, 2011, pp. 2250–2251.
- ²⁵Che, X., Shao, T., Nie, W., and Yan, P., "Numerical Simulation on a Nanosecond-Pulse Surface Dielectric Barrier Discharge Actuator in Near Space," *Journal of Physics D: Applied Physics*, Vol. 45, 2012, pp. 145201.
- ²⁶Wang, C.-C., "Energy and Force Prediction for a Nanosecond Pulsed Dielectric Barrier Discharge Actuator," *Journal of Applied Physics*, Vol. 111, No. 10, 2012, pp. 103302.
- ²⁷Uddi, M., Jiang, N., Adamovich, I. V., and Lempert, W. R., "Nitric Oxide Density Measurements in Air and Air/Fuel Nanosecond Pulse Discharges by Laser Induced Fluorescence," *Journal of Physics D: Applied Physics*, Vol. 42, 2009, pp. 075205.
- ²⁸Kossyi, I. A., Kostinsky, A. Y., Matveyev, A. A., and Silakov, V. P., "Kinetic Scheme of the Nonequilibrium Discharge in Nitrogen-Oxygen Mixtures," *Plasma Sources Science and Technology*, Vol. 1, 1992, pp. 207–220.
- ²⁹McNeal, R. J., Jr., M. E. W., and Cook, G. R., "Quenching of Vibrationally Excited N_2 by Atomic Oxygen," *Chemical Physics Letters*, Vol. 16, No. 3, 1972, pp. 507–510.
- ³⁰Huxley, L. G. H. and Crompton, R. W., *The Diffusion and Drift of Electrons in Gases*, Wiley, New York, 1974.
- ³¹Itikawa, Y., Hayashi, M., Ichimura, A., Onda, K., Sakimoto, K., Takayanagi, K., Nakamura, M., Nishimura, M., and Takayanagi, T., "Cross Sections for Collisions of Electrons and Photons with Nitrogen Molecules," *Journal of Physical and Chemical Reference Data*, Vol. 16, 1986, pp. 985–1010.
- ³²Itikawa, Y., Ichimura, A., Onda, K., Sakimoto, K., Takayanagi, K., Hatano, Y., Hayashi, M., Nishimura, H., and Tsurubichi, S., "Cross Sections for Collisions of Electrons and Photons with Oxygen Molecules," *Journal of Physical and Chemical Reference Data*, Vol. 18, 1989, pp. 23–42.
- ³³Haydon, S. C. and Williams, O. M., "Combined Spatial and Temporal Studies of Ionization Growth in Nitrogen," *Journal of Physics D: Applied Physics*, Vol. 9, 1976, pp. 523–536.
- ³⁴Chanrion, O. and Neubert, T., "A PIC-MCC Code for Simulation of Streamer Propagation in Air," *Journal of Computational Physics*, Vol. 227, 2008, pp. 7222–7245.
- ³⁵Meyyappan, M. and Kreskovsky, J. P., "Glow Discharge Simulation Through Solutions to the Moments of the Boltzmann Transport Equation," *Journal of Applied Physics*, Vol. 68, No. 4, 1990, pp. 1506–1512.
- ³⁶Wilcoxson, M. H. and Manousiouthakis, V. I., "Simulation of a Three-Moment Fluid Model of a Two-Dimensional Radio Frequency Discharge," *Chemical Engineering Science*, Vol. 51, No. 7, 1996, pp. 1089–1106.
- ³⁷Chen, G. and Raja, L. L., "Fluid Modeling of Electron Heating in Low-Pressure, High-Frequency Capacitively Coupled Plasma Discharges," *Journal of Applied Physics*, Vol. 96, No. 11, 2004, pp. 6073–6081.
- ³⁸Adamovich, I. V. and Rich, J. W., "Emission and Shock Visualization in Nonequilibrium Nitrogen Afterglow Plasma," *Journal of Applied Physics*, Vol. 102, 2007, pp. 083303.
- ³⁹Hakim, A. and Shumlak, U., "Two-Fluid Physics and Field-Reversed Configurations," *Physics of Plasmas*, Vol. 14, 2007, pp. 055911.
- ⁴⁰Poggie, J., Adamovich, I., Bisek, N., and Nishihara, M., "Numerical Simulation of Nanosecond-Pulse Electrical Discharges," *Plasma Sources Science and Technology*, Vol. 22, 2012, pp. 015001.
- ⁴¹Burgers, J. M., *Flow Equations for Composite Gases*, Academic Press, New York, 1969.
- ⁴²Golant, V. E., Zhilinsky, A. P., and Sakharov, I. E., *Fundamentals of Plasma Physics*, J. Wiley, New York, 1980, Trans. K. Z. Vedenev and V. F. Agranat.
- ⁴³Williams, F. A., *Combustion Theory*, Addison-Wesley, Menlo Park CA, 4th ed., 1988.
- ⁴⁴White, F. M., *Viscous Fluid Flow*, McGraw-Hill, New York, 2nd ed., 1991.
- ⁴⁵Mahadevan, S. and Raja, L., "Simulations of Direct-Current Air Glow Discharges at Pressures ~ 1 Torr: Discharge Model Validation," *Journal of Applied Physics*, Vol. 107, 2010, pp. 093304.
- ⁴⁶Chen, N. H. and Othmer, D. F., "New Generalized Equation for Gas Diffusion Coefficient," *Journal of Chemical and Engineering Data*, Vol. 7, No. 1, 1962, pp. 37–41.
- ⁴⁷Viehland, L. A. and Mason, E. A., "Transport Properties of Gaseous Ions over a Wide Energy Range, IV," *Atomic Data and Nuclear Data Tables*, Vol. 60, 1995, pp. 37–95.
- ⁴⁸Nelson, D., Benhenni, M., Eichwald, O., and Yousfi, M., "Ion Swarm Data for Electrical Discharge Modeling in Air and Flue Gas Mixtures," *Journal of Applied Physics*, Vol. 94, No. 1, 2003, pp. 96–103.
- ⁴⁹Deconinck, T., Mahadevan, S., and Raja, L. L., "Simulation of Direct-Current Surface Plasma Discharge Phenomena in High-Speed Flow Actuation," *IEEE Transactions on Plasma Science*, Vol. 35, No. 5, 2007, pp. 1301–1311.
- ⁵⁰Ivanov, A. V., Takhtenberg, S., Bertram, A. K., Gershenzon, Y. M., and Molina, M. J., "OH, HO_2 , and Ozone Gaseous Diffusion Coefficients," *Journal of Physical Chemistry A*, Vol. 111, 2007, pp. 1632–1637.
- ⁵¹Breden, D. and Raja, L. L., "Simulations of Nanosecond Pulsed Plasmas in Supersonic Flow," AIAA Paper 2009-3594, American Institute of Aeronautics and Astronautics, Reston, VA, June 2009.
- ⁵²Poggie, J., "Numerical Simulation of Direct Current Glow Discharges for High-Speed Flow Control," *Journal of Propulsion and Power*, Vol. 24, No. 5, 2008, pp. 916–922.

- ⁵³Poggie, J., "High-Order Numerical Methods for Electrical Discharge Modeling," AIAA Paper 2010-4632, American Institute of Aeronautics and Astronautics, Reston VA, 2011.
- ⁵⁴Beam, R. and Warming, R., "An Implicit Factored Scheme for the Compressible Navier-Stokes Equations," *AIAA Journal*, Vol. 16, No. 4, 1978, pp. 393–402.
- ⁵⁵Morrison, J., "Flux Difference Split Scheme for Turbulent Transport Equations," AIAA Paper 90-5251, American Institute of Aeronautics and Astronautics, Reston, VA, October 1990.
- ⁵⁶Walters, R. W., Cinnella, P., Slack, D. C., and Halt, D., "Characteristic-Based Algorithms for Flows in Thermo-Chemical Nonequilibrium," AIAA Paper 90-0393, American Institute of Aeronautics and Astronautics, Reston, VA, January 1990.
- ⁵⁷Gaitonde, D. and Shang, J. S., "Accuracy of Flux-Split Algorithms in High-Speed Viscous Flows," *AIAA Journal*, Vol. 31, No. 7, 1993, pp. 1215–1221.
- ⁵⁸Anderson, W. K., Thomas, J. L., and van Leer, B., "A Comparison of Finite Volume Flux Vector Splittings for the Euler Equations," AIAA Paper 85-0122, American Institute of Aeronautics and Astronautics, Reston, VA, January 1985.
- ⁵⁹Ventzek, P. L. G., Hoekstra, R. J., and Kushner, M. J., "Two-Dimensional Modeling of High Plasma Density Inductively Coupled Sources for Materials Processing," *Journal of Vacuum Science and Technology B*, Vol. 12, No. 1, 1994, pp. 461–477.
- ⁶⁰Holst, T. L., "Transonic Flow Computations Using Nonlinear Potential Methods," *Progress in Aerospace Sciences*, Vol. 36, 2000, pp. 1–61.
- ⁶¹Soloviev, V. R. and Krivtsov, V. M., "Surface Barrier Discharge Modelling for Aerodynamic Applications," *Journal of Physics D: Applied Physics*, Vol. 42, 2009, pp. 125208.

No.	Species	\mathcal{H}_s^0 (eV/particle)	σ_s (10^{-20} m ²)
1	N ₂	0	41
2	O ₂	0	39
3	O	2.58	32
4	O ₃	1.48	45
5	NO	0.94	31
6	N	4.90	38
7	O(¹ D)	4.55	32
8	N ₂ (A ³ Σ)	6.17	41
9	N ₂ (B ³ Π)	7.35	41
10	N ₂ (a ¹ Σ)	8.40	41
11	N ₂ (C ³ Π)	11.03	41
12	e ⁻	0	-
13	N ₂ ⁺	16.37	148
14	O ⁺	16.26	80
15	O ₂ ⁺	12.69	115
16	N ₂ (<i>v</i> = 1)	0.29	41
17	N ₂ (<i>v</i> = 2)	0.57	41
18	N ₂ (<i>v</i> = 3)	0.86	41
19	N ₂ (<i>v</i> = 4)	1.14	41
20	N ₂ (<i>v</i> = 5)	1.41	41
21	N ₂ (<i>v</i> = 6)	1.68	41
22	N ₂ (<i>v</i> = 7)	1.95	41
23	N ₂ (<i>v</i> = 8)	2.21	41

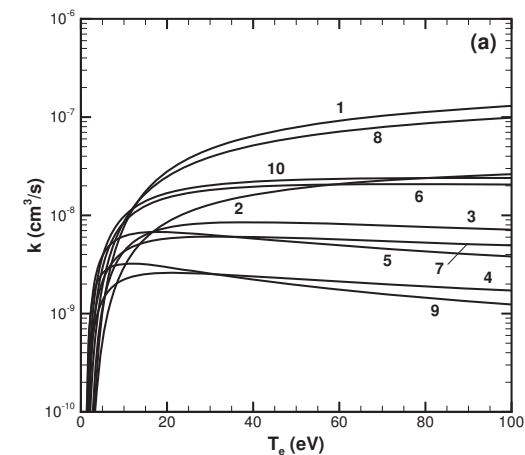
Table 1. Species included in kinetic model. Heat of formation referenced to 300 K.

No.	Reaction	Rate
1	$\text{N}_2 + \text{e}^- \rightarrow \text{N}_2^+ + \text{e}^- + \text{e}^-$	Fig. 1a
2	$\text{O}_2 + \text{e}^- \rightarrow \text{O}_2^+ + \text{e}^- + \text{e}^-$	Fig. 1a
3	$\text{O}_2 + \text{e}^- \rightarrow \text{O} + \text{O}^+ + \text{e}^- + \text{e}^-$	Fig. 1a
4	$\text{N}_2 + \text{e}^- \rightarrow \text{N}_2(\text{A}^3\Sigma) + \text{e}^-$	Fig. 1a
5	$\text{N}_2 + \text{e}^- \rightarrow \text{N}_2(\text{B}^3\Pi) + \text{e}^-$	Fig. 1a
6	$\text{N}_2 + \text{e}^- \rightarrow \text{N}_2(\text{C}^3\Pi) + \text{e}^-$	Fig. 1a
7	$\text{N}_2 + \text{e}^- \rightarrow \text{N}_2(\text{a}^1\Sigma) + \text{e}^-$	Fig. 1a
8	$\text{N}_2 + \text{e}^- \rightarrow \text{N} + \text{N} + \text{e}^-$	Fig. 1a
9	$\text{O}_2 + \text{e}^- \rightarrow \text{O} + \text{O} + \text{e}^-$	Fig. 1a
10	$\text{O}_2 + \text{e}^- \rightarrow \text{O} + \text{O}(\text{D}) + \text{e}^-$	Fig. 1a
11	$\text{N} + \text{O}_2 \rightarrow \text{NO} + \text{O}$	$k = 1.1 \times 10^{-14} T \exp(-3150./T)$
12	$\text{N} + \text{NO} \rightarrow \text{N}_2 + \text{O}$	$k = 1.1 \times 10^{-12} T^{0.5}$
13	$\text{O} + \text{O}_3 \rightarrow \text{O}_2 + \text{O}_2$	$k = 2.0 \times 10^{-11} \exp(-2300./T)$
14	$\text{O} + \text{O} + \text{N}_2 \rightarrow \text{O}_2 + \text{N}_2$	$k = 2.8 \times 10^{-34} \exp(720./T)$
15	$\text{O} + \text{O} + \text{O}_2 \rightarrow \text{O}_2 + \text{O}_2$	$k = 2.5 \times 10^{-31} T^{-0.63}$
16	$\text{O} + \text{O}_2 + \text{N}_2 \rightarrow \text{O}_3 + \text{N}_2$	$k = 5.6 \times 10^{-29} T^{-2.0}$
17	$\text{O} + \text{O}_2 + \text{O}_2 \rightarrow \text{O}_3 + \text{O}_2$	$k = 8.6 \times 10^{-31} T^{-1.25}$
18	$\text{N}_2(\text{A}^3\Sigma) + \text{O}_2 \rightarrow \text{N}_2 + \text{O} + \text{O}$	$k = 1.7 \times 10^{-12}$
19	$\text{N}_2(\text{A}^3\Sigma) + \text{O}_2 \rightarrow \text{N}_2 + \text{O}_2$	$k = 7.5 \times 10^{-13}$
20	$\text{N}_2(\text{A}^3\Sigma) + \text{O} \rightarrow \text{N}_2 + \text{O}(\text{D})$	$k = 3.0 \times 10^{-11}$
21	$\text{N}_2(\text{A}^3\Sigma) + \text{N}_2(\text{A}^3\Sigma) \rightarrow \text{N}_2 + \text{N}_2(\text{B}^3\Pi)$	$k = 7.7 \times 10^{-11}$
22	$\text{N}_2(\text{A}^3\Sigma) + \text{N}_2(\text{A}^3\Sigma) \rightarrow \text{N}_2 + \text{N}_2(\text{C}^3\Pi)$	$k = 1.6 \times 10^{-10}$
23	$\text{N}_2(\text{B}^3\Pi) + \text{N}_2 \rightarrow \text{N}_2(\text{A}^3\Sigma) + \text{N}_2$	$k = 3.0 \times 10^{-11}$
24	$\text{N}_2(\text{B}^3\Pi) \rightarrow \text{N}_2(\text{A}^3\Sigma) + h\nu$	$k = 1.5 \times 10^5$
25	$\text{N}_2(\text{B}^3\Pi) + \text{O}_2 \rightarrow \text{N}_2 + \text{O} + \text{O}$	$k = 3.0 \times 10^{-10}$
26	$\text{N}_2(\text{a}^1\Sigma) + \text{N}_2 \rightarrow \text{N}_2 + \text{N}_2$	$k = 2.0 \times 10^{-13}$
27	$\text{N}_2(\text{a}^1\Sigma) + \text{O}_2 \rightarrow \text{N}_2 + \text{O} + \text{O}(\text{D})$	$k = 2.8 \times 10^{-11}$
28	$\text{N}_2(\text{C}^3\Pi) + \text{N}_2 \rightarrow \text{N}_2(\text{B}^3\Pi) + \text{N}_2$	$k = 1.0 \times 10^{-11}$
29	$\text{N}_2(\text{C}^3\Pi) \rightarrow \text{N}_2(\text{B}^3\Pi) + h\nu$	$k = 3.0 \times 10^7$
30	$\text{N}_2(\text{C}^3\Pi) + \text{O}_2 \rightarrow \text{N}_2(\text{A}^3\Sigma) + \text{O} + \text{O}$	$k = 3.0 \times 10^{-10}$
31	$\text{O}(\text{D}) + \text{N}_2 \rightarrow \text{O} + \text{N}_2$	$k = 2.6 \times 10^{-11}$
32	$\text{O}(\text{D}) + \text{O}_2 \rightarrow \text{O} + \text{O}_2$	$k = 4.0 \times 10^{-11}$
33	$\text{O}^+ + \text{O}_2 \rightarrow \text{O}_2^+ + \text{O}$	$k = 2.0 \times 10^{-11}$
34	$\text{N}_2^+ + \text{O}_2 \rightarrow \text{N}_2 + \text{O}_2^+$	$k = 6.0 \times 10^{-11}$
35	$\text{N}_2^+ + \text{e}^- \rightarrow \text{N} + \text{N}$	$k = 8.3 \times 10^{-6} T_e^{-0.5}$
36	$\text{O}_2^+ + \text{e}^- \rightarrow \text{O} + \text{O}$	$k = 6.0 \times 10^{-5} T_e^{-1.0}$
37	$\text{N}_2^+ + \text{e}^- + \text{e}^- \rightarrow \text{N}_2 + \text{e}^-$	$k = 1.4 \times 10^{-8} T_e^{-4.5}$
38	$\text{O}_2^+ + \text{e}^- + \text{e}^- \rightarrow \text{O}_2 + \text{e}^-$	$k = 1.4 \times 10^{-8} T_e^{-4.5}$
39	$\text{O}^+ + \text{e}^- + \text{e}^- \rightarrow \text{O} + \text{e}^-$	$k = 1.4 \times 10^{-8} T_e^{-4.5}$
40	$\text{N}_2^+ + \text{e}^- + \text{M} \rightarrow \text{N}_2 + \text{M}$	$k = 3.1 \times 10^{-23} T_e^{-1.5}$
41	$\text{O}_2^+ + \text{e}^- + \text{M} \rightarrow \text{O}_2 + \text{M}$	$k = 3.1 \times 10^{-23} T_e^{-1.5}$
42	$\text{O}^+ + \text{e}^- + \text{M} \rightarrow \text{O} + \text{M}$	$k = 3.1 \times 10^{-23} T_e^{-1.5}$
43-50	$\text{N}_2(v=0) + \text{e}^- \rightarrow \text{N}_2(v=1-8) + \text{e}^-$	Fig. 1b

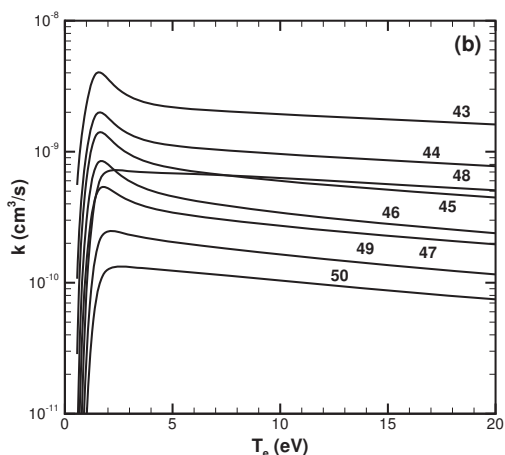
Table 2. Reaction mechanism. Units consistent with number densities in cm^{-3} , and temperatures in K, one-body rates in s^{-1} , two-body rates in cm^3/s , and three-body rates in cm^6/s .

No.	Reaction	$\Delta H/e$ (V)
1	$\text{N}_2 + \text{e}^- \rightarrow \text{N}_2^+ + \text{e}^- + \text{e}^-$	$16.37 + 3k_B T_e / (2e)$
2	$\text{O}_2 + \text{e}^- \rightarrow \text{O}_2^+ + \text{e}^- + \text{e}^-$	$12.69 + 3k_B T_e / (2e)$
3	$\text{O}_2 + \text{e}^- \rightarrow \text{O} + \text{O}^+ + \text{e}^- + \text{e}^-$	$18.84 + 3k_B T_e / (2e)$
4	$\text{N}_2 + \text{e}^- \rightarrow \text{N}_2(\text{A}^3\Sigma) + \text{e}^-$	6.17
5	$\text{N}_2 + \text{e}^- \rightarrow \text{N}_2(\text{B}^3\Pi) + \text{e}^-$	7.35
6	$\text{N}_2 + \text{e}^- \rightarrow \text{N}_2(\text{C}^3\Pi) + \text{e}^-$	11.03
7	$\text{N}_2 + \text{e}^- \rightarrow \text{N}_2(\text{a}^1\Sigma) + \text{e}^-$	8.40
8	$\text{N}_2 + \text{e}^- \rightarrow \text{N} + \text{N} + \text{e}^-$	9.80
9	$\text{O}_2 + \text{e}^- \rightarrow \text{O} + \text{O} + \text{e}^-$	5.17
10	$\text{O}_2 + \text{e}^- \rightarrow \text{O} + \text{O}({}^1\text{D}) + \text{e}^-$	7.14
43	$\text{N}_2(v=0) + \text{e}^- \rightarrow \text{N}_2(v=1) + \text{e}^-$	0.29
44	$\text{N}_2(v=0) + \text{e}^- \rightarrow \text{N}_2(v=2) + \text{e}^-$	0.57
45	$\text{N}_2(v=0) + \text{e}^- \rightarrow \text{N}_2(v=3) + \text{e}^-$	0.86
46	$\text{N}_2(v=0) + \text{e}^- \rightarrow \text{N}_2(v=4) + \text{e}^-$	1.14
47	$\text{N}_2(v=0) + \text{e}^- \rightarrow \text{N}_2(v=5) + \text{e}^-$	1.41
48	$\text{N}_2(v=0) + \text{e}^- \rightarrow \text{N}_2(v=6) + \text{e}^-$	1.68
49	$\text{N}_2(v=0) + \text{e}^- \rightarrow \text{N}_2(v=7) + \text{e}^-$	1.95
50	$\text{N}_2(v=0) + \text{e}^- \rightarrow \text{N}_2(v=8) + \text{e}^-$	2.21

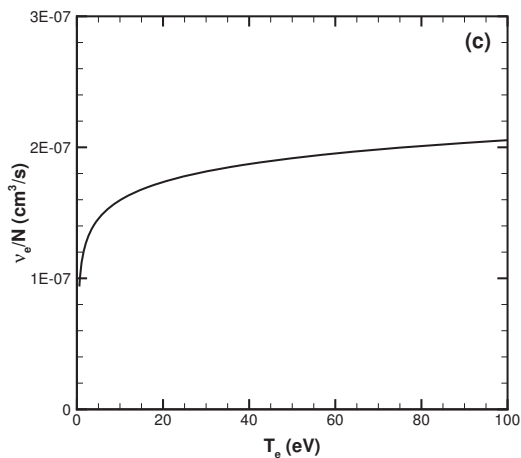
Table 3. Energy lost by electrons in inelastic collisions.



(a) Rates of ionization and electronic excitation (Reactions 1-10).



(b) Rates of vibrational excitation (Reactions 43-50).



(c) Electron-neutral collision rate.

Figure 1. Quantities determined from zero-dimensional solution of Boltzmann equation.

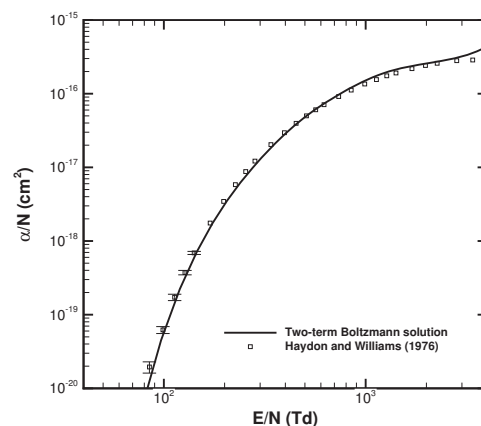


Figure 2. Test of Boltzmann solver: predicted Townsend ionization coefficient for nitrogen compared to experimental data of Haydon and Williams.³³

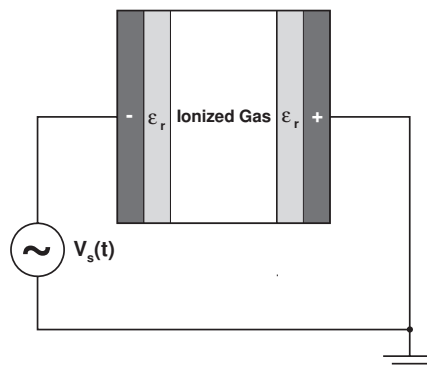
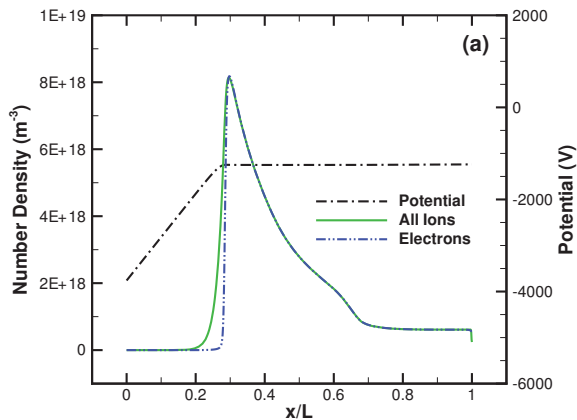
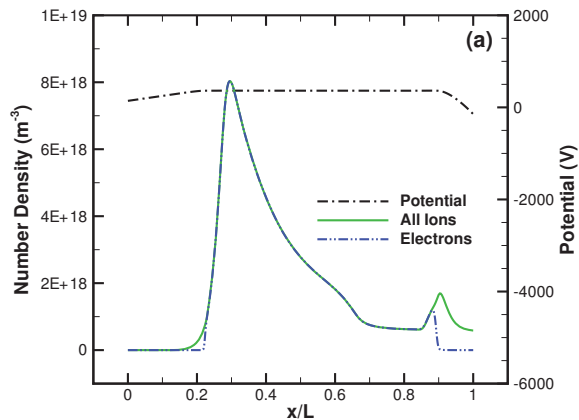


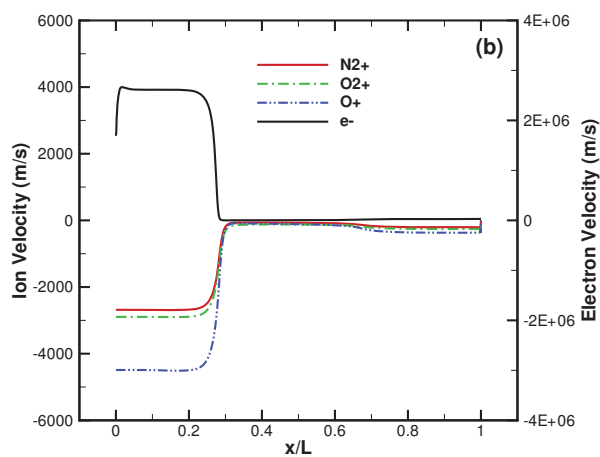
Figure 3. Diagram of computational domain.



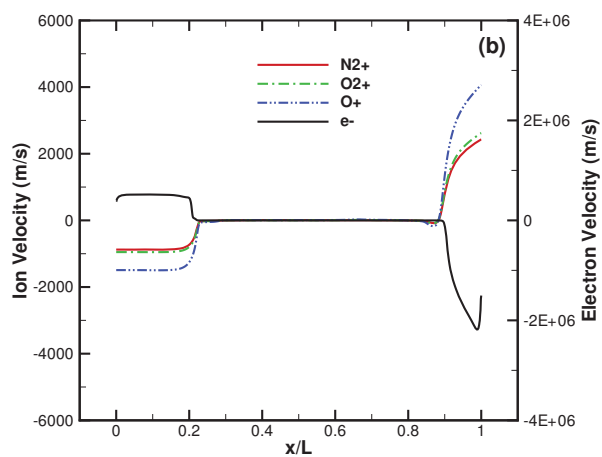
(a) Number densities and potential.



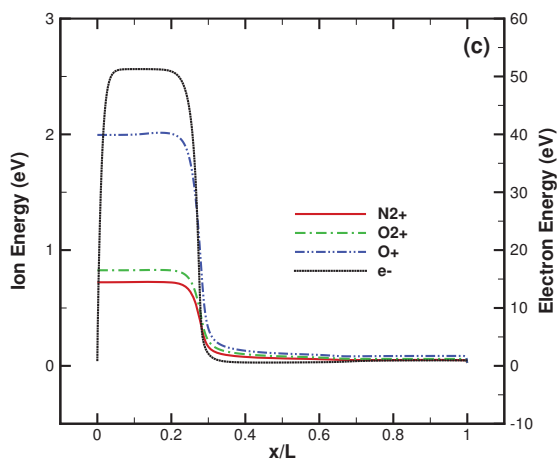
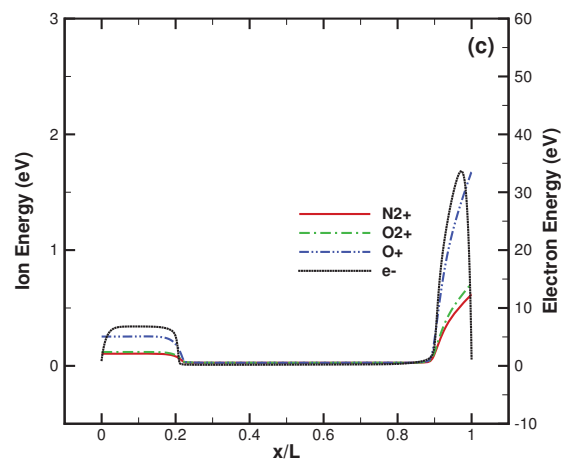
(a) Number densities and potential.



(b) Velocities.



(b) Velocities.

(c) Temperatures ($k_B T_s/e$).(c) Temperatures ($k_B T_s/e$).Figure 4. Discharge profiles at 12 ns for $V_0 = 5$ kV.Figure 5. Discharge profiles at 24 ns for $V_0 = 5$ kV.

Approved for public release; distribution unlimited.

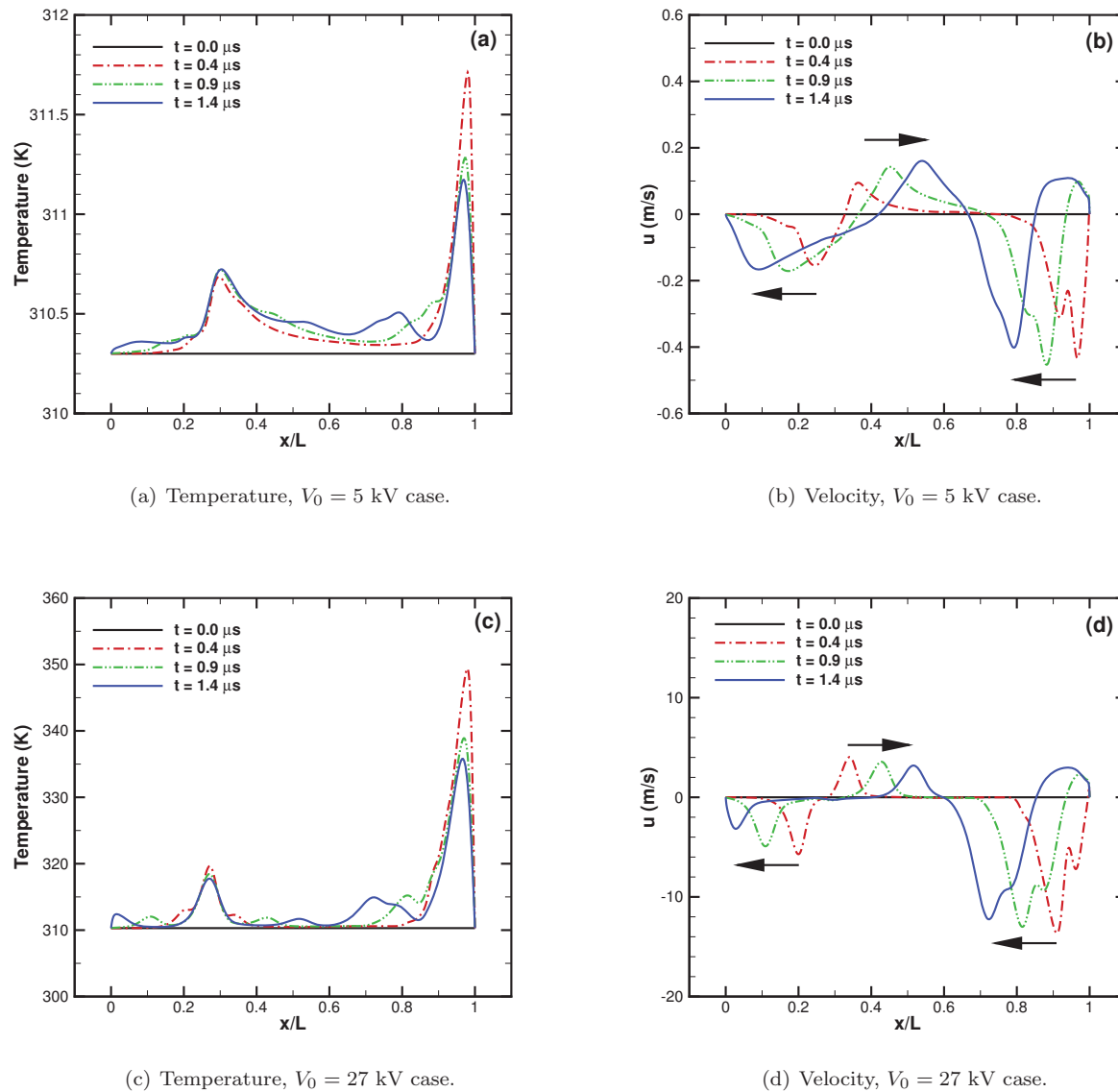


Figure 6. Profiles of the properties of the bulk gas for selected times in the simulation. Arrows indicate direction of wave motion.

On the validation of fluid plasma model for pulsed DBD plasma actuator simulations against full kinetic approach

Alexandre Likhanskii

Tech-X Corporation, Boulder, Colorado

Jonathan Poggie

Wright Patterson Air Force Research Laboratory, Dayton, Ohio

likhansk@txcorp.com

Introduction

Dielectric barrier discharge plasma (DBD) actuators have demonstrated high potential for active flow control for both subsonic and supersonic applications [1-5]. However, both experimental and numerical studies showed that the performance of DBD plasma actuators is rather sensitive to the DBD parameters, such as driving voltage and position of the actuators on the aerodynamic body. In order to start transition between research and development efforts to the implementation into the existing platforms, it is important to gain confidence in both experimental and simulation results for DBD laboratory studies.

The paper presents detailed analysis of the most commonly used physical approach for DBD plasma actuators simulations – drift-diffusion approximation for plasma dynamics – for physical accuracy, numerical convergence, and capabilities for high performance simulations. In the first part of the paper, we perform detailed comparison between numerical study of pulsed DBD plasma actuators using particle-in-cell (PIC) and fluid approach using Tech-X's code Vorpel [6]. In the second part of the paper, we present grid resolution study for the fluid plasma model for DBD simulations in Vorpel. Finally, we present speed-up results for the DBD simulations using fluid model at modern supercomputing facilities.

Physical and Numerical Models

Overview

In order to perform detailed simulations for the DBD plasma actuators, we have chosen Tech-X commercial simulation tool Vorpel with specifically developed hybrid modeling capabilities for atmospheric pressure plasma [7]. Vorpel includes two different approaches for this problem: detailed kinetic PIC (Particle-In-Cell) algorithm and fluid (drift-diffusion approximation) algorithm. The use of these two approaches, which present two extremes for the detalization of plasma simulations, allows us both validate the simulations for numerical and physical accuracy, verify the validity of computationally efficient drift-diffusion approximation and to measure critical parameters for the variety of surface discharge applications, such as characterization of maximum electric field during the streamer propagation. Below we present detailed description of the physical and numerical models, used in the simulations.

Approved for public release; distribution unlimited.

PIC model

The first model we used for DBD simulation is PIC approach. The model consisted of three major blocks: Electrostatic Solver, Particle blocks and Monte-Carlo collision blocks. The Electrostatic Solver computes the distributions of electric potential and electric field in the entire simulation domain based on the voltages at the electrodes, boundary conditions and charge species distribution. For the charge species, we are using particle approach, where we track the motion of so-called macroparticles representing groups of physical particles with same parameters. Such approach allows us resolving non-Maxwellian EEDFs (electron energy distribution functions). The motion of macroparticles is defined by two major mechanisms: acceleration in the self-consistently computed electric field and collisions with neutral gas. Simulations are performed in air, which is represented as a mixture of molecular nitrogen and molecular oxygen. Background gas is considered as a fluid, and molecular ions and electrons are considered as charged particles. In the simulation, we included ionization, excitation and elastic collisions, as well as recombination for both nitrogen and oxygen. In the simulation, we used concept of variable weight particles with numerical collisions. The idea behind this approach is the following. On one hand, we need to have sufficient number of particles to accurately resolve discharge. On the other hand, once breakdown starts, number of macroparticles grows exponentially, leading to significant reduction of computational speed as well as providing us with excessive resolution. Therefore, it is reasonable to combine macroparticles when the number of macroparticles in a cell becomes greater than a combination threshold and split particles, when number of macroparticles in a cell becomes less than a split threshold. The thresholds for particle combining were set to 1 for both nitrogen and oxygen ions and to 3 for electrons, i.e. we didn't allow more than 1 microparticle, representing oxygen and nitrogen ions and more than 3 macroparticles, representing electrons, in a cell. In order to avoid generation of electrons with excessively large weights, we also set a limit for combining electron macroparticles when weight of macroparticle reached 300, i.e. particles with weight greater than 300 were excluded from combining procedure.

Fluid Model

The second model, used for the simulations, is standard drift-diffusion approximation for the plasma dynamics. Unlike PIC model, charged species distributions are represented via continuous fields of densities, fluxes, temperatures, etc. The dynamics of these fields is resolved by the self-consistent solution of continuity equations for number densities of the charged species and Poisson Equation for electric fields. All plasma transport parameters and rate coefficients are determined by local electric field distribution. The model also has an option to either use artificial background charge number densities or the photoionization model for the description of streamer propagation. The model is similar to previously developed model for DBD simulations, described in [8].

Simulation Setup

The ultimate goal of this research effort is to compare different physical and numerical models for the description of ns-pulse driven DBD plasma actuators. In order to achieve this goal, we have chosen identical DBD geometries and identical applied voltages for all considered models.

The simulation domain consisted of 2010 by 1005 grid points for electric field and 2000 by 1000 grid points for particles or charge number density. The grid size was equal to 1x1 micron, leading to the physical domain size equal to 2x1 mm. Lower (grounded) electrode was 20 microns thick and 1.6mm in length. Upper (exposed) electrode was 20 microns thick and 0.2 mm in length. Electrodes were separated by the 100 micron thick dielectric ($\epsilon = 5.2$) with no horizontal offset. Time step for the simulations was equal to 0.15 picoseconds. We have applied 5kV 4ns Gaussian pulses to the upper (exposed) electrode and kept lower electrode grounded. The voltage at the exposed electrode reached its peak 4ns after the start of the simulations. The simulations were performed in atmospheric air.

For the simulations, we have used 4 different models:

Case A – PIC: For the first model, we used kinetic, PIC approach. In order to account for “photoionization”, we loaded several macroparticles inside simulation domain each time step. It corresponded to an increase of electron and ion number densities in the slab 100 microns above the dielectric surface by $3.2 \cdot 10^{11} \text{m}^{-3}$ at every time step.

Case B – Fluid: minimum density: For the second model, we used drift diffusion approximation. In order to account for photoionization, we kept minimum electron number density in the simulation domain equal to 10^7m^{-3} .

Case C – Fluid: constant load: For the third case, we used drift-diffusion approximation. In order to account for photoionization, we loaded additional plasma density at the rate of $3.2 \cdot 10^{11} \text{m}^{-3}$ at every time step for both electrons and ions (similar to PIC case).

Case D – Fluid: photoionization: For the forth case, we used drift-diffusion approximation with correctly computed photoionization.

Simulation Results

Streamer initiation

The first stage of the discharge development is streamer initiation. It occurs when the voltage at the exposed electrode reaches breakdown threshold, and streamer propagation starts from the edge of the exposed electrode. Figures 1 and 2 show the distributions of electron number densities and electric potential for the four above described cases. The detailed description of streamer development, including initial stage, is presented in Ref. 8. For the compared four cases, one can notice that the initial stage of all streamers propagation is similar. The main difference is in the time after the start of the simulations for the discharge initiation (2.55ns for case A, 2.85 for case B, 1.95 for case C and 2.55ns for case D), and consequently, the breakdown voltage. The explanation of this phenomenon is rather straightforward. As it has been demonstrated In Ref. 8, streamer propagation for the surface DBD is defined by the rate of plasma formation ahead of the streamer head. Since in B, C and D cases (fluid plasma model), we used different sources of “photoionization”, it is predictable that streamer development speeds are different. It’s also worth comparing case A and case C, when we used similar way of background plasma loading, but considered kinetic and fluid approaches for plasma generation. One can notice that streamer propagates faster, when fluid approach is used.

Streamer propagation

Now, let's compare streamer development and streamer characteristics for the computed cases. Figures 3-4 show electron number densities and electric potential distributions for all four cases, when streamer is fully developed, but still propagates along dielectric. Qualitatively, results look quite similar. The main visual difference is in electron number density distribution for PIC and fluid simulations: discharge is more "grainy" for the PIC and rather smooth for fluid model. This effect demonstrates the main qualitative difference between PIC and fluid models for DBD simulations: kinetic approaches manage to resolve stochastic nature of plasma dynamics in atmospheric pressure discharges, leading to the resolution of experimentally observed phenomena, such as plasma filament formation. On the other hand, fluid approaches usually provide smooth solutions and fail to resolve filamentary structures, unless some numerical tricks are used. However, it's worth mentioning that the physics of streamer development is the same in all four cases. Now, let's compare streamer characteristics. First of all, as we've noticed in the previous subsection, streamer propagation speed is different for all four cases due to the different rates of "photoelectron" production. Second, we observe that most of plasma parameters, such as plasma thickness (~40-60 microns) plasma height above dielectric (~30-40 microns), peak electron number density ($\sim 5 \cdot 10^{21} \text{ m}^{-3}$) are close for all four cases. However, we can notice, that streamer body is slightly closer to the dielectric surface, when the rate of "photo" plasma production is higher (for example, compare cases B and C).

The performed simulations also allowed us conducting detailed study of the electric field distributions for the surface DBD development. Figure 5 shows the distribution of horizontal component of the electric field during the streamer propagation for all four cases. As expected, maximum electric field is at the streamer head, supporting the streamer propagation. Figure 6 shows 1D cut of the Figure 5 along the dashed line. One can observe electric fields, supporting streamer propagation, are again close for all four cases, and in a range of 50-70 MV/m. However, the peak electric field for the kinetic simulation seems to be slightly lower than for fluid simulations. Figure 7 shows a distribution of vertical component of the electric field during streamer development. Figure 8 shows a 1D cut of the Figure 7 data along the dashed line. One can notice that there is indeed very strong electric field between streamer body and the dielectric surface. The explanation of this effect is following. Streamer body has a potential close to the one of the exposed electrode. Therefore, we can consider our configuration as quasi 1D capacitor with ~100 micron gap filled by the dielectric with 5.2 relative permittivity and ~30-40 micron air gap. Simple calculations will give us electric fields ~50-100 MV/m in this gap region, which are similar to the simulated ones. One can also notice that together with streamer propagation along the surface, there is breakdown between the dielectric surface and streamer body, i.e. the gap between streamer body and dielectric surface is smaller closer to the edge of the exposed electrode. However, the speed of this breakdown development is much smaller compared to the speed of the streamer propagation.

Grid resolution study

Previously [7], we have performed grid resolution study for the PIC model. In this section, we will present results on grid resolution study for fluid DBD model. In order to perform such study, we set up two simulations on two different grids: 1x1 microns (fine) and 2x2 microns (coarse). The simulation domain has been described in previous

section, and results for fine resolution case have been reported above for the case B. For coarse resolution case, we have chosen the same simulation conditions as in fine resolution case, except for the time step. It has also been chosen twice the fine resolution time step, i.e. 0.3 ps.

Figures 9-13 show detailed comparison between key DBD parameters. Figure 9 shows comparison between electric potential distributions during the initiation stage of discharge development. Figure 10 shows the same comparison when discharge has already propagated along dielectric. Figure 11 shows comparison between electron number density distributions when plasma has already formed. Finally, Figures 12 and 13 show comparison between instantaneous distributions of horizontal component of electric field. Note, that Figure 13 shows 1D distribution along dashed line in Figure 12. Another quantitative characteristic we have compared was time-integrated momentum transferred between plasma and gas in horizontal direction. The discrepancy was equal to 8% (coarse grid provided greater result). The described comparison shows good agreement between simulation results on coarse and fine grids for fluid plasma model. However, one should definitely keep in mind that each comparison has to be done for particular conditions, since for higher voltage or higher gas pressure cases may need finer resolution for stability as well.

Speed-up studies

In order to test the potential benefits of performing simulations at supercomputing facilities, we designed and ran speed-up tests for the DBD simulations using fluid approach. We performed simulations at our in-house cluster. It is a 32-node, quad core, dual Opteron cluster (8 GB RAM each; totaling 256 cores). This cluster uses Infiniband interconnects and has a 13 TB high-performance parallel file system. We performed simulations for 34000 time steps at 1, 2 and 4 nodes (8, 16 and 32 cores correspondingly). For the baseline case, we've chosen the simulation performed at 1 node (8 core). Figure 6 shows the speed-up of 16 and 32 core simulations compared to 8 core case. We observe almost ideal scaling with increase in number of cores.

Conclusions

The paper has presented detailed comparison between simulation results of pulsed driven DBD plasma actuators using different numerical and physical models: kinetic Particle-In-Cell approach and fluid approaches with artificial and accurately computed photoionization. The simulations showed good agreement between kinetic and fluid approaches for key DBD characteristics, such as streamer thickness, streamer height above dielectric surface, generated electric fields, etc. The main difference between PIC and fluid simulations is in the electron number density distribution within a streamer: it is rather grainy for PIC approach and smooth for fluid approach. We observed that maximum electric fields, generated at the streamer head are $\sim 5\text{-}7 \cdot 10^7$ V/m. We also observed a large region between streamer body and dielectric surface, where vertical component of electric field may reach up to 10^8 V/m. Finally, we have reported grid resolution study for fluid plasma model and results on the scaling measurements for further simulation at supercomputing facilities.

References:

1. J.R. Roth, D.M. Sherman, S.P. Wilkinson, "Electrohydrodynamic Flow Control with a Glow-Discharge Surface Plasma", *AIAA Journal*, 38, 7, 1166 (2000)
2. T.C. Corke, C.L. Enloe, and S.P. Wilkinson, "Dielectric Barrier Discharge Plasma Actuators for Flow Control", *Annu. Rev. Fluid. Mech*, 42:505-29 (2010)
3. D.V. Roupasov, A.A. Nikipelov, M.M. Nudnova, and A.Yu. Starikovskii, "Flow Separation Control by Plasma Actuator with Nanosecond Pulsed-Periodic Discharge", *AIAA Journal*, 47, 168-185 (2009)
4. J. Poggie, C. P. Tilmann, P. M. Flick, J. S. Silkey, B. A. Osbourne, G. Ervin, D. Maric, S. Mangalam, and A. Mangalam. "Closed-Loop Stall Control System", *Journal of Aircraft*, Vol. 47, No. 5 (2010), pp. 1747-1755.
5. Opaits, D., Neretti, G., Zaidi, S., Shneider, M., Miles, R., Likhanskii, A., Macheret. S., "DBD Plasma Actuators Driven by a Combination of Low Frequency Bias Voltage and Nanosecond Pulses", *Paper AIAA-2008-1372*, 46th AIAA Aerospace Sciences Meeting and Exhibit, Reno, Nevada, Jan. 7-10, 2008
6. C. Nieter, and J.R. Cary, "VORPAL: a versatile plasma simulation code," *Journal of Computational Physics*, vol. 196, pp. 448-473, 2004.
7. A. Likhanskii, V. Semak, D. Opaits, M. Shneider, R. Miles, and S. Macheret, "The role of the photoionization in the numerical modeling of the DBD plasma actuator", *AIAA-2009-841*, 47th AIAA Aerospace Sciences Meeting, Orlando FL, Jan 5-9, 2009
8. A. Likhanskii, "Particle-in-Cell Modeling of the Pulsed DBD Plasma Actuator", 41th AIAA Plasmadynamics and Lasers Conference, 2010

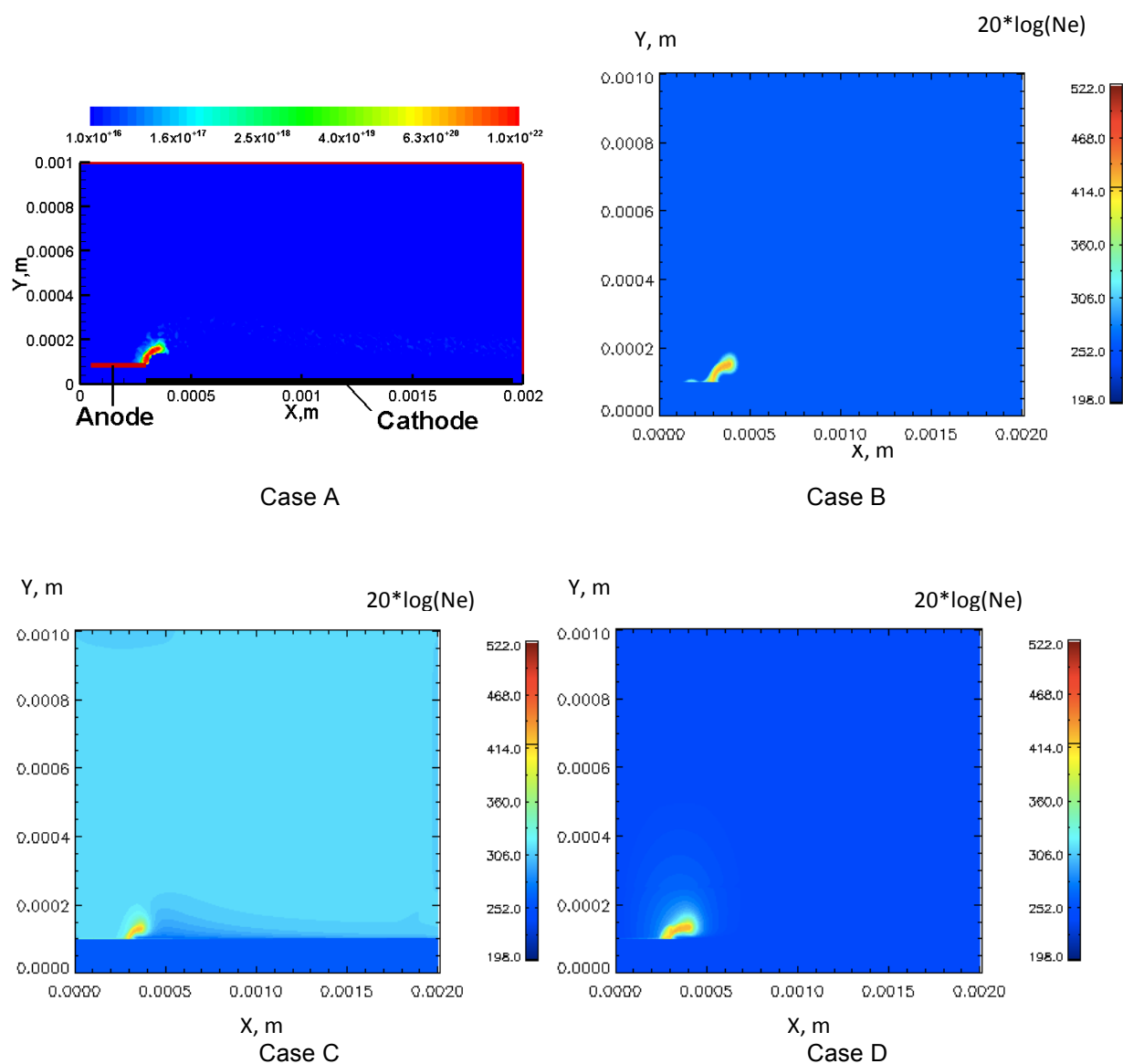


Figure 1. Electron number density distribution during discharge initiation stage. DBD is driven by 5kV, 4ns positive pulses. Case A – PIC simulation, 2.85ns after start of simulations. Case B – drift-diffusion approximation with keeping minimum electron number density, 2.85 ns after the start of simulations. Case C – drift-diffusion approximation with constant plasma loading, 1.95ns after start of simulations. Case D – drift-diffusion with photoionization, 2.55 ns after start of simulations

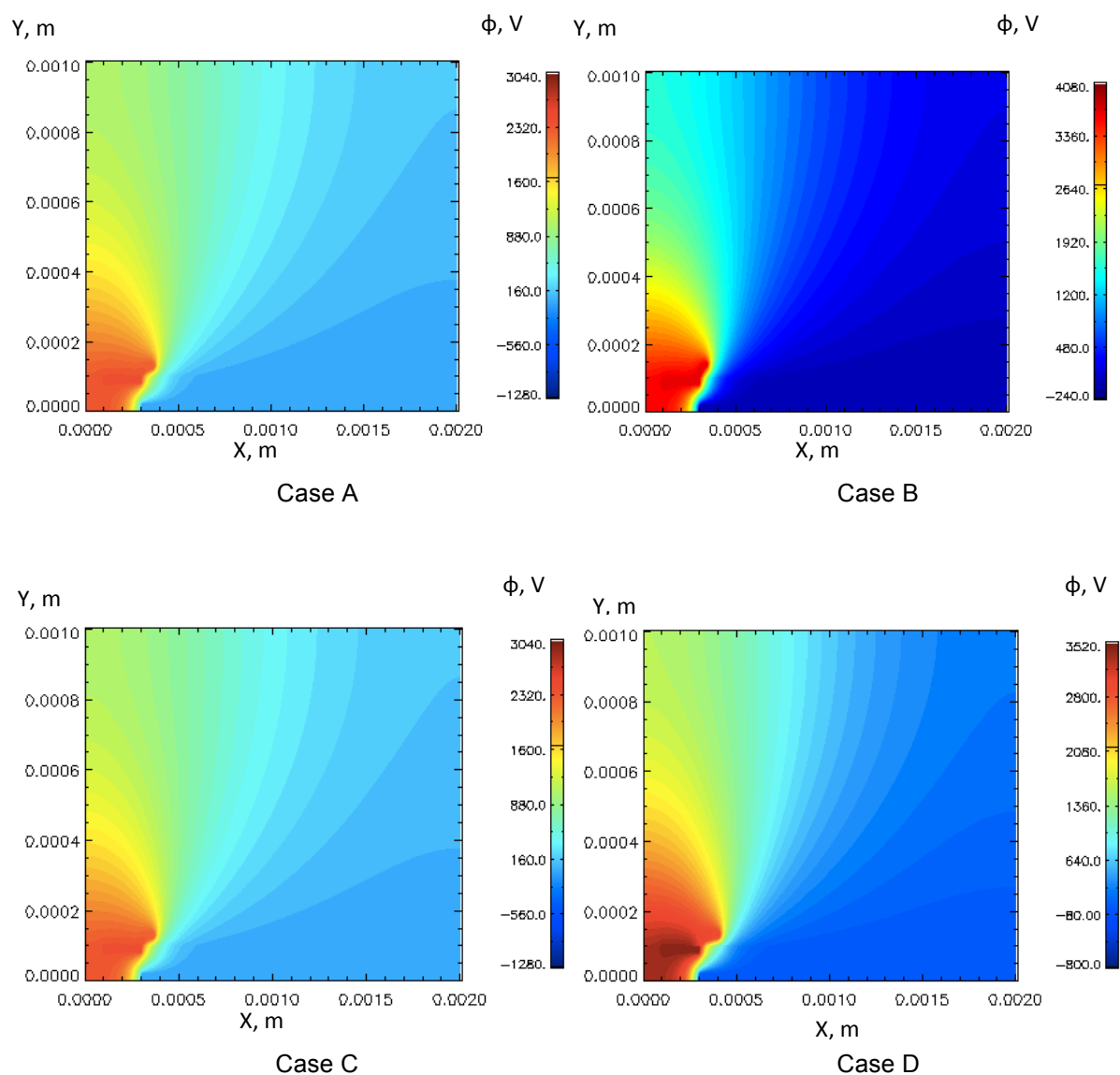


Figure 2. Electric potential distribution during discharge initiation stage. DBD is driven by 5kV, 4ns positive pulses. Case A – PIC simulation, 2.85 ns after start of simulations. Case B – drift-diffusion approximation with keeping minimum electron number density, 2.85 ns after the start of simulations. Case C – drift-diffusion approximation with constant plasma loading, 1.95 ns after start of simulations. Case D – drift-diffusion with photoionization, 2.55 ns after start of simulations

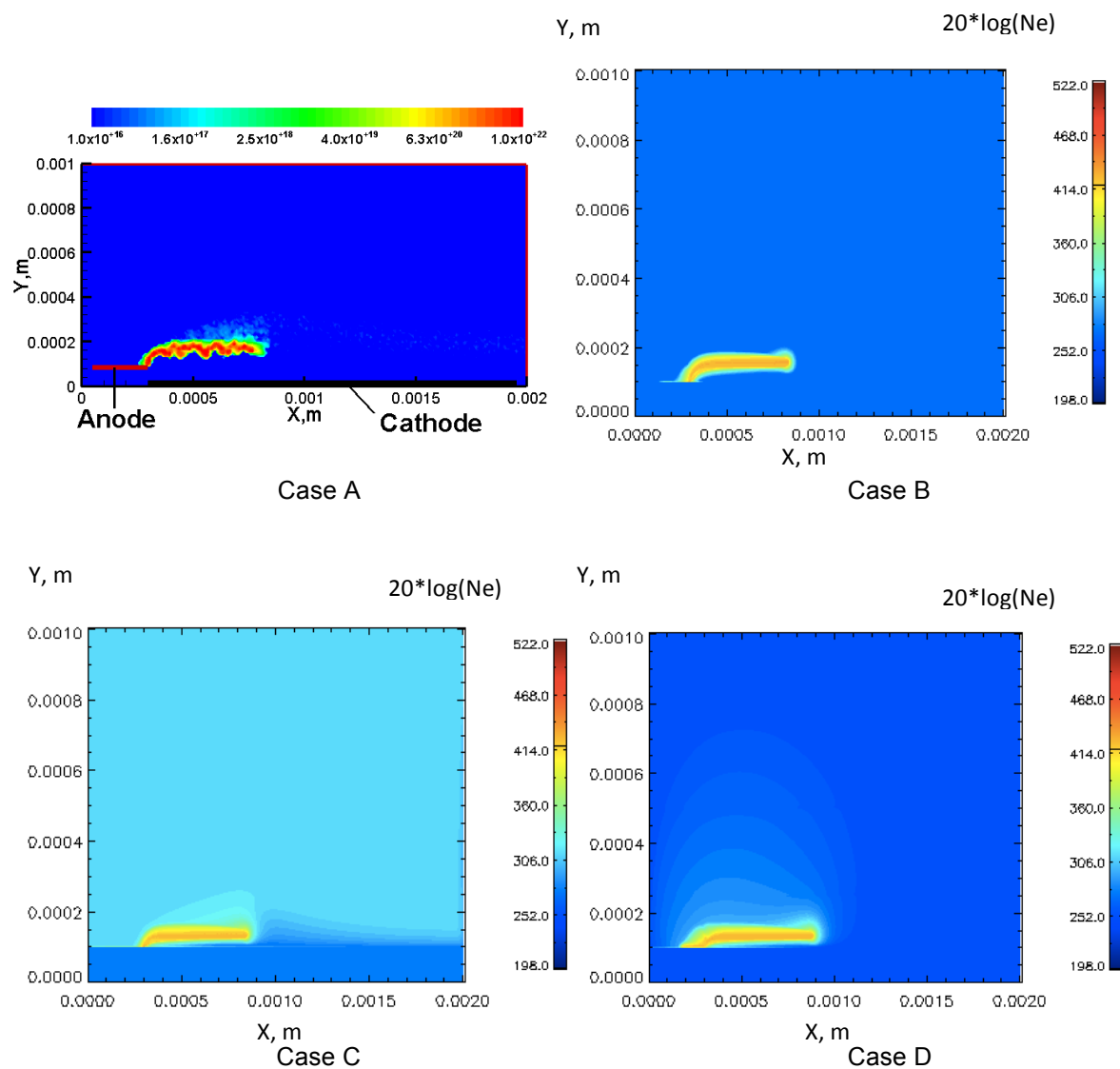


Figure 3. Electron number density distribution during discharge propagation stage. DBD is driven by 5kV, 4ns positive pulses. Case A – PIC simulation, 3.3 ns after start of simulations. Case B – drift-diffusion approximation with keeping minimum electron number density, 3.6 ns after the start of simulations. Case C – drift-diffusion approximation with constant plasma loading, 2.7 ns after start of simulations. Case D – drift-diffusion with photoionization, 3.15 ns after start of simulations

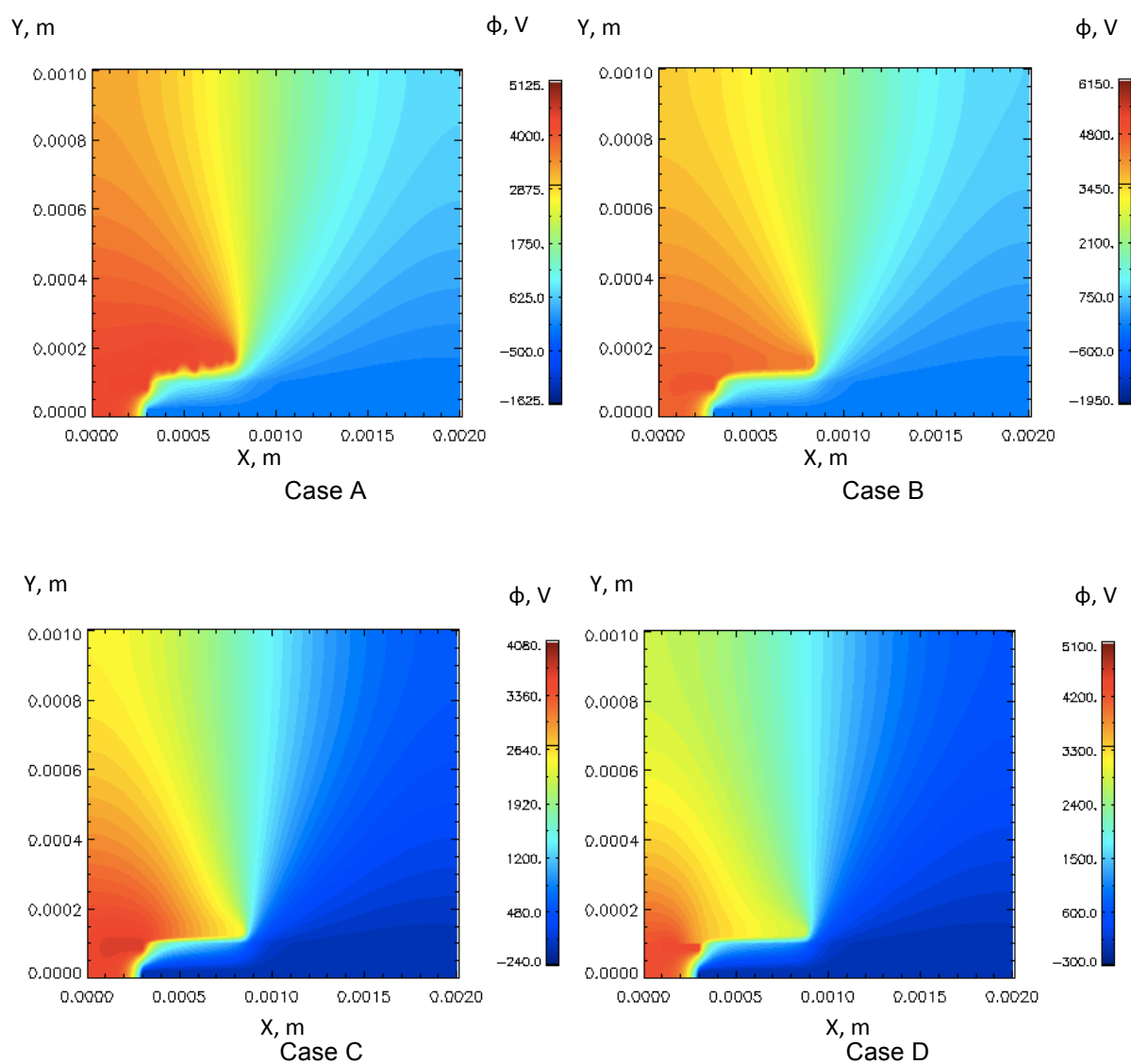


Figure 4. Electric potential distribution during discharge propagation stage. DBD is driven by 5kV, 4ns positive pulses. Case A – PIC simulation, 3.3 ns after start of simulations. Case B – drift-diffusion approximation with keeping minimum electron number density, 3.6 ns after the start of simulations. Case C – drift-diffusion approximation with constant plasma loading, 2.7 ns after start of simulations. Case D – drift-diffusion with photoionization, 3.15 ns after start of simulations

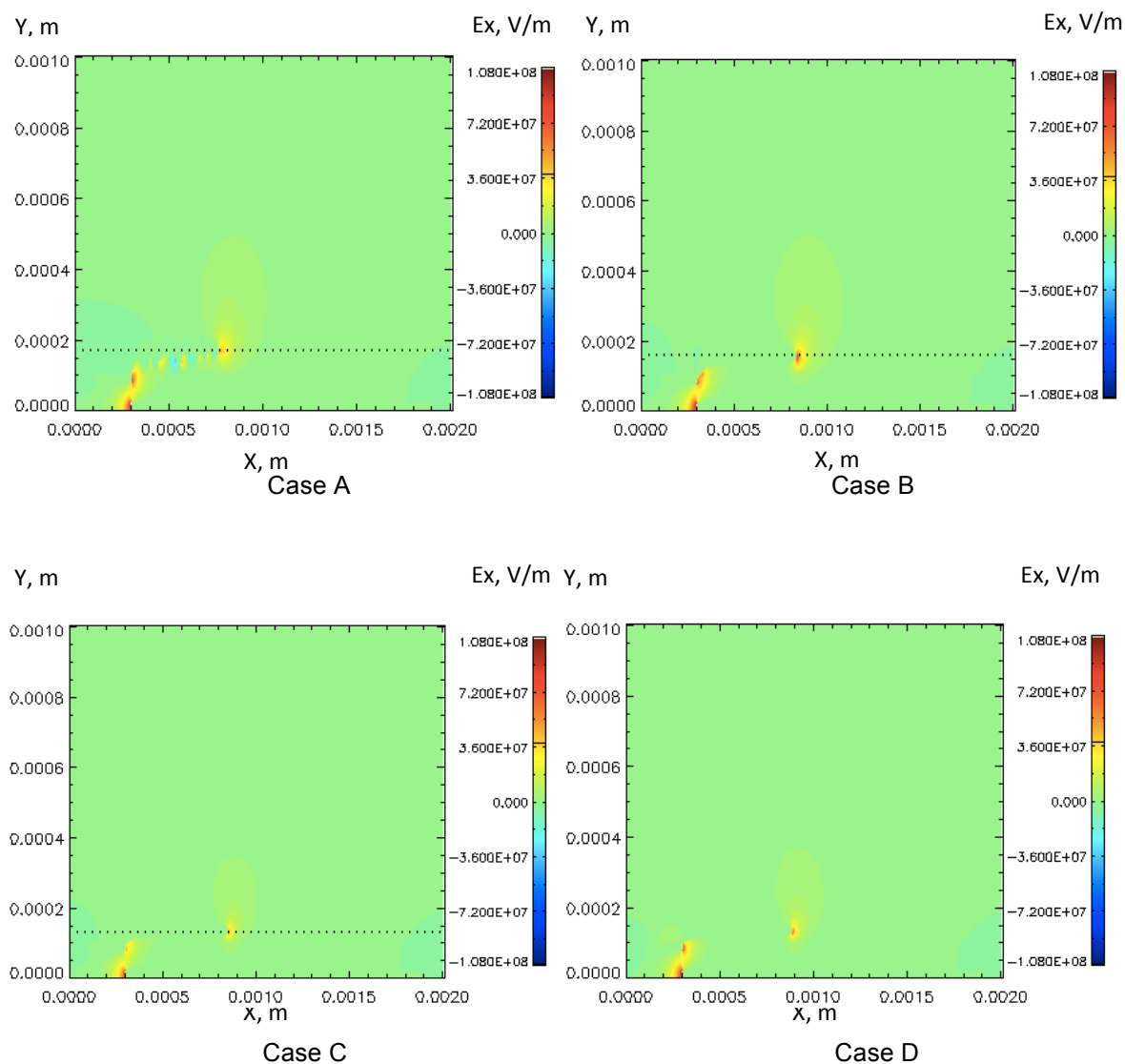


Figure 5. Horizontal component of electric field during discharge propagation stage. DBD is driven by 5kV, 4ns positive pulses. Case A – PIC simulation, 3.3 ns after start of simulations. Case B – drift-diffusion approximation with keeping minimum electron number density, 3.6 ns after the start of simulations. Case C – drift-diffusion approximation with constant plasma loading, 2.7 ns after start of simulations. Case D – drift-diffusion with photoionization, 3.15 ns after start of simulations

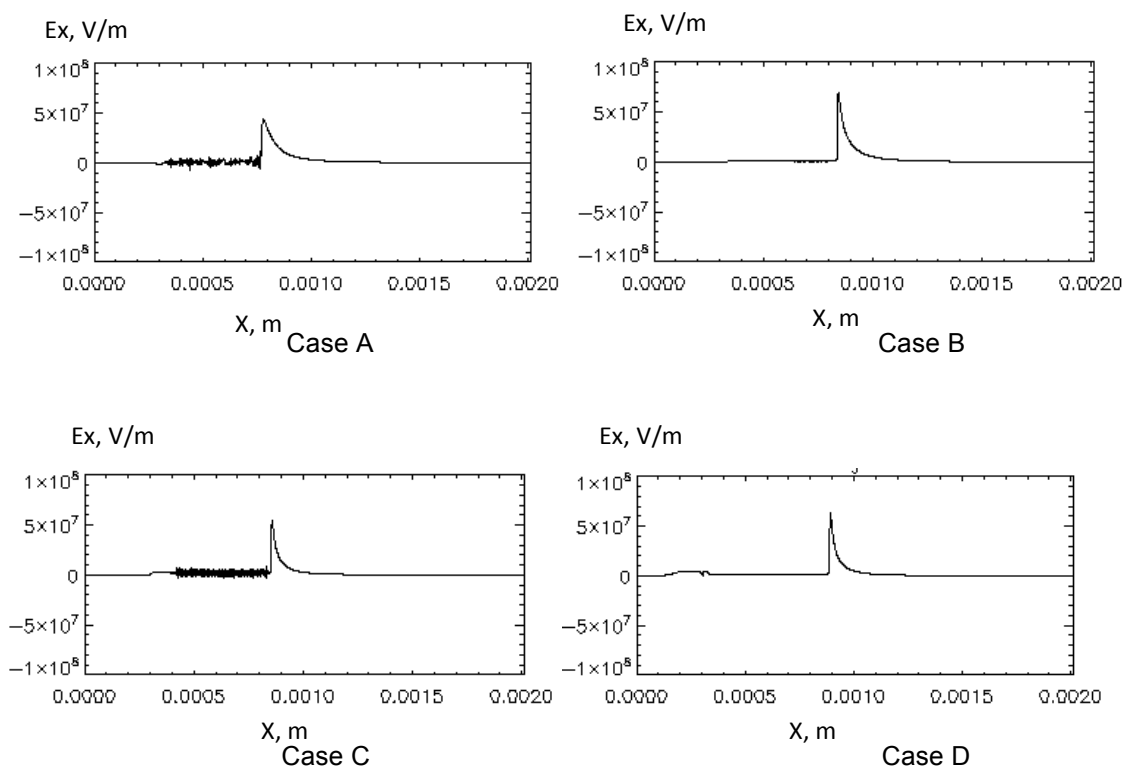


Figure 6. 1D representation of horizontal component of electric field in the cut, shown by dash line in Figure 5. DBD is driven by 5kV, 4ns positive pulses. Case A – PIC simulation, 3.3 ns after start of simulations. Case B – drift-diffusion approximation with keeping minimum electron number density, 3.6 ns after the start of simulations. Case C – drift-diffusion approximation with constant plasma loading, 2.7 ns after start of simulations. Case D – drift-diffusion with photoionization, 3.15 ns after start of simulations

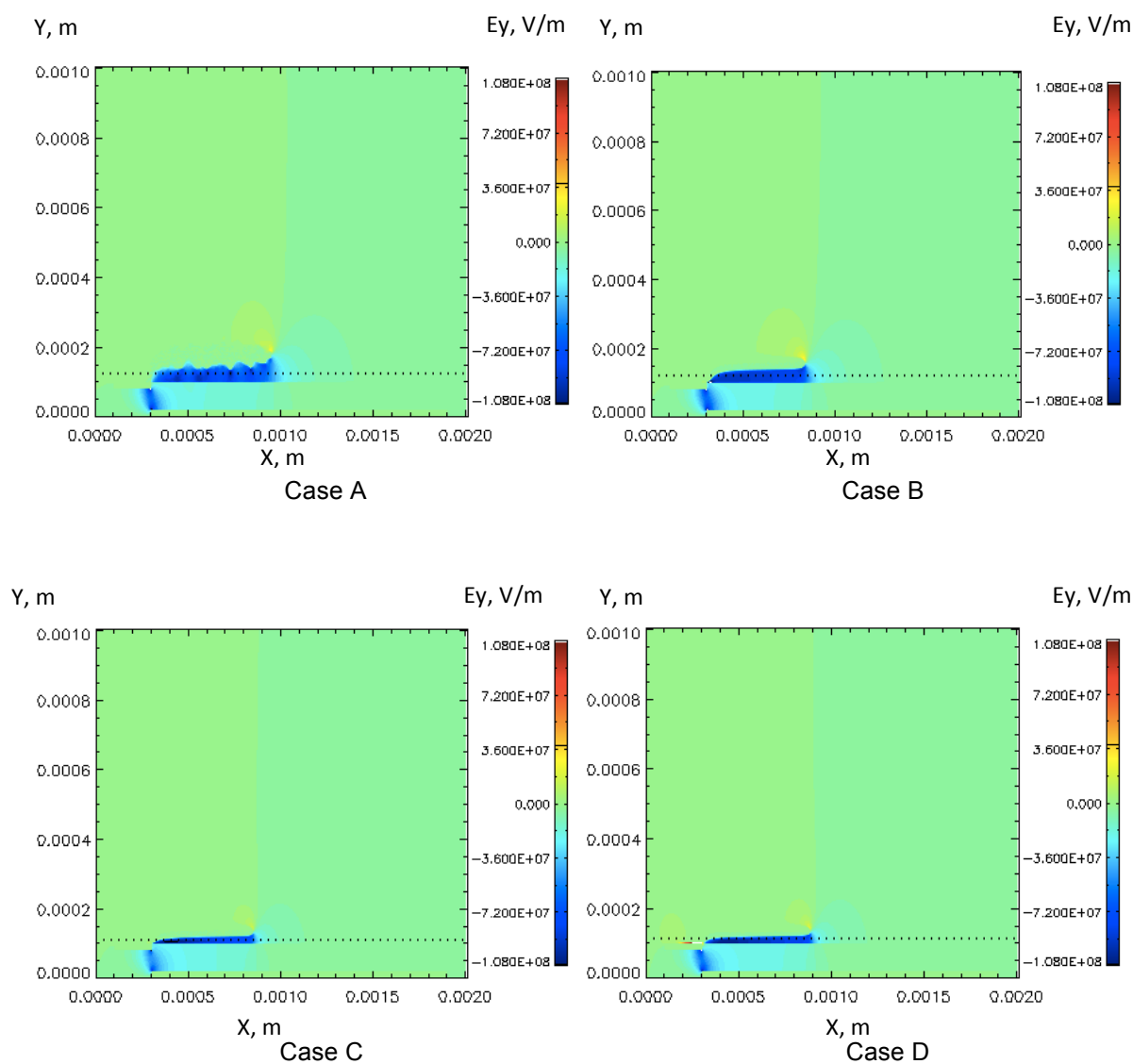


Figure 7. Vertical component of electric field during discharge propagation stage. DBD is driven by 5kV, 4ns positive pulses. Case A – PIC simulation, 3.3 ns after start of simulations. Case B – drift-diffusion approximation with keeping minimum electron number density, 3.6 ns after the start of simulations. Case C – drift-diffusion approximation with constant plasma loading, 2.7 ns after start of simulations. Case D – drift-diffusion with photoionization, 3.15 ns after start of simulations

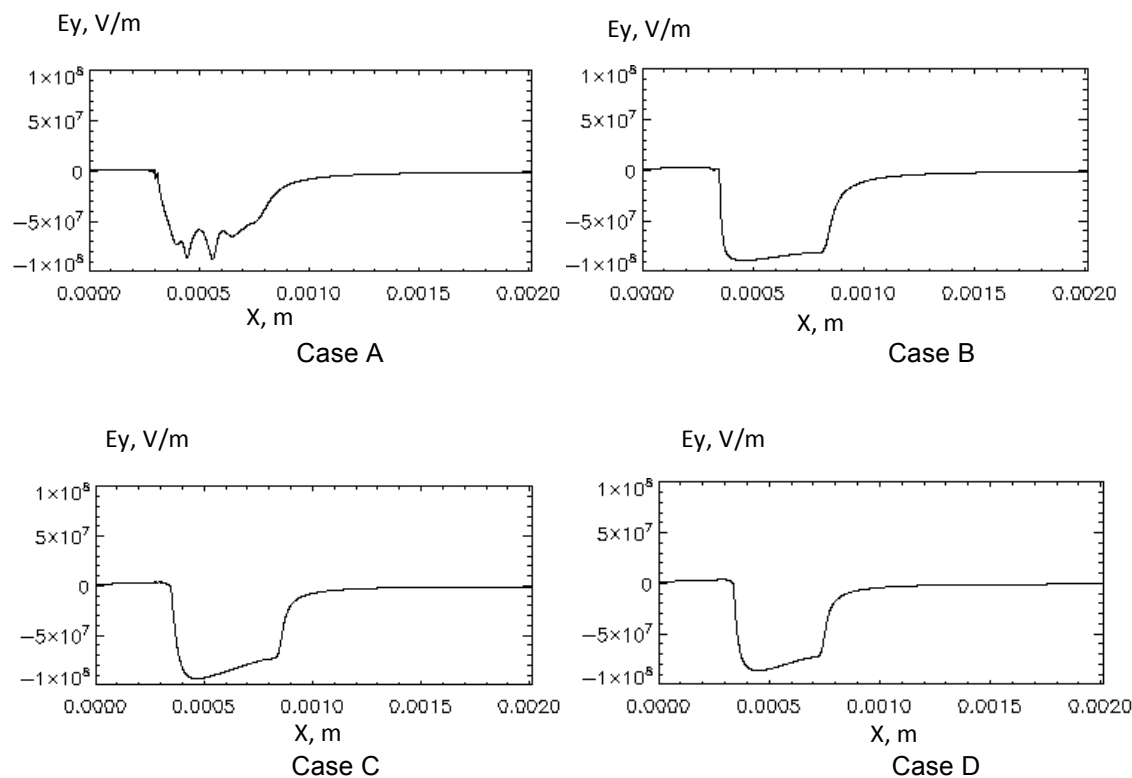


Figure 8. 1D representation of vertical component of electric field in the cut, shown by dash line in Figure 7. DBD is driven by 5kV, 4ns positive pulses. Case A – PIC simulation, 3.3 ns after start of simulations. Case B – drift-diffusion approximation with keeping minimum electron number density, 3.6 ns after the start of simulations. Case C – drift-diffusion approximation with constant plasma loading, 2.7 ns after start of simulations. Case D – drift-diffusion with photoionization, 3.15 ns after start of simulations

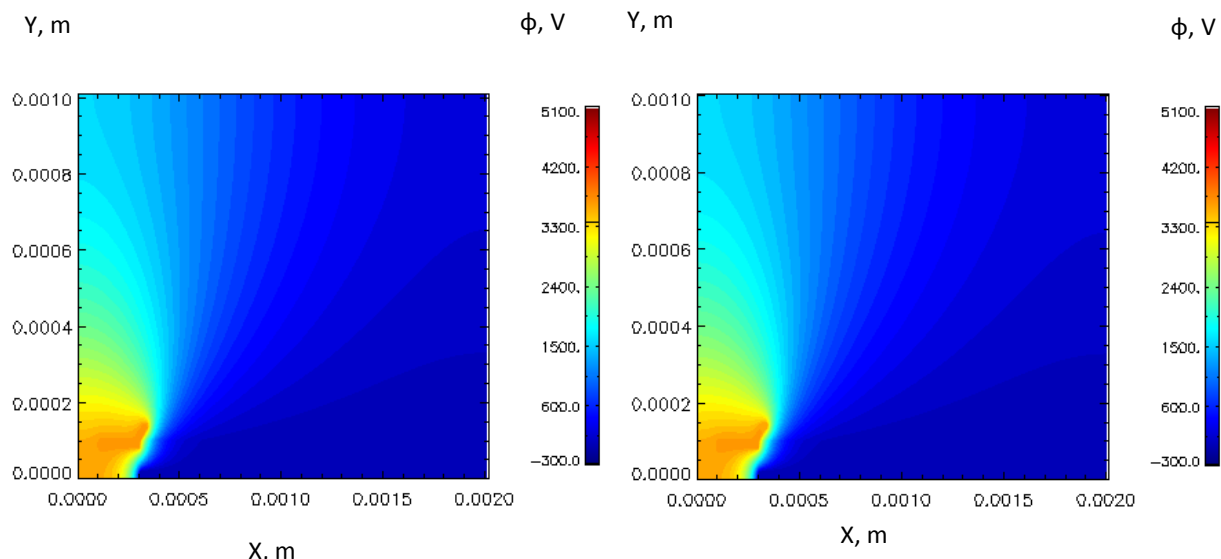


Figure 9. Electric potential distribution at discharge ignition (2.9 ns after start of the simulations) using fluid model for coarse (left) and fine (right) resolutions.

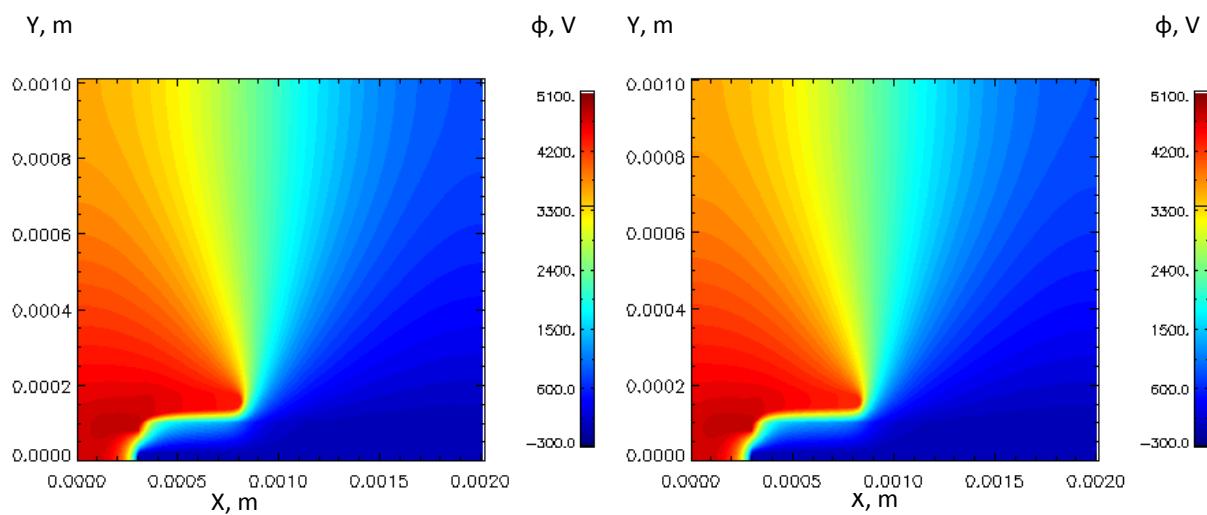


Figure 10. Electric potential distribution at discharge propagation (3.6 ns after start of the simulations) using fluid model for coarse (left) and fine (right) resolutions.

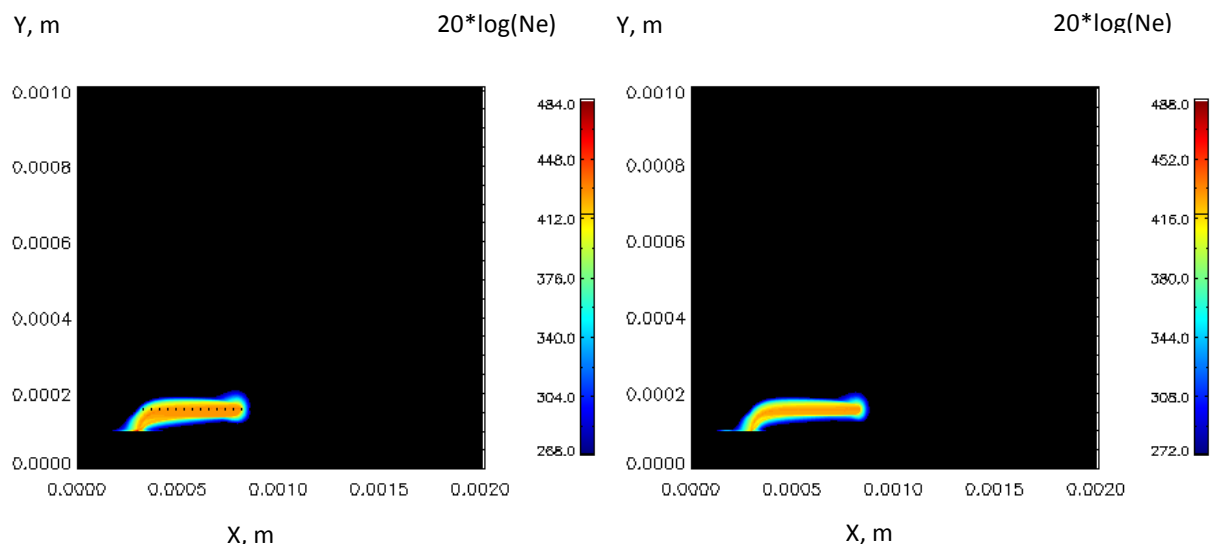


Figure 11. Electron number density distribution at discharge propagation (3.6 ns after start of the simulations) using fluid model for coarse (left) and fine (right) resolutions.

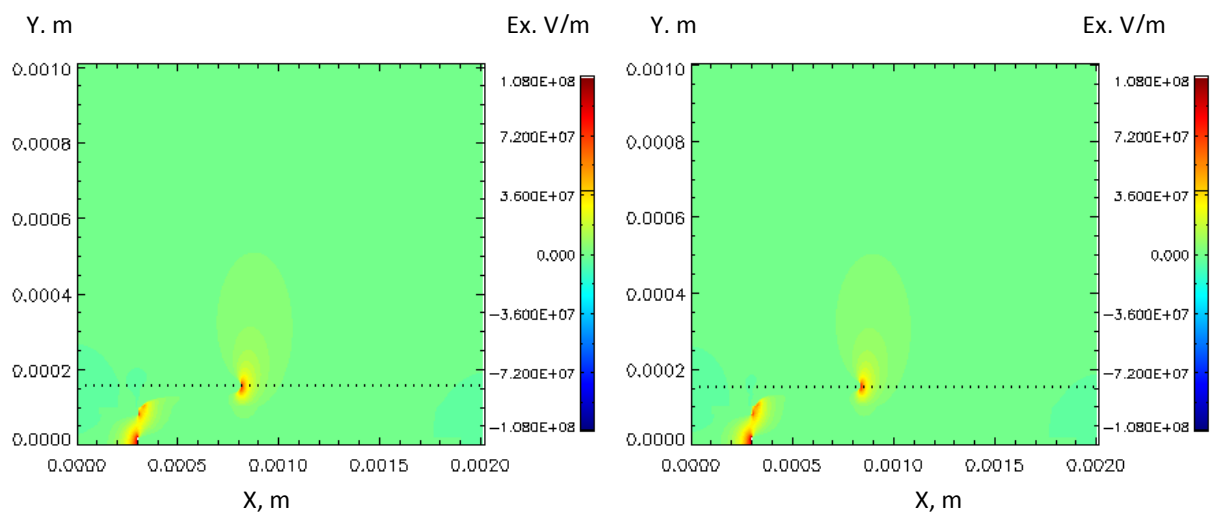


Figure 12. Horizontal component of electric field at discharge propagation (3.6 ns after start of the simulations) using fluid model for coarse (left) and fine (right) resolutions.

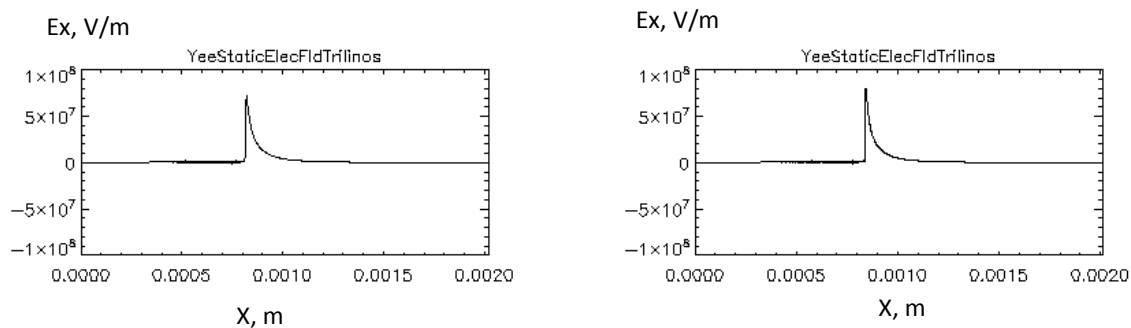


Figure 13. 1D representation of horizontal component of electric field in the cut, shown by dash line in Figure 12, at discharge propagation (3.6 ns after start of the simulations) using fluid model for coarse (left) and fine (right) resolutions.

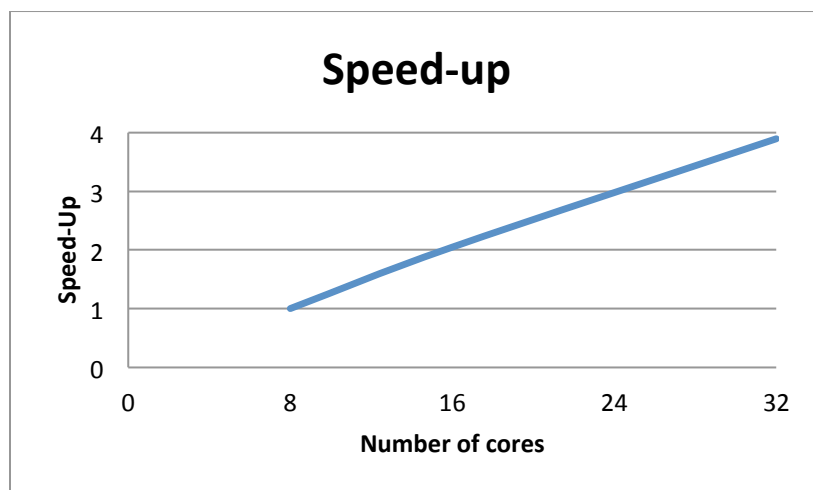


Figure 14. Speedup of the simulation for 8 to 32 cores

Appendix B

Shock-Wave/Boundary-Layer Interaction

Exploration of Plasma Control for Supersonic Turbulent Flow over a Compression Ramp

Nicholas J. Bisek,^{*} Donald P. Rizzetta,[†] and Jonathan Poggie[‡]

Air Force Research Laboratory, Wright-Patterson AFB, OH, 45433-7512, USA

The Navier-Stokes equations are solved using a high-fidelity time-implicit numerical scheme and an implicit large-eddy simulation approach to investigate plasma-based flow control for supersonic flow over a compression ramp. The configuration includes a flat-plate region to develop an equilibrium turbulent boundary layer at Mach 2.25, which is validated against a set of experimental measurements. The fully turbulent boundary-layer flow interacts with a 24° ramp and produces an unsteady shock-induced separation. A control strategy to suppress the separation through a magnetically-driven gliding-arc actuator is explored. The size, strength, and placement of the actuator are developed based on recent experiments. Three control scenarios were examined: steady control, pulsing with a 50% duty cycle, and Joule heating. The results show the control mechanism is very effective at reducing the mean separation length for all three situations. The case without pulsing and Joule heating was the most effective, with a reduction in the separation length by more than 75%. Control was also found to significantly reduce the low-frequency content of the turbulent kinetic energy spectrum.

Nomenclature

a, b	= nondimensional radii of the ellipsoid for the controller model
c_f	= skin-friction coefficient, $c_f = \left(\frac{2}{Re} \right) \frac{\partial u}{\partial y} \Big _w$
D_c	= scale parameter for counter-flow trip model
E	= nondimensional total specific energy
E_x, E_y, E_z	= nondimensional components of the electric field vector
$\mathbf{F}, \mathbf{G}, \mathbf{H}$	= inviscid vector fluxes
$\mathbf{F}_v, \mathbf{G}_v, \mathbf{H}_v$	= viscous vector fluxes
J	= transformation Jacobian
\mathcal{J}	= nondimensional Joule heating value
ℓ	= reference or characteristic length
L_x, L_y, L_z	= nondimensional components of the magnetic body force vector
M	= Mach number
p	= nondimensional static pressure
Re	= Reynolds number, $u_\infty \ell / \nu_\infty$
Δs^+	= nondimensional inner length scale, $\Delta s u_\tau / \nu_w$
t	= nondimensional time
T	= nondimensional static temperature

^{*}Research Aerospace Engineer, AFRL/RBAC. Member AIAA.

[†]Senior Research Aerospace Engineer, AFRL/RBAC. Associate Fellow AIAA.

[‡]Team Lead, High-Speed Flow Research Group, AFRL/RBAC. Associate Fellow AIAA.

\mathbf{U}	= conserved variable vector
u, v, w	= nondimensional Cartesian velocity components in the x, y, z directions
x, y, z	= streamwise, normal, and spanwise directions in nondimensional Cartesian coordinates
y^+	= nondimensional wall distance, $y u_\tau / \nu_w$
γ	= specific heat ratio, 1.4 for air
δ	= boundary-layer thickness, $0.99 u_\infty$
δ^*	= boundary-layer displacement thickness, $\int_0^\infty \left(1 - \frac{\rho u}{\rho_\infty u_\infty}\right) dy$
ξ, η, ζ	= computational coordinates
θ	= boundary-layer momentum thickness, $\int_0^\infty \frac{\rho u}{\rho_\infty u_\infty} \left(1 - \frac{\rho u}{\rho_\infty u_\infty}\right) dy$
ν	= kinematic viscosity
ρ	= nondimensional density
τ_{ij}	= components of the viscous stress tensor
<i>Subscript</i>	
c	= center of ellipsoid
w	= wall
∞	= freestream

I. Introduction

Supersonic turbulent flows are a widely studied field, both experimentally and numerically. With the rapid increase in supercomputer capabilities over the past two decades, high-fidelity computational efforts have seen significant growth and improvement as computer modeling is being used to predict turbulent flows that extend beyond unit-sized problems (in both geometric and fluid dynamic complexities). Of late, there has been a particular emphasis on turbulent shock boundary-layer interaction (SBLI), which may result in a region of separated flow under the shock foot. Unfortunately, the pressure fluctuations within the unsteady separated region can lead to localized fatigue loading and the premature failure of the structure. In addition, recent work by Toubert and Sandham¹ indicates that the separation acts as a broadband amplifier. This phenomena may lead to additional problems for a vehicle with SBLI, since any noise generated upstream of the separation could be amplified and cause damage or decreased performance to downstream subsystems.

Due to the extreme environment in which these conditions exist, it can be difficult and costly to fully study the phenomena in wind-tunnel experiments. In addition, it is complementary to study this phenomena using computational fluid dynamics, since computational results provide additional details and a wider understanding of the complex interactions existing in the flow. The ideal approach would be to simulate the flow using direct numerical simulation (DNS). In DNS, all length and time scales are fully resolved everywhere in the flow. Unfortunately, for a supersonic vehicle operating a flight conditions, a DNS of the entire flow is still beyond the reach of current computational resources. As such, large-eddy simulations (LES), are a popular alternative approach for investigating these flows. In LES, the computation domain resolves all length and timescales down to the inertia range and then relies on a subgrid-scale (SGS), model or a filtering procedure to model the energy cascade to the smaller, under-resolved, scales. The approach is predicated on the assumption turbulence energy is transferred from large to small scales in a cascade, and that intercepting the energy flow in the inertial subrange using a filter or a SGS model is equivalent to resolving the small scales on which energy dissipation occurs. Subsequently, LES has the benefit of less stringent grid and time scale requirements, while still providing physically-accurate results.

The LES approach is widely accepted and employed in the turbulence community,² because it allows the study of a much wider range of problems.^{1,3–10}

In addition to localized fatigue loading and the premature structural failure of the vehicle, separated flow due to SBLI increases the boundary-layer thickness, which decreases the cross-sectional area of the inviscid core for an internal flow. This behavior is detrimental for inlet and isolator performance as it decreases the mass flow-rate for air-breathing configurations. As such, the unfavorable behavior of the separated region of the flow motivates research to better understand the physical mechanisms driving its behavior, and to identify suitable ways of mitigating or, preferably, eliminating the region from the flow. Traditionally, boundary-layer bleed has been used to remove the unfavorable flow, but this requires additional plumbing within the vehicle and power to facilitate bleed. In addition, bleed is unfavorable for internal flows since a portion of the mass flow-rate is removed.

The present work explores the interaction of a turbulent boundary-layer due to a compression corner, as illustrated in Fig. 1. This problem has been studied numerically by several researchers, including work by Adams,¹¹ Rizzetta *et al.*,^{4,6} Wu and Pino Martín,¹² Muppidi and Mahesh,¹³ and Priebe and Pino Martín.^{14,15} All these previous computational studies correspond to a freestream Mach number of 2.9, while this study explores a freestream Mach number of 2.249. Due to the lower Mach number and the large ramp angle of 24° , the separation length due to the SBLI is larger than the aforementioned studies.

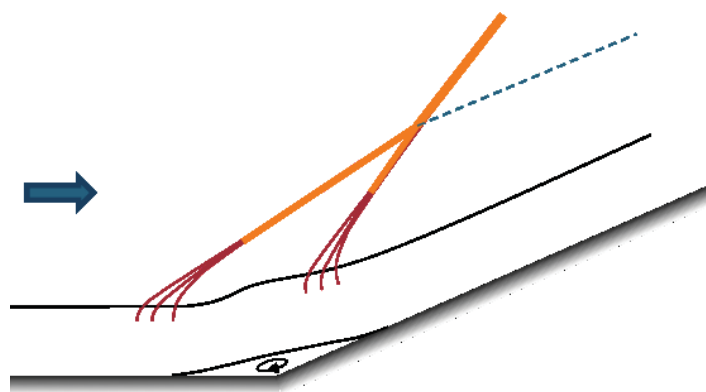


Figure 1. Flow over a 24° compression corner at Mach 2.25.

The main focus of this work is to reduce the extent of separated region of a SBLI by using an arc-discharge-based flow controller. The paper will first explore the development of a supersonic equilibrium turbulent boundary-layer flow over a compression corner to establish a baseline flow. To this end, a grid study is performed and the results are compared to experimental data which show that the LES is accurately capturing the essential flow features. In addition, the paper will discuss the mechanism for transitioning the laminar inflow to turbulence and show that the turbulent profiles upstream of the separated region are free of discrete frequencies. Having the incoming turbulent boundary-layer free of discrete frequencies is important so the effects of the controller are not obscured by discrete frequency modes from the incoming profile. Finally, a model control device is introduced into the computations and its effects on time-mean and time-dependent statistics are examined for three control strategies. The results show that the separation length is significantly reduced by the controller, and, that the the lowest frequency content is reduced with actuation.

II. Method

The simulations were carried out with a time-accurate three-dimensional compressible Navier-Stokes solver known as FDL3DI,¹⁶ which has been widely used in previous LES for both subsonic and supersonic flows.^{17–23}

A. Governing Equations

The governing equations are transformed from Cartesian coordinates into a general time-dependent curvilinear coordinate system that is recast in strong conservation-law form:

$$\frac{\partial \mathbf{U}}{\partial t} + \frac{\partial (\mathbf{F} - \mathbf{F}_v)}{\partial \xi} + \frac{\partial (\mathbf{G} - \mathbf{G}_v)}{\partial \eta} + \frac{\partial (\mathbf{H} - \mathbf{H}_v)}{\partial \zeta} = \mathbf{S}_c \quad (1)$$

where t is the time and ξ , η , and ζ are the computational coordinates. The solution vector and vector fluxes (both inviscid and viscous) are:

$$\mathbf{U} = \frac{1}{J} \begin{bmatrix} \rho \\ \rho u \\ \rho v \\ \rho w \\ \rho E \end{bmatrix}, \quad \mathbf{F} = \frac{1}{J} \begin{bmatrix} \rho U \\ \rho u U + \xi_x p \\ \rho v U + \xi_y p \\ \rho w U + \xi_z p \\ \rho E U + \xi_{x_i} u_i p \end{bmatrix}, \quad \mathbf{F}_v = \frac{1}{Re J} \begin{bmatrix} 0 \\ \xi_{x_i} \tau_{i1} \\ \xi_{x_i} \tau_{i2} \\ \xi_{x_i} \tau_{i3} \\ \xi_{x_i} (u_j \tau_{ij} - q_i) \end{bmatrix} \quad (2)$$

and

$$U = \xi_t + \xi_{x_i} u_i, \quad V = \eta_t + \eta_{x_i} u_i, \quad W = \zeta_t + \zeta_{x_i} u_i, \quad E = \frac{T}{(\gamma - 1) M_\infty^2} + \frac{1}{2} u_i^2 \quad (3)$$

where u , v , and w are the Cartesian velocity components, ρ is the density, p is the pressure, and T is the temperature. J is the transformation Jacobian, $\partial(\xi, \eta, \zeta, t)/\partial(x, y, z, t)$.²⁴ Note that the formulas for \mathbf{G} , \mathbf{G}_v , \mathbf{H} , and \mathbf{H}_v are similar to those specified in Eq. (2), and may be found in Ref. 25.

The source vector, \mathbf{S}_c , on the right side of Eq. (1), is typically set to zero, but has nonzero values at specific locations within the domain to transition the flow to fully turbulent or when the gliding-arc discharge controller is employed. The value of \mathbf{S}_c will be described in greater detail in the following subsection.

All length scales are nondimensionalized by the reference length, ℓ , and all dependent variables are normalized by their respective reference values, except for pressure, which is nondimensionalized by $\rho_\infty u_\infty^2$. The perfect gas relationship and Sutherland law for the molecular viscosity are employed with a reference temperature of 110.3 K.

B. Source Terms

The right-hand side of Eq. (1) allows various flow-control and flow-trip models to be introduced into the governing equations. This paper employs two different source models. The trip model initiates transition of the incoming laminar flow to a turbulent boundary-layer, while the control model is a phenomenological representation of a gliding-arc discharge flow controller.

This work used the counter-flow force bypass-transition method developed by Mullenix *et al.*²⁶ since the method produces a steady disturbance to transition supersonic flows. The trip model consisted of a right-triangle force region which was centered at $x = 2.5$, applied uniform in the span, and exerted a streamwise force to oppose the incoming flow. The strength of the counter-flow force was controlled by a scalar, $D_c = 6.2$.

Control of separation was accomplished by the introduction of a streamwise force which was produced by a gliding-arc discharge actuator. In a gliding-arc discharge, two flush-mounted surface electrodes are separated by an insulator. The electrodes are arranged to be slightly diverging from each other. A high voltage is applied between the electrodes. If the distance between the electrodes is sufficiently small, and the voltage is sufficiently high (~ 30 kV/cm for air²⁷), breakdown occurs and an arc forms between the electrodes at their closest point. The electric arc partially ionizes the surrounding air which carries the current path with it. If the electrodes are positioned vertically, the heated air between the electrodes would rise which would make the arc rise with it (which is also known as Jacob's Ladder). Here, the electrodes are embedded in the flat-plate, so the arc only moves with the boundary-layer flow.

Applying a strong magnetic field perpendicular to the surface causes the arc to accelerate due to the magnetic body force. Depending on the direction of the magnetic field, the discharge can be forced to move upstream or downstream at a rate several times faster than the freestream speed.²⁸ Since the magnetic field directly influences the movement of the arc, this type of actuator is also known as a magnetically-driven surface discharge, dubbed "snowplow arcs".²⁹ As the arc travels down the length of the electrodes, its core area contracts due to the slightly diverging electrode orientation. The contraction of the arc's core area leads to instabilities within the arc, and it eventually extinguishes itself. Once extinction occurs, a new arc forms at the narrow end of the electrodes and the process is repeated.

Since the magnetically-driven gliding-arc velocity is many times faster than the freestream flow, a time-mean representation of actuators influence is appropriate for fluid dynamic simulations. In addition, the time scales of the plasma involved are orders of magnitude smaller than the characteristic flow time of the fluid, so the actuator can be incorporated in the fluid through time-mean specified source terms.³⁰ Thus, depending on the orientation of the magnetic and current fields, the body force can be applied to the flow in any direction. Figure 2 illustrates the configuration of the magnetically-driven gliding-arc system applied to control the turbulent SBLI consider in this paper.

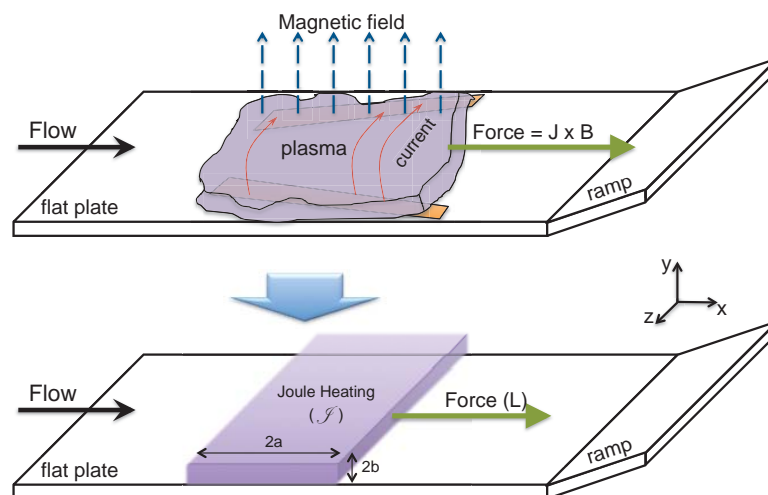


Figure 2. Illustration of the gliding-arc discharge model.

This work uses a phenomenological model of the force and energy deposition that is similar to that used in the Reynolds-averaged calculations of Atkinson *et al.*^{31,32} The deposition volume density function is described as a hyper-Gaussian function, which provides a mathematically representation of the shape of the plasma-column and the deposition density within the column:

$$S = \frac{K}{a b} \exp \left[- \left(\frac{x - x_c}{a} \right)^m - \left(\frac{y - y_c}{b} \right)^n \right] \quad (4)$$

where a and b represent the ellipsoidal radii in the x and y directions, and K is constant such that $\iint_{-\infty}^{\infty} S \, dx \, dy = 1$ for the selected values of m and n . In this work $m = n = 10$. Use of higher power values in the exponential function allows the deposition rate to be nearly uniform within the volume ($\exp \left[- \left(\frac{x - x_c}{a} \right)^n - \left(\frac{y - y_c}{b} \right)^m \right] \leq 1$), yet to decay rapidly to zero outside the region. The controller model accounts for both the mean body force and Joule heating, as seen in Eq. (5):

$$\mathbf{S}_c = \frac{S}{J} \begin{bmatrix} 0 \\ L_x \\ L_y \\ L_z \\ u L_x + v L_y + w L_z + \mathcal{J} \end{bmatrix} \quad (5)$$

where S is the deposition volume density from the hyper-Gaussian function shown in Eq. (4), \mathbf{L} represents the magnetic body force vector, and \mathcal{J} corresponds to the Joule heating. Joule heating occurs when electrons collide with neutrals, which results in energy exchange (primarily in vibrational modes of the neutral N_2 molecules²⁸). Some of the excited vibrational states quickly relax to equilibrium, while other states have a much slower relaxation time and do not relax before the molecule leaves the computational domain. The amount of energy that goes into the translational energy mode through Joule heating and reversible work reflects the thermal efficiency of the actuator and contributes to the translational temperature. The model parameters used will be described in a later section.

C. The Numerical Method

Time-accurate solutions to Eq. (1) were obtained numerically by the implicit approximately-factored finite-difference algorithm of Beam and Warming,³³ employing Newton-like subiterations,³⁴ and may be written as follows:

$$\begin{aligned} & \left[\frac{1}{J} + \left(\frac{2\Delta t}{3} \right) \delta_{\xi 2} \left(\frac{\partial \mathbf{F}^p}{\partial \mathbf{Q}} - \frac{1}{Re} \frac{\partial \mathbf{F}_v^p}{\partial \mathbf{Q}} \right) \right] J \times \left[\frac{1}{J} + \left(\frac{2\Delta t}{3} \right) \delta_{\eta 2} \left(\frac{\partial \mathbf{G}^p}{\partial \mathbf{Q}} - \frac{1}{Re} \frac{\partial \mathbf{G}_v^p}{\partial \mathbf{Q}} \right) \right] J \times \\ & \left[\frac{1}{J} + \left(\frac{2\Delta t}{3} \right) \delta_{\zeta 2} \left(\frac{\partial \mathbf{H}^p}{\partial \mathbf{Q}} - \frac{1}{Re} \frac{\partial \mathbf{H}_v^p}{\partial \mathbf{Q}} \right) \right] \Delta \mathbf{Q} = - \left(\frac{2\Delta t}{3} \right) \left[\left(\frac{1}{2\Delta t} \right) \left(\frac{3\mathbf{Q}^p - 4\mathbf{Q}^n + \mathbf{Q}^{n-1}}{J} \right) \right] \\ & + \delta_{\xi 6} \left(\mathbf{F}^p - \frac{1}{Re} \mathbf{F}_v^p \right) + \delta_{\eta 6} \left(\mathbf{G}^p - \frac{1}{Re} \mathbf{G}_v^p \right) + \left[\delta_{\zeta 6} \left(\mathbf{H}^p - \frac{1}{Re} \mathbf{H}_v^p \right) - \mathbf{S}_c^p \right] \end{aligned} \quad (6)$$

where $\delta_{\xi 2}$, $\delta_{\eta 2}$, $\delta_{\zeta 2}$, $\delta_{\xi 6}$, $\delta_{\eta 6}$, and $\delta_{\zeta 6}$ represent the second-order and sixth-order finite-difference operators in η , ζ , and ξ , respectively. Equation (6) is employed to advance the solution in time, such that \mathbf{Q}^{p+1} is the $p+1$ approximation to \mathbf{Q} at the $n+1$ time level \mathbf{Q}^{n+1} , and $\Delta \mathbf{Q} = \mathbf{Q}^{p+1} - \mathbf{Q}^p$. For $p = 1$, $\mathbf{Q}^p = \mathbf{Q}^n$. Second-order-accurate backward-implicit time differencing was used to obtain temporal derivatives.

The implicit segment of the algorithm (left-hand side of Eq. (6)), incorporates second-order-accurate centered differencing for all spatial derivatives, and utilizes nonlinear artificial dissipation³⁵ to augment stability. For simplicity, the dissipation terms are not shown in Eq. (6). Efficiency was enhanced by solving this implicit portion of the factorized equations in diagonalized form.³⁶ The temporal accuracy can be degraded when the diagonal form is used, so subiterations were employed

within each time step to minimize any degradation of the temporal solution. Any deterioration of the solution caused by use of artificial dissipation and by lower-order spatial resolution of implicit operators was also reduced by performing sub-iterations. Three applications of the flow solver per time step were applied throughout this work to preserve second-order temporal accuracy.

The compact difference scheme employed on the right-hand side of Eq. (6) is based upon the pentadiagonal system of Lele,³⁷ and is capable of attaining spectral-like resolution. This is achieved through the use of a centered implicit difference operator with a compact stencil, thereby reducing the associated discretization error. For the present computations, a sixth-order tridiagonal subset of Lele's system was utilized, which is illustrated here in one spatial dimension as:

$$\frac{1}{3} \left(\frac{\partial \mathbf{F}}{\partial \xi} \right)_{i-1} + \left(\frac{\partial \mathbf{F}}{\partial \xi} \right)_i + \frac{1}{3} \left(\frac{\partial \mathbf{F}}{\partial \xi} \right)_{i+1} = \frac{14}{9} \left(\frac{\mathbf{F}_{i+1} - \mathbf{F}_{i-1}}{2} \right) + \frac{1}{9} \left(\frac{\mathbf{F}_{i+2} - \mathbf{F}_{i-2}}{4} \right) \quad (7)$$

The scheme has been adapted by Visbal and Gaitonde³⁸ as an implicit iterative time-marching technique. It was used in conjunction with a low-pass Padé-type non-dispersive spatial filter, which was incorporated by Gaitonde *et al.*³⁹ Use of the filter has been shown to be superior to the use of explicitly added artificial dissipation for maintaining both stability and accuracy on stretched curvilinear meshes.³⁸ The filter was applied to the solution vector sequentially in each of the three computational directions following each subiteration, and was implemented in one dimension as:

$$\alpha_f \hat{Q}_{i-1} + \hat{Q}_i + \alpha_f \hat{Q}_{i+1} = \sum_{n=0}^4 \frac{a_n}{2} (Q_{i+n} + Q_{i-n}) \quad (8)$$

where \hat{Q} designates the filtered value of Q . The order of the filtering operation was permuted and was a post-processing technique. It was applied to the evolving solution in order to regularize poorly-resolved features at the grid scale. On uniform grids, the filtering procedures preserve constant functions while completely eliminating the odd-even mode decoupling.^{21,40} Equation (8) represents a one-parameter family of eighth-order filters, and numerical values for the a_n 's may be found in Ref. 16. The filter coefficient α_f is a free adjustable parameter which may be selected for specific applications, where $|\alpha_f| < 0.5$. The value of α_f determines sharpness of the filter cutoff and was set to 0.30 for the present simulations.

The spatial filter associated with the high-order compact scheme may produce spurious oscillations in the vicinity of shocks, which can be detrimental to the solver's stability and create numerical error in the solution. To this end, a 3rd order Roe scheme⁴¹ with the van Albada flux limiter⁴² was employed in regions of shocks to limit spurious oscillations due to the discontinuity. This hybrid approach was developed and successfully used in previous work for a supersonic turbulent compression-corner.⁴ During each sub-iteration of the solver, the unsteady shock was identified by the pressure gradient detector developed by Swanson and Turkel.⁴³

$$\phi = \frac{|p_{i+1} - 2p_i + p_{i-1}|}{(1 - \omega)(|p_{i+1} - p_{i-1}|) + \omega(p_{i+1} + 2p_i + p_{i-1})} \quad (9)$$

where p_i is the pressure at grid point i in the specified direction, and ω is a constant that can be varied from 0.5 to 1.0, but was set to 0.5 for this work ($\omega = 0.5$). Once the shock was located, a 5-point stencil was established around the shock, and the inviscid fluxes from the Roe scheme were substituted for the existing compact solutions. Because of the upwind nature of the Roe flux-difference scheme, it was not necessary to use the filtering technique in this region. Figure 3 shows instantaneous Mach contours and the resultant computational grid with the stencil showing where the Roe scheme replaces the high-order compact scheme.

The end points of the stencil were averaged between the two different schemes. As a result of the hybrid approach, the high-order compact scheme to capture the fine-scale structures of

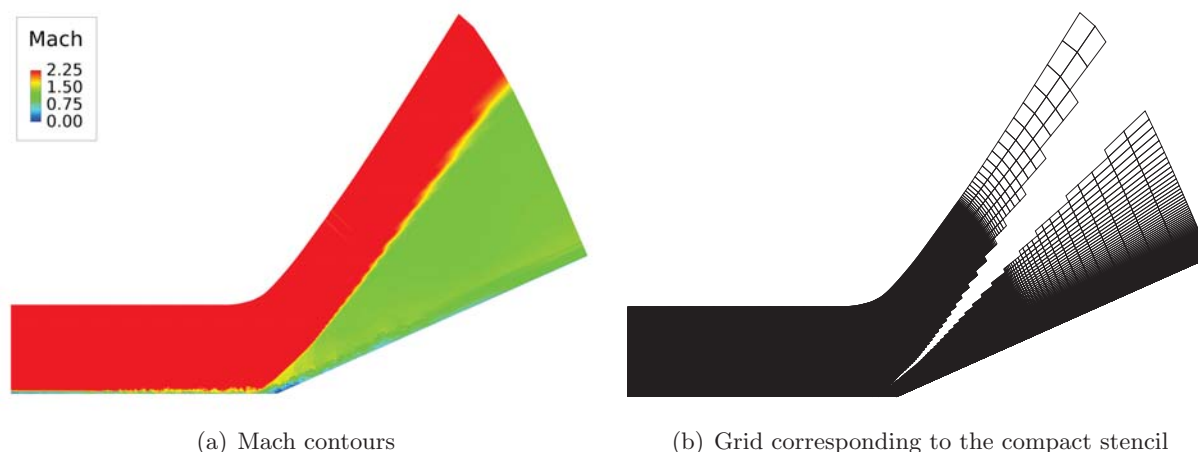


Figure 3. Mach contours with the shock-capturing stencil for Mach 2.25 flow over a 24° ramp.

the turbulent flow in regions without the spurious oscillations produced near the shock. Due to sensitivity of the shock detector, the Roe scheme was precluded in the boundary-layer and only applied in the inviscid region of the flow, as seen in Fig. 3(b).

D. The LES Approach

In the LES approach, physical dissipation at the Kolmogorov scale is not represented, thereby allowing for less spatial resolution and a savings in computational resources. For non-dissipative numerical schemes, without use of SGS models, this leads to an accumulation of energy at high mesh wave-numbers, and ultimately to numerical instability. Traditionally, SGS models are employed as a means to dissipate this energy. In the present methodology, the effect of the smallest fluid structures is accounted for by a high-fidelity implicit large-eddy simulation (HFILES) technique, which has been successfully utilized for a number of turbulent and transitional computations. The present HFILES approach was first introduced by Visbal et al.^{40,44} as a formal alternative to conventional methodologies, and is based upon the high-order compact differencing and low-pass spatial filtering schemes, without the inclusion of additional SGS modeling. This technique is similar to monotonically integrated large-eddy simulation (MILES)⁴⁵ in that it relies upon the numerical solving to provide the dissipation that takes place of the unresolved scales. Unlike MILES, dissipation is provided by the Padé-type low-pass filter only at high spatial wavenumbers, where the solution is not resolved. This provides a mechanism for the turbulence energy to be dissipated at scales that cannot be accurately represented on a given mesh system, in a fashion similar to subgrid modeling. For purely laminar flows, filtering may be required to maintain numerical stability and to preclude a transfer of energy to high-frequency spatial modes due to spurious numerical events. The HFILES methodology thereby permits a seamless transition from large-eddy simulation to direct numerical simulation as the resolution is increased. In the HFILES approach, the unfiltered governing equations may be employed, and the computational expense of evaluating subgrid models, which can be substantial, is avoided. This procedure also enables the unified simulation of flow-fields where laminar, transitional, and turbulent regions coexist simultaneously.

It should also be noted that the HFILES technique may be interpreted as an approximate deconvolution SGS model,⁴⁶ which is based upon a truncated series expansion of the inverse filter operator for the unfiltered flow-field equations. Mathew *et al.*⁴⁷ have shown that filtering provides a mathematically consistent approximation of unresolved terms arising from any type of nonlinearity.

Filtering regularizes the solution, and generates virtual subgrid model terms that are equivalent to those of approximate deconvolution.

E. Boundary Conditions

In the computation, the flow transitions from laminar to turbulent on a flat-plate situated upstream of the ramp. The flow and boundary conditions for this portion of the flow are consistent with previous studies by Rai *et al.*,⁴⁸ Rizzetta and Visbal,⁴⁹ and Pirozzoli and Grasso⁵⁰ which investigated supersonic flow on a flat-plate at Mach 2.25. In the present work, an extrapolated upper boundary condition was used to accommodate the growing boundary layer thickness as the flow transitions. The grid stretching (i.e., buffer layer⁵¹ or sponge²³), was used near the upper and exit boundaries to transfer the energy to higher spatial wave-numbers, so that the spatial filter removes it from the computation. This grid configuration helps minimize the spurious reflection of disturbances back into the computational domain.

Periodic boundary conditions were applied at the spanwise boundaries and used a five-point overlap of grid points in the z -direction. The five-point overlap maintains high-order differencing and filtering. The inflow boundary was specified using a solution to the compressible laminar boundary-layer equations,⁵² with the inflow boundary-layer height scaled to the reference length, ℓ , and freestream (reference), conditions outside the boundary-layer. The exit boundary was applied by an extrapolated boundary-condition. Along the wall surface, a no-slip velocity boundary condition was enforced with an isothermal wall set to the nominal adiabatic wall temperature. The surface pressure was computed by enforcing zero wall-normal derivative to third-order spatial accuracy.

III. Results - Inflow

Following Rai *et al.*,⁴⁸ Rizzetta and Visbal,⁴⁹ and Pirozzoli and Grasso,⁵⁰ this work explored Mach 2.25 supersonic flow on a flat plate, which was used to facilitate the development a fully turbulent boundary-layer flow. Supersonic flow over a flat-plate studied in this work is similar to a previous computation,⁴⁹ except the grid is significantly more refined and the counter-flow force bypass-transition method is used instead of the blowing and suction method, since the later introduces unwanted discrete frequencies into the energy spectrum. The reference conditions for the case are listed in Table 1, which were developed from a 1955 experiment by Shutts *et al.* (Case 55010501).⁵³

Table 1. Flow conditions for Mach 2.25 air flow over a flat plate.

Parameter	Value
M	2.249
u_∞	588 m/s
T_∞	305 °R
T_w	580 °R
p	23,830 Pa
Re/m	2.5×10^7 m ⁻¹
Re_θ	2930-5300

Reference conditions for the computations are $\ell = 6.096 \times 10^{-3}$ m, $u_\infty = 588$ m/s, $M = 2.249$, and $Re_\ell = 15,240$. In the analysis of the results that follow, the solution of the flow variables

were decomposed into time-mean values and fluctuating components (i.e., $u = u_m + u'$, where u' is the fluctuating component). Taking advantage of the spanwise periodic boundary conditions, the time-mean solutions were spanwise-averaged, unless specified otherwise. Time-average and time-dependent data was collected for ten flow-through times, where one flow-through time is defined as the time for the freestream flow to traverse the computational domain.

Using the parameters listed in Table 1, a computational domain was developed following work by Mullenix *et al.*²⁶ The nondimensional reference length, ℓ , was set to the incoming boundary-layer height, ($\ell = \delta_{(x=0)}$), and a Cartesian coordinate system was established with its origin corresponding to the upstream location of the computational domain. The streamwise extent of the domain is approximately 160ℓ and can be broken down into three regions, as shown in Figure 4.

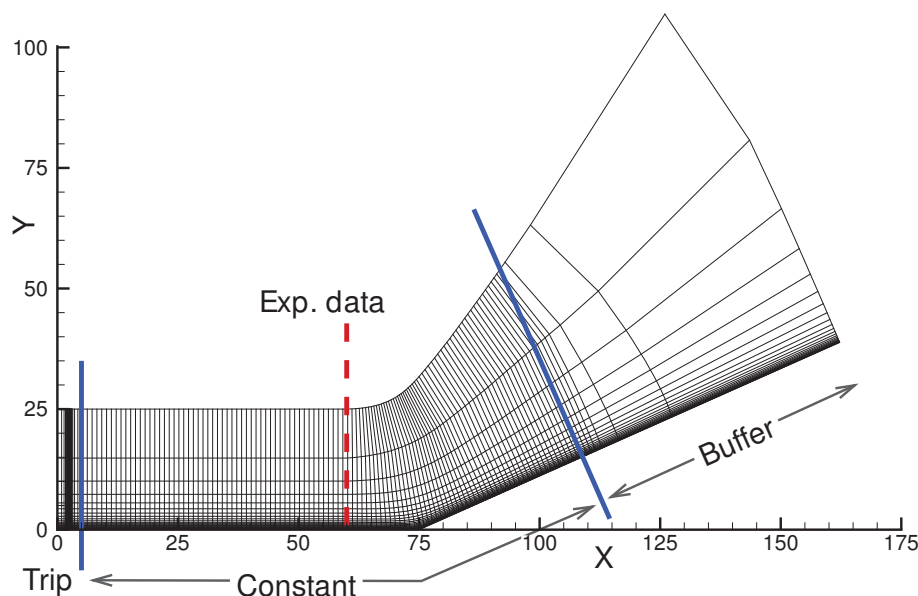


Figure 4. Schematic of the three regions of the domain.

The first region (labeled Trip), $0 \leq x \leq 3\ell$, contained the counter-flow force model. The region required a highly-refined grid to facilitate the trip model, and support the small separation the model produces, without producing detrimental behavior associated with the strength of the counter-flow trip source terms. The grid was monotonically refined from the leading edge to $x = 2\ell$, which corresponds to the start of the refined region. The refined region was 1.0ℓ long and contained 101 uniformly-spaced points.

The second region (labeled Constant), contains the rest of the flat-plate and the leading portion of the ramp. The ramp corner is situated at $x = 75\ell$, with the downstream end of the region corresponding to $x \sim 110\ell$. The grid was monotonically stretched from the end of the refined body force trip region, (i.e., $x = 3\ell$), to the start of constant grid spacing used in the second region, (i.e., $x = 5\ell$). The streamwise grid points were uniformly spaced throughout the rest of the region, except for the grid points immediately adjacent to the ramp corner, which contained a slight refinement in grid spacing to facilitate a smooth grid distribution of points through the ramp corner. Solutions for the turbulent inflow boundary-layer (upstream of the ramp corner) were compared to experiments at $x = 60\ell$.

The third region (labeled Buffer), was rapidly stretched along the ramp to the downstream boundary. Stretching the grid eliminates spurious disturbances before they reach the extrapolated outflow boundary condition. The grid spacing in the normal direction was specified at the wall

boundary such that $y^+ < 1$, then it was monotonically stretched using a hyperbolic tangent expansion. As seen in Table 2, this method resulted in the majority of the grid points being located within the boundary layer. The upper boundary of the computational domain is $y = 25\ell$ high for the flat-plate portion of the domain, but expands over the ramp to accommodate the strong oblique shock. The points near the surface were projected normal from the wall to minimize numerical error when computing surface gradients. An elliptic solver was used on the resulting grid point distribution, particularly near the ramp corner, to ensure smooth and continuous point distributions throughout the domain. The domain is 5ℓ wide, with constant grid spacing in the spanwise direction. It will subsequently be shown that this width is adequate to resolve turbulent structures.

A spatial resolution study was conducted using three different grids. While the concept of grid independence does not exist for LES,⁵⁴ it is possible to show that some of the time-mean quantities converge or approach convergence, with adequate resolution. This occurs because grid refinement allows for finer features to be captured and changes the instantaneous data, but bulk quantities that are time-averaged should converge.

Since the major limitation for LES is grid resolution, the ‘fine’ grid was developed first since it corresponds to the most resolution that could be afforded for this study. Once the ‘fine’ grid was constructed, the ‘coarse’ grid was created as a replica of the fine grid, except every other point was removed in the x -direction within in ‘Constant’ and ‘Buffer’ regions of the domain, and every other point was removed in each of the other directions. The ‘medium’ grid follows the same methodology, except having 1.5 times the points of the ‘coarse’ grid in x direction of the ‘Constant’ and ‘Buffer’ regions and the other two directions. Note that the grid was not refined in the ‘Trip’ region for the two coarser grids since the grid used in the ‘Trip’ region of the ‘fine’ grid was required to prevent potentially anomalous behavior associated with the bypass-transition method. Table 2 lists the parameters for the grids.

Table 2. Parameters for the various grids used for Mach 2.25 turbulent flow over a 24° ramp.

Parameter	Coarse	Medium	Fine
$X \times Y \times Z$	$160\ell \times 25\ell \times 5\ell$	$160\ell \times 25\ell \times 5\ell$	$160\ell \times 25\ell \times 5\ell$
$N_x \times N_y \times N_z$	$721 \times 131 \times 141$	$1017 \times 196 \times 209$	$1312 \times 261 \times 277$
N (total)	13.3×10^6	41.7×10^6	94.9×10^6
N_x ($x \leq 2\ell$)	30	30	30
N_x ($x \leq 3\ell$)	130	130	130
N_x ($x \leq 5\ell$)	150	160	170
N_x ($x \gtrsim 110\ell$)	21	31	41
Δx (refined DBD)	0.01	0.01	0.01
Δx (Constant)	0.2	0.15	0.1
Δx^+ (Constant)	46.1	35.5	23.8
Δy_w	0.004	0.003	0.002
Δy_w^+ (Constant)	0.92	0.71	0.48
N_y ($y \leq \delta_{(x=0)}$)	70	104	139
N_y ($y \leq \delta_{(x=60)}$)	85	127	169
Δz	0.0362	0.0272	0.0181
Δz^+ (Constant)	8.4	6.4	4.3

The counter-flow trip was centered in the middle of the refined ‘Trip’ region. Unlike subsonic

flows, where the height of the counter-flow trip model is typically on the order of the incoming boundary layer,²⁵ the trip model for this supersonic scenario was positioned such that it barely extends outside the viscous sublayer. The length to height ratio of the triangular force region was 4:1, and has a length of 0.125ℓ . To achieve transition, the resultant counter-flow force must be strong enough to generate a region of reverse flow. For this work, all grids achieved transition using a value of $D_c = 6.2$.

The solutions were obtained using a nondimensional time-step $\Delta t = 0.005$, which results in $\Delta t^+ = Re_\ell (\frac{u_\tau}{u_\infty})^2 (\frac{u_\infty t}{\ell}) = 0.19$. The wall friction velocity is, $u_\tau = \sqrt{\tau_w/\rho_w}$, where $\tau_w = \mu_w [\partial u/\partial y]_{y=0}$ is the wall shear stress. Figure 5 plots the time-mean spanwise-averaged skin-friction coefficient, c_f , and the boundary-layer momentum thickness, θ , for the flow as it transitions along the flat-plate region.

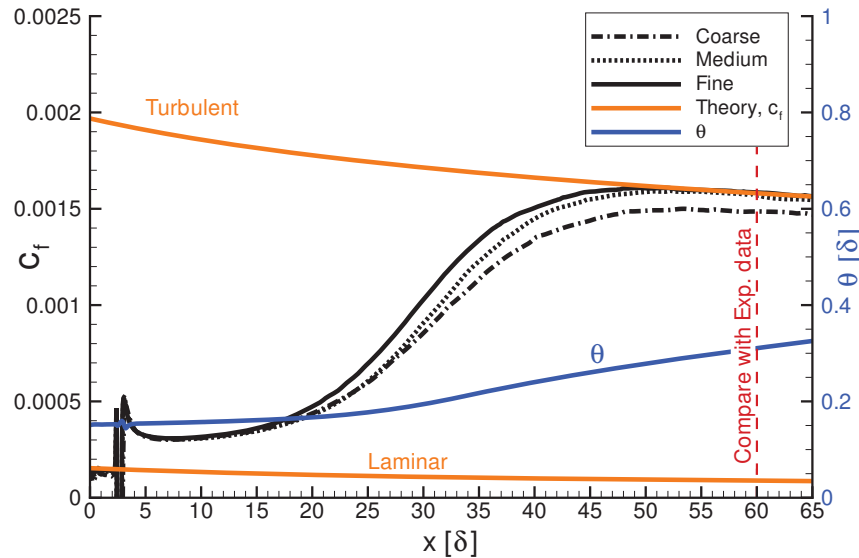


Figure 5. Spanwise-average time-mean skin-friction coefficient, c_f , and boundary-layer momentum thickness, θ , versus streamwise location.

As seen in Fig. 5, the incoming laminar flow is disturbed by the counter-flow trip ($x = 2.5\ell$). The trip is strong enough to generate a small separated region, which is evident by $c_f < 0$. The separated region results in instabilities which grow nonlinearly and began the transition process. The transitioning flow approaches the theoretical curve for equilibrium turbulence near $x \sim 50\ell$. The theoretical curves in the figure corresponds to the laminar compressible Blasius solution, and to the turbulent correlation of White and Christoff.⁵² The ‘fine’ grid transitions farther upstream than the coarser grids since the additional resolution allows for the development of smaller scale structures. Unlike the blowing-and-suction trip method used by Rai *et al.*,⁴⁸ the counter-flow force trip model eliminates the overshoot in the skin-friction coefficient as the boundary layer becomes fully turbulent.⁴⁹

At $x = 60\ell$, the boundary-layer momentum thickness $\theta = 0.32\ell$, so $Re_\theta \sim 4,900$, which is within the range of momentum thicknesses from the experiment. The time-mean spanwise-averaged quantities from the LES are extracted at this location and compared to the experimental measurements. In addition to the present computations, the computational results from Rai *et al.*⁴⁸ are also included in the figures for comparison.

To ensure the turbulent boundary layer upstream of the ramp corner has the expected properties for the law-of-the-wall, the streamwise velocity is transformed using the van Driest transformation.⁵⁵ The transformed streamwise velocity is now equivalent to incompressible flow and is

nondimensionalized by the wall friction velocity, $u^+ = u_{vD}/u_\tau$. The profiles are plotted versus the nondimensional inner length scale $y^+ = y u_\tau / \nu_w$.

Figure 6 plots the van Driest transformed velocity in the near-wall region at $x = 60 \ell$ for the various grids and includes the solutions from Rai *et al.*⁴⁸ In addition to the experimental measurements by Shutts *et al.*,⁵³ the experiment data set also includes supersonic flow measurements of Elena and LaCharme,⁵⁶ which were collected at similar flow conditions using Laser Doppler Velocimetry (LDV) and Hot-Wire Anemometry (HWA). The solutions obtained match both the inner layer and logarithmic profiles, although the 'coarse' grid over-predicts the expected solution within the logarithm region. This result is indicative of an under-resolved grid or a solution that has not yet achieved equilibrium turbulence.

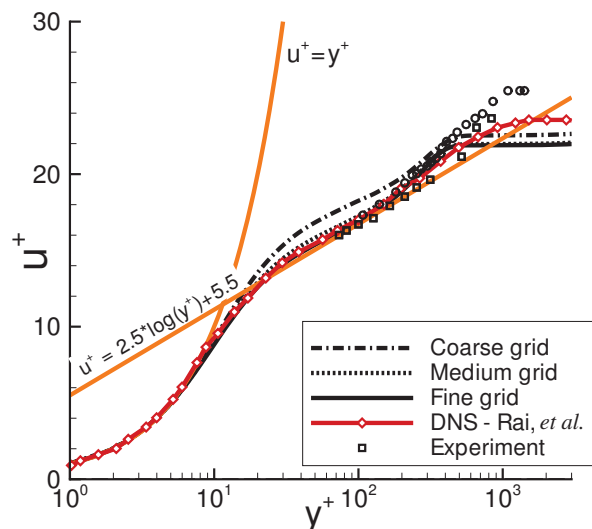


Figure 6. Spanwise-average time-mean streamwise velocity profiles using the Van Driest transform and normalized by friction velocity for $x = 60$.

Fluctuating velocity components for the near-wall region, normalized by the freestream velocity, are shown in Fig. 7. Since the experimental data by Shutts *et al.*⁵³ did not include fluctuating measurements, the results were compared to the incompressible experiment of Karlson and Johansson,⁵⁷ which was carried out using LDV techniques. This comparison is consistent with previous work by Rizzetta and Visbal,⁴⁹ who demonstrated that the comparison to incompressible data was valid because the compressibility effects were not strong for this flow (i.e., Morkovin's hypothesis⁵⁸ applies).

As seen in the figures, the present computations agree well with the experiments and the computational results by Rai *et al.*⁴⁸ The LES is consistent with the results by Rai *et al.*,⁴⁸ but the fluctuating measurement of the vertical velocity is much higher near the surface in the experiment. This discrepancy might be attributable to a higher level of experimental uncertainty in v -velocity measurement near the surface since it is more challenging to obtain experimentally. In addition, the experimental results are for incompressible flow. While compressible effects are small for this flow, they could be contributing to the discrepancy.

The Reynolds shear stress profile, which is normalized by the friction velocity, is shown in Fig. 8. As seen in the figure, the profiles are in good agreement with the experiment, even though they contain the v -velocity fluctuations. This occurs because the solution is dominated by the u -velocity fluctuations, which has higher precision than the spanwise or normal flow measurements.

For the outer region of the boundary layer, the fluctuating velocity profiles are presented versus

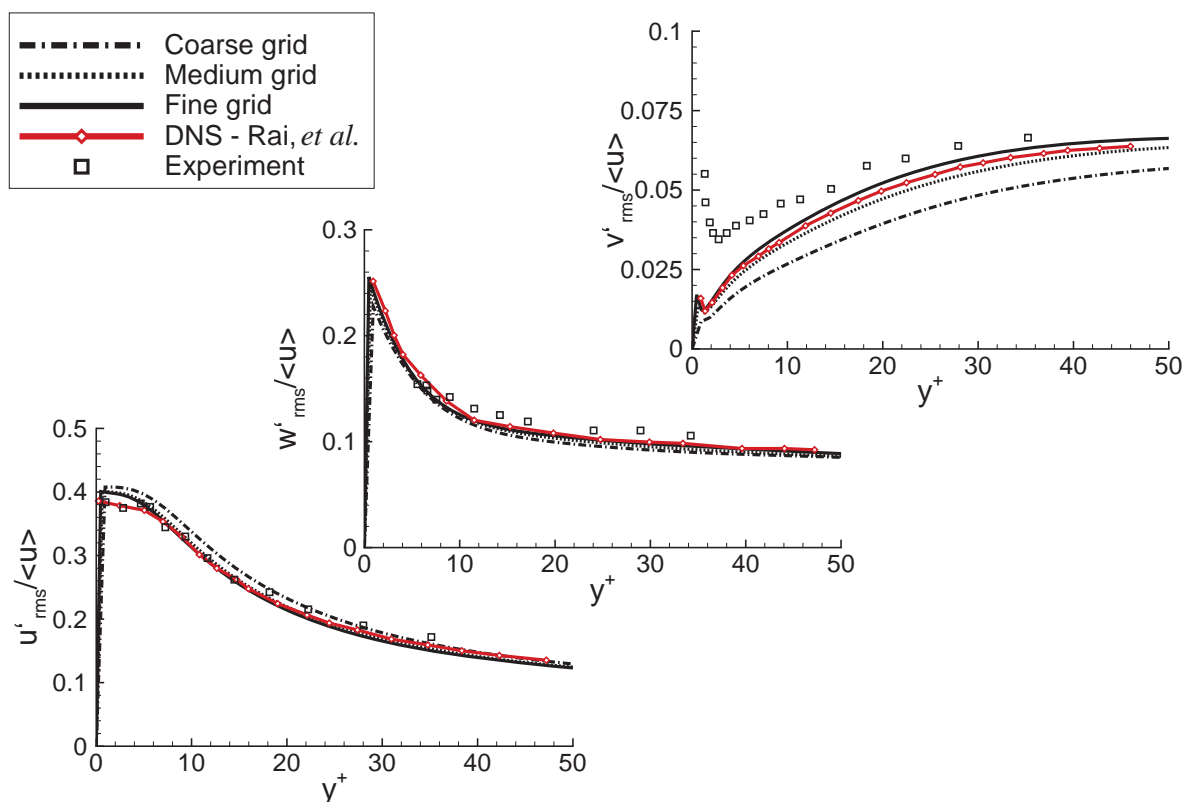


Figure 7. Spanwise-average time-mean fluctuating velocity components versus inner scaling at $x = 60$.

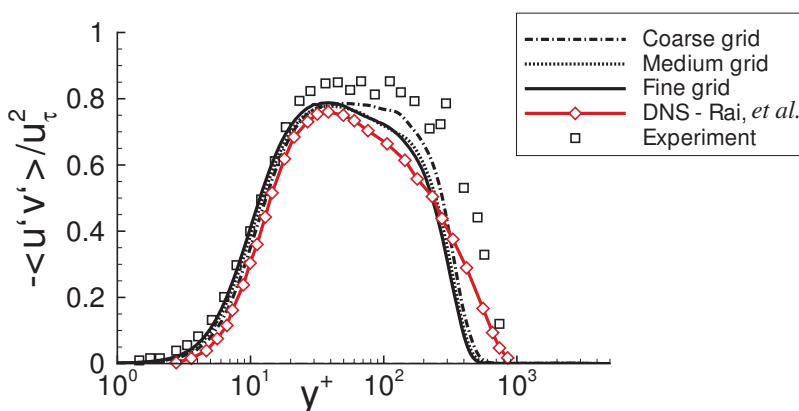


Figure 8. Spanwise-average time-mean profiles of the Reynolds stress versus inner scaling at $x = 60$.

distance from the surface, as seen in Fig. 9. That distance is normalized by the boundary-layer height δ at the location of comparison to experiments (i.e., $x = 60$), to account for the different boundary-layer heights. The experimental measurements shown were collected by Elena and LaCharme⁵⁶ using LDV, and HWA. As with the near-wall region, the vertical velocity profiles show some disagreement compared to the experiment and the computational work by Rai *et al.* While the data collected by Rai *et al.*⁴⁸ appear closer to the experimental measurements, the computation had very minimal vertical resolution (i.e., a total of 55 points in the normal direction), and the order of the numerical scheme was lower than the present work. As such, it is possible that the solution by Rai *et al.*⁴⁸ aligns better with the experimental measurements by chance.

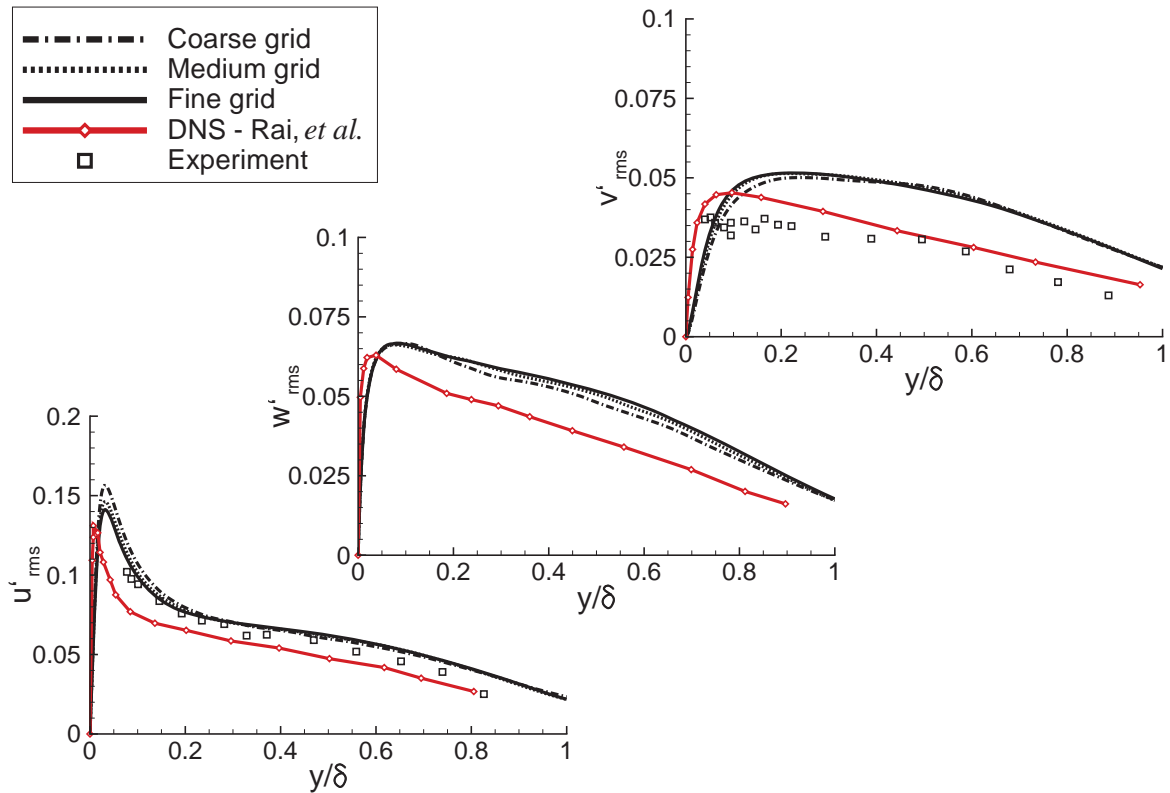


Figure 9. Spanwise-average time-mean fluctuating velocity components versus outer scaling at $x = 60$.

One-dimensional spectra of the velocity components and instantaneous pressure were collected along a line in the homogeneous spanwise direction at several discrete streamwise locations within the boundary layer. Each location was located a distance of 1.0ℓ normal to the flat-plate surface, starting at $x = 55\ell$ and ending on the ramp region where the grid starts to coarsen due to grid stretching (i.e., $x = 110$). For $x = 60\ell$, a normal distance of 1.0ℓ corresponds to a $y/\delta = 1.7$. Data sampling occurred after every computational time-step and was collected for 10 flow lengths for each simulation.

The power spectral density (PSD) was computed for both nondimensional frequency and spanwise wavenumber to confirm the grids have sufficient resolution to capture a portion of the inertial subrange. The PSD curves were developed using the standard approach as outlined in Ref. 59. A Hanning window was applied for the entire data set to suppresses side-lobe leakage. The windowed data set was also multiplied by $\sqrt{8/3}$ to account for the low-frequency bias introduced by using the window. The PSD of the Turbulent Kinetic Energy (TKE) was computed by summing the PSD of each velocity component and multiplying by a half (i.e., $\text{PSD}(\text{TKE}) = [\text{PSD}(u'^2) + \text{PSD}(v'^2) + \text{PSD}(w'^2)] / 2$).

Computation of the PSD versus spanwise wavenumber was carried out in a similar manner, except that the Fourier transform was applied along the homogenous spanwise data set (excluding the overlap points), for each time-step. It is important to note that the fluctuating quantities were not windowed and the overlap points excluded because the solution is periodic in the spanwise direction. Windowing periodic data would introduce a non-physical bias favoring the end points of the Fourier transform. Figure 10 plots the PSD of the TKE versus normalized frequency and spanwise wavenumber for the different grids.

All three curves capture a portion of the inertial range, as indicated by the $-5/3$ slope in Fig.

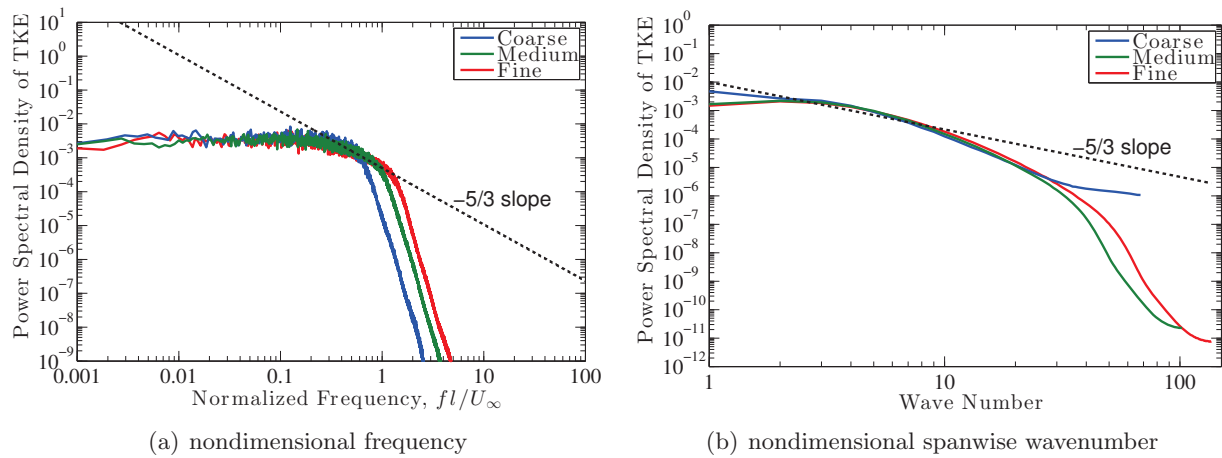


Figure 10. Power spectral density of turbulent kinetic energy at $x = 60$.

10, with the ‘fine’ grid able to capture more of the inertial range before the spatial filter eliminates the highest, under-resolved, frequencies. The extent of the inertia range is limited because the Reynolds number is low for this study. Figure 10(b) indicates that the ‘coarse’ grid is inadequate to capture the spanwise wavenumber range and should be increased.

In addition to frequency and wavenumber spectra, it is also important to investigate the spanwise extent of the domain. Specifically, it is important to verify that the computational domain was sufficiently wide such that the spanwise periodic boundary conditions did not influence the flow. This was accomplished by computing the standard two-point autocorrelations of the velocity components along a line in the spanwise direction at $x = 60$, $y = 1$, as seen in Figure 11.

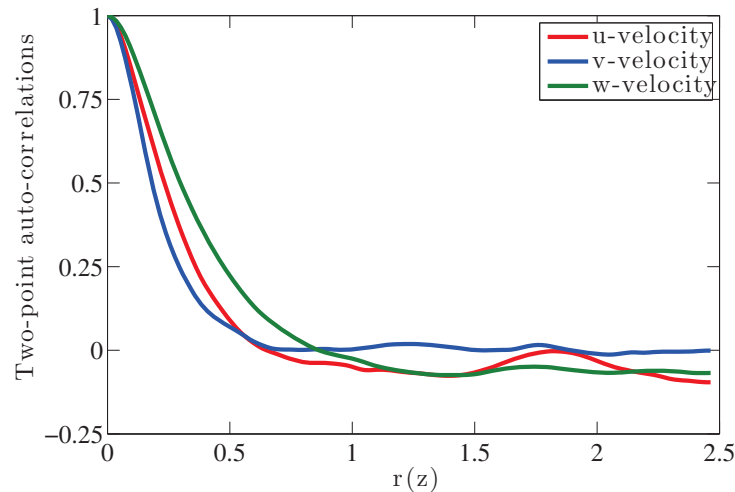


Figure 11. Two-point autocorrelations of the velocity components versus distance from the mid-span at $x = 60$ for the ‘fine’ grid.

The data in Fig. 11 is presented versus distance from the spanwise mid-plane, with the two halves of the spanwise domain presented as a straight average. The figure shows the spanwise component decays the lowest and the streamwise component is not monotonic. That said, all three components of velocity approach zero by 2.5ℓ , and confirm that a 5δ wide computation domain was sufficient for the periodic boundaries implemented.

IV. 24° Ramp

From the incoming turbulent boundary-layer, the flow continues along the flat plate until it encounters the 24° ramp. Because the flow is supersonic, an oblique shock forms above the boundary layer due to the flow turning angle. A shock foot, located just upstream of the corner corresponds to the start of separated region, with a second shock foot existing at reattachment, as illustrated in Fig. 1. This behavior gives rise to the well known λ -shock structure. Due to the flow turbulence, the shock front oscillates in the streamwise direction. These oscillations cause the shock angle to vary, and, the separated region grows and shrinks in time.

The instantaneous separated region is visible in Fig. 12, which shows an iso-surface of the Q -criterion⁶⁰ (defined in Eq. (10)), and a planar contour of the Mach number at the spanwise edge of the domain.

$$Q_{\text{criterion}} = \frac{1}{2} (\Omega^2 - S^2) \quad (10)$$

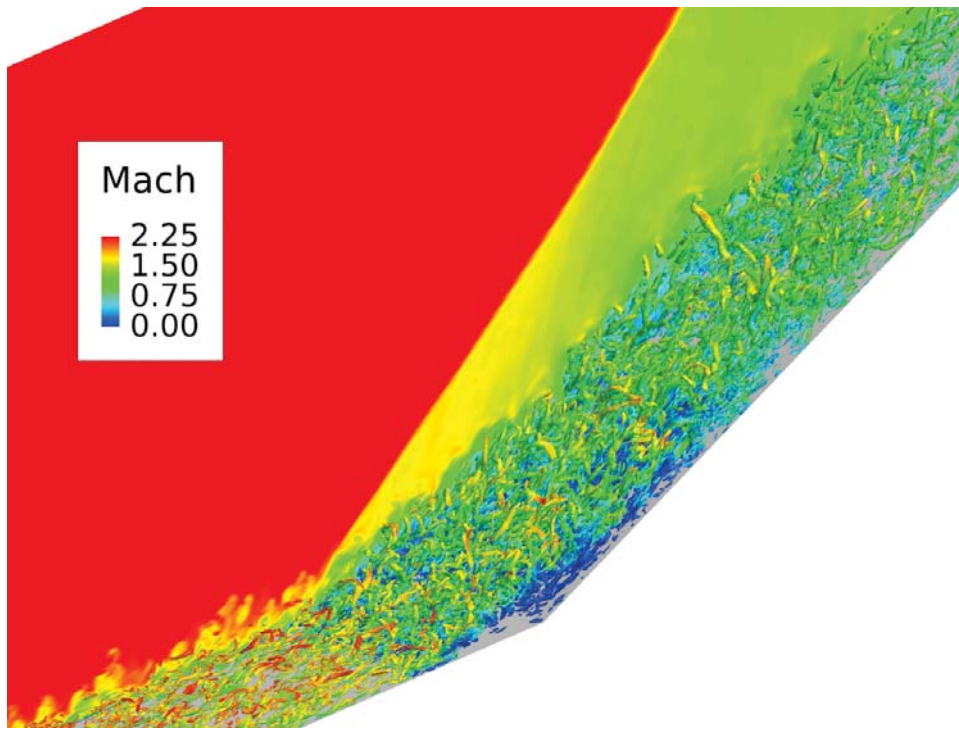


Figure 12. An instantaneous iso-surface of the Q -criterion ($Q_{\text{criterion}} = 4$), which is colored by the u -velocity and a planar contour of Mach number for Mach 2.25 air flow near a 24° ramp.

The figure highlights some of the the sub- δ -scale turbulent structures flowing over the ramp corner. These structures are moving faster higher in the boundary layer (as indicated by the red color). As the flow moves past the shock it slows down (the post-shock structures are predominately colored green in the figure). The decrease in velocity caused the structures to expand and start to readjust toward its new equilibrium turbulent profile. The blue-colored structures near the ramp corner indicate where the flow is reversed. The size of the non-uniform separated region grows and shrinks as the oblique shock responds to the incoming turbulent structures, which causes the λ -shock structure to vary in time.

While an instantaneous solution provides a representative idea of the separated region, the time-mean solution provides a better understanding of the extent of the shock-induced separation.

A plot of the skin-friction coefficient in Fig. 13(a), shows the extent of the spanwise-averaged time-mean separation. In addition, Fig. 13(b) includes the surface pressure normalized by the post-shock surface pressure. As seen in the figure, the pressure rapidly rises at the start of separation, plateaus through the center of separated region, then finishes rising as it approaches the inviscid post-shock pressure. The start and end of the pressure plateau corresponds with local maxima of the skin-friction coefficient in the separated region, which has been previously suggested in work by Priebe and Martín.¹⁵

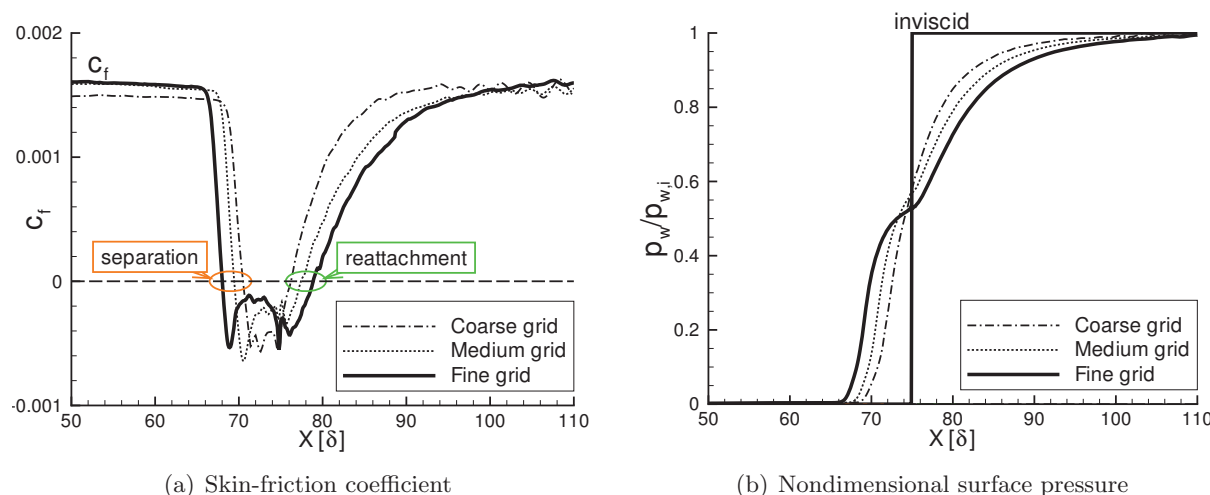


Figure 13. Spanwise-averaged mean skin-friction coefficient and nondimensional surface pressure.

As seen in Fig. 13, the size of the separated region appears to be increasing nearly linearly as the grid is refined. This behavior is deceptive because the incoming ‘coarse’ grid solution did not achieve the same equilibrium turbulence before interacting with the separation. In addition, the boundary-layer height and the boundary-layer displacement thickness, δ^* , were slightly different at the incoming boundary-layer location (i.e., $x = 60$), for each of the grids. The ‘fine’ grid transitioned more quickly and was most adequately resolved to capture the growth and behavior of the turbulent boundary-layer. Since a smaller boundary-layer displacement thickness corresponds to a fuller velocity profile, it is less susceptible to separation. After accounting for the displacement thickness, it is clear that the separation length is converging. This result, along with all the previous analysis, shows the ‘fine’ grid is sufficiently resolved. As such, the remaining figures and analysis will only use the ‘fine’ grid.

While the main focus of this work was to investigate a reduction of the shock-induced separated region, it was also important to explore the frequency content within and after the separated flow since its behavior as a broad-band amplifier, as suggested by Plotkin⁶¹ and Touber and Sandham,¹ needed verification for this scenario. Figure IV plots the PSD of TKE for the ‘fine’ grid upstream of separation ($\xi = 60$), above the separated region ($70 \leq \xi \leq 80$), and after reattachment ($\xi = 100$). From the figure it is clear that the separated region amplifies the total TKE, which is consistent with recent observations by Touber and Sandham.¹

It is important to note that the PSD curves do not resolve ultra-low frequency content, which is typically observed experimentally around $fl_{sep}/U_\infty = 0.03$. These results suggest that the simulations may need to be evolved for a longer duration to adequately resolve that range of frequencies. This consideration was beyond the scope of the present investigation, but may be addressed in future studies.

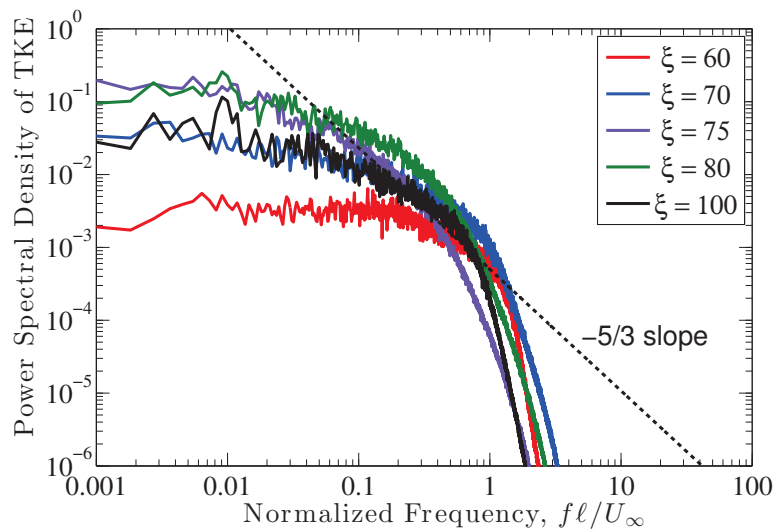


Figure 14. Spanwise-averaged power spectral density of the turbulent kinetic energy versus frequency at various locations.

A. Control

In order to reduce the time-mean separation length caused by the turbulent SBLI, a model of a magnetically-driven gliding-arc discharge actuator is placed on the flat-plate near the separation point. The actuator imparts streamwise momentum into the boundary-layer which suppresses separation by increasing the fullness of the velocity provides, and, subsequently, decreasing the boundary-layer displacement thickness. The actuator used in this work is based on an experiment conducted by Karla *et al.*²⁹

The experiment by Karla *et al.*²⁹ was run in a Mach 2.6 wind tunnel with flow parameters $u_\infty = 600$ m/s, $\rho_\infty = 0.113$ kg/m³, and $Re_\theta \sim 10,000$. The arc-discharge was produced between two flush-mounted surface electrodes buried in the bottom wall of the supersonic wind tunnel just upstream of the time-mean separated region generated by an impinging shock. The electrodes were powered by a direct-current power source with a potential $V = 3700$ volts and a current $I = 200$ mA. A 3 tesla magnetic field, ($B = 3$ T), was uniformly applied perpendicular to the flow and the discharge streamlines to accelerate the arc.

The source term \mathbf{S}_c found in the conservation of momentum and energy equations, is modeled using Eq. (5), which accounts for the work and energy added by the plasma-based controller. The total momentum added to the flow by the magnetic force is estimated by the product of the current and magnetic field, while the total energy added is the product of the current and the voltage. The nondimensional magnetic work and Joule heating terms for the experiment by Kalra *et al.*²⁹ were determined by normalizing the magnetohydrodynamic values by freestream parameters, a reference length equal to the distance between the electrodes ($l_{ref} = 14$ mm), and the estimated volume of the deposition ($vol_{ref} = 230$ mm³). The approach and size of the deposition volume is based on similar work by Atkinson *et al.*³¹ Equations 11 and 12 show how the values for the total nondimensional force and energy deposition were computed.

$$\begin{aligned}
\text{Conservation of Momentum} &= \text{magnetic force} \\
\text{Force} &= \mathbf{j} \times \mathbf{B} \\
\text{Force} &= \frac{\mathbf{I} * \mathbf{B} * l_{ref}}{\text{vol}_{ref}} \\
\mathbf{L} &= \text{Force} * \frac{l_{ref}}{\rho_{\infty} u_{\infty}^2} = 0.0125
\end{aligned} \tag{11}$$

$$\begin{aligned}
\text{Conservation of Energy} &= \text{reversible work} + \text{Joule heating} \\
\text{Energy} &= \{(\mathbf{j} \times \mathbf{E}) \times \mathbf{u}\} + \left\{ \frac{\mathbf{j} \cdot \mathbf{j}}{\sigma} \right\} \\
\text{Energy} &= \mathbf{E} \cdot \mathbf{j} \\
\text{Energy} &= \frac{\mathbf{V} \cdot \mathbf{I}}{\text{vol}_{ref}} \\
E &= \text{Energy} * \frac{l_{ref}}{\rho_{\infty} u_{\infty}^3} = 1.8 \\
E &= \{\mathbf{L} \times \mathbf{u}\} + \{\mathcal{J}\}
\end{aligned} \tag{12}$$

where σ is the electrical conductivity of the fluid, and \mathbf{u} is the instantaneous local velocity. It is important to note that the Joule heating term, \mathcal{J} , as written in Eq. (12), assumes all the energy deposited via Joule heating goes directly into the total energy equation. This is an over-estimate since in most plasma-based discharges, only 5% - 50% direct thermal energy deposition is achieved. The majority of the energy being deposited going into various vibration energy states, which can require a significant amount of time, relative to the flow's convective time, to relax back to equilibrium. As such, a reasonable approximation is to assume that only a fraction of the energy used by the discharge is actually deposited into the flow (i.e., $\mathcal{J}_{\text{actual}} \ll \mathcal{J}$).

Starting from the nondimensional numbers obtained from the experiment by Kalra *et al.*,²⁹ similar values were developed for this work. Due to the large number of variables available in the phenomenological model of the magnetically-driven gliding arc actuator, the parameters space was first explored using two-dimensional $k - \epsilon$ RANS simulations to find a set of conditions that would reduce the separated length. Since the computation domain is homogenous in the spanwise direction, the plasma-controller is uniform in that direction to remove the additional complexity of spanwise effects. As such, the reference length used to nondimensionalize the experiment by Kalra *et al.*,²⁹ was set to the domain width for this work ($l_{ref} = 5\delta$). The controller was developed to be long in the streamwise direction, 5ℓ , and was centered near the time-mean separation point, which was consistent with the approach used by Atkinson *et al.*³¹ The volume and distribution of the force and energy deposition from the phenomenological controller was set using Eq. (4), was centered 0.1ℓ above the wall, and had a normal extent of 0.04ℓ , such that: $x_c = 69, y_c = 0.1, a = 2.5, b = 0.04, m = 10$, and $n = 10$. The nondimensional value of the force deposited for this work was $\mathbf{L} = 0.075$. From Eq. (11) and using the reference parameters, it is determined that $\mathbf{I} * \mathbf{B} = 0.62 \text{ kg/s}^2$. This value consistent with the experiment by Kalra *et al.*²⁹

Three control scenarios were explored for this work. All three use a nondimensional magnetic body force of $\mathbf{L} = 0.075$ which was applied in the streamwise direction ($L_x = 0.075, L_y = 0, L_z = 0$). Since the control cases should reduce the time-mean separation, it was assumed that the 'fine' grid employed should have sufficient resolution to capture the small-scale structures present in the flow even when the controller is active. The simulations were run using a non-dimensional time-step $\Delta t = 0.005$ and were started from the equilibrium baseline simulation. Initial transients associated with the introduction of the controller were allowed to propagate out of the domain by running the simulation for 3 flow lengths before statistical information was collected. Time-dependent results were collect for 10 additional flow lengths and the time-mean results correspond to this time range.

The first scenario allows for momentum transfer by the magnetically-driven gliding-arc discharge, but excludes the reversible work produced by the magnetic force. This is accomplished by setting the Joule heating equal and opposite to the reversible work produced by the body force. It

is important to note that the local temperature could decrease due to the reversible work because the energy added (or removed) depends on the direction of the instantaneous local bulk velocity \mathbf{u} . While it is a strong assumption to ignore the effects of energy deposition, this case is referred to as the ‘perfect’ controller, since it provides all the advantages of direct momentum transfer without the unwanted heating of the boundary-layer. These results provide an upper bound for the expected performance of a magnetically-driven gliding-arc discharge controller.

The second case is the consistent with the ‘perfect’ controller, except the actuator is pulsed at a frequency of 27 kHz and a 50% duty-cycle. This frequency corresponds to the time it take for the inviscid flow to traverse a distance equal to the boundary layer height at $x = 60$. Pulsing the actuator at a 50% duty-cycle is advantageous for practical applications because it reduces the overall power consumption by a half. In addition, subsonic simulations of airfoil flow control by Rizzetta and Visbal²⁵ have shown that pulsing the actuator can achieve the same effect as leaving the actuator continuously on. This scenario is referred as the ‘pulsed’ controller.

The third situation is a more realistic representation of the actual plasma-based flow controller, which includes Joule heating effects. As such, the reversible work is appropriately accounted for in the total energy equation and a small amount of the Joule heating is also added $\mathcal{J} = 0.025$. The average value of the non-dimensional reversible work was determined to be 0.075 for the ‘perfect’ controller, so this amount of Joule heating corresponds to thermal efficiency of about 2.5%. This scenario has the force and energy deposition constantly on and is referred as the ‘real’ controller.

Figure 15 shows the time-mean, spanwise-averaged skin-friction coefficient for all three controller along with the baseline results. As seen in the figure, the ‘perfect’ controller performs the best, by reducing the separation length by more than 75%. The other two cases achieve similar results, with each controller achieving nearly 50% reduction in separation length. However, the ‘pulsed’ case used half the power compared to the ‘perfect’ or ‘real’ scenarios, so if the controller’s efficiency is determined as the reduction in separation length normalized by power used, the ‘pulsed’ controller is the most efficient. All three controllers show increase in the skin-friction in the region of the controller ($66.5 \leq x \leq 71.5$), since the magnetic force accelerates the near-wall flow.

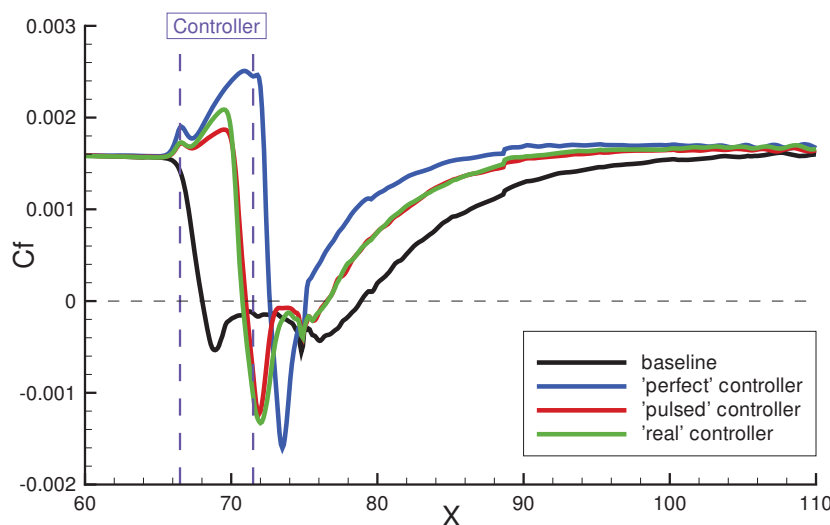


Figure 15. Spanwise-averaged mean skin friction coefficient for the various control strategies.

As expected, the reduction in the size of the separated region is caused by the local acceleration of the flow near the nominal separation point of the baseline flow. Since the flow speed locally

increases in the streamwise direction, it does not slow sufficiently to be affected or entrained by the recirculating region. This can be seen in Fig. 16 which shows the Q-criterion for the ‘perfect’ control case. Close examination of the turbulent structures just upstream of the separation compared to the structures seen in Fig. 12, shows that the structures are more organized and aligned with the streamwise direction. In addition, the structures have a much higher velocity (as is evident by the red coloring). Consistent with the baseline case, once the flow travels through the shock (and is outside the influence of the controller), it slows and readjusts toward its new equilibrium turbulent profile. It is also evident that the resulting shock structure has significantly changed with the presence of the controller since the controller has reduced the extent of the separation. As a result, the λ -shock feet are much closer together and the shock is sharper.

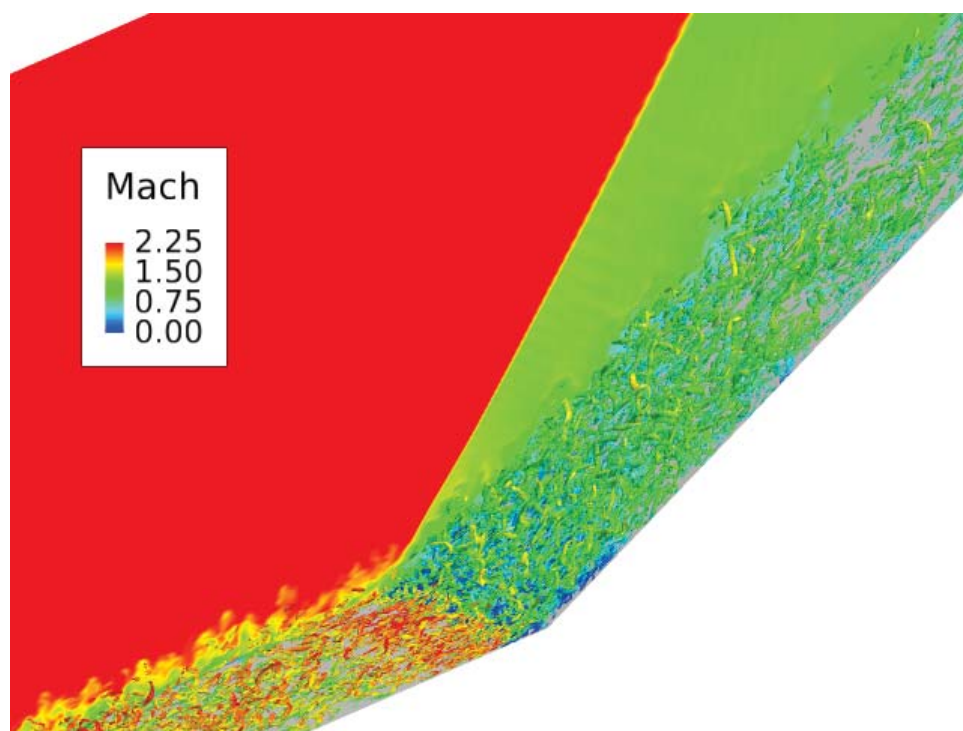
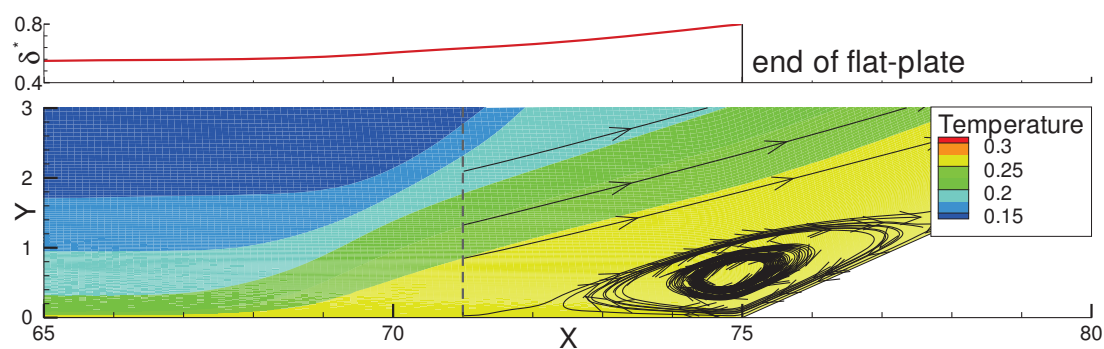


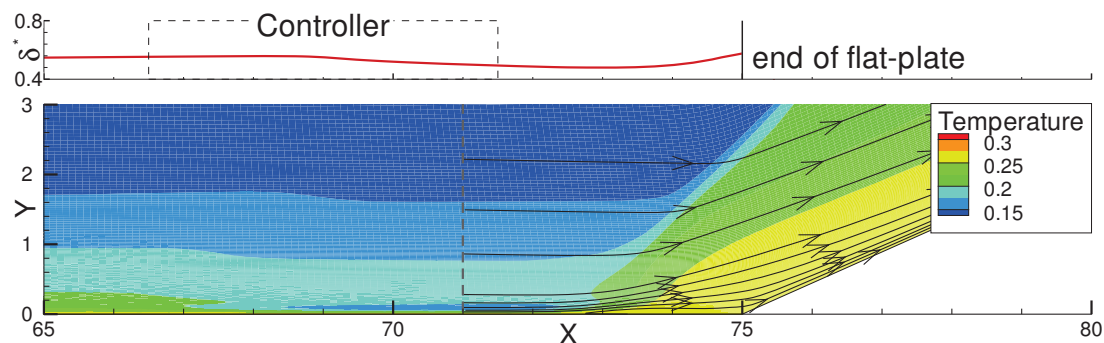
Figure 16. An instantaneous iso-surface of the Q-criterion ($Q_{\text{criterion}} = 4$), which is colored by the u -velocity and a planar contour of Mach number contours for the ‘perfect’ controller.

The time-mean temperature within the ‘perfect’ controller region drops as the flow is accelerated because the case does not modify the total energy equation (through the cancellation of reversible work by Joule heating). As the temperature falls, so does the boundary-layer height, and with the addition of streamwise momentum imparted by the controller, the boundary-layer displacement thickness decreases which makes the flow less susceptible to separation. The ‘pulsed’ case demonstrates similar characteristics as the ‘perfect’ controller, except that the flow appears to have sufficient time to recover during the period when the controller is off. In addition, the 50% duty cycle exerts less control since it uses half the power. The ‘real’ scenario always adds energy directly in the region of the controller through Joule heating and reversible work. This heat addition accumulates over the length of the controller and the boundary layer height grows, even though the magnetic body force is accelerating the near-wall flow. Temperature contours for each case are shown in Fig. 17.

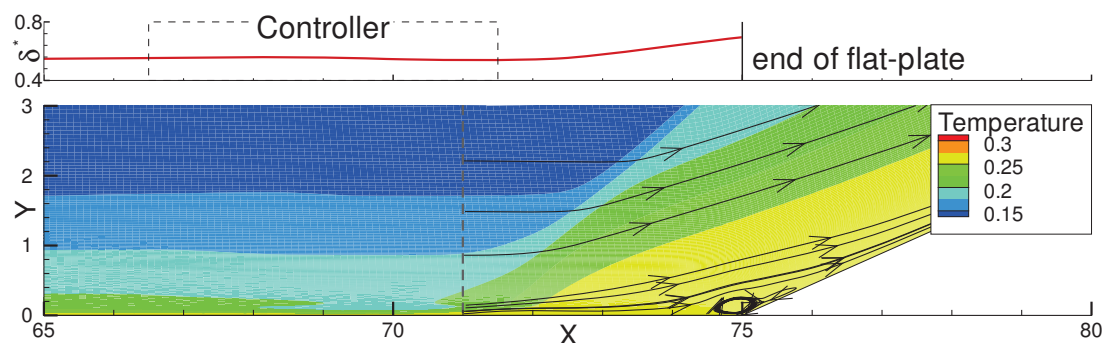
Figure 17 also includes streamlines that highlight the mean flow behavior. As seen in Fig. 17(b), the ‘perfect’ case has essentially eliminated the spanwise averaged time-mean recirculating core, even though the skin-friction coefficient is negative over part of the range. The ‘pulsed’ and ‘real’



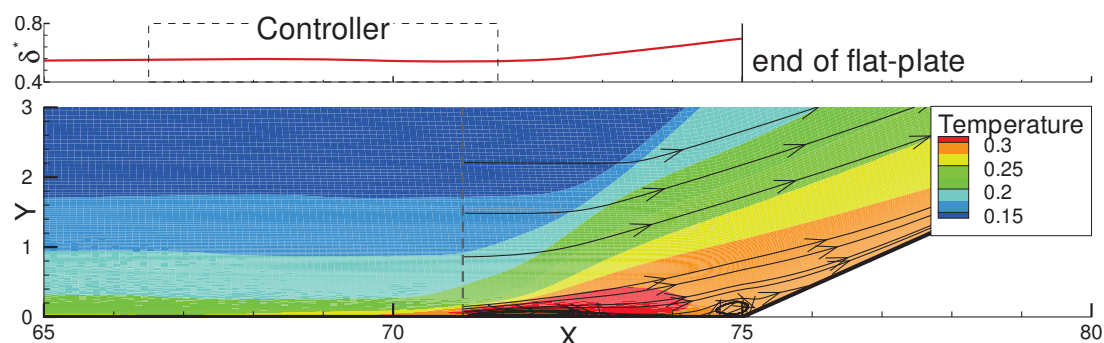
(a) Baseline



(b) Perfect controller [$L = 0.075$, $\mathcal{J} = -L$]



(c) Pulsed perfect controller



(d) Real controller

Figure 17. Spanwise-average mean temperature contours and mean-flow velocity streamlines. The streamlines have been terminated upstream of $x = 71$. The boundary-layer displacement thickness δ^* is also plotted above the flat-plate portion of each each plot.

controllers in Figs. 17(c) and 17(d) both produce a significant reduction in the size and strength of the recirculating bubble, though the recirculating core still exists in $x = 75$. As seen in the line plots of δ^* , also shown in Fig. 17 (above the temperature contours), the displacement thickness starts to increase shortly after the end of the controller for these scenarios. As a result, the flow becomes more susceptible to separation and does separate upstream of the ramp corner.

While the main purpose of the controller was to reduce the size of the time-mean separated region, it was equally advantageous to eliminate the low frequency content from the separated region. Figure 18, shows the PSD of TKE for the baseline case and the three controllers at three locations: upstream of separation ($\xi = 60$), above the separated region ($70 \leq \xi \leq 80$), and downstream of re-attachment ($\xi = 100$). A comparison between the plots shows that the total turbulent kinetic energy is slightly higher for the controller cases over the separated region, which corresponds to the additional momentum and energy added to the flow. This slight increase in magnitude of TKE is not very significant since the shift to lower frequencies is not as large. In addition, close evaluation of the downstream profiles shows the controller simulations has a lower total TKE. This occurs because the separated region is much smaller for the controlled case, so the larger structures associated with the recirculating flow have a reduced influence on the total TKE.

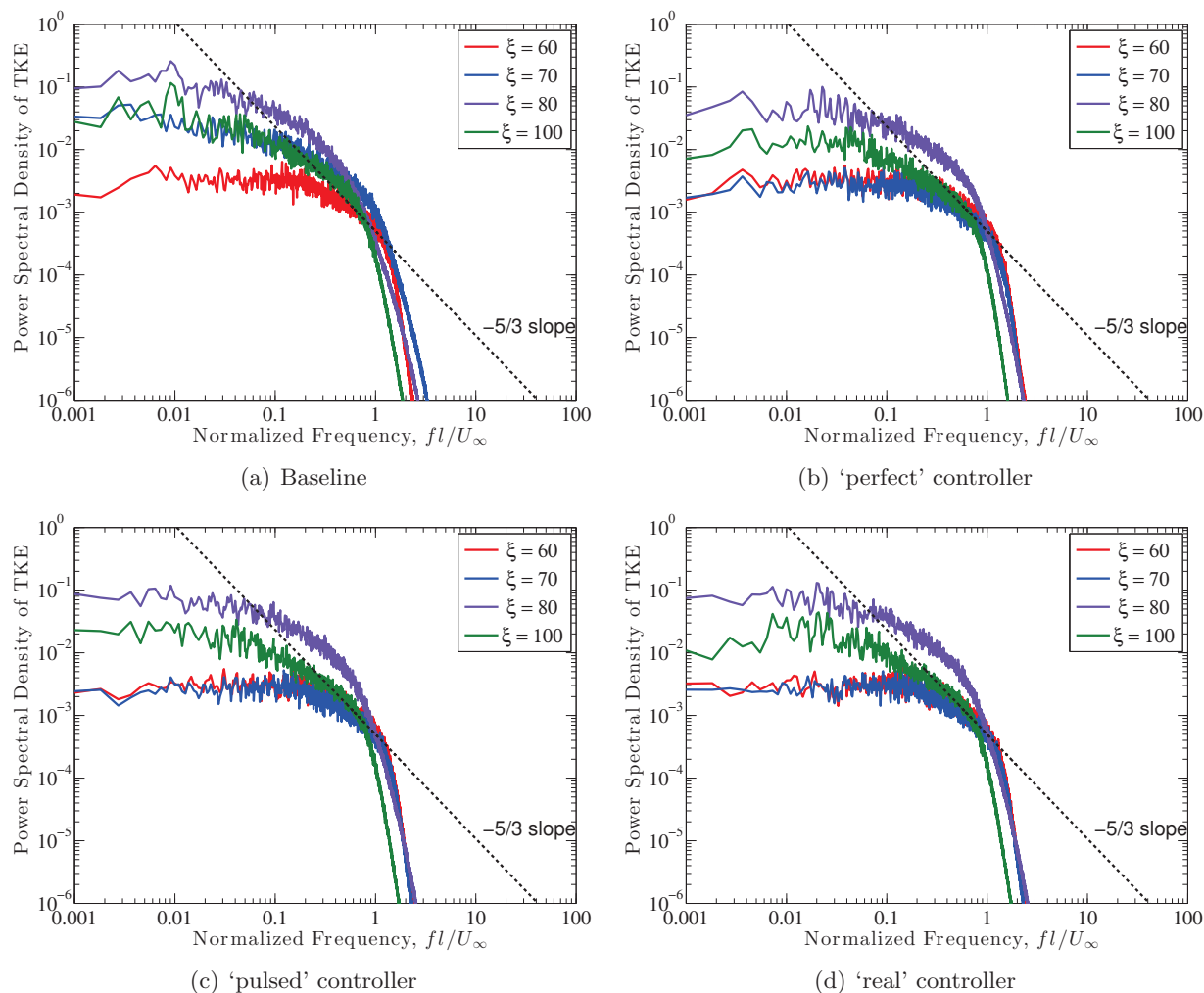


Figure 18. Power spectral density of the turbulent kinetic energy versus frequency.

As seen in the baseline Fig. 18(a), the frequency spectra exhibit a shift to lower frequencies

at the start of the separation ($\xi = 68$). In addition, the spectra between $70 \leq \xi \leq 80$ shows the magnitude of the lower frequency range ($fl/U_\infty < 0.1$) increases as the spectra moves to lower frequency and progresses farther along the separated region. The spectra flattens out after $\xi = 80$, which coincides with reattachment.

Figures 18(b), 18(c), and 18(d) show that all three of the controllers have eliminated the growth of the lowest frequency content, as seen by flatter profiles and lower magnitudes. This observation is most obvious between $\xi = 65$ and $\xi = 70$, but it is also anticipated since all three controllers delayed separation beyond $\xi = 70$. In the 'pulsed' and 'real' cases, the extent of the time-mean separation is still fairly extensive (see Fig. 15), so the PSD of TKE over the separated region has a higher value than the 'perfect' controller. For the 'perfect' controller, the additional magnetic force is sufficiently large to significantly minimize the amplification of the TKE due to the separation, thus eliminating much of the broad-band amplification of the incoming boundary-layer PSD. Some of the remaining amplification of the TKE is attributed to the shock. That said, all three controller scenarios have a lower PSD magnitudes compare to the baseline for the post-shock flow, as seen by looking at the curves for $\xi = 100$ in Fig. 18.

A close examination of Fig. 18(c) shows that the pulsing frequency (i.e., 27 kHz), is not readily apparent on the contour plot near $\xi = 70$. A detailed investigation relieved that the magnitude of the incoming TKE profile was sufficiently large to mask the discrete signal. However, looking at the PSD of pressure in Fig. 19 shows the pulsing frequency dominates the curve at the sampling location above the controller ($\xi = 70$). Figure 19 shows that while the pulsing frequency dominates the curve above the controller, the discrete frequency disappears at stations further downstream as the energy from the pulsing frequency cascades into the surrounding frequencies. This is noteworthy because it means the driving frequency of a pulsed controller scenario does not persist far downstream, so its potential influence on the post-shock flow is inconsequential.

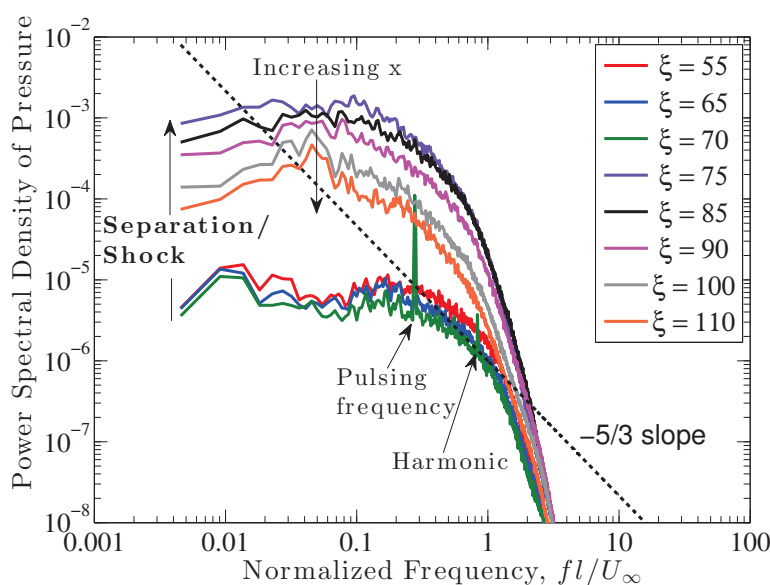


Figure 19. Power spectral density of the pressure versus frequency for Mach 2.249 flow over a 24° ramp using a magnetically-driven gliding-arc discharge pulsed at 27kHz and a 50% duty-cycle.

As seen in Figs. 15 and 17, the magnetically-driven gliding arc discharge is capable of reducing the time-mean separation by locally accelerating the flow near the baseline separation. While the additional force and energy does increase the overall power spectral density spectrum for the 'pulsed' and 'real' cases near the controller, the overall effect of the controller reduces the magnitude of the total TKE downstream of the shock. In addition to reducing the separation length, all three

controllers removed the lowest frequency content from the PSD spectra thus providing relieve to the wall from localized fatigue loading which could lead to premature structural failure. Although the ‘perfect’ controller demonstrates the greatest effect, the ‘pulsed’ strategy accomplished nearly the same control while using half the power, thus making the ‘pulsed’ controller the most efficient.

V. Conclusions

A high-order compact difference scheme and third-order Roe scheme were used in a hybrid approach to perform large eddy simulations for a Mach 2.249 turbulent flow over a 24° ramp in order to investigate the effect of plasma-based flow control. The computational domain was developed with a large flat-plate upstream of the ramp corner where a laminar boundary-layer was perturbed to transition to turbulence through a counter-flow force bypass-transition method. The fully turbulent boundary-layer was analyzed, and found to agree well with experiments and other computational results. A grid study was performed and showed that each grid captured a portion of the inertial energy range. Analysis of the frequency spectra showed a major shift to lower frequency content as the flow moved over the separated region, though the spectra did not exhibit a secondary ultra-low frequency mode that has been seen in some turbulent shock boundary-layer interaction flows.

A magnetically-driven gliding-arc discharge actuator was modeled from a recent turbulent shock boundary-layer interaction experiment and applied to the flow. A control strategy was developed and explored some of the controller parameters. The first case assumed the reversible work created by the magnetic body force momentum transfer was cancelled by Joule heating, which provided the upper limit of the expected control authority in the actuator. The second scenario operated with the same assumption except it pulsed the actuator at a frequency of 27 kHz and a 50% duty cycle. A 50% duty cycle reduced the total power consumption of the actuator by a half. The third case allowed for Joule heating and reversible work such that the mean thermal efficiency of the actuator was 2.5%. The controllers were centered near the time-mean separation point and extended across the entire span of the computational domain. All three controllers effectively reduced the separation length, based on the skin-friction coefficient, with the first case reducing the size by over 75%. The pulsed and 2.5% thermal efficiency controllers each reduced the separation size by over 45%. The reduction in separated length coincided with the elimination of the lowest-frequency energy content from the flow. Although the total turbulent kinetic energy increased slightly near each of the controllers, the resultant flow achieved a lower total turbulent kinetic energy downstream of the ramp due to advantageous effects provided by the controllers.

While the three controllers simulated yielded a significant reduction in the separation length, the frequency spectra still exhibited a shift towards lower frequency, particularly over the remaining separated region. The controller model has many parameters which could be investigated in future studies in order to optimize the control strategy for reducing the detrimental effects of turbulent shock boundary-layer interaction. This include changing the strength, location and size of the controller, and exploring the use of multiple controllers that are pulsed at different phases with each other. In addition, it may prove beneficial to explore finite-span controllers that would develop a pair of vortical structures at each spanwise end of the actuator and would act to roll high-momentum inviscid freestream flow into the boundary layer. It may also be useful to look at strategies where the arc is driven by a nonuniform magnetic field.

Acknowledgments

The first author would also like to thank D. Garmann for his useful discussions regarding FDL3DI, signal analysis and Matlab® scripts. This work was funded in part by the Air Force Office

of Scientific Research, under a laboratory task monitored by Dr. J. Schmisser, AFOSR/RSA. The computational resources were supported by a grant of supercomputer time from the U.S. Department of Defense Supercomputing Resource Center at the U.S. Army Engineer Research and Development Center, Vicksburg, MS and the Air Force Research Laboratory, Wright-Patterson Air Force Base, OH.

References

- ¹Touber, E. and Sandham, N. D., "Low-Order Stochastic Modelling of Low-Frequency Motions in Reflected Shock-Wave/Boundary-Layer Interactions," *Journal of Fluid Mechanics*, Vol. 671, No. Low-Order Stochastic Modelling of Low-Frequency Motions in Reflected Shock-Wave/Boundary-Layer Interactions, 2011, pp. 417–465.
- ²Georgiadis, N. J., Rizzetta, D. P., and Fureby, C., "Large-Eddy Simulation: Current Capabilities, Recommended Practices, and Future Research," *AIAA Journal*, Vol. 48, No. 8, August 2010, pp. 1772–1784.
- ³Shan, H., Jiang, L., Zhao, W., and Liu, C., "Large Eddy Simulation of Flow Transition in a Supersonic Flat-Plate Boundary Layer," *AIAA Paper* 1999-425, 1999.
- ⁴Rizzetta, D. P., Visbal, M. R., and Gaitonde, D. V., "Large-Eddy Simulation of Supersonic Compression-Ramp Flow by a High-Order Method," *AIAA Journal*, Vol. 39, No. 12, December 2001, pp. 2283–2292.
- ⁵Garnier, E. and Sagaut, P., "Large Eddy Simulation of Shock/Boundary-Layer Interaction," *AIAA Journal*, Vol. 20, No. 10, October 2002, pp. 1935–1944.
- ⁶Rizzetta, D. P. and Visbal, M. R., "Application of Large-Eddy Simulation to Supersonic Compression Ramps," *AIAA Journal*, Vol. 40, No. 8, August 2002, pp. 1574–1581.
- ⁷Touber, E. and Sandham, N. D., "Comparison of Three Large-Eddy Simulations of Shock-Induced Turbulent Separation Bubbles," *Shock Waves*, Vol. 19, No. 6, August 2009, pp. 469–478.
- ⁸Urbin, G. and Knight, D., "Large-Eddy Simulation of a Supersonic Boundary Layer Using an Unstructured Grid," *AIAA Journal*, Vol. 39, No. 7, July 2001, pp. 1288–1295.
- ⁹Yan, H. and Knight, D., "Large Eddy Simulation of Supersonic Flat Plate Boundary Layer Part I," *AIAA Paper* 2002-132, 2002.
- ¹⁰Yan, H. and Knight, D., "Large Eddy Simulation of Supersonic Flat Plate Boundary Layer Part II," *AIAA Paper* 2002-4286, 2002.
- ¹¹Adams, N. A., "Direct simulation of the turbulent boundary layer along a compression ramp at $M = 3$ and $Re_\theta = 1685$," *Journal of Fluid Mechanics*, Vol. 420, No. 1, 2000, pp. 47–83.
- ¹²Wu, M. and Pino Martín, M., "Direct Numerical Simulation of Supersonic Turbulent Boundary Layer Over a Compression Ramp," *AIAA Journal*, Vol. 45, No. 4, April 2007, pp. 879–889.
- ¹³Muppidi, S. and Mahesh, K., "DNS of Unsteady Shock Boundary Layer Interaction," *AIAA Paper* 2011-724, 2011.
- ¹⁴Priebe, S. and Pino Martín, M., "Low-Frequency Unsteadiness in the DNS of a Compression Ramp Shockwave and Turbulent Boundary Layer Interaction," *AIAA Paper* 2010-108, 2010.
- ¹⁵Priebe, S. and Pino Martín, M., "Low-Frequency Unsteadiness in Shock Wave/Turbulent Boundary Layer Interaction," *Journal of Fluid Mechanics*, April 2012, Available online, doi:10.1017/jfm.2011.560.
- ¹⁶Gaitonde, D. and Visbal, M. R., "High-order Schemes for Navier-Stokes Equations: Algorithm and Implementation into FDL3DI," Tech. rep., Air Force Research Laboratory, August 1998, AFRL-VA-WP-TR-1998-3060.
- ¹⁷Visbal, M. R., "Computational Study of Vortex Breakdown on a Pitching Delta Wing," *AIAA Paper* 1993-2974, 1993.
- ¹⁸Gordnier, R. E. and Visbal, M. R., "Numerical Simulation of Delta-Wing Roll," *Aerospace Science and Technology*, Vol. 2, No. 6, September 1998, pp. 347–357.
- ¹⁹Visbal, M. R., Gaitonde, D. V., and Gogineni, S., "Direct Numerical Simulation of a Forced Transitional Plane Wall Jet," *AIAA Paper* 1998-2643, 1998.
- ²⁰Rizzetta, D. P., Visbal, M. R., and Blaisdell, G. A., "Application of a High-Order Compact Difference Scheme to Large-Eddy and Direct-Numerical Simulation," *AIAA Paper* 1999-3714, 1999.
- ²¹Morgan, P. E., Rizzetta, D. P., and Visbal, M. R., "High-Order Numerical Simulation of Turbulent Flow over a Wall-Mounted Hump," *AIAA Journal*, Vol. 44, No. 2, February 2006, pp. 239–251.
- ²²Garmann, D. J. and Visbal, M. R., "Implicit LES Computations for a Rapidly Pitching Plate," *AIAA Paper* 2010-4282, 2010.
- ²³White, M. D. and Visbal, M. R., "High Fidelity Analysis of Aero-Optical Interaction with Compressible Boundary Layers," *AIAA Paper* 2010-4496, 2010.

- ²⁴Anderson, D., Tannehill, J., and Pletcher, R., *Computational Fluid Mechanics and Heat Transfer*, 1984, McGraw-Hill.
- ²⁵Rizzetta, D. P. and Visbal, M. R., "Numerical Investigation of Plasma-Based Control for Low-Reynolds-Number Airfoil Flows," *AIAA Journal*, Vol. 49, No. 2, February 2011, pp. 411–425.
- ²⁶Mullenix, N. J., Gaitonde, D. V., and Visbal, M. R., "A Plasma-Actuator-Based Method to Generate a Supersonic Turbulent Boundary Layer Inflow Condition for Numerical Simulation," AIAA Paper 2011-3556, 2011.
- ²⁷Raizer, Y. P., *Gas Discharge Physics*, 1991, Springer-Verlag.
- ²⁸Macheret, S., "Physics of Magnetically Accelerated Nonequilibrium Surface Discharges in High-Speed Flow," AIAA Paper 2006-1005, 2006.
- ²⁹Kalra, C., Shneider, M. N., and Miles, R., "Numerical Study of Boundary Layer Separation Control using Magnetogasdynamic Plasma Actuators," *Physics of Fluids*, Vol. 21, October 2009, pp. 106101.
- ³⁰MacCormack, R. W., "Flow Calculations with Strong Magnetic Fields," AIAA Paper 2003-3623, 2003.
- ³¹Atkinson, M., Poggie, J., and Camberos, J., "Numerical Investigation of Oblique Shock-Wave/Turbulent Boundary-Layer Interaction Control Using Plasma Actuators," AIAA Paper 2011-3427, 2011.
- ³²Atkinson, M. D., *Hypersonic Flow and Flight Control Using Plasma Actuators*, 2012, PhD thesis, Department of Aerospace Engineering, University of Dayton.
- ³³Beam, R. and Warming, R., "An Implicit Factored Scheme for the Compressible Navier-Stokes Equations," *AIAA Journal*, Vol. 16, No. 4, April 1978, pp. 393–402.
- ³⁴Gordnier, R. E. and Visbal, M. R., "Numerical Simulation of Delta-Wing Roll," AIAA Paper 1993-544, 1993.
- ³⁵Jameson, A., Schmidt, W., and Turkel, E., "Numerical Solutions of the Euler Equations by Finite Volume Methods Using Runge-Kutta Time Stepping Schemes," AIAA Paper 1981-1259, 1981.
- ³⁶Pulliam, T. H. and Chaussee, D. S., "A Diagonal Form of an Implicit Approximate-Factorization Algorithm," *Journal of Computational Physics*, Vol. 39, No. 2, February 1981, pp. 347–363.
- ³⁷Lele, S., "Compact Finite Difference Schemes with Spectral-like Resolution," *Journal of Computational Physics*, Vol. 103, 1992, pp. 16–42.
- ³⁸Visbal, M. R. and Gaitonde, D. V., "High-Order-Accurate Methods for Complex Unsteady Subsonic Flows," *AIAA Journal*, Vol. 37, No. 10, October 1999, pp. 1231–1239.
- ³⁹Gaitonde, D., Shang, J. S., and Young, J. L., "Practical Aspects of High-Order Accurate Finite-Volume Schemes for Electromagnetics," AIAA Paper 1997-363, 1997.
- ⁴⁰Visbal, M. R. and Rizzetta, D. P., "Large-Eddy Simulation on Curvilinear Grids Using Compact Differencing and Filtering Schemes," *Journal of Fluids Engineering*, Vol. 124, 2002, pp. 836–847.
- ⁴¹Roe, P. L., "Approximate Riemann Solvers, Parameter Vectors, and Difference Schemes," *Journal of Computational Physics*, Vol. 43, No. 2, 1981, pp. 357–372.
- ⁴²van Albada, G. D., van Leer, B., and Roberts, W. W., J., "A Comparative Study of Computational Methods in Cosmic Gas Dynamics," *Astronomy and Astrophysics*, Vol. 108, April 1982, pp. 76–84.
- ⁴³Swanson, R. C. and Turkel, E., "On Central-Difference and Upwind Schemes," *Journal of Computational Physics*, Vol. 101, No. 2, August 1992, pp. 292–306.
- ⁴⁴Visbal, M. R., Morgan, P. E., and Rizzetta, D. P., "An Implicit LES Approach Based on High-Order Compact Differencing and Filtering Schemes," AIAA Paper 2003-4098, 2003.
- ⁴⁵Fureby, C. and Grinstein, F. F., "Monotonically Integrated Large Eddy Simulation," *AIAA Journal*, Vol. 37, No. 5, May 1999, pp. 544–556.
- ⁴⁶Stoltz, S. and Adams, N. A., "An Approximate Deconvolution Procedure for Large-Eddy Simulation," *Physics of Fluids*, Vol. 11, No. 7, July 1999, pp. 1699–1701.
- ⁴⁷Mathew, J., Lechner, R., Foysi, H., Sesterhenn, J., and Friedrich, R., "An Explicit Filtering Method for Large Eddy Simulation of Compressible Flows," *Physics of Fluids*, Vol. 15, No. 8, August 2003, pp. 2279–2289.
- ⁴⁸Rai, M. M., Gatski, T. B., and Erlebacher, G., "Direct Simulation of Spatially Evolving Compressible Turbulent Boundary Layers," AIAA Paper 1995-583, 1995.
- ⁴⁹Rizzetta, D. P. and Visbal, M. R., "Large-Eddy Simulation of Supersonic Boundary-Layer Flow by a High-Order Method," *International Journal of Computational Fluid Dynamics*, Vol. 18, No. 1, January 2004, pp. 15–27.
- ⁵⁰Pirozzoli, S., Grasso, F., and Gatski, T. B., "Direct Numerical Simulation and Analysis of a Spatially Evolving Supersonic Turbulent Boundary Layer at $M=2.25$," *Physics of Fluids*, Vol. 16, No. 3, March 2004, pp. 530–545.
- ⁵¹Pirozzoli, S. and Grasso, F., "Direct Numerical Simulation of Impinging Shock Wave/Turbulent Boundary Layer Interaction at $M=2.25$," *Physics of Fluids*, Vol. 18, No. 065113, 2006, pp. 1–17.
- ⁵²White, F. M., *Viscous Fluid Flow, 3rd Ed.*, 2006, McGraw Hill.
- ⁵³Fernholz, H. H. and Finley, P. J., "A Critical Compilation of Compressible Turbulent Boundary Layer Data," Tech. rep., 1977, AFARDograph No. 223, Case 55010501.

- ⁵⁴Ghosal, S., "Mathematical and Physical Constraints on Large-Eddy Simulation of Turbulence," *AIAA Journal*, Vol. 37, No. 4, 1999, pp. 425–433.
- ⁵⁵van Driest, E. R., "On the Turbulent Flow Near a Wall," *Journal of the Aeronautical Sciences*, Vol. 23, 1956, pp. 1007–1011.
- ⁵⁶Elena, M. and LaCharme, J. P., "Experimental Study of a Supersonic Turbulent Boundary Layer Using Laser Doppler Anemometer," *Journal de Mécanique Théorique et Appliquée*, Vol. 7, 1988, pp. 175–190.
- ⁵⁷Karlson, R. I. and Johansson, T. G., "LDV Measurements of Higher-Order Moments of Velocity Fluctuations in a Turbulent Boundary Layer," Proceedings from the 3rd International Symposium on Applications of Laser Anemometry to Fluid Mechanics, (Instituto Superior Tecnico, Lisbon, Portugal), 1986.
- ⁵⁸Smits, A. J. and Dussauge, J.-P., *Turbulent Shear Layers in Supersonic Flow*, 2nd Ed., 2006, Springer.
- ⁵⁹Bendat, J. S. and Piersol, A. G., *Random Data*, 2nd Ed., 1986, John Wiley & Sons.
- ⁶⁰Jeong, J. and Hussain, F., "On the Identification of a Vortex," *Journal of Fluid Mechanics*, Vol. 285, 1995, pp. 69–94.
- ⁶¹Plotkin, K. J., "Shock wave oscillation driven by turbulent boundary-layer fluctuations," *AIAA Journal*, Vol. 13, No. 8, August 1975, pp. 1036–1040.

51st AIAA Aerospace Sciences Meeting

Large-Eddy Simulations of Separated Supersonic Flow with Plasma Control

Nicholas J. Bisek* and Jonathan Poggie†

Air Force Research Laboratory, Wright-Patterson AFB, OH, 45433-7512, USA

High-order implicit large-eddy simulations were performed for supersonic turbulent flow over a 24° compression ramp. The interaction between the turbulent flow and the corner led to a low-frequency, unsteady, shock-induced separation. A magnetically-driven plasma-based flow controller was modeled and applied to the flow to minimize the separated region and its adverse effects. The controller consisted of two streamwise separated segments pulsed 180° out of phase at a 50% duty-cycle. The results show that this controller configuration was very effective at reducing the separation while only using 80% of the power reported for previous studies.

Nomenclature

C_f	= skin-friction coefficient, $\left(\frac{2}{Re}\right) \frac{\partial u}{\partial y} \Big _w$
J	= transformation Jacobian
\mathcal{J}	= scale Joule heating parameter for the controller model
l_{sep}	= separation length
\mathbf{L}	= scale magnetic body-force vector for the controller model
M	= Mach number
p	= nondimensional static pressure
p_t	= nondimensional compressible total pressure, $p \left(1 + (\gamma - 1)M^2/2\right)^{\gamma/(\gamma-1)}$
\mathbf{Q}	= conserved variable vector
Re	= Reynolds number, $u_\infty L/\nu_\infty$
t	= nondimensional time
t_p	= nondimensional actuator fundamental period
u, v, w	= nondimensional Cartesian velocity components in the x, y, z directions
u_τ	= wall friction velocity, $\sqrt{\tau_w/\rho_w}$
x, y, z	= streamwise, normal, and spanwise directions in nondimensional Cartesian coordinates
y^+	= nondimensional wall distance, $u_\tau y/\nu_w$
δ	= boundary-layer height, $0.99 u_\infty$
Δs^+	= value normalized by the inner length scale, $\Delta s u_\tau/\nu_w$
ξ, η, ζ	= computational coordinates
θ	= compressible boundary-layer momentum thickness, $\int_0^\infty \frac{\rho u}{\rho_\infty u_\infty} (1 - u/u_\infty) dy$
ν	= kinematic viscosity
ρ	= nondimensional density

*Research Aerospace Engineer, AFRL/RQHF. Member AIAA.

†Senior Research Aerospace Engineer, AFRL/RQHF. Associate Fellow AIAA.

Subscript

vD	= van Driest transformation ¹
w	= wall
∞	= reference or freestream value

Superscript

$-$	= time-mean value
\wedge	= filtered value
$'$	= fluctuating component

I. Introduction

High-speed flight holds some of the most challenging unsolved problems in multidisciplinary aerodynamic sciences. One of the most common, yet poorly understood, physical phenomenon encountered in high speed flight is the interaction of shock waves with turbulent boundary layers, which may result in a region of separated flow. Turbulent shock boundary-layer interaction (SBLI) has practical implications in many high-speed applications since the pressure fluctuations within the unsteady separated region can lead to localized fatigue loading and the premature failure of the structure. Moreover, work by Plotkin,² Poggie and Smits,³ and Toubert and Sandham⁴ indicated that the separated region amplified the low-frequency disturbances, which may damage or decrease performance to downstream subsystems.

In addition to localized fatigue loading, separated flow due to SBLI increases the boundary-layer thickness, which decreases the cross-sectional area of the inviscid core for an internal flow path which degrades inlet/isolator performance. The unfavorable characteristics of shock-induced separated flow motivates research to better understand the physical mechanisms driving the phenomenon and to identify suitable ways of mitigating or, preferably, to eliminate the region from the flow path.

This paper presents large-eddy simulations (LES), to study turbulent SBLI with and without flow control. The LES approach is used because direct numerical simulation (DNS) requires that all length and time scales are fully resolved everywhere in the computational domain, a strict requirement that is beyond the computational resources available for even the size and complexity of the canonical scenario considered here. The LES approach is predicated on the assumption that turbulent kinetic energy is transferred from large to small scales in the energy cascade, and that intercepting the energy flow in the inertial subrange is equivalent to resolving the smaller scales on which energy dissipation physically occurs. As such, LES accurately resolves all length and time-scales down to the inertial subrange everywhere in the computational domain, and then relies on a subgrid-scale (SGS) model, or a filtering procedure to model the energy cascade to the smaller, under-resolved, scales. It is also possible to dissipate the energy from the inertial subrange as a direct result of the inherent dissipation of the numerical method. In those simulations, the numerics do not require an SGS model or filter and, thus, are sometimes referred to as direct simulation or DNS in the literature. Those numerical simulations do not resolve all the time and length scales everywhere in the flow, so they are regarded as LES or implicit-LES in this work since the dissipation of energy from the cascade occurs on scales larger than the Kolmogorov scale for most of the computational domain. Regardless of semantics, LES has the benefit of less stringent grid and time-scale requirements, while still providing physically-accurate results. The LES approach is widely accepted and employed in the turbulence community,⁵ because it allows for the study of a much wider range of problems that can currently be addressed using DNS.⁶⁻¹¹

The present work explores the interaction of a turbulent boundary-layer with a compression

corner, as illustrated in Fig. 1. This canonical problem has been studied numerically by several researchers, including work by Adams,¹² Rizzetta *et al.*,^{9,13} Loginov *et al.*,¹⁴ Wu and P. Martín,¹⁵ Muppidi and Mahesh,¹⁶ Priebe and Pino Martín,^{17,18} and Grilli *et al.*¹⁹ All these previous computational studies correspond to a freestream Mach number near 2.9, while this study explored a freestream Mach number of 2.25. The lower Mach number and the large ramp angle of 24° yielded a larger separated region than those observed in the aforementioned studies, so the loading levels near separation were more pronounced and changes in separation length due to the controller were more apparent.

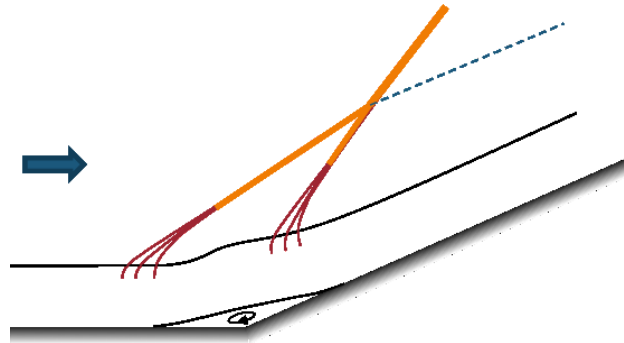


Figure 1. Flow over a 24° compression corner at Mach 2.25.

Based on experimental work, Selig and Smits²⁰ suggested that the shock unsteadiness found in Mach 3 turbulent flow over a 24° compression corner was partially driven by the large-scale fluctuations in the separated region. From this observation, Dolling²¹ hypothesized that a significant reduction in the separated flow length-scales would probably reduce the loading levels found near separation.

Traditionally, boundary-layer bleed has been used to siphon-off the separated flow. Micro vortex generators (VGs) have also been studied for flow control as they entrain high-momentum inviscid flow into the boundary-layer.²² While these methods successfully reduced the extent of separation, loss of mass-flow, power requirements, and plumbing constraints regarding bleed and challenges with off-design conditions for micro VGs have motivated research in active control methods. In particular, more recent experimental work has explored controllers that operate without mass transfer, using a plasma-based mechanism.^{23–25} These plasma-based devices are advantageous because they have no moving parts, have a minimal aero-thermal penalty when they are not operating, do not require plumbing or fluid supply, have a response time that can match characteristic flow time-scales, and, thus, provide on-demand control.

This paper continues previous work²⁶ which investigated a turbulent shock boundary-layer interaction, and explored the effect of a magnetically-driven gliding-discharge controller for reducing the length of the separated region. In the previous work,²⁶ three different control strategies were explored, all of which used a single controller segment. The first case neglected the energy deposition and was constantly active, thereby providing the upper bounds for the expected level of control provided by the controller system (i.e., perfect). The second also neglected energy deposition from the controller, but was pulsed at a 50% duty-cycle and a Strouhal number of 0.28 to investigate the flow's response while the controller was inactive (pulsed). The third was constantly active and included energy deposition to quantify heating effects from the controller (real). In each scenario, the controller was found to substantially reduce the separation length and, consequently, reduce the total turbulent kinetic energy (TKE) downstream of the compression corner.

In the current work, additional analysis of the baseline flow was performed using a significantly longer time history. The additional data allowed for better resolution of the low-frequency oscilla-

tions observed near separation. In addition, results from a computational domain with twice the spanwise extent were compared with the nominal grid. The solution confirmed that the nominal grid had sufficient resolution and spanwise extent to minimize the influence of the spanwise-periodic boundary conditions. Finally, a new flow controller configuration was explored to further reduce the extent of separation. The controller consisted of two streamwise-separated segments, pulsed 180° out of phase with each other, at a 50% duty-cycle. The first segment was located upstream of separation, while the second was positioned within the separated region. The results show the new configuration was very effective at reducing the separation length, which improved the downstream flow quality to a level consistent with a single controller strategy, while using 80% of the power used in the previous computational controller strategies.²⁶

II. Numerical Method

Flow-field results were obtained using a time-accurate three-dimensional compressible Navier-Stokes solver known as FDL3DI,²⁷ which has been widely used in previous calculations for both steady and unsteady, subsonic and supersonic flows.^{28–33} The governing equations were transformed from Cartesian coordinates (x , y , and z) into a general time-dependent curvilinear coordinate system (ξ , η , and ζ), that was recast in strong conservation-law form. The variables in the compressible governing equations were nondimensionalized by their respective reference values, except for pressure which was nondimensionalized by $\rho_\infty u_\infty^2$. The Sutherland law for the molecular viscosity, the perfect gas relationship, and a constant Prandtl number ($Pr = 0.72$), were also employed.

The basic algorithm employed the Beam-Warming approximate factorization,³⁴ which was run using 3 sub-iterations in the present simulations to maintain temporal accuracy since the implicit portion of the factorization was solved in diagonalized form. A compact-difference scheme was used, based on the pentadiagonal system by Lele.³⁵ Specifically, FDL3DI uses a sixth-order centered implicit-difference operator on the compact stencil, thus reducing discretization error. In one-dimension, the finite difference approximation (f'_i) to the first derivative ($\frac{df}{d\xi}(x_i)$) at the node i is evaluated by solving a tridiagonal system of the form:

$$\frac{1}{3}f'_{i-1} + f'_i + \frac{1}{3}f'_{i+1} = \frac{14}{9}\left(\frac{f_{i+1} - f_{i-1}}{2}\right) + \frac{1}{9}\left(\frac{f_{i+2} - f_{i-2}}{4}\right) \quad (1)$$

The scheme was adapted by Visbal and Gaitonde³⁶ as an implicit iterative time-marching technique. It was used in conjunction with a low-pass Padé-type non-dispersive spatial filter, which was incorporated by Gaitonde *et al.*³⁷ Use of the filter has been shown to be superior to the use of explicitly added artificial dissipation for maintaining both stability and accuracy on stretched curvilinear meshes.³⁶ The filter was applied to the solution vector (\mathbf{Q}) sequentially, in each of the three computational directions, after each sub-iteration, and was implemented in one dimension as:

$$\alpha_f \hat{\mathbf{Q}}_{i-1} + \hat{\mathbf{Q}}_i + \alpha_f \hat{\mathbf{Q}}_{i+1} = \sum_{n=0}^4 \frac{a_n}{2} (\mathbf{Q}_{i+n} + \mathbf{Q}_{i-n}) \quad (2)$$

where $\hat{\mathbf{Q}}$ designates the filtered value of \mathbf{Q} . The filter regularizes poorly-resolved features at the grid scale. Equation (2) represents a one-parameter family of eighth-order filters. The numerical values for a_n are available in Ref. 27. The filter coefficient (α_f), is a freely adjustable parameter that determines sharpness of the filter cutoff and was set to 0.3 for the eighth-order filter terms and 0.45 for all lower-order terms in the current work. Note that the filtering technique may be interpreted as an approximate deconvolution SGS model,³⁸ which is based upon a truncated series expansion of the inverse filter operator for the unfiltered flow-field equations. Mathew *et al.*³⁹ have shown that filtering provides a mathematically consistent approximation of unresolved terms arising from any

type of nonlinearity. Filtering regularizes the solution and generates virtual SGS model terms that are equivalent to those of an approximate deconvolution. As such, the methodology in FDL3DI permits a seamless transition from LES to DNS as the resolution is increased.

It is important to note that the spatial filter associated with the high-order compact scheme may produce spurious oscillations in the vicinity of strong shocks that could prove detrimental to the solver's stability. To overcome this potential pitfall, a 3rd order Roe flux-difference scheme⁴⁰ with the van Albada flux limiter⁴¹ was employed near shocks. This hybrid approach was developed and successfully used in previous studies of a supersonic turbulent compression-corner.^{13,26} During each sub-iteration of the solver, the shock location was identified using the pressure gradient detector developed by Swanson and Turkel.⁴² Once the shock was located, a 5-point stencil was established around the shock, and the inviscid fluxes were computed using the Roe scheme. Because of the upwind nature of the Roe scheme, the filtering technique was not applied within the stencil.

The hybrid approach allowed the high-order compact-difference scheme to capture the fine-scale structures in the shock-free regions of the turbulent flow, while the Roe scheme accurately modeled the shock. Due to the high sensitivity of the shock detector, the Roe scheme was only applied in the inviscid region of the flow. Additional details about the hybrid code are available in Ref. 26.

III. Computational Setup and Development of the Turbulent Inflow

This work explored the interaction of a turbulent supersonic boundary-layer flow over a compression corner. Reference conditions for the scenario are listed in Table 1, which were developed from a 1955 experiment by Shutts *et al.* (Case 55010501 compiled by Fernholz and Findley)⁴³ and were consistent with previous work.²⁶

Table 1. Flow conditions for Mach 2.25 air flow over a flat plate.

Parameter	Value
M	2.249
u_∞	588 m/s
T_∞	169.4 K
T_w	322.2 K
p	23,830 Pa
Re/m	2.5×10^7 m ⁻¹
Re_θ	2930-5300

Since FDL3DI uses nondimensional variables, the reference variables used were: $\ell = 6.096 \times 10^{-4}$ m, $u_\infty = 588$ m/s, $M_\infty = 2.249$, and $Re_\ell = 15,240$. In the analysis of the results that follow, the solution flow variables were decomposed into time-mean values and fluctuating components (i.e., $u = \bar{u} + u'$, where \bar{u} is the time-mean value and u' is the fluctuating component).

The inflow boundary was specified using a solution to the compressible laminar boundary-layer equations,⁴⁴ with the inflow boundary-layer height (δ) scaled to the reference length (ℓ) and freestream conditions applied outside the boundary-layer. An extrapolated upper-boundary condition was used to accommodate the growing boundary-layer which transitioned from laminar to fully turbulent on the flat plate portion of the computational domain. Spanwise-periodic boundary conditions maintained high-order differencing and filtering via a five grid-point overlap. An extrapolated boundary condition was used at the exit boundary. Along the wall surface, a no-slip velocity boundary condition was imposed with an isothermal wall set to the nominal adiabatic wall tem-

perature specified in Table 1. The surface pressure was computed by enforcing a zero wall-normal derivative to third-order spatial accuracy. Figure 2 illustrates the boundary conditions employed.

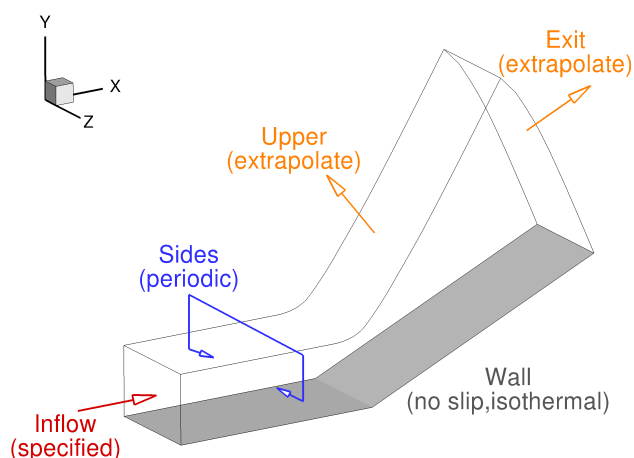


Figure 2. Boundary conditions for supersonic flow over a compression corner.

A structured grid, consistent with the ‘fine’ grid used previously,²⁶ was employed for the present work. The grid was used because a previous computational study²⁶ verified the mean flow quantities were consistent with experimental measurements and were converging with increased resolution. A summary of the grid is outlined below, but additional discussion about its development, along with the two coarser grids used in the grid study, is available in Ref. 26. The computational domain was $160\ell \times 5\ell \times 25\ell$ (length \times width \times height), with the ramp corner located at $x = 75\ell$, and consisted of three parts, (Trip, Constant, and Buffer), as seen in Fig. 3.

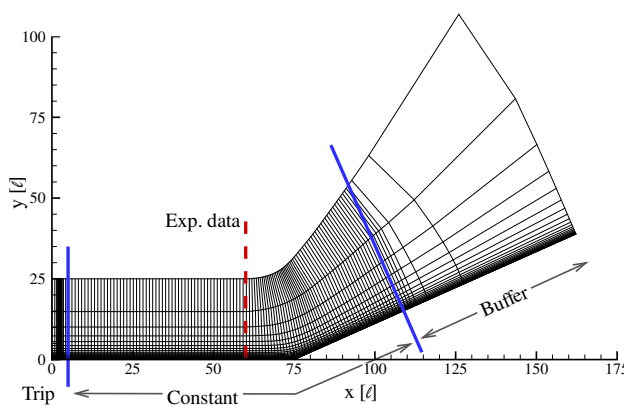


Figure 3. Schematic of the three regions of the computational domain.

The Trip region contained 130 streamwise grid points and initiated bypass-transition. Bypass-transition was accomplished using a counter-flow body-force model developed by Mullenix *et al.*,⁴⁵ which was consistent with the previous work.²⁶ The Constant region had 1141 uniformly-spaced streamwise grid points ($\Delta x_w^+ = 23.8$), and was the primary region of interest since this region was where the flow transitioned to fully turbulent, separated due to the SBLI, and, consequently, employed the flow controller. The Buffer region contained 41 monotonically-stretched streamwise points which transferred turbulent energy to higher spatial wave-numbers, where the spatial filter removed it from the computation before reaching the exit boundary condition. The existence of fluctuating quantities at an extrapolated boundary could lead to spurious oscillations being reflected

back into the computational domain.

The grid spacing in the normal direction was specified such that the first point was 0.002ℓ from the wall ($\Delta y_w^+ = 0.48$). The grid point distribution was monotonically stretched using 260 additional points and a hyperbolic tangent expansion. The distribution included 169 grid points within the fully-developed turbulent boundary-layer, with a grid spacing of 0.038ℓ at the outer edge of the boundary layer ($\Delta y^+ = 9$). The spanwise domain contained 277 uniformly-spaced points. However, 4 of these points existed within the 5-point spanwise-periodic overlap region ($\Delta z_w^+ = 4.3$). The grid contained $1312 \times 261 \times 277 = 94.9$ million points.

Previous work⁴⁶ demonstrated the grid was sufficiently resolved for LES to capture the small-scale structures present in a wall-bounded turbulent flow and the corresponding two-point autocorrelations indicated that the spanwise extent of the domain was sufficiently wide for the spanwise-periodic boundary conditions used. However, to validate that the domain was sufficiently wide, a second grid, with identical resolution was developed, except its spanwise extent was doubled. The computational domain was $160\ell \times 10\ell \times 2\ell$ (length \times width \times height), contained $1312 \times 261 \times 549 = 188$ million points, and is referred to as ‘double-wide’ in the results that follow.

IV. Compression Ramp Results

For all cases presented in the current work, the solutions were obtained using a nondimensional time-step $\Delta t = 0.005$, which resulted in $\Delta t^+ = Re_\ell (\frac{u_\tau}{u_\infty})^2 (\frac{u_\infty t}{\ell}) = 0.19$. The simulations were allowed to evolve for 3 flow-through lengths in order to allow the initial transients to propagate out of the domain. A flow-through length is defined as the time for the freestream flow to traverse the resolved-portion of computational domain (110ℓ or 22,000 iterations). Time-dependent data were collected for at least 10 additional flow-through lengths with the time-mean quantities corresponding to a time range of 10 flow-through lengths (220,000 iterations), unless otherwise noted.

Consistent with previous work,²⁶ the counter-flow body-force bypass-transition model successfully transitioned the laminar inflow to fully turbulent, with both grids obtaining a fully-developed equilibrium turbulent boundary-layer upstream of the SBLI. At $x = 60\ell$, the boundary-layer momentum thickness, $\theta = 0.31\ell$ ($Re_\theta = 4700$), which was consistent with the momentum thickness in the experiments by Shutts *et al.*⁴³ The streamwise velocity profile was transformed using the van Driest transformation¹ and nondimensionalized by the wall friction velocity ($u^+ = u_{vD}/u_\tau$). The profiles were plotted versus the nondimensional inner length scale $y^+ = y u_\tau / \nu_w$. Figure 4 plots the van Driest transformed velocity in the near-wall region at $x = 60\ell$ for both grids and includes a numerical solution by Rai *et al.*⁴⁷ In addition to the experimental measurements by Shutts *et al.*,⁴³ the experiment data set also included supersonic flow measurements of Elena and LaCharme,⁴⁸ which were collected under similar flow conditions using Laser Doppler Velocimetry (LDV) and Hot-Wire Anemometry (HWA). The numerical solutions match both the inner layer and logarithmic profiles. Note the ‘double-wide’ solution was nearly identical to the ‘fine’ grid solution, which indicates that a computational domain 5δ wide was sufficient for the development of the fully turbulent boundary-layer. Additional plots verifying the equilibrium turbulent boundary-layer are available in Ref. 46.

Figure 5 plots surface contours of the time-mean spanwise-averaged skin-friction coefficient (Cf) for both grids. Areas with a negative skin-friction coefficient indicate reverse flow, or separation. The figure shows that doubling the spanwise extent of the domain did not change the size or behavior of the separated region. The figure also shows pockets of unseparated flow that exist within the time-mean separated region. As seen in the figure, separation occurred at $x = 68\ell$, with the flow reattaching near $x = 79\ell$, and a separation length of 11ℓ .

The standard two-point autocorrelations along a line in the spanwise direction were computed. Since spanwise-periodic boundary conditions were enforced, the two-point autocorrelations were

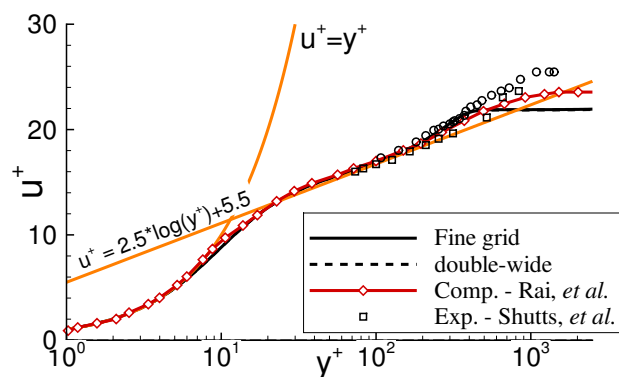


Figure 4. Spanwise-average time-mean streamwise velocity profiles using the Van Driest transform and normalized by friction velocity at $x = 60\ell$.

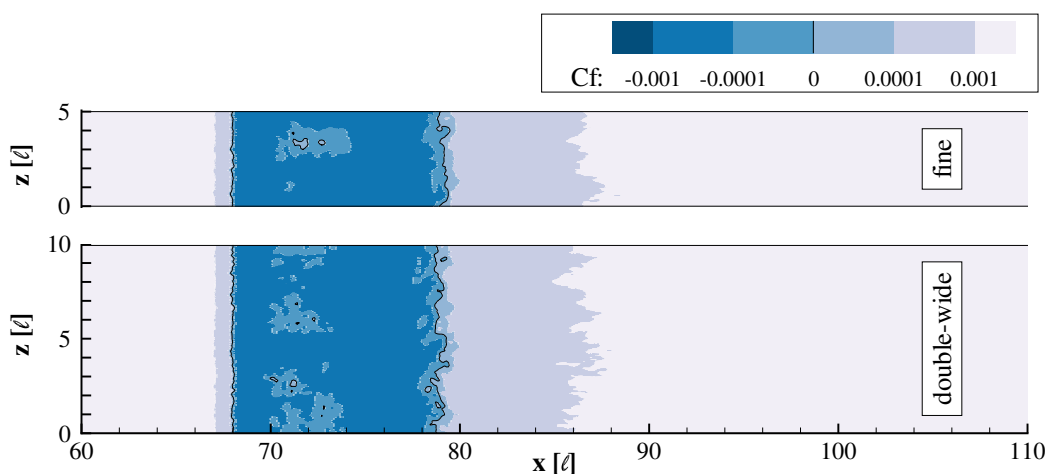


Figure 5. Time-mean contours of the skin-friction coefficient. The ramp corner is at $x = 75\ell$.

generated by averaging individual two-point autocorrelation curves which were created by assuming each point on the spanwise line was the center point. This procedure generated a smoother profile than just studying the two-point autocorrelation curve from the midspan point and was a valid approach because of the spanwise homogeneity.

$$R_{u_i, u_j} = \frac{\overline{u'_i u'_j}}{\sqrt{\overline{u'^2_i} \overline{u'^2_j}}} \quad \text{for each spanwise point } i \quad (3)$$

$$R_{u, u_j} = \frac{1}{\text{kdm}} \sum_{i=1}^{\text{kdm}} R_{u_{|i-\text{kdm}/2|}, u_j}$$

where kdm is the number of points in the span, u'_i and u'_j are the fluctuating component of the streamwise velocity at grid points i and j , respectively. The over-bar indicates the time-mean of the instantaneous fluctuations was computed. A perfectly correlated solution would have a value of one, while a perfectly un-correlated solution has a value of zero. A negative value means the two points are still correlated, but the fluctuations are going in opposite directions. Figure 6 plots the two-point autocorrelations for each of the velocity components and pressure fluctuations as a function of the distance from the spanwise midpoint at various streamwise locations.

As seen in the figures, the u -velocity correlation goes slightly negative near the midspan. This suggests that small vortical structures, with a spanwise orientation, existed in the instantaneous

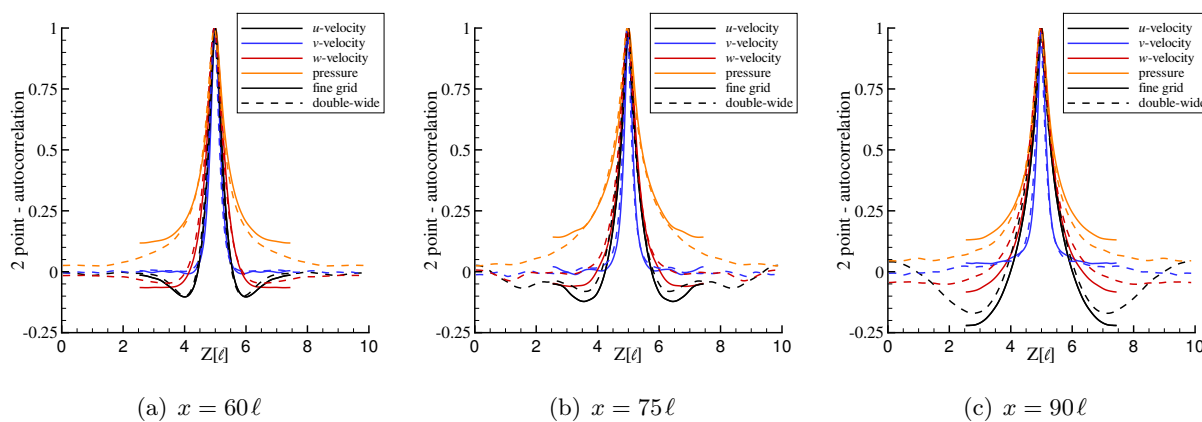


Figure 6. Two-point autocorrelations of the velocity components and pressure fluctuations versus distance from the midspan for both grids.

boundary layer. Likewise, w -velocity correlation also became slightly negative near the midspan, indicating the small structures have a finite width and their orientation contained a streamwise component. The v -velocity did not exhibit much variation outside the initial peak and was very insensitive to spanwise extent. It is worth noting that the pressure fluctuations required a wider domain to de-correlate from the time-mean midspan flow. It is also clear that the ‘fine’ grid curves were consistent with the ‘double-wide’ solutions throughout most of the spanwise extent and only start to deviate during the last 1.0ℓ from the spanwise edge of the domain.

Figures 7 and 8 show contours of the two-point autocorrelations near the corner of the ramp for both u -velocity and pressure, respectively. As seen in the figures, the behavior of the two-point autocorrelations was consistent between the narrow and wide span solutions throughout the streamwise extent of the domain, and not just at the discrete locations illustrated in Fig. 6. However, the contours plots do highlight the slight inconsistency between the two grids, particularly downstream of reattachment.

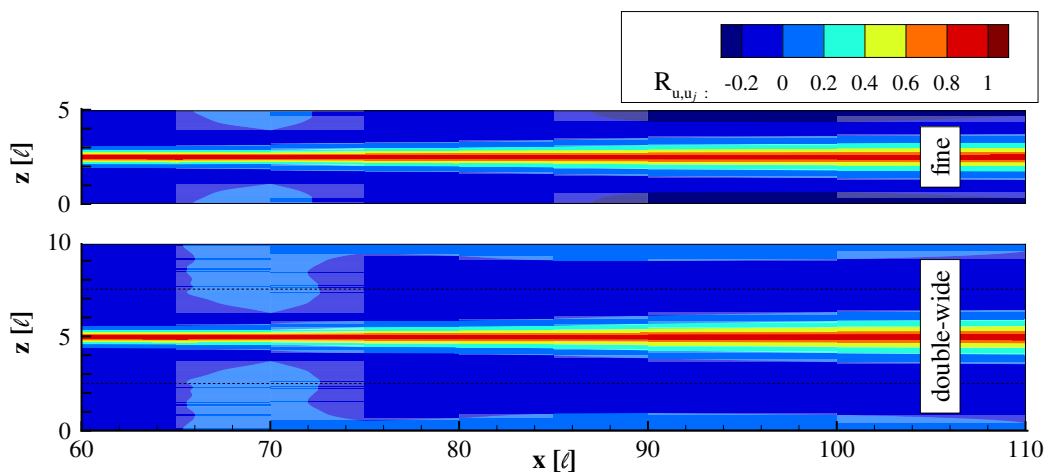


Figure 7. Contours of the two-point autocorrelations of u -velocity fluctuations ($\eta = 1$).

As seen in the Fig. 7, the two-point correlations were negatively-correlated near the spanwise edge ($x > 85\ell$) on the fine grid only, while Fig. 8 shows the pressure fluctuations retained a higher positive correlation in the same area for the narrower ‘fine’ grid. This discrepancy was partially

due to an increase in flow Reynolds number downstream of the shock, which requires a wider spanwise domain to accommodate the non-equilibrium turbulent boundary-layer. Nonetheless, the deviation downstream of reattachment was minor. As such, the spanwise extent of the 'fine' grid was sufficient for the present work, so the 'fine' grid was employed in the remaining analysis.

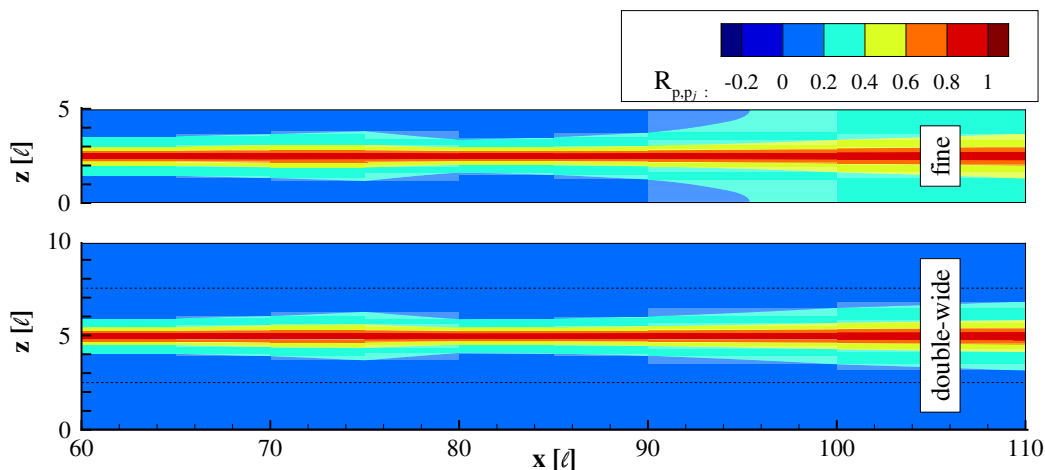


Figure 8. Contours of the two-point autocorrelations of pressure fluctuations ($\eta = 1$).

Surface pressure measurements are one of the easier measurements to obtain experimentally in a SBLI, and so, are an important quantity to study. Figure 9 shows the time-history of the instantaneous pressure at a few surface locations in the incoming boundary layer and near separation. Each pressure time-history trace also includes the time-mean wall pressure as a dashed line. The traces plotted show very little indication that the shock front had moved upstream of $x = 65\ell$ during any point in the time-history. However, the figure clearly shows the flow has traveled through the unsteady-shock and, thus, separated by $x = 70\ell$, although the pressure-time history at that location does contain more scatter. The zone between these locations is where the unsteady-shock oscillations occurred, and is commonly referred to as the intermittent region.⁴⁹ As seen in the pressure-time history at $x = 68\ell$, the pressure rapidly increases, which is followed by slower decay. The behavior is consistent with that observed by Dolling and Murphy.⁴⁹

The behavior of the shock in the intermittent region is also observed by exploring the higher-order moments of the pressure signal. Skewness, Eq. (4), is a measure of the asymmetry of the data around the sample mean, while kurtosis, Eq. (5), indicates the flatness or peakedness of the probability distribution function (i.e., the heaviness of the probability distribution function's tail). A normal Gaussian distribution would have a skewness of 0 and a kurtosis of 3.

$$s_i = \frac{\frac{1}{n} \sum_{t=1}^n (p_{i,t} - \bar{p}_i)^3}{\sqrt{\frac{1}{n} \sum_{t=1}^n (p_{i,t} - \bar{p}_i)^2}}^3 \quad (4)$$

$$k_i = \frac{\frac{1}{n} \sum_{t=1}^n (p_{i,t} - \bar{p}_i)^4}{\left(\frac{1}{n} \sum_{t=1}^n (p_{i,t} - \bar{p}_i)^2\right)^2} \quad (5)$$

where n is the number of iterations in the pressure-time history, and $p_{i,t}$ is the instantaneous pressure at point i for time t . Figure 10 plots the higher-order moments of the surface pressure fluctuations. It is important to note that higher-moment statistics require more data to converge. While the skin-friction coefficient is commonly used to define the separation and reattachment points, the skewness and kurtosis can also indicate where separation and reattachment occur. As seen in the

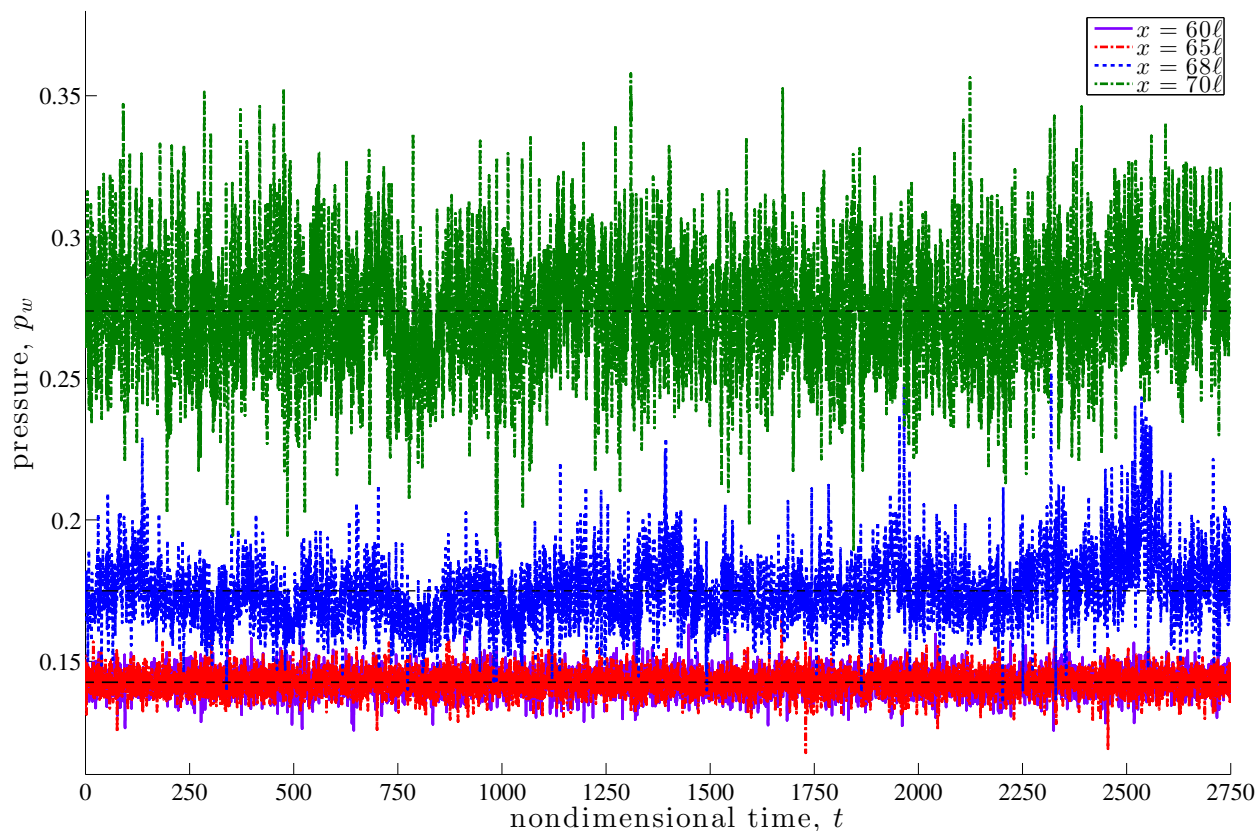


Figure 9. Midspan surface-pressure time-histories near separation.
($t = 2750$ corresponds to 25 flow-through lengths or 550,000 iterations)

figures, the solutions did not exhibit a lot of variation between 10 flow-through lengths and 20 flow-through lengths, which indicates that a time-history of 10 flow-through lengths was sufficiently long to examine these statistics. As seen in Fig. 10(d), the flow upstream of separation (i.e., $x < 65\ell$) has a Kurtosis greater than 3 (i.e., leptokurtic). This means the distribution function of pressure fluctuations in the turbulent boundary-layer had long tails. This is the result of small turbulent structures that develop and breakdown in the incoming boundary layer which were observed as acoustic disturbances in the surface pressure.

As seen in Fig. 10(b), a peak in the standard deviation occurred at $x = 69\ell$, which was 1.0ℓ downstream of the separation location predicted by the skin-friction coefficient in Fig. 5. However, the skewness and kurtosis, Figs. 10(c) and 10(d), show a peak at $x = 68\ell$ and $x = 68.2\ell$, respectively. Interestingly, the skewness does exhibit a secondary bend in the curve at $x = 67\ell$, though this behavior may disappear with additional time-history. While the higher-order moments were consistent with the skin-friction coefficient when identifying the separation point, they dramatically overestimated reattachment, whereas the standard deviation underestimated the reattachment location. The second peak in Fig. 10(b) occurred at $x = 77.9\ell$, which was 1.0ℓ shorter than the reattachment point predicted by the skin-friction coefficient. Likewise, both the skewness and kurtosis exhibited a peak associated with reattachment at $x = 82.5\ell$, making the separation length 3.5ℓ longer when estimated from higher-order moments of the surface pressure fluctuations (an increase in the separation length by over 30%). This disagreement highlights the importance of considering several different measurements to define separation and reattachment.

Figure 11 plots the power spectral density (PSD) of the surface pressure fluctuations at various

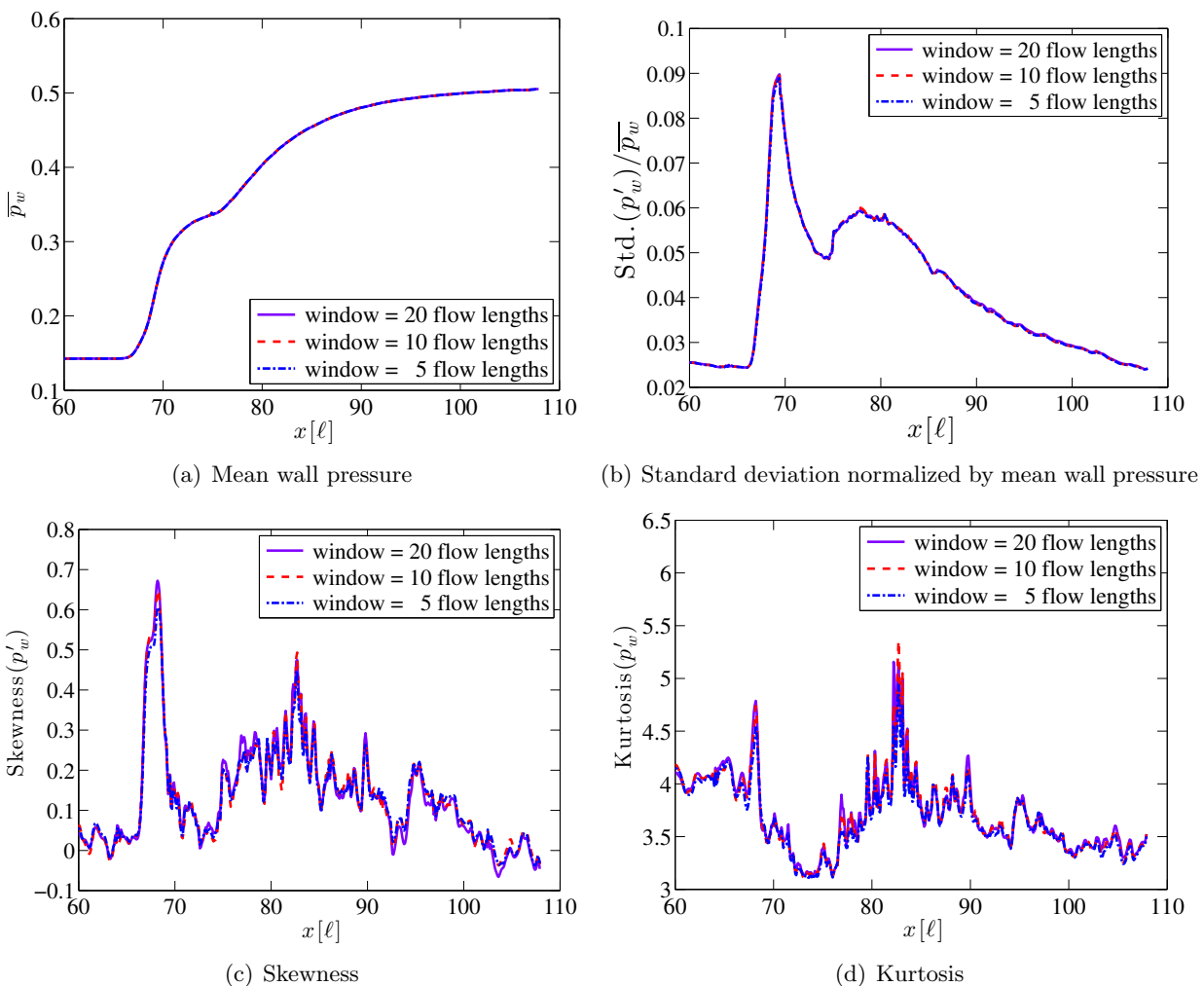


Figure 10. Midspan surface-pressure fluctuation statistics for Mach 2.25 air flow over a 24° ramp.

streamwise locations in the first subfigure and several locations near the separation point in the second. The PSD curves were developed using the standard approach as outlined in Ref. 50. At each spanwise location, a Hanning window was applied to suppress side-lobe leakage. A window length of 5 flow-through lengths was used with a 50% overlap of the raw signal. The raw signal had a time-history that was 25 flow-through lengths long (550,000 iterations), so the results shown were averaged from 9 solutions. Averaging multiple solutions removes noise from the solution, making important frequencies more apparent.

As seen in the figures, the PSD shows a rapid increase in the low frequency content near $f\ell/u_\infty = 0.004$. However, the separation length was 11ℓ based on the skin-friction coefficient, so the low-frequency peak occurred at a Strouhal number based on the separation length of 0.044 ($St_{sep} = f\ell_{sep}/u_\infty = 0.044$). This is consistent with the ultra-low frequency content typically observed in experiments, where the low-frequency peak occurred a Strouhal number based on the separation length near 0.03.²¹ As seen in Fig. 11(b), the pressure fluctuations near the beginning of the intermittent zone had a slope of -1 (as indicated by the thin dashed black line), but the slope got steeper as the flow progressed through the zone. Once the flow was well into the separated region, the low-frequency peak in the pressure spectra diffused into the surround frequencies and was no longer observed, as seen the $x = 75\ell$ curve in Fig. 11(a). In addition, the pressure fluctuations

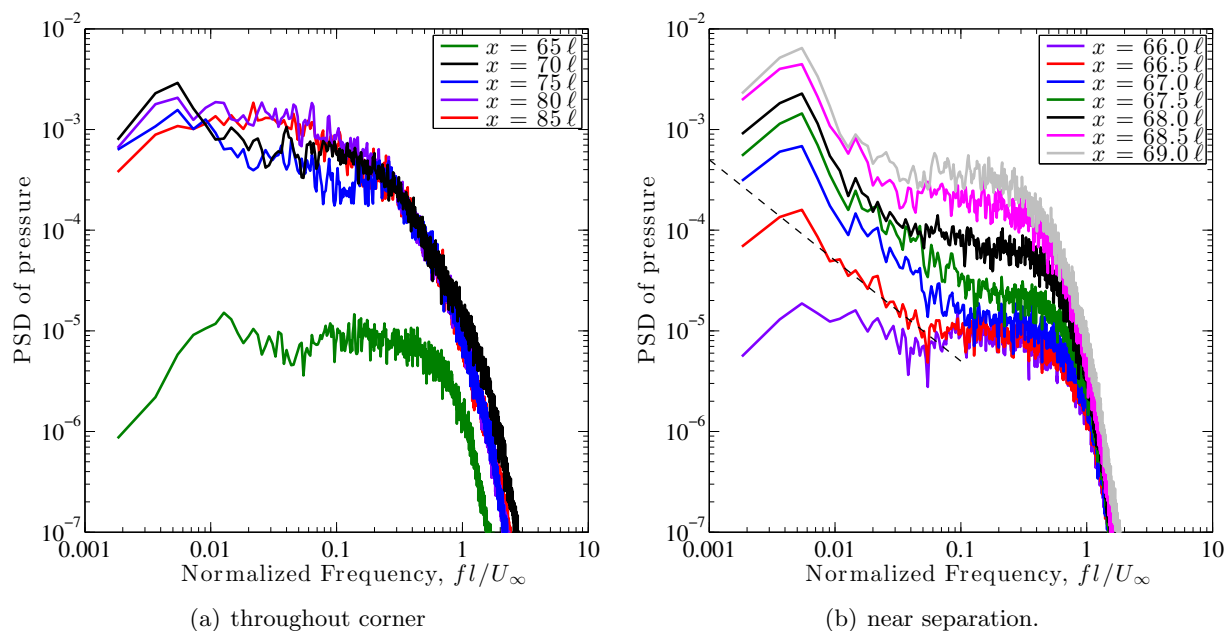


Figure 11. Power spectral density of surface pressure fluctuations at the midspan.

downstream of the unsteady-shock were dominated by the broad-band increase in the spectra due to the shock.

V. Control

Following previous work,²⁶ a model magnetically-driven surface-discharge actuator was positioned on the flat plate just upstream of separation to reduce the extent of separation length caused by the turbulent SBLI. The actuator imparted streamwise momentum into the boundary-layer, which suppressed separation by increasing the fullness of the u -velocity profile and decreased the boundary-layer displacement thickness. The actuator model parameters used in the present study were based on the experimental work of Karla *et al.*²³ and were consistent with the previous study,²⁶ which explored 3 different controller strategies mentioned in the Introduction. Figure 12 shows a conceptual drawing of the controller.

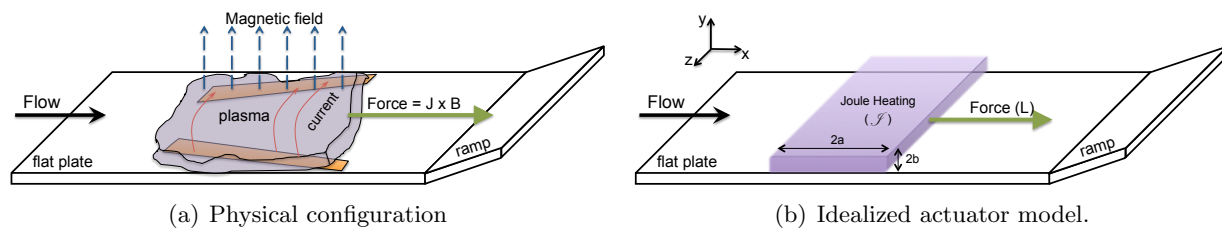


Figure 12. Illustration of the gliding surface-discharge.

The present work used a phenomenological model of the force and energy deposition that was similar to that used in the Reynolds-averaged calculations of Atkinson *et al.*⁵¹ A time-mean representation of the actuator was used because in the externally applied magnet used in the experiment²³ accelerated the surface-discharge to a speed many times faster than the bulk velocity.⁵² In addition, the time-scales of the plasma were several orders of magnitude smaller than the characteristic flow

time of the fluid, so the actuator was incorporated in the fluid equations via time-mean source terms.⁵³ A hyper-Gaussian function was used to describe the deposition volume density function, which provided a mathematical representation of the shape of the time-mean plasma-column and the deposition density within the column:

$$\begin{aligned} V_d &= \frac{K}{a^b} \cdot f(x, y) \\ f(x, y) &= \exp \left[- \left(\frac{x-x_c}{a} \right)^{10} - \left(\frac{y-y_c}{b} \right)^{10} \right] \end{aligned} \quad (6)$$

where a and b represent the ellipsoidal radii in the x and y directions, x_c and y_c represent the center of the ellipse, and K is a constant such that $\iint_{-\infty}^{\infty} V_d dx dy = 1$. The model provided a nearly uniform the deposition rate within the volume (i.e., $f(x, y) \leq 1$), yet smoothly and rapidly decayed to zero outside the region. The controller model accounted for both the time-mean magnetic body-force and Joule heating, as indicated in Eq. (7):

$$\mathbf{S}_c = \frac{V_d}{J} \begin{bmatrix} 0 \\ L_x \\ L_y \\ L_z \\ u L_x + v L_y + w L_z + \mathcal{J} \end{bmatrix} \quad (7)$$

where \mathbf{S}_c is the source term added to the right-hand side of the conservation equations, J is the transformation Jacobian, and V_d is the deposition volume density described in Eq. (6). The components of the nondimensional magnetic body-force vector, L_x , L_y , and L_z , are proportional to the cross product of the current and the magnetic field produced by the magnetically-drive discharge controller. The modified total energy equation included both the reversible work ($u L_x + v L_y + w L_z$), and Joule heating, \mathcal{J} , which reflects the direct thermalization of the electrical power. Joule heating, occurs when directed electron motion in the plasma is randomized into heat via electron-neutrals collisions. An energy exchange, primarily in vibrational modes of the neutral nitrogen molecules,⁵² occurs as a result of these collisions. Some of these excited vibrational states quickly relax to equilibrium (i.e., direct thermalization), while the remaining states do not relax before leaving the computational domain and, thus, were not accounted for in the present calculations.

The controller strategy in the current work explored the influence of having to two separate controller segments that were separated in the streamwise direction by a finite length of 0.5ℓ . The controllers were pulsed at a Strouhal number $St = f\ell/u_\infty = 0.75$. Previous work²⁶ had shown that pulsing a single controller pulsed at a $St = 0.28$ was sufficiently high to prevent the flow from readjusting to its baseline position between pulses, so it was anticipated that the flow would respond in a similarly manner (even with the two segments pulsed 180° out of phase with each other).

The first segment was centered at $x = 68\ell$, $y = 0.1\ell$, and had a streamwise length of 4ℓ ($x_c = 68\ell$, $y_c = 0.1\ell$, and $a = 2\ell$). The controller volume was uniform across the span and had a normal extent of 0.08ℓ ($b = 0.04\ell$). Since the hyper-Gaussian function in Eq. (6) was used to prescribe the plasma column, the total volume of the controller was very nearly $2a \times 2b \times 5\ell = 1.6\ell^3$, which was 80% of the volume of the controllers considered in the previous work.²⁶

The second segment was the same size, but was centered at $x = 72.5\ell$ ($x_c = 72.5\ell$, $y_c = 0.1\ell$, $a = 2\ell$, and $b = 0.04\ell$). This meant that neither controller was present in the streamwise domain between $x = 70\ell$ and $x = 70.5\ell$. In the previous work,²⁶ the total force and energy deposited into the control volume was set to be consistent with the estimated force and energy deposition used in the experiment by Kalra *et. al.*²³ Since the volume of each controller segment used in the current work was 20% smaller than the previous study, the total force and Joule heating deposited were also reduce by 20% (i.e., $L_x = 0.06$ and $\mathcal{J} = 0.02$ for the present calculations). This kept the force

and energy deposition density consistent between current and previous investigation.²⁶ Note that the momentum was only added to the streamwise direction, which was consistent with the previous work.²⁶ Figure 13 illustrates of the 2 segment controller strategy.

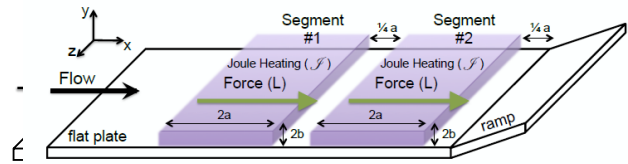


Figure 13. Illustration of the 2 segment controller strategy.

The two controller segments were pulsed at a $St = f\ell/u_\infty = 0.75$, which was expected to be sufficiently high to prevent the local flow-field from recovering between pulses. To keep the total and peak power required at a level equal to 80% of the power used in the previous study,²⁶ the two segments were pulsed 180° out of phase with each other, as illustrated in Fig. 14. In the figure, t_p is the nondimensional actuator fundamental period, which was set to 270 iterations. The amplitude in the figure is the scalar fraction used to modulate the force and energy deposition for each segment of the 2-segment controller system.

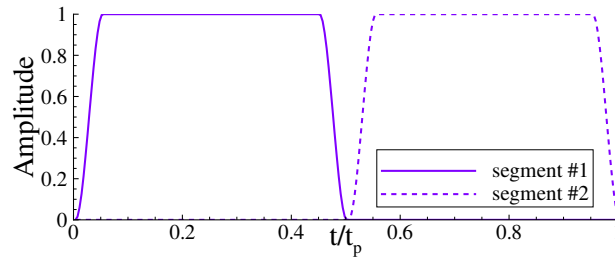


Figure 14. Amplitude of each controller segment versus time for the pulse period.

Consistent with the previous study,²⁶ the current controller strategy reduced in the size of the separated region, which was the result of local streamwise acceleration of the flow near the baseline separation. Figure 15(b) which shows the Q-criterion for both the baseline and the controller scenarios. In addition, the figure includes a planar contour of the instantaneous nondimensional pressure to highlight the unsteady-shock front. Note the instantaneous images were not taken at the same time instance, but rather were chosen to emphasize the differences observed between the two scenarios.

In addition to the significant reduction in the size of the separated region, which was highlighted by the blue-colored structures, a close examination of the turbulent structures above the first controller segment show that the structures were slightly elongated in the streamwise direction and have increased in streamwise velocity. The second controller segment existed downstream of the shock front and within the instantaneous separated region. Here, the turbulent structures in that area were less influenced by the controller's streamwise momentum addition. This was partially due to the reverse flow upstream of the the ramp corner, which formed in order to minimize the entropy jump through the shock by generating a shallower shock angle at the shock foot. As such, the streamwise momentum added by the second segment was working against a primarily-reversed flow, and would need additional strength to fully eliminate the recirculation region. However, it is worth noting that the reversible work done by the second controller actually removed some energy from the domain due to the negative streamwise velocity (i.e., reversible work = $u L_x < 0$, when $u < 0$). In both the baseline and control scenarios, once the flow traveled through the shock

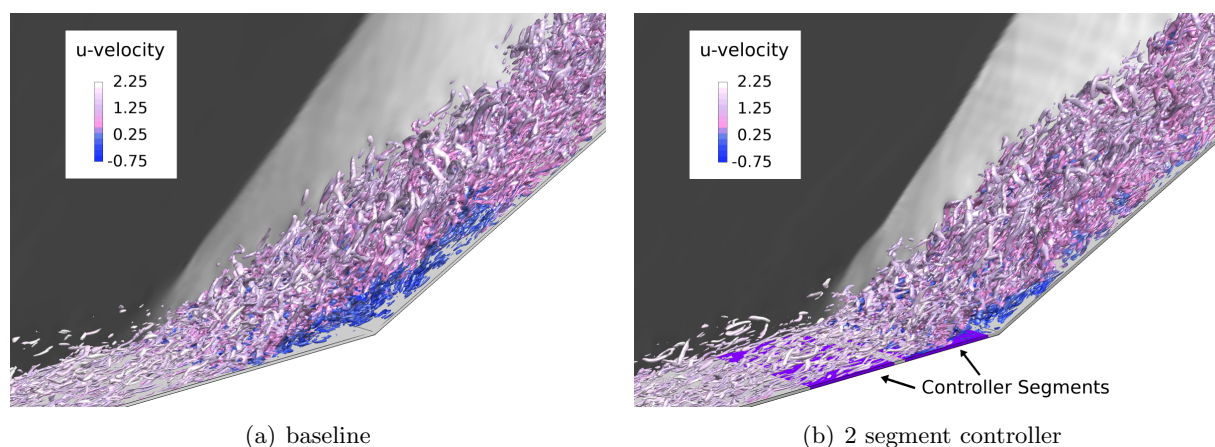


Figure 15. An instantaneous iso-surface of the Q -criterion colored by the u -velocity and a planar contour of pressure to identify the shock.

(and was outside the influence of the controller), it slowed and started readjusting toward its new equilibrium turbulent boundary-layer.

Figure 16 plots the span-averaged time-mean skin friction coefficient near the corner with and without control. The first subplot, Fig. 16(a) shows the skin-friction coefficient from the 3 previous control strategies,²⁶ all of which used a single controller segment. As previously mentioned in the Introduction, the first of the 3 previous scenarios neglected the energy deposition and was constantly active (perfect). The second also neglected the energy deposition from the controller, but was pulsed at $St = 0.28$ and a 50% duty-cycle (pulsed), while the third included energy deposition and was constantly-active (real). Note that the previous controllers strategies had a plasma-column that was 20% longer in the streamwise direction, and, thus, required 20% more power (except for the pulsed scenario due to the 50% duty-cycle).

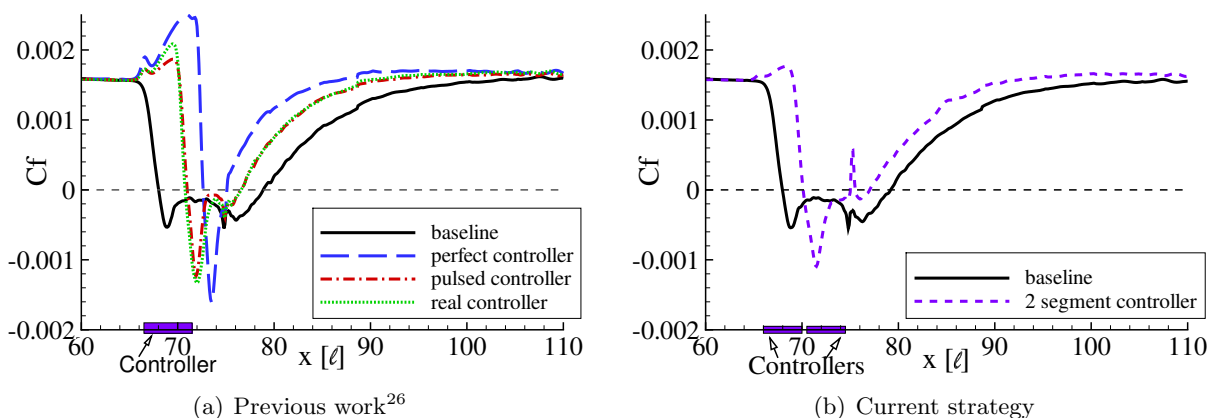


Figure 16. Spanwise-average mean skin friction coefficient with and without control.

Figure 16(b) plots the span-averaged time-mean skin friction coefficient for the two segment controller (2 segment), investigated in the current work. As seen in the figure, the flow separated soon after the end of the first controller segment, which was consistent with the 3 previous scenarios shown in Fig. 16(a). However, the second controller segment was able to provide sufficient streamwise momentum to reattach the flow near the ramp corner. Unfortunately, the flow separated again, soon after the end of second controller segment, which created a small secondary separated

region. Nonetheless, the first segment delayed separation to $x = 70\ell$ and the first reattachment point occurred near $x = 75\ell$, making the time-mean spanwise-averaged separation length 5ℓ , which was a reduction in the separation length by 55%. As a comparison, the real controller,²⁶ was able to reduce the separation length by only 45% and required 20% more power. Note that both the 2 segment and real controller strategies accounted for the controller's energy deposition.

The PSD of TKE and pressure fluctuations were computed at various streamwise locations at a distance of 1.0ℓ normal from the surface. Since the upstream boundary-layer height was 1.7ℓ , the location corresponds to about 60% of boundary-layer height (δ). Figures 17 and 18 show the resultant plots for a window length of 10 flow-through lengths. Note that for both the baseline and control scenario, only the first 10 flow-through lengths of time-history were used, even though the baseline flow has 25 flow-through lengths available. As seen in the figures, the controller strategy was able to delay separation beyond $x = 70\ell$. Figure 18(b) shows the pulsing frequency in the pressure fluctuations as a discrete spike in the energy content at $St=0.75$. However, the sub-harmonics of the frequency were not visible and the discrete frequency was not observed in the PSD of TKE plot shown in Fig. 17(b).

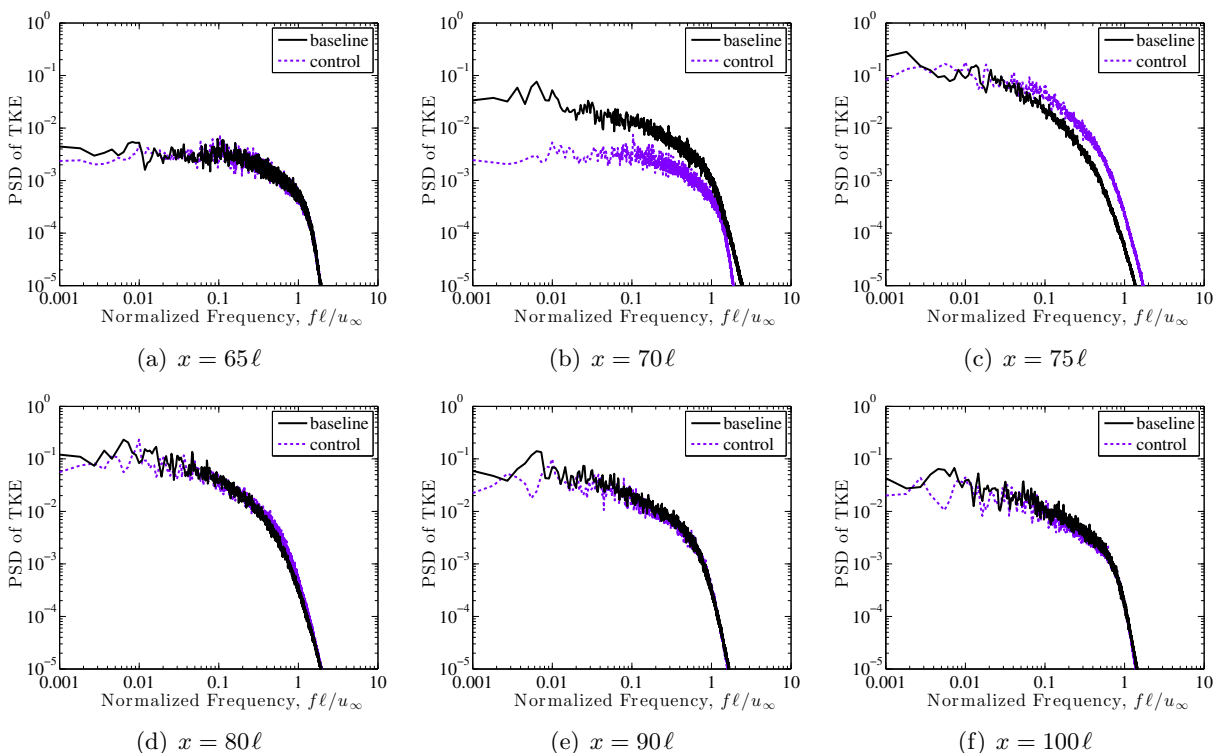


Figure 17. Spanwise-averaged PSD of TKE versus normalized frequency at various streamwise locations 1.0ℓ above the surface.

While the PSD of pressure in Fig. 18(b) clearly shows that separation was delayed beyond $x = 70\ell$, a low-frequency spike still existed in the spectra near a $St = 0.02$. This peak indicates that the intermittent zone includes $x = 70\ell$ with the controller active. While the control strategy was unable to eliminate the low-frequency peak, it did shift the peak frequency by a factor of 5. The movement of the peak to a higher frequency may mitigate potential damage to the underlying structure depending on its natural frequency. Consistent with previous work,²⁶ downstream of reattachment (i.e., $x > 85\ell$), the PSD of TKE plots in Fig. 17 show the controller has a lower total TKE and that there is less energy associated with the pressure fluctuations in Fig. 18. This result occurred because the time-mean separation length decreased, so the flow was less influenced by the

frequency-selective amplifier associated with the separated flow.

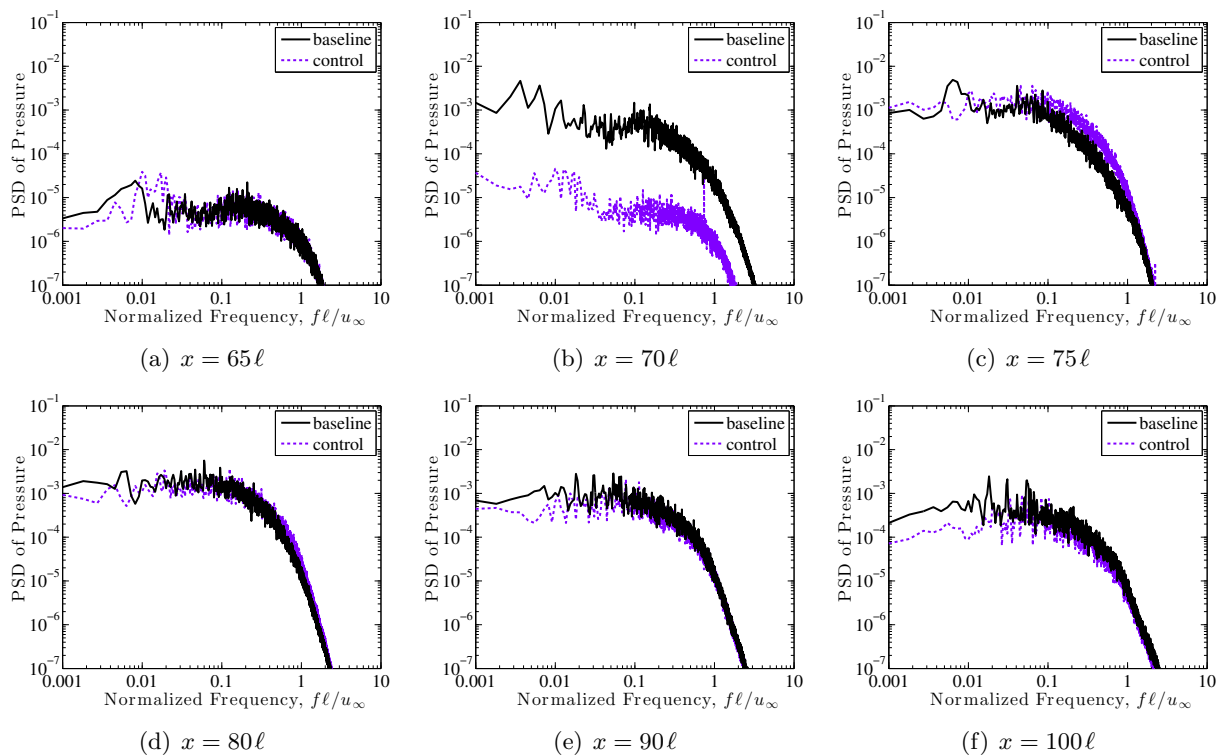


Figure 18. Spanwise-averaged PSD of pressure fluctuations versus normalized frequency at various locations 1.0ℓ above the surface.

Figure 19 plots the higher-moment statistics for the surface pressure fluctuations from both the two segment controller scenario and the baseline case for a pressure-time history of 10 flow-through lengths (220,000 iterations). Consistent with the plot of spanwise-average time-mean skin-friction, the two segment controller significantly shrank the separation length, as seen in the standard deviation of wall pressure fluctuations shown in Fig. 19(b). While the second controller segment was not as successful at reattaching the flow, its presence was observed in the plot of skewness, Fig. 19(c) which shows 2 peak near the separation point. The two peaks correspond with each of the two controller segments. The reattachment location is less obvious, with the higher-moment plots generating a lot of noise in that region, thus making it impractical to use the higher-order moments of the pressure fluctuations to predict either the reattachment or secondary separation. It is also important to note that the secondary separation was not indicated in either the mean or standard deviation of the wall pressure measurements.

Using the spanwise-averaged time-mean solutions, the total TKE at a given streamwise location was computed by integrating the TKE along a line normal to the surface, total TKE = $\int_0^\eta (\bar{u}'^2 + \bar{v}'^2 + \bar{w}'^2)/2 \, d\eta$, where η corresponds to the top boundary of the computational domain. The same procedure was followed to estimate the average total pressure, $p_t = p (1 + (\gamma - 1)M^2/2)^{\gamma/(\gamma-1)}$, at each streamwise location. However, the average total pressure was limited to the first 5ℓ from the surface, average $p_t = 1/5\ell \int_0^{5\ell} p_t \, d\eta$, since the controller only affects the first few boundary-layer thicknesses. The total pressure was evaluated because it is a critical parameter when designing an internal flow-path of an air-breathing configuration. The total TKE and the average total pressure were plotted versus distance along the wall in Fig. 20.

As seen in Fig. 20(a), the total TKE decreased monotonically with control. The average to-

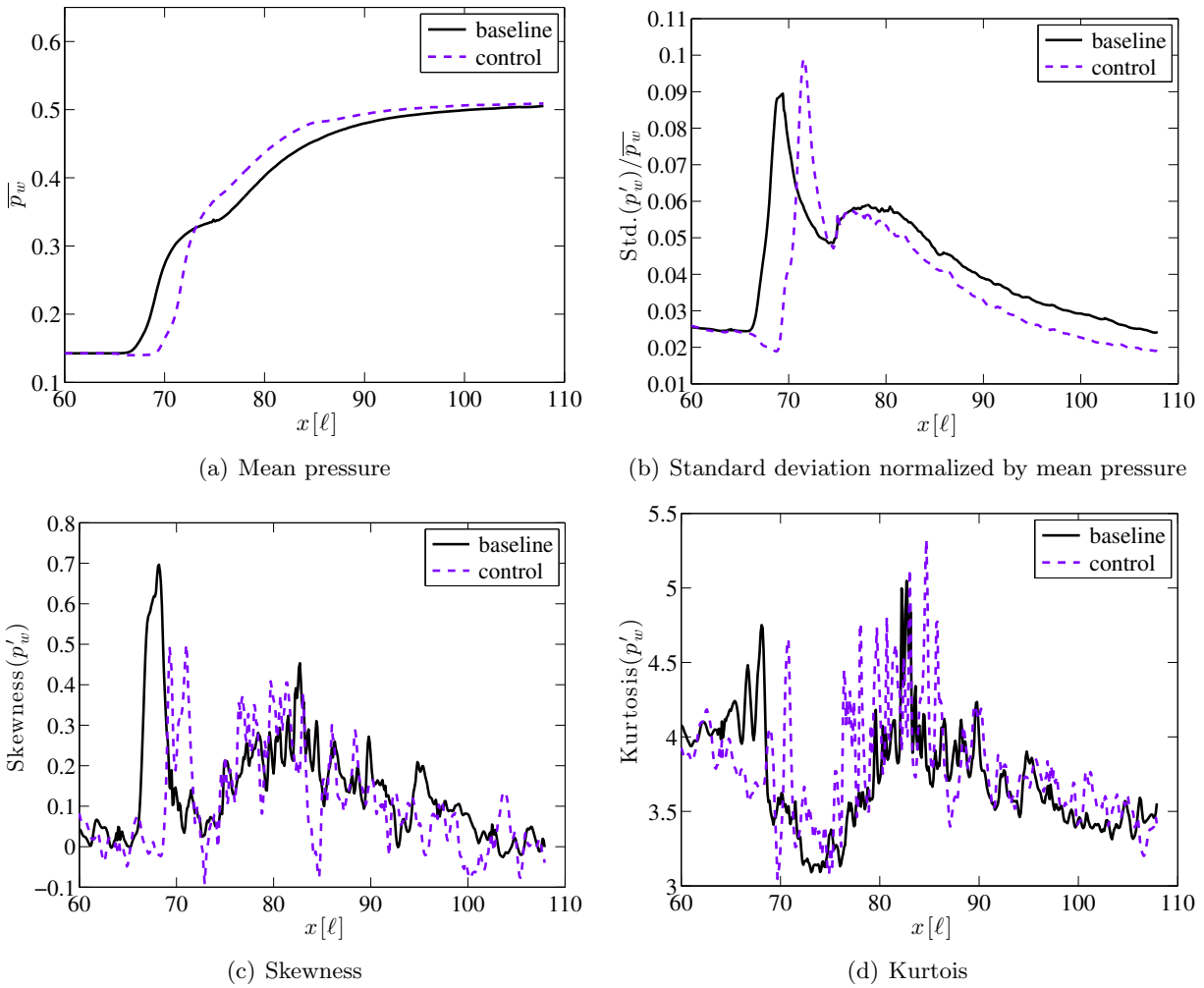


Figure 19. Midspan surface pressure fluctuation statistics for Mach 2.25 air flow over a 24° compression corner with and without a 2 segment controller.

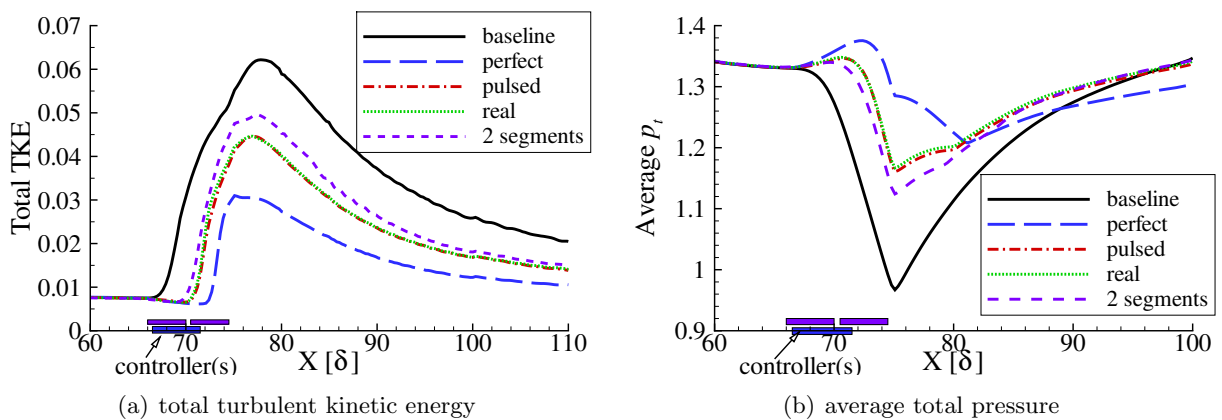


Figure 20. Integrated quantities versus distance along the geometry. The corner is at $x = 75$.

tal pressure was significantly higher throughout the ramp corner, but this improvement was less impressive downstream of reattachment. The perfect controller exhibited the largest change in

total pressure near the corner, but its steeper shock angle produced a greater entropy rise through the shock and, consequently, a greater stagnation pressure loss downstream of reattachment. This pressure loss allowed the ‘baseline’ scenario to achieve a slightly higher average total pressure by the end of the computational domain. The three other control scenarios also mitigated the stagnation pressure loss through the ramp corner, but maintained a shallower shock angle than the perfect controller case. As such, less entropy was generated through the shock which provided a moderate improvement to the average total pressure, even far downstream of reattachment.

VI. Conclusions

A high-order compact difference scheme and third-order Roe scheme were used in a hybrid approach to perform large eddy simulations for a Mach 2.25 turbulent flow over a 24° ramp in order to investigate the effect of plasma-based flow control for turbulent shock boundary-layer interaction. The computational domain included a large flat plate upstream of the ramp corner, where a laminar boundary-layer was perturbed to transition to turbulence through a counter-flow body-force bypass-transition method. The fully turbulent boundary-layer was analyzed, and found to agree well with experiments and other computational results. A second grid which doubled the spanwise extent of the computational domain was studied. The results showed that the mean flow experienced only minor differences due to the wider computational domain, even downstream of reattachment. Analysis of the frequency spectra showed a major increase in lower frequency content as the flow moved through the separated region. A sufficiently long time-history was collected, and the results clearly showed the ultra-low frequency content that has been observed experimentally in some turbulent shock boundary-layer interaction flows.

A model of a magnetically-driven surface-discharge actuator, based on recent experiments at Princeton University Applied Physics Group, was applied to the flow. A control strategy was developed that used 2 controller segments; one located upstream of separation, the other located within the time-mean separated region. The two segment controller system was pulsed with a Strouhal number of 0.75, a 50% duty-cycle, and a 180° phase shift between the two segments. The two controller system used 80% of the estimated power used in the experiment and previous work, but was found to still significantly delay separation. Consistent with previous work, the pulsing frequency was found to be sufficiently high such that the flow did not adjust between pulses and the discrete driving frequency did not persist far downstream. The reduction in separated length coincided with a shift of the lowest-frequency energy content and a lower total turbulent kinetic energy in the flow. In addition, the total pressure downstream of reattachment was found to be higher with control, which should increase the efficiency of downstream systems.

Acknowledgments

The authors would like to thank Dr. D. Rizzetta, Dr. M. Visbal, and Prof. D. Gaitonde for their valuable conversations and advice. This work was sponsored, in part, by the Air Force Office of Scientific Research under grant number LRIR 12RB01COR monitored by Dr. J. Schmisser, AFOSR/RSA. The computational resources were supported by a grant of supercomputer time from the U.S. Department of Defense Supercomputing Resource Center at the U.S. Army Engineer Research and Development Center, Vicksburg, MS and the Air Force Research Laboratory, Wright-Patterson Air Force Base, OH.

References

- ¹van Driest, E. R., "On the Turbulent Flow Near a Wall," *Journal of the Aeronautical Sciences*, Vol. 23, 1956, pp. 1007–1011.
- ²Plotkin, K. J., "Shock wave oscillation driven by turbulent boundary-layer fluctuations," *AIAA Journal*, Vol. 13, No. 8, August 1975, pp. 1036–1040.
- ³Poggie, J. and Smits, A. J., "Experimental Evidence for Plotkin Model of Shock Unsteadiness in Separated Flow," *Physics of Fluids*, Vol. 17, 2005, pp. 018107.
- ⁴Touber, E. and Sandham, N. D., "Low-Order Stochastic Modelling of Low-Frequency Motions in Reflected Shock-Wave/Boundary-Layer Interactions," *Journal of Fluid Mechanics*, Vol. 671, 2011, pp. 417–465.
- ⁵Georgiadis, N. J., Rizzetta, D. P., and Fureby, C., "Large-Eddy Simulation: Current Capabilities, Recommended Practices, and Future Research," *AIAA Journal*, Vol. 48, No. 8, August 2010, pp. 1772–1784.
- ⁶Shan, H., Jiang, L., Zhao, W., and Liu, C., "Large Eddy Simulation of Flow Transition in a Supersonic Flat-Plate Boundary Layer," AIAA Paper 1999-425, 1999.
- ⁷Urbin, G. and Knight, D., "Large-Eddy Simulation of a Supersonic Boundary Layer Using an Unstructured Grid," *AIAA Journal*, Vol. 39, No. 7, July 2001, pp. 1288–1295.
- ⁸Yan, H. and Knight, D., "Large Eddy Simulation of Supersonic Flat Plate Boundary Layer Part I," AIAA Paper 2002-132, 2002.
- ⁹Rizzetta, D. P. and Visbal, M. R., "Application of Large-Eddy Simulation to Supersonic Compression Ramps," *AIAA Journal*, Vol. 40, No. 8, August 2002, pp. 1574–1581.
- ¹⁰Garnier, E. and Sagaut, P., "Large Eddy Simulation of Shock/Boundary-Layer Interaction," *AIAA Journal*, Vol. 20, No. 10, October 2002, pp. 1935–1944.
- ¹¹Touber, E. and Sandham, N. D., "Comparison of Three Large-Eddy Simulations of Shock-Induced Turbulent Separation Bubbles," *Shock Waves*, Vol. 19, No. 6, August 2009, pp. 469–478.
- ¹²Adams, N. A., "Direct simulation of the turbulent boundary layer along a compression ramp at $M = 3$ and $Re_\theta = 1685$," *Journal of Fluid Mechanics*, Vol. 420, No. 1, 2000, pp. 47–83.
- ¹³Rizzetta, D. P., Visbal, M. R., and Gaitonde, D. V., "Large-Eddy Simulation of Supersonic Compression-Ramp Flow by a High-Order Method," *AIAA Journal*, Vol. 39, No. 12, December 2001, pp. 2283–2292.
- ¹⁴Loginov, M. S., Adams, N. A., and Zheltovodov, A. A., "Large-eddy Simulation of Shock-wave / Turbulent-boundary-layer interaction," *Journal of Fluid Mechanics*, Vol. 565, 2006, pp. 135–169.
- ¹⁵Wu, M. and Pino Martín, M., "Direct Numerical Simulation of Supersonic Turbulent Boundary Layer Over a Compression Ramp," *AIAA Journal*, Vol. 45, No. 4, April 2007, pp. 879–889.
- ¹⁶Muppidi, S. and Mahesh, K., "DNS of Unsteady Shock Boundary Layer Interaction," AIAA Paper 2011-724, 2011.
- ¹⁷Priebe, S. and Pino Martín, M., "Low-Frequency Unsteadiness in the DNS of a Compression Ramp Shockwave and Turbulent Boundary Layer Interaction," AIAA Paper 2010-108, 2010.
- ¹⁸Priebe, S. and Pino Martín, M., "Low-Frequency Unsteadiness in Shock Wave/Turbulent Boundary Layer Interaction," *Journal of Fluid Mechanics*, April 2012, Available online, doi:10.1017/jfm.2011.560.
- ¹⁹Grilli, M., Schmid, P. J., Hickel, S., and Adams, N. A., "Analysis of Unsteady Behavior in Shockwave Turbulent Boundary Layer Interaction," *Journal of Fluid Mechanics*, Vol. 700, 2012, pp. 16–28.
- ²⁰Selig, M. S. and Smits, A. J., "Effect of Periodic Blowing on Attached and Separated Supersonic Turbulent Boundary Layers," *AIAA Journal*, Vol. 29, No. 10, October 1991, pp. 1651–1658.
- ²¹Dolling, D. S., "Unsteady Phenomena in Shock Wave/Boundary Layer Interaction," Tech. rep., Advisory Group for Aerospace Research & Development, May 1993, Special Course on Shock-Wave/Boundary-Layer Interaction in Supersonic and Hypersonic Flows, AGARD-R-792, pp. 4-1–4-46.
- ²²Babinsky, H. and Ogawa, H., "SBLI Control for Wings and Inlets," *Shock Waves*, Vol. 18, No. 2, 2008, pp. 89–96.
- ²³Kalra, C., Shneider, M. N., and Miles, R., "Numerical Study of Boundary Layer Separation Control using Magnetogasdynamic Plasma Actuators," *Physics of Fluids*, Vol. 21, October 2009, pp. 106101.
- ²⁴Im, S., Do, H., and Cappelli, M. A., "Dielectric Barrier Discharge Control of a Turbulent Boundary Layer in a Supersonic Flow," *Applied Physics Letters*, Vol. 97, 2010, pp. 041503.
- ²⁵Webb, N., Clifford, C., Porter, A., and Samimy, M., "Control of Oblique Shock Wave-Boundary Layer Interactions Using Plasma Actuators," AIAA Paper 2012-2810, 2012.
- ²⁶Bisek, N. J., Rizzetta, D. P., and Poggie, J., "Plasma Control of a Turbulent Shock Boundary-Layer Interaction," *AIAA Journal*, 2012, (accepted for publication).
- ²⁷Gaitonde, D. and Visbal, M. R., "High-order Schemes for Navier-Stokes Equations: Algorithm and Implementation into FDL3DI," Tech. rep., Air Force Research Laboratory, August 1998, AFRL-VA-WP-TR-1998-3060.

- ²⁸Visbal, M. R., "Computational Study of Vortex Breakdown on a Pitching Delta Wing," AIAA Paper 1993-2974, 1993.
- ²⁹Visbal, M. R., Gaitonde, D. V., and Gogineni, S., "Direct Numerical Simulation of a Forced Transitional Plane Wall Jet," AIAA Paper 1998-2643, 1998.
- ³⁰Rizzetta, D. P., Visbal, M. R., and Blaisdell, G. A., "Application of a High-Order Compact Difference Scheme to Large-Eddy and Direct-Numerical Simulation," AIAA Paper 1999-3714, 1999.
- ³¹Morgan, P. E., Rizzetta, D. P., and Visbal, M. R., "High-Order Numerical Simulation of Turbulent Flow over a Wall-Mounted Hump," *AIAA Journal*, Vol. 44, No. 2, February 2006, pp. 239–251.
- ³²Garmann, D. J. and Visbal, M. R., "Numerical Investigation of a Transitional Flow over a Rapidly Pitching Plate," *Physics of Fluids*, Vol. 23, No. 9, 2011, pp. 094106.
- ³³White, M. D. and Visbal, M. R., "High Fidelity Analysis of Aero-Optical Interaction with Compressible Boundary Layers," AIAA Paper 2010-4496, 2010.
- ³⁴Beam, R. and Warming, R., "An Implicit Factored Scheme for the Compressible Navier-Stokes Equations," *AIAA Journal*, Vol. 16, No. 4, April 1978, pp. 393–402.
- ³⁵Lele, S., "Compact Finite Difference Schemes with Spectral-like Resolution," *Journal of Computational Physics*, Vol. 103, 1992, pp. 16–42.
- ³⁶Visbal, M. R. and Gaitonde, D. V., "High-Order-Accurate Methods for Complex Unsteady Subsonic Flows," *AIAA Journal*, Vol. 37, No. 10, October 1999, pp. 1231–1239.
- ³⁷Gaitonde, D., Shang, J. S., and Young, J. L., "Practical Aspects of High-Order Accurate Finite-Volume Schemes for Electromagnetics," AIAA Paper 1997-363, 1997.
- ³⁸Stoltz, S. and Adams, N. A., "An Approximate Deconvolution Procedure for Large-Eddy Simulation," *Physics of Fluids*, Vol. 11, No. 7, July 1999, pp. 1699–1701.
- ³⁹Mathew, J., Lechner, R., Foysi, H., Sesterhenn, J., and Friedrich, R., "An Explicit Filtering Method for Large Eddy Simulation of Compressible Flows," *Physics of Fluids*, Vol. 15, No. 8, August 2003, pp. 2279–2289.
- ⁴⁰Roe, P. L., "Approximate Riemann Solvers, Parameter Vectors and Difference Schemes," *Journal of Computational Physics*, Vol. 43, No. 2, 1981, pp. 357–372.
- ⁴¹van Albada, G. D., van Leer, B., and Roberts, W. W., J., "A Comparative Study of Computational Methods in Cosmic Gas Dynamics," *Astronomy and Astrophysics*, Vol. 108, April 1982, pp. 76–84.
- ⁴²Swanson, R. C. and Turkel, E., "On Central-Difference and Upwind Schemes," *Journal of Computational Physics*, Vol. 101, No. 2, August 1992, pp. 292–306.
- ⁴³Fernholz, H. H. and Finley, P. J., "A Critical Compilation of Compressible Turbulent Boundary Layer Data," Tech. rep., 1977, AFARDograph No. 223, Case 55010501.
- ⁴⁴White, F. M., *Viscous Fluid Flow, 3rd Ed.*, 2006, McGraw Hill.
- ⁴⁵Mullenix, N. J., Gaitonde, D. V., and Visbal, M. R., "A Plasma-Actuator-Based Method to Generate a Supersonic Turbulent Boundary Layer Inflow Condition for Numerical Simulation," AIAA Paper 2011-3556, 2011.
- ⁴⁶Bisek, N. J., Rizzetta, D. P., and Poggie, J., "Exploration of Plasma Control for Supersonic Turbulent Flow over a Compression Ramp," AIAA Paper 2012-2700, 2012.
- ⁴⁷Rai, M. M., Gatski, T. B., and Erlebacher, G., "Direct Simulation of Spatially Evolving Compressible Turbulent Boundary Layers," AIAA Paper 1995-583, 1995.
- ⁴⁸Elena, M. and LaCharme, J. P., "Experimental Study of a Supersonic Turbulent Boundary Layer Using Laser Doppler Anemometer," *Journal de Mécanique Théorique et Appliquée*, Vol. 7, 1988, pp. 175–190.
- ⁴⁹Dolling, D. S. and Murphy, M. T., "Unsteadiness of the Separation Shock Wave Structure in a Supersonic Compression Ramp Flowfield," *AIAA Journal*, Vol. 21, No. 12, December 1983, pp. 1628–1634.
- ⁵⁰Bendat, J. S. and Piersol, A. G., *Random Data, 2nd Ed.*, 1986, John Wiley & Sons.
- ⁵¹Atkinson, M., Poggie, J., and Camberos, J., "Control of Separated Flow in a Reflected Shock Interaction Using a Magnetically-Accelerated Surface Discharge," *Physics of Fluids*, (accepted for publication), 2012.
- ⁵²Macheret, S., "Physics of Magnetically Accelerated Nonequilibrium Surface Discharges in High-Speed Flow," AIAA Paper 2006-1005, 2006.
- ⁵³MacCormack, R. W., "Flow Calculations with Strong Magnetic Fields," AIAA Paper 2003-3623, 2003.

Spectral Characteristics of Separation Shock Unsteadiness

Jonathan Poggie,^{*} Nicholas J. Bisek,[†] and Roger L. Kimmel[‡]
Air Force Research Laboratory, Wright-Patterson AFB, OH 45433

Scott A. Stanfield[§]
Spectral Energies LLC, Dayton, OH 45431

Spectra of wall pressure fluctuations caused by separation shock unsteadiness were compared for data obtained from wind tunnel experiments, the HIFiRE-1 flight test, and large-eddy simulations. The results were found to be in generally good agreement, despite varying Mach number and two orders of magnitude difference in Reynolds number. Relatively good agreement was also obtained between these spectra and the predictions of a theory developed by Plotkin, which depicts the separation shock unsteadiness as linearly damped Brownian motion. Further, the predictions of this theory are qualitatively consistent with the results of experiments in which the shock motion was synchronized to controlled perturbations. The results presented here support the idea that separation unsteadiness has common features across a broad range of compressible flows.

I. Introduction

Shock-wave / boundary-layer interactions, or (more broadly) inviscid-viscous interactions, are at the heart of many of the design difficulties associated with flight at high Mach number.¹ They occur wherever the vehicle shape deviates from a simple, smooth surface. Such flows are typically characterized by flow separation, large-scale unsteadiness, and extremely high heat transfer rates. They are the source of much of the aero-thermo-acoustic load that a high-speed vehicle must resist.

The inherent complexity of shock-wave / boundary-layer interaction was recognized early on. In 1958 Trilling wrote “It is well known that most shock waves observed in wind tunnels and in flight are not steady” (Ref. 2, p. 301), and in 1970 Green stated that “a geometrically two-dimensional experimental arrangement can produce a highly three-dimensional flow” (Ref. 3, p. 260). To illustrate this point, Green’s Fig. 16(a) shows a surface oil flow pattern, from a geometrically two-dimensional reflected shock experiment, that displays the classic “owl face” pattern⁴ of three-dimensional separation. The large-scale unsteadiness^{5–7} and the three-dimensionality⁸ of these flows have continued to be emphasized in recent work, and connections between them are beginning to be investigated.⁹

In the present paper, we focus on the large-scale unsteadiness of these interactions. This unsteadiness is of particular concern in flight applications because the associated wall pressure fluctuations have significant energy content¹⁰ between 10 Hz and 1000 Hz, which encompasses the range of typical resonant frequencies of flat panels on high Mach number aircraft.¹¹

Correlations for the form of the wall pressure fluctuation spectra^{12,13} are of interest for design against fatigue loading. Further, reduced-order models of the separation unsteadiness can assist in design decisions, and aid the development of feedback flow control systems. Here we attempt to quantify some the universal features of the separation unsteadiness by examining data from wind tunnel experiments, flight test experiments, and well-resolved large-eddy simulation. We compare the results to a reduced-order model of shock

^{*}Senior Aerospace Engineer, AFRL/RQHF. Associate Fellow AIAA.

[†]Research Aerospace Engineer, AFRL/RQHF. Member AIAA.

[‡]Principal Aerospace Engineer, AFRL/RQHF. Associate Fellow AIAA.

[§]Research Scientist. Member AIAA.

unsteadiness originally postulated by Plotkin,¹⁴ and recently derived from the integral momentum equation by Toubert and Sandham.¹⁵ We begin by presenting a brief overview of research on separation shock unsteadiness.

A. Experiments on Separation Unsteadiness

Although shock unsteadiness was noted by Bogdonoff¹⁶ in early flow visualisation experiments on separated turbulent boundary layers, Kistler¹⁷ was apparently the first to make a systematic study of separation shock unsteadiness. In a study of a forward-facing step flow, he observed an intermittent wall-pressure signal, in which fluctuations due to turbulence in the incoming boundary layer and in the separation bubble appeared alternately as the separation shock moved back and forth across a transducer mounted on the wall ahead of the step. This behavior has now been observed in wind tunnel experiments for a variety of experimental configurations at Mach 2–5, including diffusers, ramps, flares, sharp fins, and cylinders/blunt fins.^{10, 13, 18–33} Similar results have also been obtained in experiments in quiet wind tunnel facilities³⁴ and in flight experiments.³⁵

The position of the separation shock foot has been inferred from the intermittency of the wall-pressure signal using the nested boxcar conversion technique. (This is a method of signal analysis that determines the time-history of the shock position from data obtained simultaneously from a streamwise array of pressure transducers at the wall.³⁶) Statistics based on this technique indicate that, for a broad range of interactions, the root-mean-square shock speed is $U_s/U_\infty \approx 0.03$, and the maximum shock crossing frequency is $f_c L_i/U_\infty \approx 0.02$, where L_i is the length of the region where the intermittent pressure signal is observed.^{13, 32} This frequency is typically an order of magnitude lower than the characteristic frequency U_∞/δ of the large-scale, organized structures in the incoming turbulent boundary layer. The spectrum of the shock position time-history is monotonic, and most of the energy appears at relatively low frequency (below a few kHz). Further, conditional cross-correlations and conditional averages, of wall pressure data based on shock position, indicate that the separation bubble undergoes a coherent, large-scale expansion and contraction.^{37, 38}

Although most of the energy in the shock motion is concentrated at relatively large length- and time-scales, significant motion at smaller scales is also observed in experiments. Shock wrinkling, for example, has been detected over a broad range of length scales using a spanwise array of pressure transducers.^{39, 40} Conditional averages of pressure fluctuations in the incoming boundary layer, based on shock motions downstream, have shown that δ -scale organized structures are responsible for small-scale motions of the separation shock foot, but no direct link has been found between the boundary layer structures and large-scale shock motions.⁴¹

Flow visualization techniques have provided a complement to fluctuating wall pressure measurements. Kussoy *et al.*²² used cinematic shadow photography to visualize the large-scale motion of the separation bubble and λ -shock system in a three-dimensional separated flow. Simultaneous laser velocimetry and measurements of wall-pressure fluctuations showed that the expansion and contraction of the recirculating zone in the velocity field and the rise in wall pressure were synchronized with the motion of the front leg of the λ -shock system. The rear leg of the shock system was observed to move in the opposite direction from the front leg, for an overall expansion and contraction motion.

Planar laser visualisation methods have revealed the smaller-scale shock distortion. In an early experiment of this kind, Smith⁴² studied a compression ramp flow using Rayleigh scattering from nm-scale particles of condensate. He noted both splitting of the separation shock and a tendency for the shock to wrap around large-scale structures in the incoming turbulent boundary layer. Similar results were later obtained with this technique in a variety of shock / boundary layer interactions,^{43, 44} and related work, using direct seeding with an ethanol fog, has been carried out.⁴⁵ Imaging at MHz-rates of compression ramp flows at Mach 2.5 reveals the distortion of the separation shock as large structures convect through it, and its subsequent return, after the structures pass, to the position imposed by the background flow.⁴⁶

A recent development in the field has been the experimental observation by Ganapathisubramani *et al.*,^{47–49} through particle image velocimetry and laser scattering visualization, of structures in the incoming turbulent boundary layer with an extremely long streamwise length scale, $\ell > 40\delta$. These elongated structures seem to be correlated with large-scale motion of the separation shock. They have been observed in another experimental facility by Humble *et al.*,^{50, 51} but the question of whether these structures are the product of particular experimental facilities or are a universal feature of turbulent boundary layers remains open. Because they appear in the streamwise velocity field but not the spanwise velocity field, the structures are more likely to be hairpin packets or turbulent superstructures than Görtler vortices. Nonetheless, these

structures offer a possible mechanism for driving the large-scale separation bubble unsteadiness.

B. Computational Simulation of Separation Unsteadiness

The computational resources necessary for large-eddy simulations of separated, turbulent flows have only become available in about the last fifteen years. Possibly the first (very) large eddy simulation of a shock-wave / boundary-layer interaction was carried out by Hunt and Nixon,⁵² who computed a Mach 2.8, $Re_\delta = 10^6$, 24° compression ramp flow on a coarse mesh (4×10^5 cells) using a subgrid-scale model. Later, Urbin *et al.*⁵³ computed a Mach 3, $Re_\delta = 2 \times 10^4$, 25° compression corner using an implicit large-eddy simulation approach with 4×10^6 cells.

Well-resolved large-eddy simulations were first reported in the literature around the turn of the millenium, but these computations did not predict the experimentally observed large-scale separation unsteadiness. Adams^{54,55} studied an 18° compression ramp flow at $M = 3.0$ and $Re_\theta = 2 \times 10^3$, using a computational mesh of about 15×10^6 cells. Rizzetta *et al.*^{56,57} computed compression ramp flows under similar conditions, for ramp angles of 8° – 24° . Rizzetta and Visbal⁵⁷ appear to have been the first to capture the pressure plateau that is characteristic of separation. Garnier *et al.*⁵⁸ and Teramoto⁵⁹ computed reflected shock interactions at $M = 2.3$.

As greater computational resources became available, it became possible carry out computations over sufficiently long physical time scales to observe large-scale unsteadiness. Pirozzoli and Grasso⁶⁰ computed a reflected shock interaction at $M = 2.3$ and $Re_\theta = 4 \times 10^3$, with a mesh of about 75×10^6 cells. Their wall pressure spectra (their Figs. 20 and 22) resemble experimental data. Loginov *et al.*⁶¹ computed a compression ramp interaction at $M = 3.0$ and $Re_\theta = 5 \times 10^3$ using about 19×10^6 cells. Indications of large-scale shock motion were observed, and fairly good agreement was obtained with experiment. Wu and Martín^{62,63} carried out a computation of a 24° compression ramp flow for $M = 2.9$ and $Re_\theta = 2 \times 10^3$, with about 21×10^6 total cells in the computational mesh. The basic results compared well with experiment. Some evidence of separation shock motion was evident in wall pressure time-histories and spectra (their Figs. 25–26).

Even greater fidelity has become possible in the last five years, as the computational resources have become available to run calculations out to physical times that are one to two orders of magnitude larger than the characteristic separation bubble time scale. Priebe *et al.*⁶⁴ studied a reflected shock interaction at $M = 2.9$ and $Re_\theta = 2 \times 10^3$ with a computational mesh of about 23×10^6 cells. Wall pressure time-histories show indications of the classic ‘boxcar’ signal, and spectra capture some of the low-frequency peak (their Fig. 11). Toubert and Sandham^{65,66} computed reflected shock interactions with Mach 1.7–2.3, $Re_{\delta 1} = 1 \times 10^4$ – 2×10^4 , and wedge angle 6–8 degrees using grids of 3×10^6 – 19×10^6 cells. They obtained power spectra that looked much like the experimental data (see Fig. 17 of Ref. 65), and all cases showed evidence of low-frequency shock oscillation. Bisek *et al.*^{67,68} have obtained analogous results for a 24° compression ramp flow ($M = 2.3$, $Re_\theta = 5 \times 10^3$, 13×10^6 – 190×10^6 cells), and Mullenix and Gaitonde⁶⁹ for a reflected shock interaction ($M = 2.3$, $Re_\theta = 3 \times 10^3$, 20×10^6 – 66×10^6 cells).

Experiments¹⁰ have indicated, however, that fluctuations occur in an even lower frequency range than has been resolved in recent large-eddy simulations, with significant energy content as low as 10 Hz. This observation motivates exploration of alternative computational approaches. Edwards *et al.*⁷⁰ carried out a hybrid RANS/LES calculation of a 28° compression corner at Mach 5, $Re_\delta = 9 \times 10^5$ using 7×10^6 – 9×10^6 cells. They obtained evidence of large-scale shock motion, and their power spectra looked much like experimental results. They also saw evidence of the influence of long, streamwise boundary layer structures on the shock motion. Garnier⁹ studied a reflected shock interaction using detached eddy simulation, focusing on the effect of corner flows on the interaction and its unsteadiness. He concluded that the presence of corner separation reduced the effective width of the wind tunnel and strengthened the interaction, and also generated vertically-oriented vorticity. These results suggest that large-scale three-dimensionality may interact strongly with large-scale unsteadiness, and this possibility warrants continued investigation.

C. Analytical Models of Separation Unsteadiness

One of the earliest attempts to understand separation shock unsteadiness was made by Trilling.² He first developed a simplified steady-flow model of the interaction of a boundary layer with an oblique shock wave, and then applied an unsteady perturbation. The separation streamline was represented as a straight line with superposed sinusoidal disturbances, and the model included supersonic potential flow together with the jump

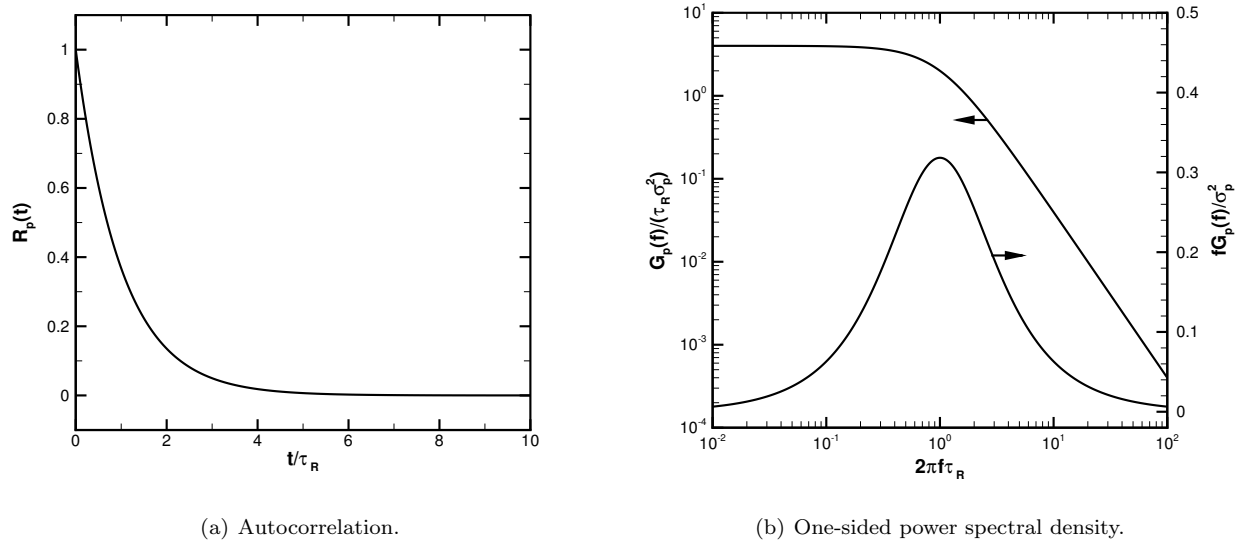


Figure 1. Statistics of pressure fluctuations predicted by the Plotkin¹⁴ theory.

conditions across the oblique shock. Trilling obtained a set of critical frequencies and shock strengths that gave neutrally-stable self-sustaining oscillations. Although the discrete frequencies predicted by the model are not observed experimentally, more recent studies have emphasized the importance of the separated shear layer in setting the characteristic time scales of the interaction.^{6,71}

Related studies have addressed the effect of freestream disturbances on shock waves. For example, Hui⁷² studied the effect of such disturbances on a wedge flow. Using small disturbance theory, he showed that freestream disturbances distorted the oblique shock, which led to downstream disturbances that reflected back and forth between the shock and the wedge surface (see Hui's Fig. 1). Such disturbances are visible in modern large-eddy simulations,⁵⁶ and probably have an influence on the overall interaction unsteadiness.

A very different analytical approach was adopted by Plotkin,¹⁴ who developed a reduced-order model of the motion of the separation bubble and its associated shock system. We will compare the predictions of this model to data from wind tunnel, flight, and numerical experiments in the present paper, and therefore give a relatively detailed outline of the theory here.

For simplicity, Plotkin considered a one-dimensional model of streamwise shock motion (or equivalently separation bubble motion). The shock velocity \dot{x} was taken to be the superposition of a random forcing function u and a restoring velocity that is proportional to the displacement x of the shock from its equilibrium position:

$$\dot{x} = u(t) - x/\tau_R \quad (1)$$

Here t is time, and τ_R is a constant (with units of time) specifying how rapidly the shock recovers from a perturbation. The variables x and u are defined to have zero mean. This stochastic ordinary differential equation represents a reduced-order model of the interaction of the separation bubble with the incoming turbulent flow.

For a given history of velocity perturbations, Eq. (1) can be solved to give the resulting time-history of shock position. Assuming that $x(0) = 0$, the solution can be put in the form:

$$x = \int_0^t u(\xi) \exp\left(-\frac{\xi-t}{\tau_R}\right) d\xi \quad (2)$$

Plotkin used Eq. (2) to relate the statistical properties of the shock motion to those of the fluctuations in the turbulent boundary layer.

The integral time scale of the auto-correlation was used to quantify the relative time scales of the incoming turbulence and the shock response. This scale is defined as:

$$\tau_i = \int_0^\infty R_i(\tau) d\tau \quad (3)$$

where i is replaced by u , x , or p to indicate the auto-correlation of the fluctuations in the turbulent boundary layer, the shock position, or the wall pressure fluctuations. (The auto-correlation function is defined in the usual manner for time-series data.) Assuming that the shock response is much slower than the turbulent fluctuations ($\tau_R \gg \tau_u$), Plotkin found an approximate expression for the mean square shock excursion at large time ($t \gg \tau_u$):

$$\overline{x^2} = \overline{u^2} \tau_u \tau_R \quad (4)$$

where an overbar indicates a time average. From the same assumptions, he also derived the following simplified forms for the auto-correlation and the power spectrum of the shock position:

$$R_x(t) = e^{-t/\tau_R} \quad (5)$$

$$\frac{G_x(f)}{\overline{x^2} \tau_R} = \frac{4}{1 + (2\pi f \tau_R)^2} \quad (6)$$

Note that the approximation requires that $t \gg \tau_u$ and $f \ll 1/(2\pi\tau_u)$. Equations (4)-(6) are the fundamental results of Plotkin's theory. At this level of approximation, the auto-correlation and spectrum of the shock position are independent of the detailed statistical properties of the boundary layer turbulence, and the integral time scale of the shock position is the same as the time constant of the restoring velocity: $\tau_x = \tau_R$.

Plotkin went on to assume that the pressure distribution induced by the oscillating shock can be approximated by the mean pressure distribution translated to the instantaneous shock position. Expanding the mean pressure distribution in a Taylor series about the mean shock location, and retaining terms through first order, he showed that the mean square fluctuating pressure is proportional to the mean square shock excursion:

$$\overline{p'^2} = \left(\frac{\partial \bar{p}}{\partial x} \right)^2 \overline{x^2} = \left(\frac{\partial \bar{p}}{\partial x} \right)^2 \overline{u^2} \tau_u \tau_R \quad (7)$$

where a prime indicates the fluctuating component of the pressure. Further, the auto-correlation and power spectrum of the wall pressure fluctuations have the same form as those of the shock position:

$$R_p(t) = e^{-t/\tau_R} \quad (8)$$

$$\frac{G_p(f)}{\overline{p'^2} \tau_R} = \frac{4}{1 + (2\pi f \tau_R)^2} \quad (9)$$

The integral time scales of pressure and shock position are the same under this approximation: $\tau_p = \tau_x = \tau_R$. The form of Eq. (8) is shown in Fig. 1a, and that of Eq. (9) in Fig. 1b. (In the plots, the notation $\sigma_p^2 = \overline{p'^2}$ is used.)

An alternative, pre-multiplied form of the spectrum is often plotted on semi-logarithmic axes in the literature on shock unsteadiness. In that case, Eq. (9) takes the alternative form:

$$\frac{f G_p(f)}{\overline{p'^2}} = \frac{4 f \tau_R}{1 + (2\pi f \tau_R)^2} \quad (10)$$

The form of Eq. (10) is shown in Fig. 1b. A nice feature of this form is that the spectral function has a maximum at $2\pi f_p \tau_R = 1$, which can be used to identify the characteristic time scale τ_R from experimental data.

Although Eq. (1) is linear, some of the underlying nonlinearity of the interaction is incorporated in τ_R , the restoring time-scale.^{15,73} Plotkin's model mimics the way in which broad-band perturbations in the incoming flow lead to low-frequency motion of the separation bubble and its associated shock system. In this way, the model incorporates some of the nonlinear aspects of the interaction of organized turbulent structures and a shock in a separated flow.

Recently, Touber and Sandham¹⁵ have addressed some of the *ad-hoc* assumptions of the Plotkin model. They derived the model of shock unsteadiness from the momentum integral equation, using data from large-eddy simulation as a guide in neglecting small terms. They have thus provided a physical and mathematical basis for Plotkin's assumptions. Their results also offer a means of predicting the characteristic time scale τ_R from first principles.

An alternative approach for predicting the separation bubble time scale was developed by Piponniau *et al.*⁷¹ The analysis was based on mass conservation for the separation bubble. They related the separation bubble Strouhal number to mixing layer growth rate parameters, and provided an explanation for the reduction from the incompressible value ($fL/U_\infty \approx 0.12$) to the high Mach number value ($fL/U_\infty \approx 0.03$).

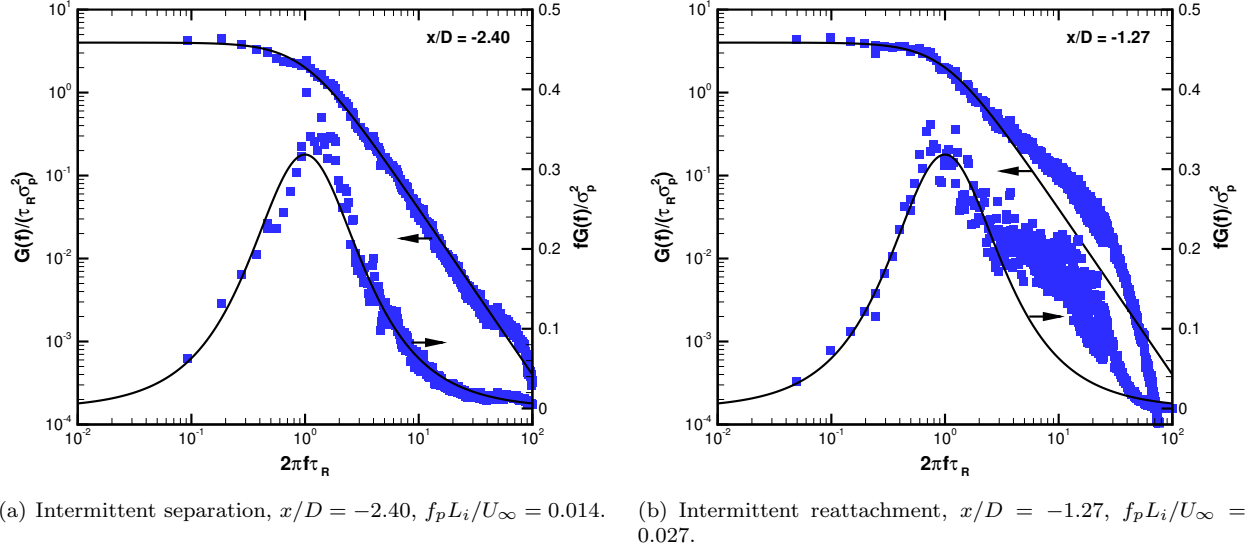


Figure 2. Comparison of the Plotkin model to measurements in a Mach 3 blunt fin flow: power spectral density.

D. Present Work

Here we compare spectral data obtained from wind tunnel experiments,^{13,25,74} the HIFiRE-1 flight test,³⁵ and large-eddy simulations^{15,67} with the predictions of Plotkin's model of shock unsteadiness. We also compare experimental wall-pressure time-histories obtained in a pulsed blowing experiment⁷⁵ to the instantaneous predictions of Plotkin's model.

II. Wind Tunnel Experiments

Equations (8), (9), and (10) have been shown to be a good fit^{14,15,73,76} to pressure fluctuation data from wind tunnel experiments.^{10,13,25,36,73} The characteristic frequency scales lie in the range $f_p L_i / U_\infty = 0.01$ – 0.03 for a variety of separated flows, where $f_p = 1/(2\pi\tau_R)$, U_∞ is the freestream speed, and L_i is the interaction length scale defined in terms of intermittency or separation zone length. Here we summarize some of those results.

The first set of measurements considered here was obtained by Evans et al.⁷⁴ in the Princeton University 8 in by 8 in, Mach 3 wind tunnel. The nondimensional test conditions corresponded to $M_\infty = 2.9$ and $Re_\theta = 8 \times 10^4$. The nominal freestream conditions were $p_\infty = 23$ kPa, $T_\infty = 96$ K, and $U_\infty = 565$ m/s, and the incoming tunnel wall boundary layer thickness was $\delta = 28$ mm ($\theta = 1.2$ mm). The test article was an unswept blunt fin, mounted perpendicular to the wind tunnel floor at zero angle of attack. The fin was 127 mm long and 122 mm high, and the leading edge was a half-cylinder of 19 mm diameter.

In the experiments, measurements of wall pressure fluctuations were made along the symmetry line of the fin. Power spectra corresponding to two measurement stations are shown in Fig. 2, in both log-log form (Eq. (9), left axis) and semi-log form (Eq. (10), right axis). The spectra in Fig. 2a correspond to the station $x/D = -2.40$, and those in Fig. 2b correspond to $x/D = -1.27$. (Here x is measured downstream from the nose of the fin, and $D = 19$ mm is the fin thickness.) The two stations are respectively representative of intermittent separation and reattachment, and a local maximum in the intensity of the pressure fluctuations occurs at both locations.

For the upstream station (Fig. 2a), the theoretical spectrum is a good fit to the experimental data over more than two decades of normalized frequency. The experimental data depart from the model for frequencies greater than $2\pi f\tau_R \approx 50$, where Plotkin's approximation $f \ll 1/(2\pi\tau_u)$ fails to hold. Similar results are obtained for the downstream station (Fig. 2b), but the agreement holds over a shorter range of frequency, with departure from the model for frequencies greater than $2\pi f\tau_R \approx 2$.

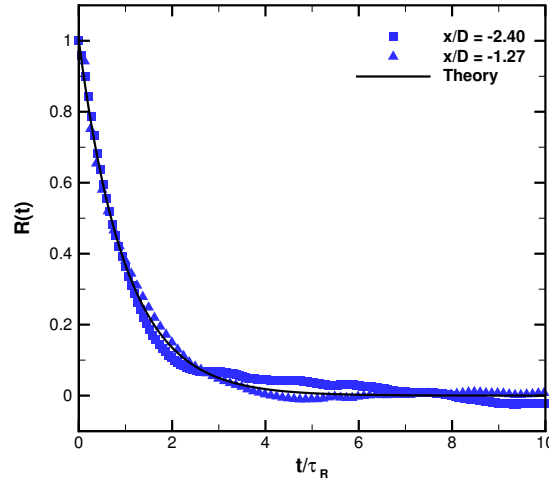


Figure 3. Comparison of the Plotkin model to measurements in a Mach 3 blunt fin flow: autocorrelations.

For both cases, the characteristic frequency was obtained from the maximum in the semi-log form of the plots. For the downstream case, the scale of the pressure fluctuation intensity has been adjusted to $\sigma_p^2 = 0.87 \overline{p'^2}$ to match the data to the theory. Assuming an interaction length scale of $L_i = 0.8 D$, the nondimensional characteristic frequencies are $f_p L_i / U_\infty = 0.014$ and $f_p L_i / U_\infty = 0.027$ for the two stations.

The corresponding auto-correlations are shown in Fig. 3. Again, good agreement between the measured and predicted auto-correlation is observed for both cases. (Note that the use of a four-pole Butterworth filter in the experiments may lead to some problems with time domain statistics. The Butterworth filter produces excellent passband flatness, but relatively poor phase characteristics. See Horowitz and Hill,⁷⁷ pp. 153–155.)

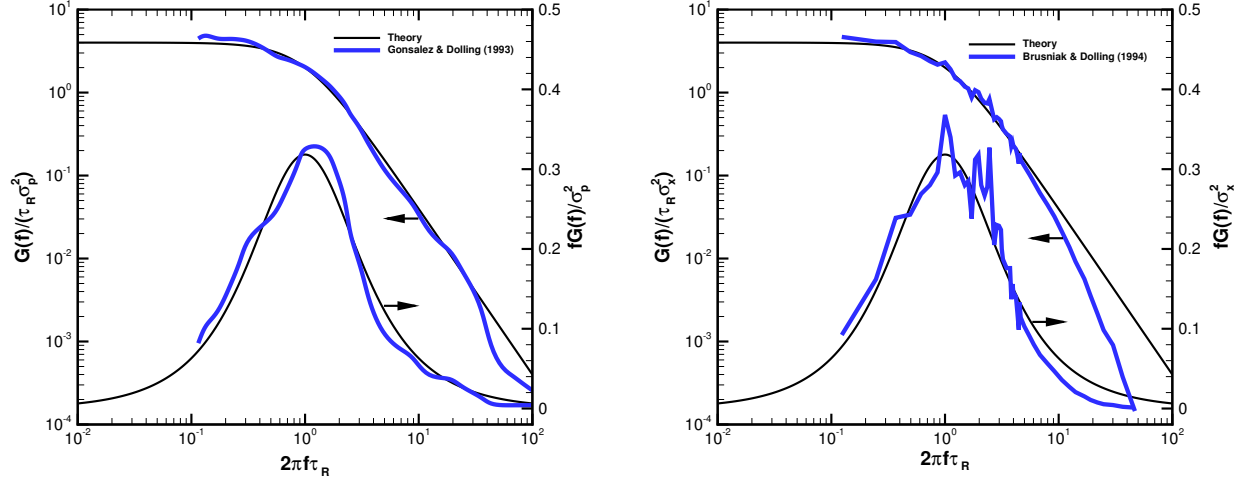
Two additional data sets are considered here, both obtained in the Mach 5 wind tunnel at the University of Texas at Austin. The nondimensional test conditions corresponded to $M_\infty = 5.0$ and $Re_\theta = 3 \times 10^4$. The nominal freestream conditions were $p_\infty = 4.6$ kPa, $T_\infty = 59$ K, and $U_\infty = 762$ m/s, and the incoming tunnel wall boundary layer thickness was $\delta = 15$ mm ($\theta = 0.66$ mm). The test articles were unswept blunt fins, with leading edge diameters of 6.4 mm to 19 mm. The fin heights were 76 mm to 102 mm, and the fin lengths 127 mm to 151 mm.

Gonsalez and Dolling¹³ were able to collapse wall pressure spectra obtained in these flows using a nondimensional frequency of the form $f L_i / U_\infty$, where $L_i = 0.8 D$. Data from the universal curve presented in their Fig. 18 were digitized and compared to the Plotkin model. The experimental station lay near the 50% intermittency point. The results are shown in Fig. 4a. The nondimensional characteristic frequency used to fit the spectrum is $f_p L_i / U_\infty = 0.011$. Again, good agreement is obtained between the experimental data and the Plotkin model. A good fit is obtained over almost three decades of nondimensional frequency.

Brusniak and Dolling²⁵ used a method of signal analysis called the nested boxcar conversion technique to transform a set of pressure time-histories at different streamwise stations into a time-history of shock position. A comparison of Eq. (6) to their experimental shock position spectrum for the 19 mm diameter fin is made in Fig. 4b. Again, good fit is obtained over about two decades of nondimensional frequency. The relatively rapid roll-off of the experimental data at high frequency may be a result of the limited spatial resolution of the nested boxcar technique.

One objection to the Plotkin model has been that the agreement between Eqs. (8)-(9) and the experimental data may be a result of the character of the random ‘boxcar’ pressure signal rather than the mechanism proposed by Plotkin. (See pp. 332–333 of Smits and Dussauge.⁷⁸) The boxcar pattern in the wall pressure signal is a result of pressure jumps as the shock translates back and forth over a given transducer station. (This will be discussed further in conjunction with Fig. 17.) Such jumps are not present in the shock position time-history, so the good agreement between measurements and Eq. (6) for the shock position spectrum (Fig. 4b) offers a rebuttal to this objection.

An additional data set of interest are the hot-film measurements made by Weiss and Chokani³⁴ in



(a) Wall pressure fluctuations, $f_p L_i / U_\infty = 0.011$. Data from Fig. 18 of Ref. 13. (b) Shock position, $f_x L_i / U_\infty = 0.007$. Data from Ref. 25.

Figure 4. Comparison of the Plotkin model to measurements in Mach 5 blunt fin flows.

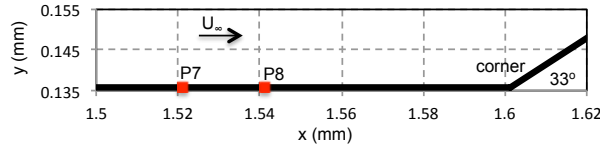


Figure 5. Transducer stations for the HIFiRE-1 fluctuating wall pressure measurements. Station P7: $x = 1.5213$ m; Station P8: $x = 1.5413$ m. The station $x = 0$ corresponds to the nose of the flight test vehicle.

a 24 deg compression ramp flow in the Mach 3.5 Supersonic Low Disturbance Wind Tunnel at NASA Langley Research Center. It is unfortunately not possible to directly compare the Plotkin model their measurements; the authors note that the “shape of the spectra should be only interpreted qualitatively, because the frequency response of hot-film anemometers is generally not flat up to the cutoff frequency” (Ref. 34, p. 2354). Nonetheless, the quiet tunnel results are qualitatively consistent with other wind tunnel experiments, and only small differences were observed by Weiss and Chokani between the results obtained in quiet flow and in conventional tunnel operation.

III. Flight Test Experiments

The experiments considered here were performed as part of Flight 1 of the Hypersonic International Flight Research Experimentation (HIFiRE) program, carried out by the Air Force Research Laboratory (AFRL) and the Australian Defence Science and Technology Organisation (DSTO). This flight test (HIFiRE-1) occurred on March 22, 2010 at Woomera Prohibited Area, Australia. The test article consisted of a 1.1 m long, 7 deg half-angle cone, with 2.5 mm nose radius, followed by a 0.5 m long cylinder and a 33 deg flare. The cylinder/flare configuration generated a separated shock-wave / turbulent boundary-layer interaction. Additional information on the flight test is available in Ref. 79.

High-bandwidth pressure transducers mounted in the interaction region upstream of the flare recorded the fluctuating wall pressure during the flight. Two stations were considered for the present work, as illustrated in Fig. 5. These stations were selected because they gave clearly intermittent signals for portions of the flight and did not exhibit any signal saturation during the times considered. Station P7 was located 1.5213 m downstream of the nose of the flight vehicle, and Station P8, 1.5413 m downstream. Intermittent pressure signals were recorded at these stations during the ascent phase of the flight.

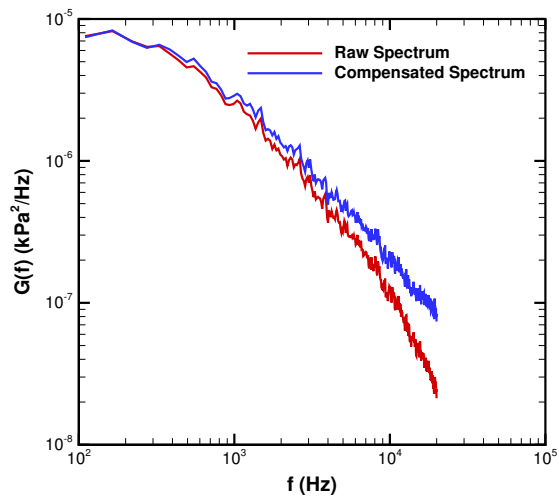
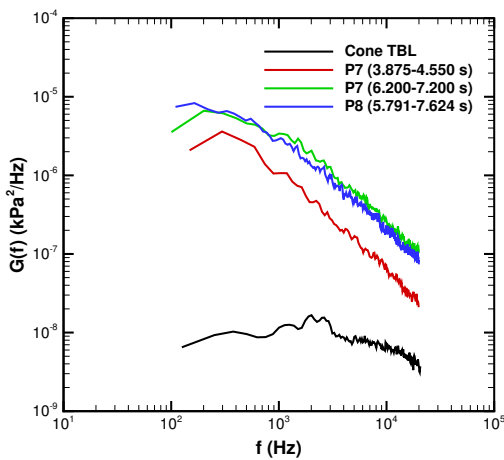
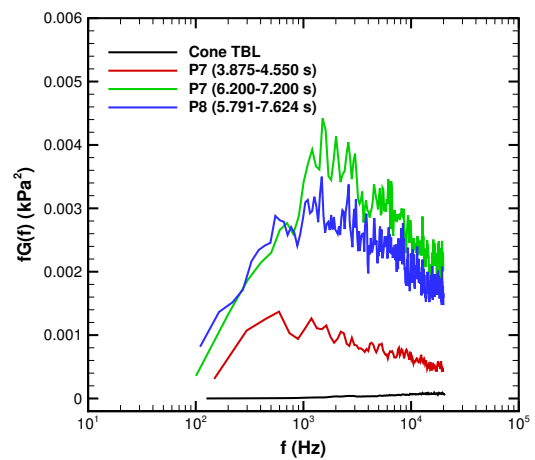


Figure 6. Compensation to account for effect of uneven sampling on spectra. Station P8, 5.991–7.624 s

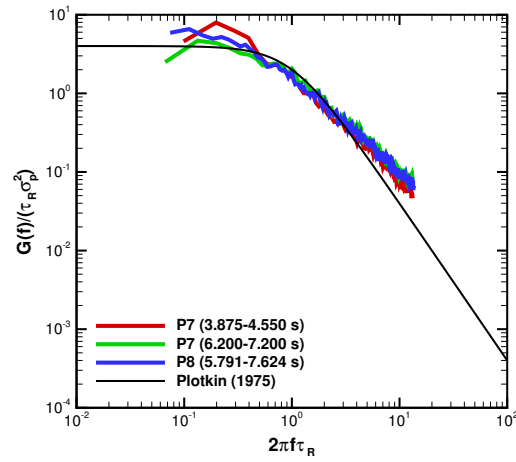


(a) Standard form.

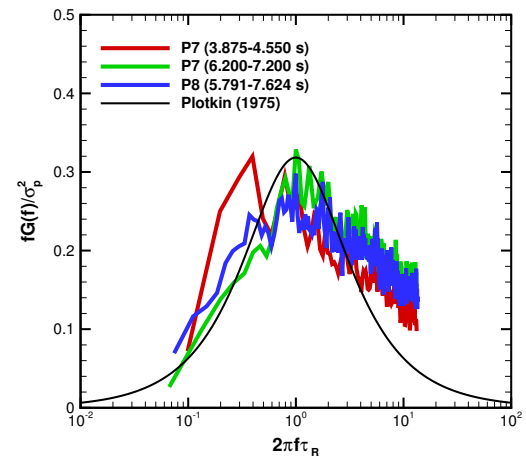


(b) Premultiplied, semi-log form.

Figure 7. Power spectral density of fluctuating pressure from HIFiRE-1 at several stages in the flight profile. Transducer locations identified in Fig. 5; trajectory point identified by flight time on plot.

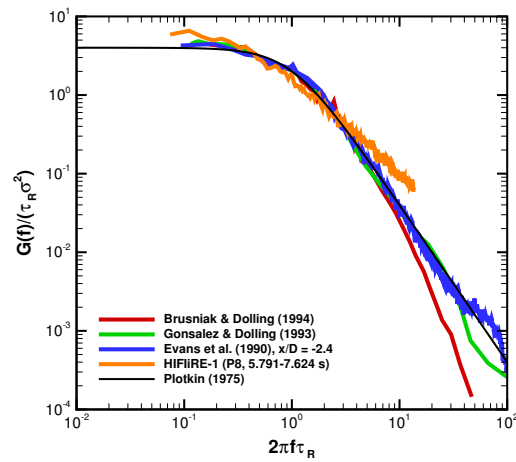


(a) Standard form.

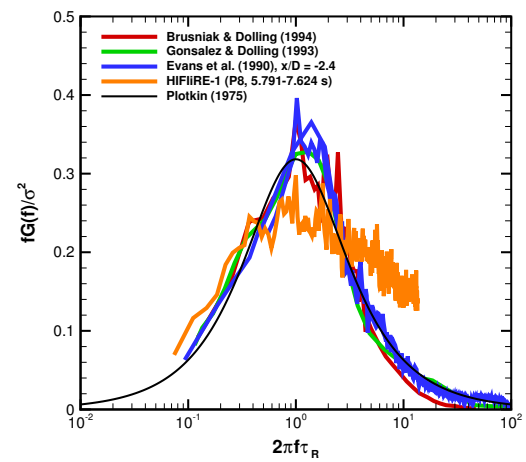


(b) Premultiplied, semi-log form.

Figure 8. Power spectral density from HIFIRe-1 flight test compared to Plotkin theory. Transducer locations identified in Fig. 5; trajectory point identified by flight time on plot. For all three cases, $f_p = 1.5$ kHz and $f_p \delta / U_\infty \approx 0.01$.



(a) Standard form.



(b) Premultiplied, semi-log form.

Figure 9. Spectra from several experiments collected and compared to the Plotkin model.

Time (sec)	Mach Number	Unit Reynolds Number (m^{-1})
3.870	2.14	4.26×10^7
4.550	2.61	4.95×10^7
6.200	3.43	5.57×10^7
7.200	3.25	4.71×10^7
5.791	3.41	5.80×10^7
7.624	3.19	4.44×10^7

Table 1. Freestream conditions for HIFiRE-1 flight tests, estimated from numerical computations.

The pressure signals were acquired using Kulite XCE-093 differential pressure transducers. The transducers were referenced to the payload internal pressure to avoid a large DC bias on the signal, and the signals were band-pass filtered between 100 Hz and 20 kHz. The transducers were sampled with a non-constant time interval to provide the maximum stable data throughput on the flight processors used for signal acquisition. The spectral analysis of unevenly sampled time series data is inherently nonlinear and requires special methods, as discussed in Stanfield and Kimmel.⁸⁰ The Nyquist frequency was 24.6 kHz for the sampling scheme used by the transducers mounted on the cylinder.

Significant errors occur when computing the Fourier transform of the unevenly sampled surface pressure data. This error occurs both when computing the Fourier transform directly by numerical integration and when using the least squares method, commonly referred to as the Lomb-Scargle method.^{80–82} These methods estimate the spectrum of the physical process convolved with the sampling function. The sampling function of unevenly spaced data has side-lobes caused by spectral leakage.^{81,82} Resampling the unevenly spaced pressure data onto an evenly spaced grid via linear interpolation eliminates side-lobe leakage from uneven sampling, but effectively low-pass filters the data. For the sampling scheme used, resampling significantly reduces the power spectral density at frequencies greater than 1 to 3 kHz. In this paper, the power loss caused by resampling the data onto an evenly spaced grid was compensated for using the procedures given by Stanfield and Kimmel.⁸⁰ For completeness, this method is summarized below.

The compensation method estimates and compensates for the spectral distortion created by resampling the data. A first-order autoregressive model is used to generate a time series with a power spectrum approximating the spectrum of the expected physical signal. The power spectrum of the autoregressive series is calculated analytically. The autoregression coefficients are used to generate an unevenly sampled time series, with a sampling function identical to that used to digitize the pressure data. This time series is in turn resampled via interpolation onto an evenly spaced temporal grid, using the same method and time intervals employed on the pressure signals. The power spectrum of the interpolated autoregressive series is then calculated. The ratio of the power spectrum of the interpolated autoregressive series to the analytically-derived power spectrum of the autoregressive series at each frequency provides a frequency-dependent gain factor. This gain factor is then applied to the power spectrum of the unevenly-sampled and interpolated pressure signal to compensate for the filtering effect of interpolation onto an evenly spaced grid. This method assumes that the spectral distortion created by the interpolation and resampling is identical for signals with similar spectra. This compensation changes the roll-off from about 9 dB/octave to about 8 dB/octave (see Fig. 6). Both values of roll-off are within the range that has been measured in similar wedge-induced turbulent shock boundary layer interactions.¹⁹

Figure 7 shows the power spectral density of fluctuating pressure from HIFiRE-1 for several situations on log-log (Fig. 7a) and semi-log (Fig. 7b) scales. Table 1 summarizes the flight conditions for the time windows shown in Fig. 7. For times prior to $t = 6$ seconds, the vehicle is accelerating under first stage boost. For $t > 6$ seconds, the vehicle is gaining altitude but decelerating during the unpowered coast phase following the first stage burn. The mean flow structure showed a slow evolution as flight conditions changed.³⁵ Generally, as the vehicle accelerated and Reynolds number increased, the size of the separated region decreased, and vice-versa. No direct measurements or calculations of boundary layer thickness for the times shown in the table are available, but Re_δ and Re_θ were estimated from computed boundary layer profiles provided by Yentsch (personal communication) for $x = 1.45$ m at $t = 5$ seconds. These calculations indicate $\delta = 7.7$ mm and $\theta = 4.8$ mm at this time. Re_δ and Re_θ are 3×10^5 and 2×10^5 , respectively, with edge values of $U_e = 976$ m/s and $Re_e = 4.87 \times 10^6$ per meter. The analog filter range of 100 Hz to 20 kHz under these

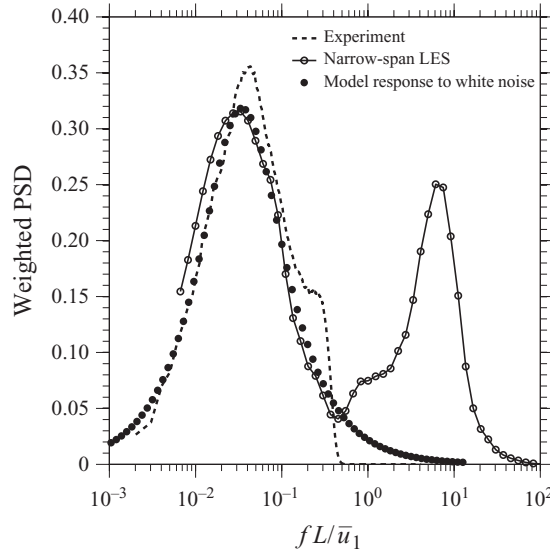


Figure 10. Power spectra (pre-multiplied, semi-log form) comparing the Plotkin model (filled symbols), large-eddy simulation (open symbols, Ref. 65), and experiment (dashed line, Ref. 10). (This is Fig. 15 on p. 449 of Ref. 15, reproduced under the terms of use published by Cambridge University Press for the reproduction of a single figure.)

conditions translates to nondimensional frequencies $f\delta/U_e$ of 8×10^{-4} to 0.16. Due to the combination of high Reynolds number and high edge velocities, this upper bound of non-dimensional frequency is lower than is typically achieved in wind tunnel experiments, but captures the important range of low-frequency fluctuations and their initial roll-off with frequency.¹⁹

For reference, the black curve illustrates the pressure spectrum obtained in the attached turbulent boundary layer on the upstream cone section of the flight vehicle at $x = 0.8563$ m. The remaining curves show results for intermittent pressure fluctuations at stations P7 and P8 just upstream of the flare segment of the vehicle, at times in the trajectory that are believed to correspond to intermittent separation at these stations. About two decades of frequency are captured in the spectra, and the results are qualitatively similar in form to those obtained in wind tunnel experiments. Consistent with wind tunnel results (Schmisser and Dolling,²⁶ for example), the undisturbed cone boundary layer spectrum, expressed in pre-multiplied semi-log form, shows little low frequency content compared to the spectra obtained in the region of separation shock motion.

The data from the region of intermittent separation are presented in Fig. 8, rescaled for comparison to Plotkin's model. Figure 9 shows an analogous comparison including all the experiments considered here. There is reasonable agreement between the theory, wind tunnel experiments, and flight experiments. The spectra measured in the HIFiRE-1 flight test roll off at a somewhat slower rate than that predicted by the Plotkin model and measured in wind tunnels. It is not clear whether this discrepancy is a result of the uneven sampling interval discussed previously, or whether it reflects a significant difference in the flow conditions between flight and wind tunnel tests. Nonetheless, the flight data show significant low-frequency unsteadiness that is in general agreement with wind tunnel data.

IV. Computations

In a recent article, Touber and Sandham¹⁵ have compared spectra derived from large-eddy simulations to the Plotkin model. Their results are reproduced here in Fig. 10. In this figure, the filled symbols represent the predictions of the Plotkin model, the dashed line represents the experimental results of Dupont *et al.*,¹⁰ and the open symbols indicate the results of Touber and Sandham's large-eddy simulations.⁶⁵ (The flow conditions were approximately $M = 2.3$ and $Re_\theta = 7 \times 10^3$, as reported by Dupont *et al.*¹⁰) Excellent agreement between the three curves is seen in the low-frequency regime, and the data from the large-eddy simulations depart from the Plotkin model at high frequency in a manner very similar to that observed for

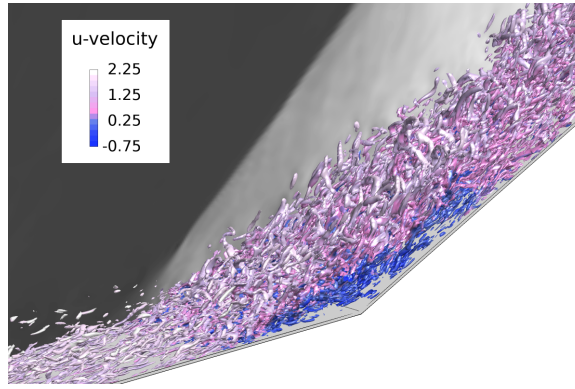


Figure 11. Contours of Q -criterion colored by streamwise velocity for a 24° compression ramp flow at $M = 2.3$ and $Re_\theta = 5 \times 10^3$. Back plane shows greyscale contours of pressure.

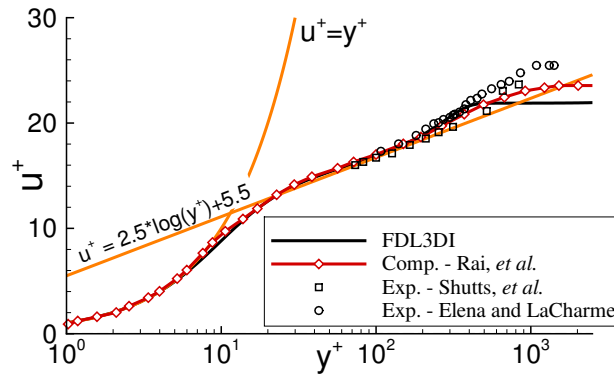


Figure 12. Mean streamwise velocity profiles using the Van Driest transform and presented in inner layer coordinates for $x/\delta_0 = 60$. Also plotted are computational results of Rai *et al.*,⁸³ and experimental measurements of Shutts *et al.*⁸⁴ and Elena and LaCharme.⁸⁵

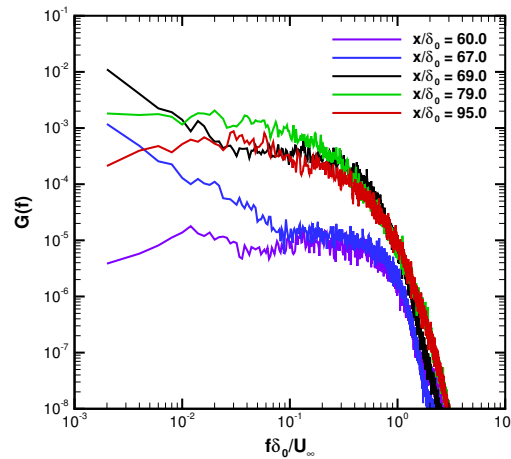


Figure 13. Power spectral density of fluctuation wall pressure illustrates low-frequency content captured by large-eddy simulation. Incoming boundary layer: $x/\delta_0 = 60$, separation: $x/\delta_0 = 67-69$, reattachment: $x/\delta_0 = 79$, redeveloping boundary layer: $x/\delta_0 = 95$.

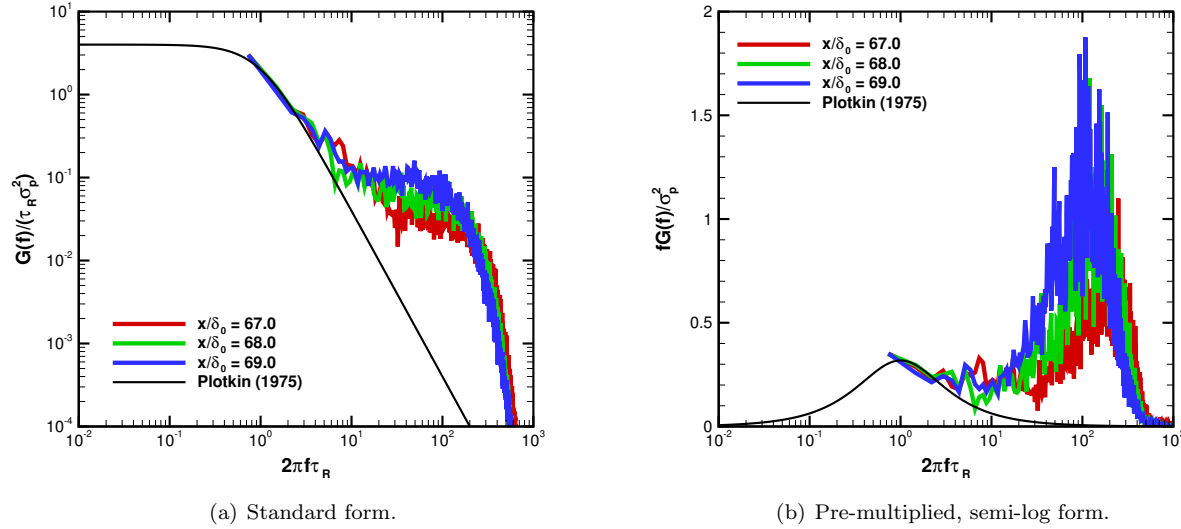


Figure 14. Computational spectra compared to the Plotkin theory ($f_p L_i / U_\infty = 0.03$).

experimental data. (For example, compare Fig. 10 to Fig. 2b.)

In order to obtain a smooth spectrum at high frequencies, Toubert and Sandham “processed the LES signals several times with an increasing number of segments and then reconstructed the entire frequency range to obtain the plots” (Ref. 65, p. 97). Further, only a few cycles of the lowest frequency reported on the plot were captured in the simulation. In recent work, the present authors have constructed similar spectra from computations, using conventional signal processing techniques⁸⁶ to generate the spectra, and carrying out long computations to capture many cycles of the low-frequency unsteadiness.

To this end, large-eddy simulations⁶⁷ of a Mach 2.3 flow over a 24 deg compression ramp were carried out using the Air Force Research Laboratory code FDL3DI. FDL3DI is a high-order, structured-grid solver for the ideal-gas Navier-Stokes equations. The code employs a high-order compact finite-difference approximation with a high-order low-pass spatial filter. The methodology in FDL3DI permits a seamless transition from implicit large-eddy simulation (ILES) to direct numerical simulation (DNS) as the resolution is increased.

Time integration of the conservation equations was carried out using a second-order implicit scheme, based on a three-point backward difference of the time terms. Approximate factoring and quasi-Newton subiterations were employed. The formulation is similar to the techniques of Beam and Warming⁸⁷ and Pulliam and Chaussee.⁸⁸ The implicit terms were linearized in the standard ‘thin layer’ manner, and a scalar pentadiagonal system of equations was solved for each factor. Three applications of the flow solver per time-step were employed for the present work.

Spatial discretization was carried out using a sixth-order compact difference scheme.^{89,90} Stability was enforced using a eighth-order, low-pass, Padé-type, non-dispersive spatial filter.⁹¹ Use of the filter has been shown to be superior to the use of explicitly added artificial dissipation for maintaining both stability and accuracy on stretched curvilinear meshes.⁹⁰ The filter was applied to the solution vector as a post-processing step following each sub-iteration. Filtering was applied sequentially along each of the three grid coordinate directions, and the order of these operations was permuted to avoid introducing bias in the solution.

The filter regularizes poorly-resolved features at the grid scale. It should also be noted that the filtering technique can be interpreted as an approximate deconvolution subgrid-scale (SGS) model,⁹² which is based on a truncated series expansion of the inverse filter operator for the unfiltered flow-field equations. Mathew *et al.*⁹³ have shown that filtering provides a mathematically consistent approximation of unresolved terms arising from any type of nonlinearity. Filtering regularizes the solution and generates virtual SGS model terms that are equivalent to those of an approximate deconvolution.

The computational domain consisted of a flat plate, followed by a 24 deg ramp. The flow and boundary conditions of the simulation were consistent with previous studies by Rai *et al.*,⁸³ Rizzetta and Visbal,⁹⁴ and Pirozzoli and Grasso,⁹⁵ which investigated supersonic flow on a flat plate at Mach 2.3.

The inflow boundary was specified using a solution to the compressible laminar boundary-layer equations,⁹⁶ with the inflow boundary-layer height scaled to the reference length, $\delta_0 = 6.096 \times 10^{-4}$ m, and freestream conditions applied outside the boundary-layer. Along the wall surface, a no-slip velocity boundary condition was imposed with an isothermal wall set to the nominal adiabatic wall temperature. The surface pressure was computed by enforcing a zero wall-normal derivative to third-order spatial accuracy.

The conditions for the incoming boundary layer were based on a 1955 experiment by Shutts *et al.* (Case 55010501 of Ref. 84). The nondimensional flow conditions were $M = 2.3$ and $Re_\theta = 5 \times 10^3$. The freestream conditions were $p_\infty = 23.8$ kPa, $T_\infty = 305$ K, and $U_\infty = 588$ m/s.

Large-eddy simulation of natural transition for supersonic wall-bounded turbulent flows is impractical for most configurations and flow conditions, so the present work used the counter-flow force trip developed by Mullenix *et al.*⁹⁷ This method has been shown to produced a steady broad-band disturbance which causes supersonic flow to undergo transition.

The character of the overall flowfield is illustrated in Fig. 11. The grey surface at bottom of the image represents the flat plate and the 24 deg ramp. Isosurfaces of the Q -criterion, colored by the streamwise component of velocity, mark organized structures in the turbulent flow. Dark blue indicates upstream flow, and highlights the region of separated flow near the corner of the ramp. The back plane includes greyscale contours of pressure to show the shock location.

For comparison to the experiments, the van Driest transformation⁹⁸ was applied to the mean streamwise velocity profile. The velocity was nondimensionalized in the form $u^+ = u_{vD}/u_\tau$, where u_{vD} is the transformed velocity and u_τ is the wall friction velocity. The profiles were plotted against the nondimensional inner coordinate $y^+ = y u_\tau / \nu_w$. Figure 12 shows the velocity profile for $x/\delta_0 = 60$, and includes the results of the boundary layer computations of Rai *et al.*⁸³ In addition to the experimental measurements by Shutts *et al.*,⁸⁴ the plotted experimental data include supersonic flow measurements of Elena and LaCharme,⁸⁵ which were collected under similar flow conditions. The numerical solutions are in good agreement with both the inner layer and logarithmic profiles.

Figure 13 shows the power spectral density of the fluctuating pressure for stations between $x/\delta_0 = 60$ and $x/\delta_0 = 95$ in the large-eddy simulations of the compression ramp flow. The large-eddy simulation was run for about 330 cycles of the large-scale motion (1045000 iterations, $U_\infty t / \delta_0 = 5.0 \times 10^3$, $t^+ = 2.0 \times 10^5$) in order to capture sufficient data to obtain statistical convergence of the spectra in the low-frequency range. Wall pressure data were saved every ten iterations of the computation, for a sampling interval of $U_\infty \Delta t / \delta_0 = 5.0 \times 10^{-2}$, and the spectra were computed by averaging 19 windows of 10000 points with 50% overlap. The station $x/\delta_0 = 60$ lies in the undisturbed boundary layer flow, and has little energy content at low frequency. Mean separation occurs at about $x/\delta_0 = 68$, and significant low-frequency energy content is observed for $x/\delta_0 = 67$ – 69 . Mean reattachment occurs near $x/\delta_0 = 79$. Farther downstream in the redeveloping boundary layer ($x/\delta_0 = 95$), the low frequency content begins to disappear.

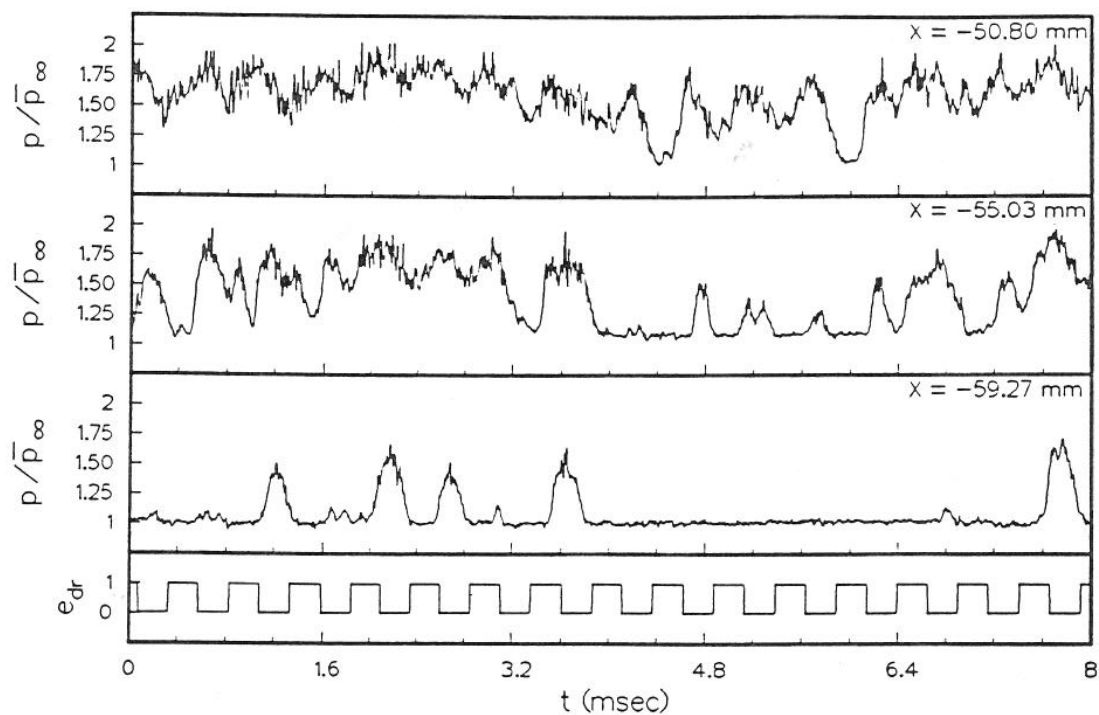
Figure 14 compares the results of the large-eddy simulations with the Plotkin model. The characteristic frequency corresponds to $f_p \delta_0 / U_\infty = 2.7 \times 10^{-3}$ or $f_p L_i / U_\infty = 3.0 \times 10^{-2}$, where $L_i = 11\delta_0$ is the streamwise length scale of the separated zone. The low-frequency shock unsteadiness is present in the computations, but runs for much longer physical time are required to fully resolve the spectrum.

V. Response of Separation Bubble to Pulsed Input

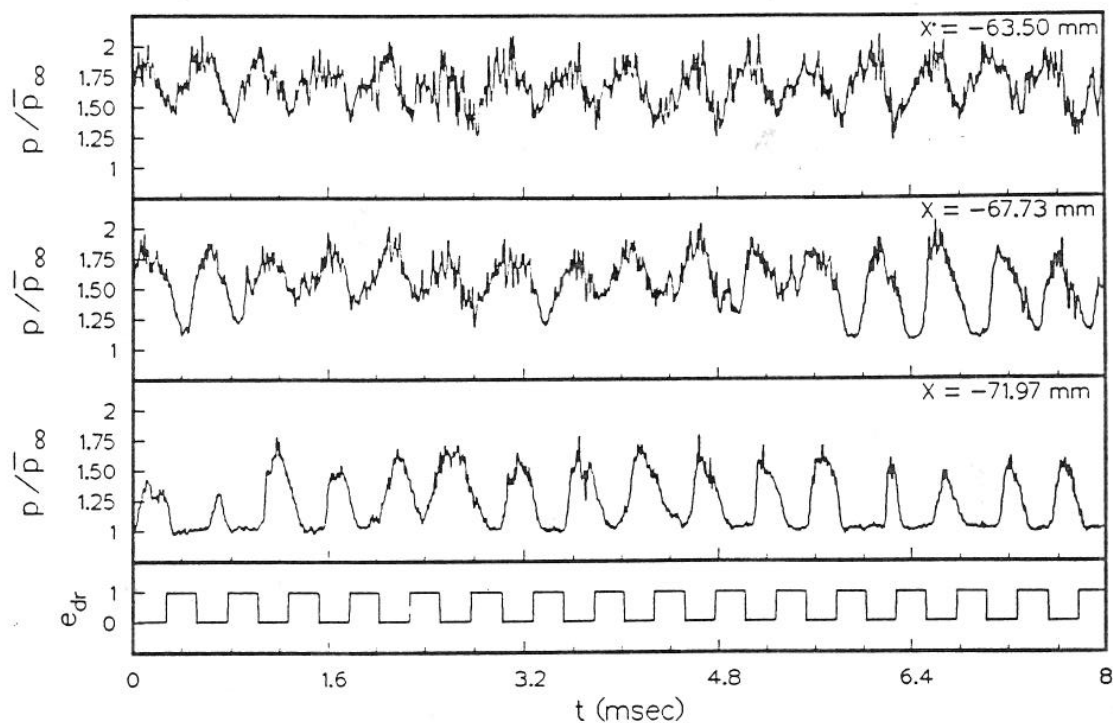
It is also of interest to examine the behavior of the separation bubble system in an instantaneous sense. Selig and Smits⁷⁵ carried out an experiment in which pulsed blowing through a spanwise slot in the wall was used to control a separated compression ramp flow. The experiments were carried out in the Princeton University 8 in by 8 in, Mach 3 wind tunnel. The nondimensional test conditions corresponded to $M_\infty = 2.9$ and $Re_\theta = 8 \times 10^4$. The nominal freestream conditions were $p_\infty = 23$ kPa, $T_\infty = 96$ K, and $U_\infty = 565$ m/s, and the incoming tunnel wall boundary layer thickness was $\delta = 26$ mm ($\theta = 1.3$ mm).

The experimental model was a 24 deg ramp, mounted on the wind tunnel floor. A rotating drum apparatus introduced periodic blowing through a spanwise slot in the wall. This siren-like device introduced a disturbance that was relatively uniform along the spanwise direction, at blowing frequencies of up to $f_0 = 5$ kHz.

Three stations for the blowing slot were considered: 0.0 mm, 25.4 mm, and 50.8 mm upstream of the corner. For comparison, the mean separation line was about 34 mm upstream of the corner for the baseline flow. Keeping in mind that blowing altered the position of separation, the first two cases can be considered



(a) Case B: blowing 25.4 mm upstream of corner. (Fig. 12 of Ref. 99.)



(b) Case C: blowing 50.8 mm upstream of corner. (Fig. 13 of Ref. 99)

Figure 15. Results from the experiments of Selig *et al.*^{75,99} (Figures used with permission of the copyright holder.)

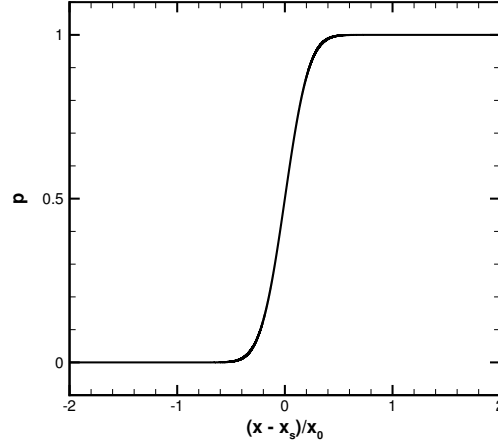


Figure 16. Model of translating pressure distribution.

roughly as perturbations to the separation bubble, and the final case a perturbation near the shock foot.

Figure 15 shows results from Cases B and C of the experiments. For both cases, the blowing frequency was $f_0 = 2$ kHz, and the blowing mass flux ratio was $(\rho U)_{\text{slot}}/(\rho U)_{\infty} = 0.09$. For Case B, the blowing slot was located 25.4 mm upstream of the corner (Fig. 15a), and for Case C, 50.8 mm upstream (Fig. 15b). Each group of plots consists of three simultaneous wall pressure time-histories at different stations upstream of the corner, along with the forcing function. (The forcing function has a value of one when blowing is on, and zero otherwise.)

In the absence of blowing, Selig and Smits found that shock crossing events occurred at random intervals for a given transducer station. Although blowing at the 0.0 mm and 25.4 mm stations caused changes to the flow, the shock unsteadiness was still not synchronized to the forcing. This result is illustrated in the wall-pressure time-histories shown in Fig. 15a. When the blowing slot was located farther upstream at 50.8 mm slot station, the shock motion was observed to lock into the forcing. The synchronization is illustrated in Fig. 15b.

It is interesting to examine whether this behavior can be replicated by the Plotkin model. To mimic the blowing in the experiment, consider a symmetric square wave forcing function of period $2T$:

$$u(t) = \begin{cases} +1 & \text{for } 0 \leq \hat{t} < T \\ -1 & \text{for } T \leq \hat{t} < 2T \end{cases} \quad (11)$$

where $\hat{t} = t \bmod 2T$. (A symmetric square wave, with zero mean, is convenient for use here. An analogous solution can easily be obtained for a function with values of zero and one.) The corresponding forcing frequency is $f_0 = 1/(2T)$.

For the forcing equation (11), the model ordinary differential equation (1) has the following periodic solution for the shock position:

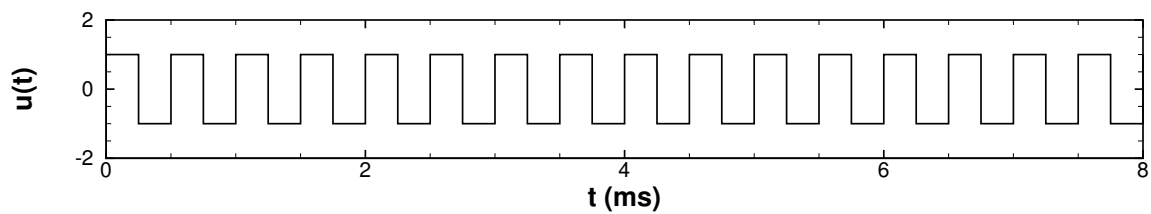
$$x_s(t) = \begin{cases} x_0 e^{-\hat{t}/\tau_R} + \tau_R (1 - e^{-\hat{t}/\tau_R}) & \text{for } 0 \leq \hat{t} < T \\ x_0 e^{-\hat{t}/\tau_R} + \tau_R (2e^{-(\hat{t}-T)/\tau_R} - 1 - e^{-\hat{t}/\tau_R}) & \text{for } T \leq \hat{t} < 2T \end{cases} \quad (12)$$

where the initial value:

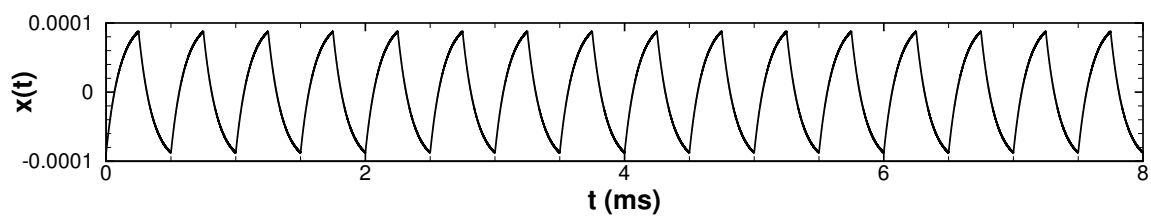
$$x_0 = -\tau_R \tanh\left(\frac{T}{2\tau_R}\right) \quad (13)$$

is chosen to make the solution periodic.

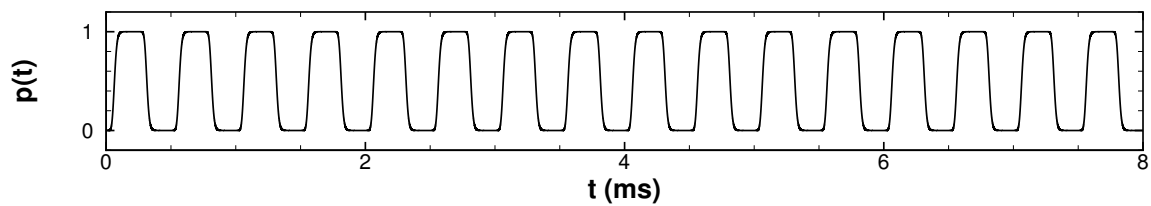
Following Plotkin's ideas, we convert the shock position function to an equivalent fluctuating wall pressure. Considering the conditionally-averaged pressure distributions from the experiments of Erenkil and



(a) Forcing function.



(b) Shock position.



(c) Pressure.

Figure 17. Response of separation bubble to square wave input: prediction of Plotkin model for $f_0 = 2.0$ kHz and $f_p = 1.5$ kHz.

Dolling,³⁸ we take the instantaneous pressure distribution to be a smooth function that translates back and forth with the shock, and take the scale over which the pressure rises to be about one-fourth the amplitude of the shock motion. Specifically, we assume the following functional form:

$$p(x, t) = \frac{1}{2} \left[\operatorname{erf} \left(\frac{x - x_s(t)}{x_0/4} \right) + 1 \right] \quad (14)$$

This function is illustrated in Fig. 16; it is qualitatively consistent with experiment.

Selig and Smits did not plot their spectra in a manner that allows the characteristic frequency to be easily identified. Dolling and Murphy¹⁸ studied essentially the same flow, however, and reported a characteristic shock crossing frequency of $f_p = 1.5$ kHz.

The predictions of Eqs. (11)–(14) are plotted in Fig. 17 for $f_0 = 2$ kHz and $f_p = 1.5$ kHz. Figure 17a shows the square wave input $u(t)$, Fig. 17b shows the predicted shock position $x_s(t)$, and Fig. 17c shows the corresponding wall pressure signal $p(0, t)$. The model is seen to be qualitatively consistent with the experiments (Fig. 15b). The shock position signal displays an interesting asymmetry, which is also sometimes seen in the experimental wall pressure data. The predicted wall pressure signal illustrates how the shock motion is converted into pressure jumps at given station on the wall, generating the typical ‘boxcar’ pressure trace.

VI. Discussion

Spectra of wall pressure fluctuations caused by separation shock unsteadiness were compared for data obtained from wind tunnel experiments, the HIFiRE-1 flight test, and large-eddy simulations. The flow conditions spanned the supersonic range and two orders of magnitude of Reynolds number. In order of Reynolds number, the cases examined here included: computations of a 24 deg compression ramp flow at $M = 2.3$ and $\operatorname{Re}_\theta = 5 \times 10^3$, wind tunnel experiments on blunt fin flows at $M_\infty = 5.0$ and $\operatorname{Re}_\theta = 3 \times 10^4$, wind tunnel experiments on blunt fin flows at $M_\infty = 2.9$ and $\operatorname{Re}_\theta = 8 \times 10^4$, and flight experiments on a 33 deg cylinder/flare at $M \approx 3$ and $\operatorname{Re}_\theta \approx 2 \times 10^5$. Despite the broad range of flow conditions, the spectra were qualitatively consistent, and could be cast in a common form in suitable nondimensional coordinates.

The experimental data were also compared with the predictions of a theory developed by Plotkin,¹⁴ which depicts the separation shock unsteadiness as linearly damped Brownian motion. This model, which has been derived from the integral momentum equation by Toubert and Sandham,¹⁵ describes the manner in which broad-band perturbations in the incoming flow lead to low-frequency motion of the separation shock. It predicts a universal form for the spectrum and autocorrelation of the pressure fluctuations. Relatively good agreement was obtained between the theory and data obtained from the flight tests, wind tunnel experiments, and large-eddy simulations.

Selig and Smits⁷⁵ introduced controlled disturbances into a separated compression ramp flow, and found that the shock motion was synchronized to the forcing when it was introduced near the shock foot, but not when introduced downstream of that location. Here we have shown that the Plotkin model responds to a periodic input in a similar manner to that observed experimentally for the synchronized case.

The results presented here support the idea that separation unsteadiness has common features across a broad range of compressible flows. It may be possible to exploit this in the design of high Mach number aircraft. Correlations for the form of the wall pressure fluctuation spectra are of interest for design against fatigue loading. Reduced-order models of the separation unsteadiness can assist in design decisions, and aid the development of feedback flow control systems.

VII. Acknowledgements

This work was supported in part by the Air Force Office of Scientific Research, under grants monitored by Dr. J. Schmisser. Computational resources were supplied by the Department of Defense Supercomputing Resource Centers at the Army Engineer Research and Development Center and at the Air Force Research Laboratory. The authors would like to thank Robert Yentsch of The Ohio State University for providing boundary layer and momentum thicknesses for the HIFiRE-1 flight conditions. Cleared for public release, distribution unlimited (88ABW-2013-2494, 28 May 2013).

References

- ¹Korkegi, R. H., "Survey of Viscous Interactions Associated with High Mach Number Flight," *AIAA Journal*, Vol. 9, No. 5, 1971, pp. 771–784.
- ²Trilling, L., "Oscillating Shock Boundary-Layer Interaction," *Journal of the Aeronautical Sciences*, Vol. 25, No. 5, 1958, pp. 301–304.
- ³Green, J. E., "Interactions Between Shock Waves and Turbulent Boundary Layers," *Progress in Aerospace Sciences*, Vol. 11, 1970, pp. 235–340.
- ⁴Perry, A. E. and Hornung, H., "Some Aspects of Three-Dimensional Separation, Part II: Vortex Skeletons," *Zeitschrift für Flugwissenschaften und Weltraumforschung*, Vol. 8, 1984, pp. 155–160.
- ⁵Dolling, D. S., "Unsteady Phenomena in Shock Wave / Boundary Layer Interaction," *Special Course on Shock Wave / Boundary Layer Interactions in Supersonic and Hypersonic Flows*, AGARD Report 792, Advisory Group for Aerospace Research and Development, NATO, Neuilly sur Seine, France, August 1993.
- ⁶Dussauge, J.-P., Dupont, P., and Debiève, J.-F., "Unsteadiness in Shock Wave Boundary Layer Interactions with Separation," *Aerospace Science and Technology*, Vol. 10, 2006, pp. 85–91.
- ⁷Clemens, N. T. and Narayanaswamy, V., "Shock / Turbulent Boundary Layer Interactions: Review of Recent Work on Sources of Unsteadiness," AIAA Paper 2009-3710, American Institute of Aeronautics and Astronautics, Reston VA, June 2009.
- ⁸Bruce, P. J. K., Burton, D. M. F., Titchener, N. A., and Babinsky, H., "Corner Effect and Separation in Transonic Channel Flows," *Journal of Fluid Mechanics*, Vol. 679, 2011, pp. 247–262.
- ⁹Garnier, E., "Stimulated Detached Eddy Simulation of Three-Dimensional Shock / Boundary Layer Interaction," *Shock Waves*, Vol. 19, 2009, pp. 479–486.
- ¹⁰Dupont, P., Haddad, C., and Debiève, J.-F., "Space and Time Organization in a Shock-Induced Separated Boundary Layer," *Journal of Fluid Mechanics*, Vol. 559, 2006, pp. 255–277.
- ¹¹Zuchowski, B., "Air Vehicle Integration and Technology Research (AVIATR) Delivery Order 0023: Predictive Capability for Hypersonic Structural Response and Life Prediction: Phase II – Detailed Design of Hypersonic Cruise Vehicle Hot-Structure," Final Report AFRL-RQ-WP-TR-2012-0280, Air Force Research Laboratory, Wright-Patterson AFB OH, May 2012, Approved for public release; distribution unlimited.
- ¹²Robertson, J. E., "Prediction of In-Flight Fluctuating Pressure Environments Including Protuberance Induced Flow," Report WR 71-10, Wyle Laboratories, Huntsville, AL, March 1971.
- ¹³Gonzalez, J. C. and Dolling, D. S., "Correlation of Interaction Sweepback Effects on the Dynamics of Shock-Induced Turbulent Separation," AIAA Paper 93-0776, American Institute of Aeronautics and Astronautics, Reston VA, January 1993.
- ¹⁴Plotkin, K. J., "Shock Wave Oscillation Driven by Turbulent Boundary-Layer Fluctuations," *AIAA Journal*, Vol. 13, No. 8, 1975, pp. 1036–1040.
- ¹⁵Touber, E. and Sandham, N. D., "Low-Order Stochastic Modelling of Low-Frequency Motions in Reflected Shock-Wave / Boundary-Layer Interactions," *Journal of Fluid Mechanics*, Vol. 671, 2011, pp. 417–465.
- ¹⁶Bogdonoff, S., "Some Experimental Studies of the Separation of Supersonic Turbulent Boundary Layers," Report 336, Aeronautical Engineering Department, Princeton University, Princeton, NJ, June 1955.
- ¹⁷Kistler, A. L., "Fluctuating Wall Pressure under a Separated Supersonic Flow," *The Journal of the Acoustical Society of America*, Vol. 36, No. 3, 1964, pp. 543–550.
- ¹⁸Dolling, D. S. and Murphy, M. T., "Unsteadiness of the Separation Shock Wave Structure in a Supersonic Compression Ramp Flowfield," *AIAA Journal*, Vol. 21, No. 12, 1983, pp. 1628–1634.
- ¹⁹Dolling, D. S. and Or, C. T., "Unsteadiness of the Shock Wave Structure in Attached and Separated Compression Ramp Flows," *Experiments in Fluids*, Vol. 3, 1985, pp. 24–32.
- ²⁰Bogar, T. J., "Structure of Self-Excited Oscillations in Transonic Diffuser Flows," *AIAA Journal*, Vol. 24, No. 1, 1986, pp. 54–61.
- ²¹Andreopoulos, J. and Muck, K. C., "Some new aspects of the shock-wave boundary layer interaction in compression ramp corner," *Journal of Fluid Mechanics*, Vol. 180, 1987, pp. 405–428.
- ²²Kussoy, M. I., Brown, J. D., Brown, J. L., Lockman, W. K., and Horstman, C. C., "Fluctuations and Massive Separation in Three-Dimensional Shock-Wave / Boundary-Layer Interactions," *Transport Phenomena in Turbulent Flows: Theory, Experiment, and Numerical Simulation*, edited by M. Hirata and N. Kasagi, Hemisphere, New York, 1988, pp. 875–887.
- ²³Selig, M. S., Andreopoulos, J., Muck, K. C., Dussauge, J. P., and Smits, A. J., "Simultaneous Wall-Pressure and Mass-Flux Measurements Downstream of a Shock-Wave / Turbulent Boundary-Layer Interaction," *AIAA Journal*, Vol. 27, No. 7, 1989, pp. 862–869.
- ²⁴Thomas, F. O., Putnam, C. M., and Chu, H. C., "On the Mechanism of Unsteady Shock Oscillation in Shock Wave / Turbulent Boundary Layer Interactions," *Experiments in Fluids*, Vol. 18, 1994, pp. 69–81.
- ²⁵Brusniak, L. and Dolling, D. S., "Physics of Unsteady Blunt-Fin-Induced Shock Wave / Turbulent Boundary Layer Interactions," *Journal of Fluid Mechanics*, Vol. 273, 1994, pp. 375–409.
- ²⁶Schmisser, J. D. and Dolling, D. S., "Fluctuating Wall Pressures near Separation in Highly Swept Turbulent Interactions," *AIAA Journal*, Vol. 32, No. 6, 1994, pp. 1151–1157.
- ²⁷Garg, S. and Settles, G. S., "Unsteady Pressure Loads Generated by Swept-Shock-Wave / Boundary-Layer Interactions," *AIAA Journal*, Vol. 34, No. 6, 1996, pp. 1174–1181.
- ²⁸Ünal, Ö. H. and Dolling, D. S., "Experimental Study of Causes of Unsteadiness of Shock-Induced Turbulent Separation," *AIAA Journal*, Vol. 36, No. 3, 1998, pp. 371–378.
- ²⁹Beresh, S. J., Clemens, N. T., and Dolling, D. S., "Relationship Between Upstream Turbulent Boundary-Layer Velocity Fluctuations and Separation Shock Unsteadiness," *AIAA Journal*, Vol. 40, No. 12, 2002, pp. 2412–2422.
- ³⁰Hou, Y. X., Ünal, Ö. H., Bueno, P. C., Clemens, N. T., and Dolling, D. S., "Effects of Boundary-Layer Velocity Fluctuations on Unsteadiness of Blunt-Fin Interactions," *AIAA Journal*, Vol. 42, No. 12, 2004, pp. 2615–2618.

- ³¹Bookey, P., Wyckham, C., and Smits, A., "Experimental Investigations of Mach 3 Shock-Wave Turbulent Boundary Layer Interactions," AIAA Paper 2005-4899, American Institute of Aeronautics and Astronautics, Reston VA, June 2005.
- ³²Dussauge, J.-P. and Piponniau, S., "Shock / Boundary-Layer Interactions: Possible Sources of Unsteadiness," *Journal of Fluids and Structures*, Vol. 24, 2008, pp. 1166–1175.
- ³³Souverain, L. J., Dupont, P., Debiève, J.-F., Dussauge, J.-P., van Oudheusden, B. W., and Scarano, F., "Effect of Interaction Strength on Unsteadiness in Turbulent Shock-Wave-Induced Separations," *AIAA Journal*, Vol. 48, No. 7, 2010, pp. 1480–1493.
- ³⁴Weiss, J. and Chokani, N., "Effect of Freestream Noise on Shock-Wave / Turbulent-Boundary-Layer Interactions," *AIAA Journal*, Vol. 45, No. 9, 2007, pp. 2352–2355.
- ³⁵Stanfield, S. A., Kimmel, R. L., and Adamczak, D., "HiFiRE-1 Flight Data Analysis: Turbulent Shock-Boundary-Layer Interaction Experiment During Ascent," AIAA Paper 2012-2703, American Institute of Aeronautics and Astronautics, Reston, VA, June 2012.
- ³⁶Erengil, M. E. and Dolling, D. S., "Physical Causes of Separation Shock Unsteadiness in Shock Wave / Turbulent Boundary Layer Interactions," AIAA Paper 93-3134, American Institute of Aeronautics and Astronautics, Reston, VA, July 1993.
- ³⁷Gramann, R. A. and Dolling, D. S., "Detection of Turbulent Boundary Layer Separation Using Fluctuating Wall Pressure Signals," *AIAA Journal*, Vol. 28, No. 6, 1990, pp. 1052–1056.
- ³⁸Erengil, M. E. and Dolling, D. S., "Separation Shock Motion and Ensemble-Averaged Wall Pressures in a Mach 5 Compression Ramp Interaction," *AIAA Journal*, Vol. 29, No. 5, 1991, pp. 728–735.
- ³⁹Muck, K. C., Dussauge, J. P., and Bogdonoff, S. M., "Structure of the Wall Pressure Fluctuations in a Shock-Induced Separated Turbulent Flow," AIAA Paper 85-0179, American Institute of Aeronautics and Astronautics, Reston, VA, January 1985.
- ⁴⁰Marshall, T. A. and Dolling, D. S., "Spanwise Properties of the Unsteady Separation Shock in a Mach 5 Unswept Compression Ramp Interaction," AIAA Paper 90-0377, American Institute of Aeronautics and Astronautics, Reston, VA, January 1990.
- ⁴¹Erengil, M. E. and Dolling, D. S., "Correlation of Separation Shock Motion with Pressure Fluctuations in the Incoming Boundary Layer," *AIAA Journal*, Vol. 29, No. 11, 1991, pp. 1868–1877.
- ⁴²Smith, M. W., *Flow Visualization in Supersonic Turbulent Boundary Layers*, Ph.D. thesis, Princeton University, Princeton, NJ, October 1989.
- ⁴³Smith, D. R., Poggie, J., Konrad, W., and Smits, A. J., "Visualization of the Structure of Shock Wave Turbulent Boundary Layer Interactions using Rayleigh Scattering," AIAA Paper 91-0651, American Institute of Aeronautics and Astronautics, Reston, VA, January 1991.
- ⁴⁴Forkey, J., Cogne, A., A. Smits, A., and Bogdonoff, S., "Time-Sequenced and Spectrally-Filtered Imaging of Shock Wave and Boundary Layer Structure for Inlet Characterization," AIAA Paper 93-2300, American Institute of Aeronautics and Astronautics, Reston, VA, June 1993.
- ⁴⁵Beresh, S. J., Comninou, M., Clemens, N. T., and Dolling, D. S., "The Effects of the Incoming Turbulent Boundary Layer Structure on a Shock-Induced Separated Flow," AIAA Paper 98-0620, American Institute of Aeronautics and Astronautics, Reston, VA, January 1998.
- ⁴⁶Wu, P., Lempert, W. R., and Miles, R. B., "Megahertz Pulse-Burst Laser and Visualization of Shock-Wave / Boundary-Layer Interaction," *AIAA Journal*, Vol. 38, No. 4, 2000, pp. 672–679.
- ⁴⁷Ganapathisubramani, B., Clemens, N. T., and Dolling, D. S., "Large-Scale Motions in a Supersonic Turbulent Boundary Layer," *Journal of Fluid Mechanics*, Vol. 556, 2006, pp. 271–282.
- ⁴⁸Ganapathisubramani, B., Clemens, N. T., and Dolling, D. S., "Effects of Upstream Boundary Layer on the Unsteadiness of Shock-Induced Separation," *Journal of Fluid Mechanics*, Vol. 585, 2007, pp. 369–394.
- ⁴⁹Ganapathisubramani, B., Clemens, N. T., and Dolling, D. S., "Low-Frequency Dynamics of Shock-Induced Separation in a Compression Ramp Interaction," *Journal of Fluid Mechanics*, Vol. 636, 2009, pp. 397–425.
- ⁵⁰Humble, R. A., Scarano, F., and van Oudheusden, B. W., "Particle Image Velocimetry Measurements of a Shock Wave / Turbulent Boundary Layer Interaction," *Experiments in Fluids*, Vol. 43, 2007, pp. 173–183.
- ⁵¹Humble, R. A., Elsinga, G. E., Scarano, F., and van Oudheusden, B. W., "Three-Dimensional Instantaneous Structure of a Shock Wave / Turbulent Boundary Layer Interaction," *Journal of Fluid Mechanics*, Vol. 622, 2009, pp. 33–62.
- ⁵²Hunt, D. and Nixon, D., "A Very Large Eddy Simulation of an Unsteady Shock Wave / Turbulent Boundary Layer Interaction," AIAA Paper 95-2122, American Institute of Aeronautics and Astronautics, Reston VA, June 1995.
- ⁵³Urbin, G., Knight, D., and Zheltovodov, A. A., "Large Eddy Simulation of a Supersonic Compression Corner. Part I," AIAA Paper 2000-0398, American Institute of Aeronautics and Astronautics, Reston VA, January 2000.
- ⁵⁴Adams, N. A., "Direct Numerical Simulation of Turbulent Compression Ramp Flow," *Theoretical and Computational Fluid Dynamics*, Vol. 12, 1998, pp. 109–129.
- ⁵⁵Adams, N. A., "Direct Simulation of the Turbulent Boundary Layer Along a Compression Ramp at $M = 3$ and $Re_\theta = 1685$," *Journal of Fluid Mechanics*, Vol. 420, 2000, pp. 47–83.
- ⁵⁶Rizzetta, D. P., Visbal, M. R., and Gaitonde, D. V., "Large-Eddy Simulation of Supersonic Compression-Ramp Flow by High-Order Method," *AIAA Journal*, Vol. 39, No. 12, 2001, pp. 2283–2292.
- ⁵⁷Rizzetta, D. P. and Visbal, M. R., "Application of Large-Eddy Simulation to Supersonic Compression Ramps," *AIAA Journal*, Vol. 40, No. 8, 2002, pp. 1574–1581.
- ⁵⁸Garnier, E., Sagaut, P., and Deville, M., "Large Eddy Simulation of Shock / Boundary-Layer Interaction," *AIAA Journal*, Vol. 40, No. 10, 2002, pp. 1935–1944.
- ⁵⁹Teramoto, S., "Large-Eddy Simulation of Transitional Boundary Layer with Impinging Shock Wave," *AIAA Journal*, Vol. 43, No. 11, 2005, pp. 2354–2363.

- ⁶⁰Pirozzoli, S. and Grasso, F., "Direct Numerical Simulation of Impinging Shock Wave / Turbulent Boundary Layer Interaction at $M = 2.25$," *Physics of Fluids*, Vol. 18, 2006, pp. 065113.
- ⁶¹Loginov, M. S., Adams, N. A., and Zheltovodov, A. A., "Large-Eddy Simulation of Shock-Wave / Turbulent-Boundary-Layer Interaction," *Journal of Fluid Mechanics*, Vol. 565, 2006, pp. 135–169.
- ⁶²Wu, M. and Martín, M. P., "Direct Numerical Simulation of Supersonic Turbulent Boundary Layer over a Compression Ramp," *AIAA Journal*, Vol. 45, No. 4, 2007, pp. 879–889.
- ⁶³Wu, M. and Martín, M. P., "Analysis of Shock Motion in Shockwave and Turbulent Boundary Layer Interaction Using Direct Numerical Simulation Data," *Journal of Fluid Mechanics*, Vol. 594, 2008, pp. 71–83.
- ⁶⁴Priebe, S., Wu, M., and Martín, M. P., "Direct Numerical Simulation of a Reflected-Shock-Wave / Turbulent-Boundary-Layer Interaction," *AIAA Journal*, Vol. 47, No. 5, 2009, pp. 1173–1185.
- ⁶⁵Touber, E. and Sandham, N. D., "Large-Eddy Simulation of Low-Frequency Unsteadiness in a Turbulent Shock-Induced Separation Bubble," *Theoretical and Computational Fluid Dynamics*, Vol. 23, No. 2, 2009, pp. 79–107.
- ⁶⁶Touber, E. and Sandham, N. D., "Comparison of Three Large-Eddy Simulations of Shock-Induced Turbulent Separation Bubbles," *Shock Waves*, Vol. 19, 2009, pp. 469–478.
- ⁶⁷Bisek, N. J., Rizzetta, D. P., and Poggie, J., "Plasma Control of a Turbulent Shock Boundary-Layer Interaction," *AIAA Journal*, 2013, Accepted for publication. DOI: 10.2514/1.J052248.
- ⁶⁸Bisek, N. J. and Poggie, J., "Large-Eddy Simulations of Separated Supersonic Flow with Plasma Control," AIAA Paper 2013-0528, American Institute of Aeronautics and Astronautics, Reston, VA, January 2013.
- ⁶⁹Mullenix, N. J. and Gaitonde, D. V., "Analysis of Unsteady Behavior in Shock / Turbulent Boundary Layer Interactions with Large-Eddy Simulations," AIAA Paper 2013-0404, American Institute of Aeronautics and Astronautics, Reston, VA, January 2013.
- ⁷⁰Edwards, J. R., Choi, J.-I., and Boles, J. A., "Large-Eddy / Reynolds-Averaged Navier-Stokes Simulation of a Mach 5 Compression-Corner Interaction," *AIAA Journal*, Vol. 46, No. 4, 2008, pp. 977–991.
- ⁷¹Piponniau, S., Dussauge, J. P., Debiève, J. F., and Dupont, P., "A Simple Model for Low-Frequency Unsteadiness in Shock-Induced Separation," *Journal of Fluid Mechanics*, Vol. 629, 2009, pp. 87–108.
- ⁷²Hui, W. H., "Effects of Upstream Unsteadiness on Hypersonic Flow Past a Wedge," *The Physics of Fluids*, Vol. 15, No. 10, 1972, pp. 1747–1750.
- ⁷³Poggie, J. and Smits, A. J., "Shock Unsteadiness in a Reattaching Shear Layer," *Journal of Fluid Mechanics*, Vol. 429, 2001, pp. 155–185.
- ⁷⁴Evans, T., Poddar, K., and Smits, A. J., "Compilation of Wall Pressure Data for a Shock Wave Boundary Layer Interaction Generated by a Blunt Fin," MAE Report 1908 T, Department of Mechanical and Aerospace Engineering, Princeton University, Princeton, NJ, December 1990.
- ⁷⁵Selig, M. S. and Smits, A. J., "Effect of Periodic Blowing on Attached and Separated Supersonic Turbulent Boundary Layers," *AIAA Journal*, Vol. 29, No. 10, 1991, pp. 1651–1658.
- ⁷⁶Poggie, J. and Smits, A. J., "Experimental Evidence for Plotkin Model of Shock Unsteadiness in Separated Flow," *Physics of Fluids*, Vol. 17, 2005, pp. 018107.
- ⁷⁷Horowitz, P. and Hill, W., *The Art of Electronics*, Cambridge University Press, New York, 1980.
- ⁷⁸Smits, A. J. and Dussauge, J.-P., *Turbulent Shear Layers in Supersonic Flow*, Springer, New York, 2nd ed., 2006.
- ⁷⁹Stanfield, S. A., Kimmel, R. L., and Adamczak, D., "HIFiRE-1 Flight Data Analysis: Boundary Layer Transition Experiment During Reentry," AIAA Paper 2012-1087, American Institute of Aeronautics and Astronautics, Reston, VA, January 2012.
- ⁸⁰Stanfield, S. A. and Kimmel, R. L., "Compensation Method for the Estimation of the Autospectral Density Function of the Unevenly Spaced HIFiRE-1 Flight Data," AIAA Paper 2013-xxxx, American Institute of Aeronautics and Astronautics, Reston, VA, June 2013.
- ⁸¹Deeming, T. J., "Fourier Analysis with Unequally-Spaced Data," *Astrophysics and Space Sciences*, Vol. 36, 1975, pp. 137–158.
- ⁸²Scargle, J. D., "Studies in Astronomical Time Series Analysis. II. Statistical Aspects of Spectral Analysis of Unevenly Spaced Data," *The Astrophysical Journal*, Vol. 263, 1982, pp. 835–853.
- ⁸³Rai, M. M., Gatski, T. B., and Erlebacher, G., "Direct Simulation of Spatially Evolving Compressible Turbulent Boundary Layers," AIAA Paper 1995-583, American Institute of Aeronautics and Astronautics, Reston, VA, January 1995.
- ⁸⁴Fernholz, H. H. and Finley, P. J., "A Critical Compilation of Compressible Turbulent Boundary Layer Data," AGARDograph 223, Advisory Group for Aerospace Research and Development, NATO, Neuilly sur Seine, France, 1977, Case 55010501.
- ⁸⁵Elena, M. and LaCharme, J. P., "Experimental Study of a Supersonic Turbulent Boundary Layer Using Laser Doppler Anemometer," *Journal de Mécanique Théorique et Appliquée*, Vol. 7, 1988, pp. 175–190.
- ⁸⁶Bendat, J. S. and Piersol, A. G., *Random Data: Analysis and Measurement Procedures*, J. Wiley, New York, 2nd ed., 1986.
- ⁸⁷Beam, R. and Warming, R., "An Implicit Factored Scheme for the Compressible Navier-Stokes Equations," *AIAA Journal*, Vol. 16, No. 4, 1978, pp. 393–402.
- ⁸⁸Pulliam, T. H. and Chaussee, D. S., "A Diagonal Form of an Implicit Approximate-Factorization Algorithm," *Journal of Computational Physics*, Vol. 39, No. 2, 1981, pp. 347–363.
- ⁸⁹Lele, S., "Compact Finite Difference Schemes with Spectral-like Resolution," *Journal of Computational Physics*, Vol. 103, 1992, pp. 16–42.
- ⁹⁰Visbal, M. R. and Gaitonde, D. V., "High-Order-Accurate Methods for Complex Unsteady Subsonic Flows," *AIAA Journal*, Vol. 37, No. 10, 1999, pp. 1231–1239.
- ⁹¹Gaitonde, D., Shang, J. S., and Young, J. L., "Practical Aspects of High-Order Accurate Finite-Volume Schemes for Electromagnetics," AIAA Paper 1997-363, American Institute of Aeronautics and Astronautics, Reston, VA, January 1997.

- ⁹²Stoltz, S. and Adams, N. A., “An Approximate Deconvolution Procedure for Large-Eddy Simulation,” *Physics of Fluids*, Vol. 11, No. 7, 1999, pp. 1699–1701.
- ⁹³Mathew, J., Lechner, R., Foysi, H., Sesterhenn, J., and Friedrich, R., “An Explicit Filtering Method for Large Eddy Simulation of Compressible Flows,” *Physics of Fluids*, Vol. 15, No. 8, 2003, pp. 2279–2289.
- ⁹⁴Rizzetta, D. P. and Visbal, M. R., “Large-Eddy Simulation of Supersonic Boundary-Layer Flow by a High-Order Method,” *International Journal of Computational Fluid Dynamics*, Vol. 18, No. 1, 2004, pp. 15–27.
- ⁹⁵Pirozzoli, S., Grasso, F., and Gatski, T. B., “Direct Numerical Simulation and Analysis of a Spatially Evolving Supersonic Turbulent Boundary Layer at $M=2.25$,” *Physics of Fluids*, Vol. 16, No. 3, 2004, pp. 530–545.
- ⁹⁶White, F. M., *Viscous Fluid Flow*, McGraw Hill, New York, 3rd ed., 2006.
- ⁹⁷Mullenix, N. J., Gaitonde, D. V., and Visbal, M. R., “A Plasma-Actuator-Based Method to Generate a Supersonic Turbulent Boundary Layer Inflow Condition for Numerical Simulation,” AIAA Paper 2011-3556, American Institute of Aeronautics and Astronautics, Reston, VA, June 2011.
- ⁹⁸van Driest, E. R., “On the Turbulent Flow Near a Wall,” *Journal of the Aeronautical Sciences*, Vol. 23, 1956, pp. 1007–1011.
- ⁹⁹Selig, M. S. and Smits, A. J., “The Dynamic Behavior of a Shock-Wave / Turbulent Boundary Layer Interaction,” *Near Wall Turbulence: 1988 Zoran Zaric Memorial Conference*, edited by S. J. Kline and N. H. Afgan, Hemisphere, New York, 1990.

Computational Analysis of Shock Wave Turbulent Boundary Layer Interaction

Tim Leger¹ and Jonathan Poggie²

U.S. Air Force Research Laboratory, Wright-Patterson Air Force Base, 45433-7512 Ohio

An investigation was conducted to evaluate the error involved in predicting aero-thermodynamic loads (surface pressure, skin friction, and heat transfer) using a Reynolds Averaged Navier Stokes (RANS) solver. Numerical simulations of Shock Wave / Turbulent Boundary Layer Interaction (SWTBLI) at Mach 5 are performed and compared with vetted experimental data. These simulations include three 2-D impinging shock, and two 3-D swept shock cases. The impinging shock cases involve different levels of interaction intensity, which result in attached, incipiently separated, and fully separated flows. Comparisons between the numerical results and experimental data for each case are used to evaluate the error in predicting the associated SWTBLI aero-thermodynamic loads. The result shows that while wall pressure is accurately predicted, skin friction is under predicted, and heat transfer is over predicted. However, the trends in skin friction and heat transfer are captured by the RANS simulations.

Nomenclature

β	= Shock generator or fin deflection angle
x	= Streamwise distance from flat plate or fin leading edge
y	= Normal distance from the flat plate
z	= Spanwise distance from fin leading edge
M	= Mach number
δ	= Boundary layer height
δ^*	= Boundary layer displacement thickness
θ	= Boundary layer momentum thickness
H	= Boundary layer shape factor or intersection point of separation and incident shocks
γ	= Angle of reattachment
ε	= Shock angle
φ	= Angle of separation
ψ	= Angle of upstream influence
S	= Line of separation
R	= Line of reattachment
UI	= Line of upstream influence
P	= Pressure
T	= Temperature
M	= Mach number
Re/m	= Unit Reynolds number
U	= Streamwise Velocity
H_o	= Enthalpy
ρ	= Density
μ	= Dynamic viscosity
μ_s	= Dynamic viscosity from Sutherlands' law
μ_K	= Dynamic viscosity from Keyes' law
f	= Viscosity blending function
$\tilde{\nu}$	= Eddy viscosity

¹ Research Scientist, Ohio Aerospace Institute, Member AIAA.

² Senior Aerospace Engineer, AFRL/RQHF, Associate Fellow AIAA.

u^+	=	Dimensionless wall velocity
y^+	=	Dimensionless wall distance
C_f	=	Skin friction coefficient
St	=	Stanton number

Abbreviations

LE	=	Leading Edge
BL	=	Boundary Layer
GISF	=	Global Interferometry Skin Friction technique
VCO	=	Virtual Conical Origin

Subscripts

0	=	Stagnation
∞	=	Freestream
W	=	Value at the wall
1	=	Primary
2	=	Secondary

I. Introduction

Design exploration of new hypersonic vehicles is reliant on Reynolds Averaged Navier Stokes (RANS) solvers for the foreseeable future.¹ Although higher fidelity Computational Fluid Dynamic (CFD) solvers are becoming widely available,² ranging in scale and complexity from Large Eddy Simulation (LES) to Direct Numerical Simulation (DNS), they also require significantly more computational resources and have much longer turnaround times than RANS solvers. Initial design work often entails parametric studies, requiring the solution of the flow field for numerous configurations. The increased computational resources and simulation times of higher fidelity models renders them impractical for such early design work, even with modern supercomputers.

While turnaround time and computational resource requirements are important considerations for CFD use during early design work, the uncertainty in predicting the flow field is even more important. For hypersonic work, in particular, the accuracy and confidence in the calculation of aero-thermodynamic loadings is very important.³ Without such knowledge, predictions from a CFD simulation cannot be effectively utilized to make important decisions in the design space.

The process of accessing the accuracy of a physical model is referred to as code validation, and can only be accomplished by detailed comparisons with vetted experimental data.⁴ It is important to note that the validation process for any particular solver is almost impossible to fully complete. First, there are always cases of interest for which the solver is used, but no experimental data are available for comparison. In addition, most solvers provide several different combinations of physical models (such as for viscosity or turbulence) and numerical algorithms, each combination of which may produce very different results from the other. While numerous standardized configurations, including experimental and high fidelity CFD data sets, exist for such use in hypersonic flows,⁵⁻⁷ one of the most important and commonly encountered phenomena in this flow regime is Shock Wave / Turbulent Boundary Layer Interaction (SWTBLI).

II. Background

SWTBLI has been extensively studied, both in experiments and with high fidelity CFD simulations.⁵⁻⁷ It is known from such work that the aero-thermodynamic loads resulting from such interactions can have a significant effect on the design of hypersonic vehicles. While different configurations have been devised to study SWTBLI, the 2-D impinging shock configuration illustrated in figure 1 is often employed to study the phenomenon due to its rather simple geometry and ability to easily vary the interaction strength. This type of SWTBLI typically occurs in internal flows where shocks generated by disturbances near the leading edge of a supersonic engine inlet impinge on the boundary layer of the opposite wall of the inlet.

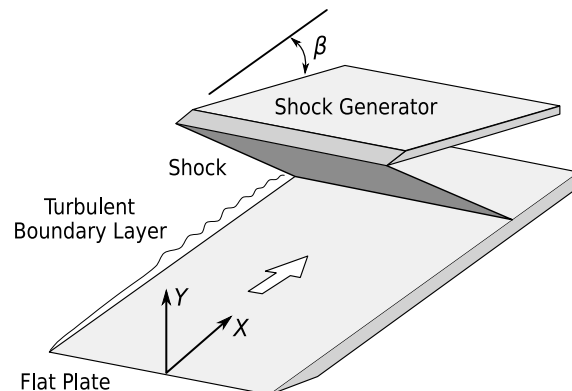


Figure 1. Basic 2-D impinging SWTBLI geometry (Adapted from Schülein et al.⁸).

In the 2-D impinging shock configuration, a turbulent boundary layer develops along the flat plate, which is then impinged upon by an oblique shock formed by the shock generator. The strength of the shock and thus the SWTBLI created is controlled by the angle, β , of the shock generator to the incoming flow and results in either fully attached, incipiently separated, or fully separated flow. Figure 2 illustrates the weak interaction case, in which the flow remains fully attached. The oblique or incident shock (C1) formed by the shock generator progressively curves as it penetrates the turbulent boundary layer due to the Mach number gradient. A pressure rise caused by the impinging shock then propagates upstream in the subsonic region of the boundary layer where the thickening subsonic region generates outgoing compression waves that coalesce into a reflected shock (C2). This reflected shock is weakened downstream of the impingement point by the expansion fan which forms at the end of the shock generator. A double shock situation results from the impinging and reflected shocks, which causes an overall increase in the wall pressure and a decrease in the wall shear stress near the impingement point.

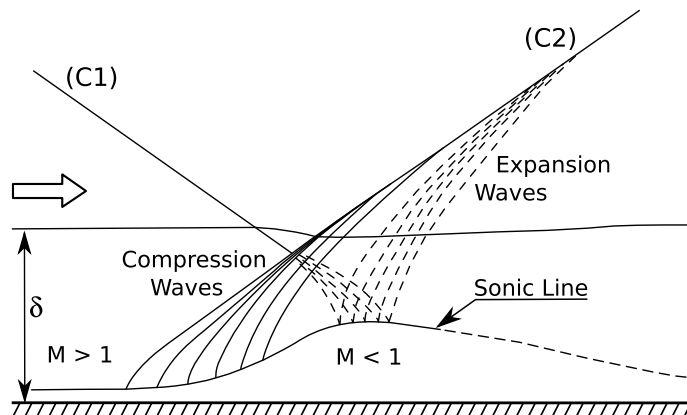


Figure 2. Illustration of weak (unseparated) impinging SWTBLI (Adapted from Delery and Marvin⁹).

As the shock generator angle is increased, so too is the oblique shock strength, which causes the wall shear stress near the impingement point to decrease further. Once the shear stress at the impingement point reaches zero, a small separation shock and bubble structure is formed. With further increases in the shock strength, the separation bubble grows and the flow becomes fully separated, as illustrated in figure 3. The boundary layer becomes separated at point S, well upstream of where the incident shock would meet the surface in an inviscid flow. At the point of separation, a rapid pressure rise occurs as a result of compression waves which propagate in the supersonic part of the boundary layer and coalesce to form a separation or lambda shock (C2). The separation shock intersects the incident shock at point H, which generates the refracted shocks (C3) and (C4). Since the entropy rise through (C1) and (C4) is different than through (C2) and (C3), point H also denotes the origin of a slip line. Refracted shock (C3) enters the boundary layer, where it reflects off the separation bubble and forms an expansion fan. This expansion fan turns the flow back towards the downstream portion of the separation bubble, until the flow reattaches at point

R. As a result of this flow turning, compression waves are formed above the downstream portion of the separation bubble. These compression waves coalesce and merge with refracted shock (C4) to form the reflected shock (C5).

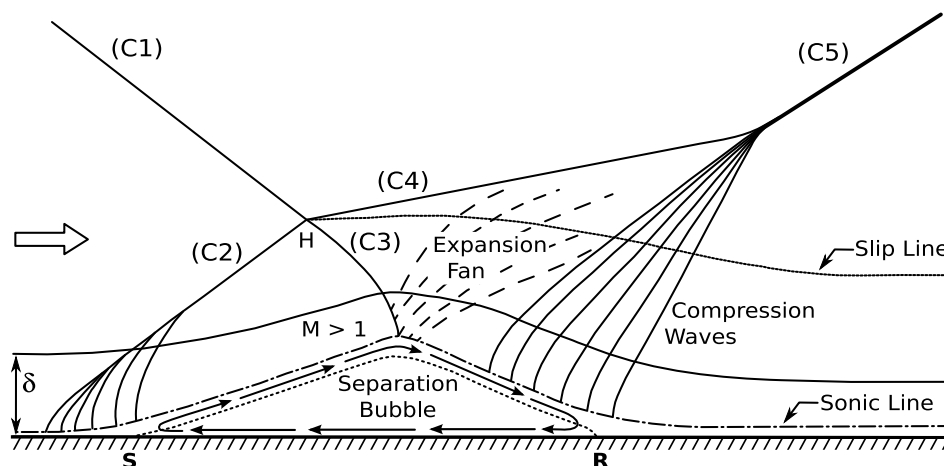


Figure 3. Illustration of strong (separated) impinging SWTBLI (Adapted from Delery and Marvin⁹).

As noted in experiments by Dolling and Brusniak¹⁰ and later computationally using RANS simulations by Brown,¹¹ Brown et al.,¹² and Fedorova & Fedorchenko,¹³ the associated lambda shock is unsteady, having time scales larger than, and comparable to, the turbulent boundary layer itself. This unsteadiness has also been studied computationally using higher fidelity models, such as LES.¹⁵ Thus, the shock unsteadiness is undoubtedly a main source of uncertainty when utilizing a RANS solver (with traditional turbulence closure models) to predict such flow phenomena.

One of the most commonly studied 3-D SWTBLI configurations is a sharp fin on a flat plate, with the fin placed at an angle of attack, β , to the incoming flow,¹⁵ as illustrated in figure 4. This configuration produces a 3-D swept SWTBLI, which is a simplified version of more complex interactions that can occur in engine inlets and fin/body junctions of hypersonic vehicles. The oblique shock generated by the sharp fin, sweeps across the turbulent boundary layer that develops along the flat plate, producing a complex, 3-D flow field. Spanwise pressure gradients near the fin generate secondary flows, which induce one or more large scale flattened/elliptical vortices that grow with downstream distance from the fin Leading Edge (LE).

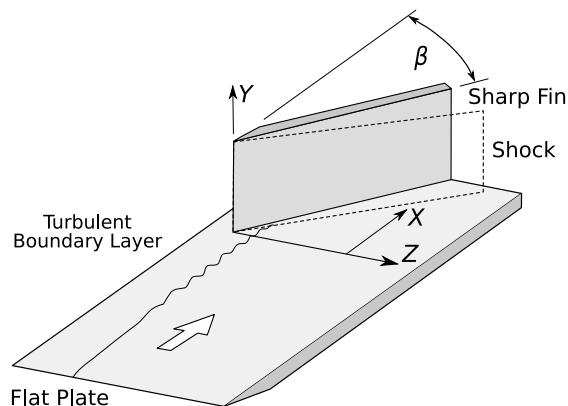


Figure 4. Basic 3-D swept SWTBLI geometry.

For all but the smallest angle of attack, β , the growth of these vortices and thus the interaction, has been experimentally observed as conical in nature beyond a small inception region near the fin LE.¹⁶ By using a Virtual Conical Origin (VCO), the footprint of the interaction on the flat plate can be collapsed to polar coordinates as illustrated in figure 5. In figure 5, UI denotes the line of upstream influence, while S1 and R1 denote the line of flow separation and reattachment respectively from the primary separation vortex. A secondary separation vortex

can also form downstream of the primary separation vortex for moderately strong interactions, but disappears as the interaction strength increases.¹⁷ This secondary separation vortex is denoted by S2 and R2 in figure 5 for the associated lines of separation and reattachment.

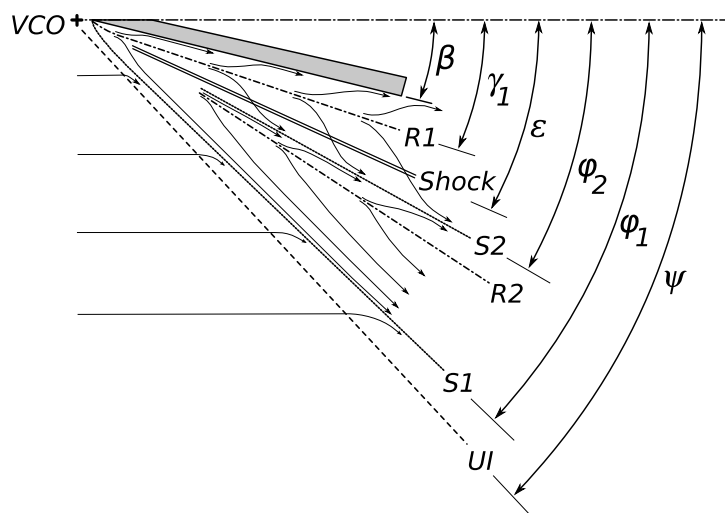


Figure 5. Swept SWTBLI footprint with surface flow streamlines (Adapted from Schülein and Zheltovodov¹⁸).

From a conical cross-plane point of view, as illustrated in figure 6, the interaction is similar to the 2-D impinging SWTBLI. However there are some main differences between the two. First, the separation or lambda shock structure is absent of the refracted shock C4, since the shock from the fin is normal to the flat plate. Second, the separation bubble is replaced with a separation vortex which grows as it extends downstream. Third, the compression waves at the rear of the separation form a jet (transonic in the cross-plane) that impinges on the plate surface just outbound of the fin. This impinging jet is believed to be responsible for the high surface pressure, skin friction, and heat transfer in this region.¹⁹ When present, the secondary separation vortex forms underneath the primary separation vortex and rotates in the opposite direction. As with the 2-D impinging SWTBLI, the separation vortex is unsteady and has been found to produce fluctuating wall pressures.²⁰

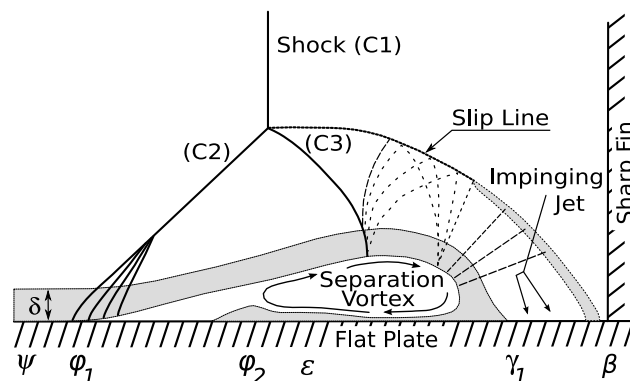


Figure 6. Illustration of the swept SWTBLI structure (Adapted from Rodi et al.¹⁹).

III. Overview of Experiments

For the work presented here, the thoroughly documented experiments of Schülein et al. for a 2-D impinging⁸ and 3-D sharp fin/swept¹⁸ SWTBLI are utilized. They were conducted at the Institute of Fluid Mechanics DLR (Göttingen, Germany) in the Ludwig Tube Facility (RWG, Tunnel B), which had a useful test time of 0.3 seconds

for the test conditions. The nominal flow conditions at the inlet were $P_o = 2.12$ MPa, $T_o = 410$ K, $M_\infty = 5$, $T_w = 300$ K, $Re/m = 37E6/m$, and $H_{o,\infty} = 410$ kJ/kg, with air as the working fluid. Run to run variations were less than 0.5% for M_∞ and U_∞ , and within 2% for T_∞ . The wall temperature of the models was held at 300 ± 5 K during all runs, with the exception of heat flux measurements, which showed a noticeable adiabatic heating of the models.

A. 2-D Impinging SWTBLI

In the impinging SWTBLI experiments, a flat plate 500 mm long by 400 mm wide was used along with a shock generator which was 300 mm long by 400 mm wide. Measurements on the flat plate are given for four cases: G0, undisturbed (no shock generator) turbulent boundary layer. G6, shock generator mounted at an angle $\beta = 6^\circ$, producing a weak interaction with completely attached flow. G10, shock generator at an angle $\beta = 10^\circ$, resulting in critical interaction, and incipient separated flow. G15, shock generator mounted at angle $\beta = 14^\circ$ causing strong interaction and fully separated flow.

The reported measurements from the experiment included wall pressure (with 67 static pressure taps along a streamline on the surface of the flat plate), boundary layer profiles (at 10 streamwise and 4 spanwise locations), and skin friction (via optical and oil film techniques). In a later publication,²¹ Schülein presented revised skin friction measurements, obtained using the Global Interferometry Skin Friction (GISF) technique, along with heat flux measurements, obtained using a thin skin technique, for the same experiment. The measurement techniques and instrumentation employed for this experiment were documented in detail. Reported uncertainty was ± 100 Pa for wall pressure, ± 138 PA for static pressure and ± 0.05 mm for the distance above the plate for profile surveys, skin friction within $\pm 4\%$ (in the undisturbed boundary layer) to $\pm 10\%$ (near the flow reattachment area), and $\pm 5\%$ for heat transfer.

This experiment has been used to assess the computational results (and turbulence models) from other solvers, allowing for comparison of the current work with other independent simulations. Steelant²² investigated the effects of including compressibility corrections in Wilcox's Low Reynolds and Mentors non-linear SST turbulence models. Lenahan²³ used NASA's Wind-US solver with both the Spalart-Allmaras and SST turbulence models. Lindblad et al.²⁴ used an Explicit Algebraic Reynolds Stress Model (EARSIM) and Fedorova and Fedorchenko¹³ extended the work by investigating the effects of external turbulence and the separated shock unsteadiness for the G14 case. Brown¹¹ used NASA's DPLR production solver with Spalart-Allmaras, $k-\omega$, and SST turbulence models.

B. 3-D Sharp Fin / Swept SWTBLI

The 3-D sharp fin experiments were a follow on to the 2-D impinging SWTBLI experiments and the same flat plate was used along with either one or two 100 mm tall unswept sharp fins. However for the work presented here, only configurations with a single fin are considered. The fin was mounted with its' LE on the streamwise centerline of the plate at an angle of attack to the incoming flow of β . Two cases were simulated; LF12 ($\beta = 12^\circ$), with the fin LE 249.5 mm downstream of plate LE, and LF23 ($\beta = 23^\circ$), with the fin LE 286.0 mm downstream of the plate LE.

Reported measurements from this experiment include wall pressure (with 143 static pressure taps, in 10 mm intervals both streamwise and spanwise), flow pattern visualization, skin friction (via optical, oil film, and GISF techniques), and heat flux (via the thin-skin technique and an insert along the plates' streamwise centerline with 29 thermocouples). Unfortunately, skin friction measurements are only available for LF23 case. To obtain continuous data throughout the interaction region, the fins were moved 5 mm in both spanwise and streamwise directions. As with the 2-D impinging SWTBLI experiments, the measurement techniques and instrumentation used is well documented. Reported uncertainty was $\pm 2.5\%$ for surface pressure, skin friction within $\pm 10\%$, and $\pm 5\%$ for heat flux.

IV. Computational Approach

A. Numerical Model

Simulations were carried out using US3D, a well-validated, cell-centered, finite-volume, solver for the solution of the nonequilibrium, compressible Navier-Stokes equations on unstructured grids, developed at the University of Minnesota.²⁵ The modified Steger-Warming flux vector splitting scheme of MacCormack and Candler²⁶ is used to evaluate the inviscid fluxes. This modified Steger-Warming method uses a pressure-dependent weighting function to

switch smoothly from a low-dissipation method in regions of low gradients to the original Steger–Warming scheme when a large-pressure gradient is detected across a face (such as for a strong shock). MUSCL reconstruction²⁷ is used at the faces, resulting in second order spatial accuracy. Diffusive fluxes are computed using a second-order scheme, in which the gradients are computed using a deferred correction approach similar to that of Nompelis et al.,^{25,28,29} McCormack and Candler,^{30,31} and Kim et al.³² Weighted least square fits are used to calculate the viscous fluxes from second order accurate gradients.

Solutions are driven to a steady state convergence using a backward Euler time stepping, which is fully implicit, but only first order accurate. Future time level fluxes are approximated by linearizing the fluxes about the current time level using exact flux jacobians. The data-parallel line relaxation (DPLR) method, based on the Gauss–Seidel line relaxation method of McCormack³³, is then employed to solve the resulting linear system. To improve performance on parallel systems, the DPLR method replaces Gauss–Seidel sweeps with a series of line relaxation sweeps.³⁴ Overall, the DPLR method has high parallel efficiency and good convergence characteristics, particularly when solving large compressible flow problems.

US3D is designed for high enthalpy (high temperature) flows, such as those encountered in hypersonic flight or shock tunnels. In contrast, the experiments simulated here have a rather low enthalpy flow, with a static inlet temperature of 68 K. While US3D has an option to use Sutherland’s viscosity law (with < 2% error for temperatures down to 200 K), a modified viscosity model, blended with Keyes low temperature viscosity law as described in Ref. 35, was employed:

$$\mu = \mu_S = 1.4858 \times 10^{-6} T^{3/2} / (T + 110.4) \quad T > 100 \text{ K} \quad (1)$$

$$\mu = f\mu_S + (1 - f)\mu_K \quad 100 \text{ K} \leq T \leq 88.8 \text{ K} \quad (2)$$

$$\mu = \mu_K = 1.488 \times 10^{-6} \sqrt{T} / (1 + 122.1 \times 10^{-5} / T) \quad T < 88.8 \text{ K} \quad (3)$$

Where T is the static temperature, μ is the dynamic viscosity, μ_S is the dynamic viscosity from Sutherlands’ law, μ_K is the dynamic viscosity from Keyes’ law, and f is the blending function, given by:

$$f = (T - 88.8) / 11.2 \quad (4)$$

The Negative Spalart–Allmaras (SA-NEG) turbulence closure model³⁶, with trip term and corrections for compressible flow was used for all work presented here. This modified form of the Spalart–Allmaras model is an extension to the original (positive) model and is activated only when $\tilde{\nu}$ becomes negative, such as areas with under-resolved grids or non-physical transient states. For regions where $\tilde{\nu}$ is not negative, the original (positive) Spalart Allmaras model is recovered. From the wall skin friction data for the experiment, the boundary layer becomes turbulent at approximately 100 mm from the leading edge of the flat plate. Hence a trip point was specified for this location, using the Spalart–Allmaras trip term, for all the cases presented here.

B. Grid Generation

Three dimensional structured grids were used for all the simulations in this work. Since the interaction is assumed to be 2-D for the impinging SWTBLI, a periodic boundary condition is employed for these cases in the spanwise direction. Additionally, only 1.5 mm of the plate width is modeled using three cells in the spanwise direction.

For the undisturbed boundary layer, case G0, the modeled domain was 30 mm high (roughly half the height of the interaction region) and 500 mm long. Three successively refined grids were used in order to check for grid independence and convergence; 512x128x3 cells, 1024x256x3 cells, and 2048x512x3 cells corresponding to the coarse, medium, and fine grids respectively. The coarse grid was constructed first, with cells clustered in the normal direction near the plate surface using a hyperbolic tangent function. Initial grid spacing was adjusted until the maximum Δy^+ was approximately unity, or $\Delta y_1 = 1.6\text{E-}2$ mm. This resulted in roughly 80, 166, and 330 cells within the boundary layer height for the coarse, medium, and fine grids respectively. A portion of the coarse grid is shown in figure 7 with every other grid point removed, to give an idea of the clustering used near the wall in order to properly capture and define the turbulent boundary layer. To make post processing a bit easier, the grid was translated in the spanwise direction such that the plate centerline corresponded to $z = 0$. The medium grid was then constructed from the coarse grid using a cubic spline to divide each cell into four cells while maintaining the same

grid point distribution in each direction as the coarse grid. Next, the fine grid was constructed from the medium grid using the same process.

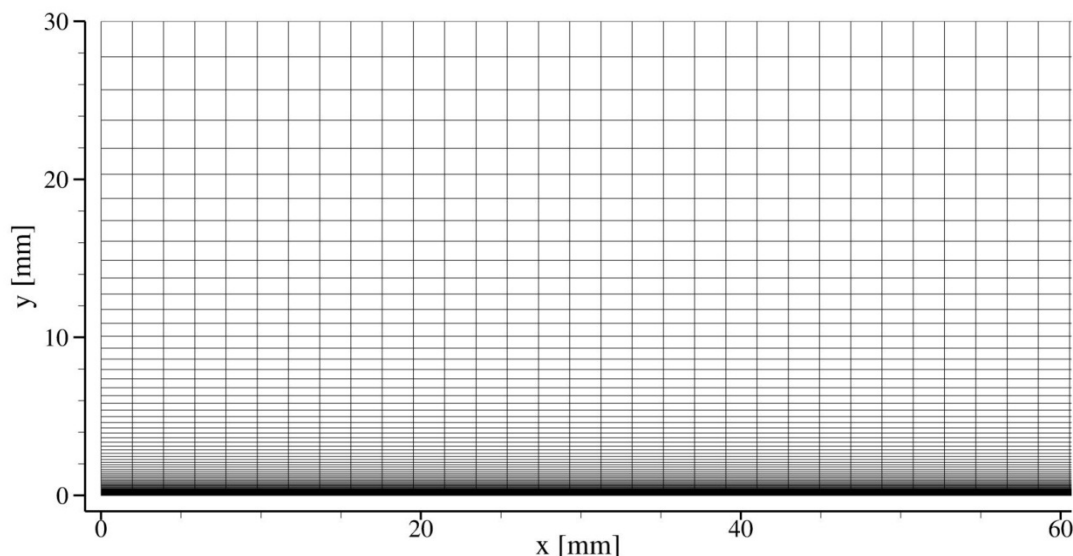


Figure 7. Portion of the coarse grid for the G0 case (Every other grid point removed for clarity).

Grids for the G6, G10, and G14 cases were all constructed in the same manner. As with the G0 case, three successively refined grids were constructed for each of these interaction cases; 512x256x3 cells, 1024x512x3 cells, and 2048x1024x3 cells corresponding to the coarse, medium, and fine grids. The coarse grids for these cases were constructed first. To help reproduce the same turbulent boundary layer in the interaction cases as in the G0 case, the domain was first split in the streamwise direction into an upper and lower half. The lower half was the same size as the G0 case and the same grid spacing in the normal direction was used. For the upper half, the normal grid spacing was clustered in both directions using a hyperbolic tangent function. The initial grid spacing near the shock generated side was $1.6\text{E-}2$ mm and the other side was set to match the lower domain spacing where they met. In the streamwise direction, grid spacing was initially made as even as possible. Following this, 30% of the grid points from the section before the shock generator were subtracted and evenly distributed to the rest of the domain. This was done to help make better use of the grids cells utilized in resolving the interaction region. To help smooth the grid, the portions of the grid before and after the shock generator were clustered in the streamwise direction using the hyperbolic tangent function and matching the grid spacing were they met the center section. As with the G0 case, the grid was translated in the spanwise direction such that the plate centerline corresponded to $z = 0$. The medium grid was then constructed from the fine grid using the same cubic spline function as with the G0 case. However, because the cubic spline tends to round off corners, the grids were first divided up into three pieces in the streamwise direction (before, including, and after the shock generator). Each of these three grid pieces was then refined separately using the cubic spline function and then joined back together again to form the final grid. This same process was then used to generate the fine grid from the medium grid.

The LF23 and LF12 case grids were created using the same procedure. Once again, three successively refined grids were constructed for each interaction case. However unlike the 2-D cases, the grids were refined in all three dimensions using a refinement factor of 1.5. The three grid sizes were 128x128x96 cells, 192x192x144 cells, and 288x288x216 cells, corresponding to the coarse, medium, and fine grids respectively. As with the 2-D cases, the coarse grid was constructed first. In the normal direction, cells were clustered along the flat plate surface using a hyperbolic tangent function and an initial grid spacing of $\Delta y_1 = 1.6\text{E-}2$ mm. Next, the domain was divided in the streamwise direction at the fin LE. For the region ahead of the fin, cells were clustered in the spanwise direction near the fin side using a hyperbolic tangent function and an initial grid spacing of $\Delta z_1 = 1.0\text{E-}3$ mm. The outlet domain was split in the spanwise direction at a location corresponding to where an inviscid shock from the fin would cross. Two thirds of the spanwise grid points were then assigned to the portion between the fin and the shock, while a third of the spanwise grid points was assigned to the remaining section on the other side of the shock. Cells were clustered in the region between the fin and shock using a hyperbolic tangent function and initial grid spacing of $1\text{E-}2$ mm and $5\text{E-}1$ mm along the fin and shock respectively. The cells near the shock on the other side were also

clustered using a hyperbolic tangent function and an initial grid spacing of 5E-1 mm. In the streamwise direction, the grid points were initially uniformly distributed, then 30% of them were subtracted from the region ahead of the fin and added to the fin region. The grid was then clustered in the streamwise directions using a hyperbolic tangent function. An initial grid spacing of 1E-1 mm was used along the streamwise division about the fin LE. To help smooth the grid, the initial grid spacing at the flat plate LE and outlet were chosen to mirror the spacing in the spanwise directions at the maximum span, i.e. side away from the fin. A normal slice of the LF23 coarse grid is shown in figure 8, with every other grid point removed for clarity. As with the 2-D cases, the medium grid was then generated from the coarse grid using a cubic spline function. Once again, to avoid sharp corner round off of the domain, the coarse grid was split into two portions about the fin LE. Each portion was refined separately and then joined together to form the final grid. The same procedure was used to generate the fine grid from the medium grid.

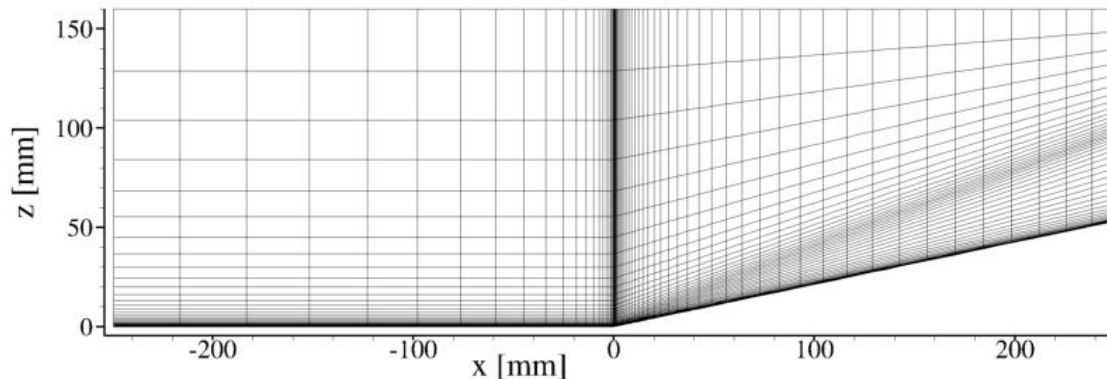


Figure 8. Normal slice of the LF12 case coarse grid (Every other grid point removed for clarity).

V. Results

A list of the six cases examined in this paper is given in table 1, along with the deflection angle, β , of the shock generator (for 2D impinging shock cases) or the fin (for 3D swept shock cases).

Table 1. Summary of cases examined.

Case	β	Description
G0	-	Undisturbed turbulent boundary layer
G6	6°	2-D Impinging shock, weak interaction with fully attached flow
G10	10°	2-D Impinging shock, critical interaction with incipient separated flow
G14	14°	2-D Impinging shock, strong interaction with separated flow
LF12	12°	3-D swept shock, intermediate interaction
LF23	23°	3-D swept shock, strong interaction

A. G0 Case, Undisturbed Turbulent Boundary Layer

The primary purpose of this case is to ensure the proper turbulent boundary layer develops along the flat plate and that the flow conditions are correct before adding the impinging or swept shock. Inlet conditions were calculated from the total pressure, total temperature, and Mach number reported for the experiments using isentropic properties giving $\rho = 0.2043 \text{ kg/m}^3$, $T = 68.33 \text{ K}$, and $U = 828.5 \text{ m/s}$. The plate was treated as an isothermal surface with a fixed temperature of 300 K.

Turbulent boundary layer properties were calculated from the simulation results by first extracting a line of data from each solution using Tecplot's Extract Precise Polyline add-on. Lines of data were extracted normal to plate surface, starting at 336 mm from the plate LE and at midspan, and ending 5 mm above this, with 2000 points extracted from cell volumes. The boundary layer thickness was then determined from this line of data based on the distance from the flat plate where 99.5% of the maximum streamwise velocity was reached. Displacement and momentum thicknesses were calculated next using numerical integration with the trapezoidal rule. For these calculations, the boundary layer edge was assumed to coincide with the location of maximum streamwise velocity. Hence, values for the velocity and density at the boundary layer edge were taken from this location and the integration was performed from the flat plate surface to this location as well. The iterative method of Huang et al.³⁵ was used in the experiment to determine the displacement and momentum thicknesses from measured velocity profiles. This was done due to a limited number of data points in the profile, and was also used to estimate skin friction. A Richardson extrapolation was performed for each of the calculated quantities from the three grids to determine the value and tolerance towards which the simulations were converging. A summary/comparison of the boundary layer properties at 336 mm from the plate LE (corresponding to location 5 in the experiment), is given in table 2.

Table 2. Summary of turbulent boundary layer properties for the G0 case at 336 mm downstream of the plate LE (corresponding to section 5 in the experiment).

	Coarse grid	Medium grid	Fine grid	Richardson Extrapolation	Experiment
Grid size	512x128x3	1024x256x3	2048x512x3	-	-
Δy_1	1.6E-2 mm	8.0E-3 mm	4.0E-3 mm	-	-
y^+_{max}	1.028	0.523	0.262	-	-
δ	4.652 mm	4.522 mm	4.518 mm	4.518 mm \pm 0.004%	4.658 mm \pm 1%
δ^*	1.916 mm	1.868 mm	1.865 mm	1.864 mm \pm 0.02%	1.894 mm \pm 2.6%
θ	0.189 mm	0.188 mm	0.188 mm	0.188 mm \pm 8E-8%	0.189 mm \pm 13%
H	10.12	9.94	9.92	9.92 \pm 0.03%	10.0 \pm 15%
c_f	1.2167E-3	1.2159E-3	1.2155E-3	1.2151E-3 \pm 0.04%	1.31E-3 \pm 4%
St	0.4637E-3	0.4648E-3	0.4651E-3	0.5652E-3 \pm 0.03%	0.456E-3 \pm 5%

Comparisons of the velocity, density, and temperature profiles are given in figures 9-11 respectively between the experimentally determined and CFD predicted profiles at 336 mm from the plate LE (corresponding to section 5 in the experiment). In figure 9, all three grid solutions have converged together for the lower half of the boundary layer and at the freestream, but the coarse grid shows a slightly quicker increase towards the freestream velocity than the medium and fine grids in the upper half of the boundary layer. In comparison to the experimental profile, the agreement is good, with the computational results showing a slightly slower growth in velocity in the lower third of the boundary layer. In figure 10, the medium and fine grids show good convergence, with the coarse grid showing a slightly faster increase in density from about a quarter of the boundary layer thickness off the wall to the boundary layer thickness. After this point, the coarse grid solution lags the fine and medium grids till it reaches the freestream value. The experimental profile shows a faster growth in the density than all there grids, especially near the lower third of the boundary layer. In figure 11, the fine and medium grids show good convergence in the temperature profile. The coarse grid matches the fine and medium grids along the first third of the boundary layer and again at the freestream, but similar to velocity, shows a slightly faster decrease in temperature in between. The experimental profile shows a quicker decrease in temperature than the CFD results, especially in the first third of the boundary layer, but agrees with the CFD results at the freestream.

Figure 12 shows the boundary layer profile using Van Driest II transformation given by Huang, Brandshaw, and Coakley.³⁷ Also shown in figure 10 is the linear relationship $u^+ = y^+$ for the viscous sublayer, the log law for the log layer, and Spaldings' law of the wall with no wake term.³⁸ All three grid solutions have converged and show fairly good agreement with the experimental profile up to about a y^+ of 200. Beyond this point, the deviation between the computational and experimental results is due to the under prediction of friction velocity caused by the turbulence model. Since the reciprocal of the friction velocity is used in the Van Driest II transformation as part of the scaling function for the non-dimensional u^+ , a lower friction velocity gives a higher u^+ at the edge of the boundary layer.

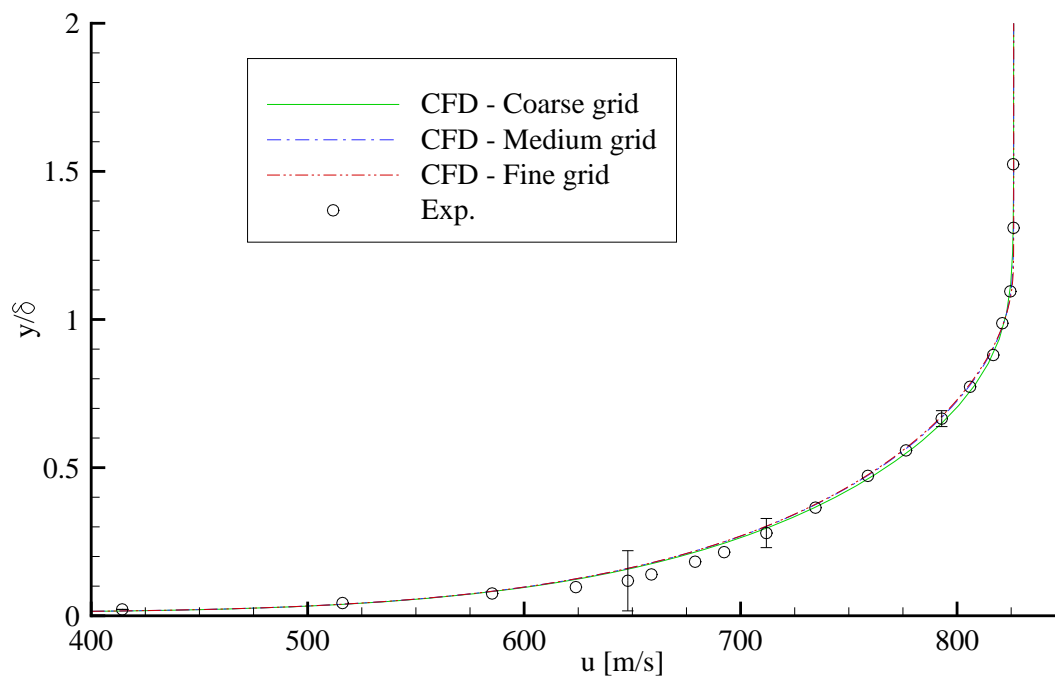


Figure 9. Velocity profile for the G0 undisturbed boundary layer case.

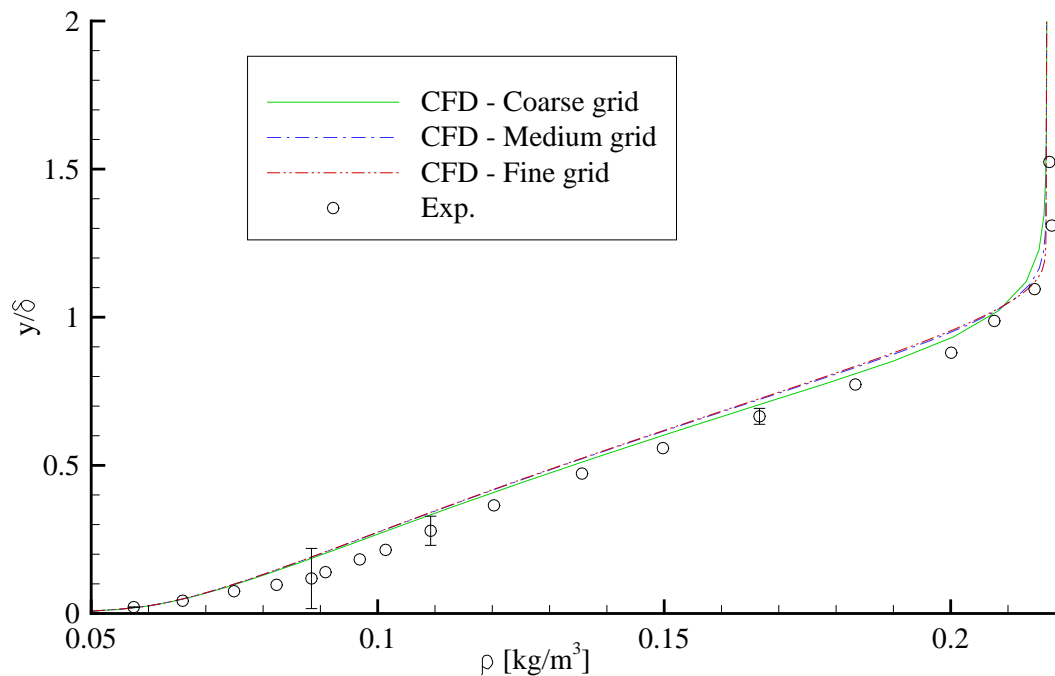


Figure 10. Density profile for the G0 undisturbed boundary layer case.

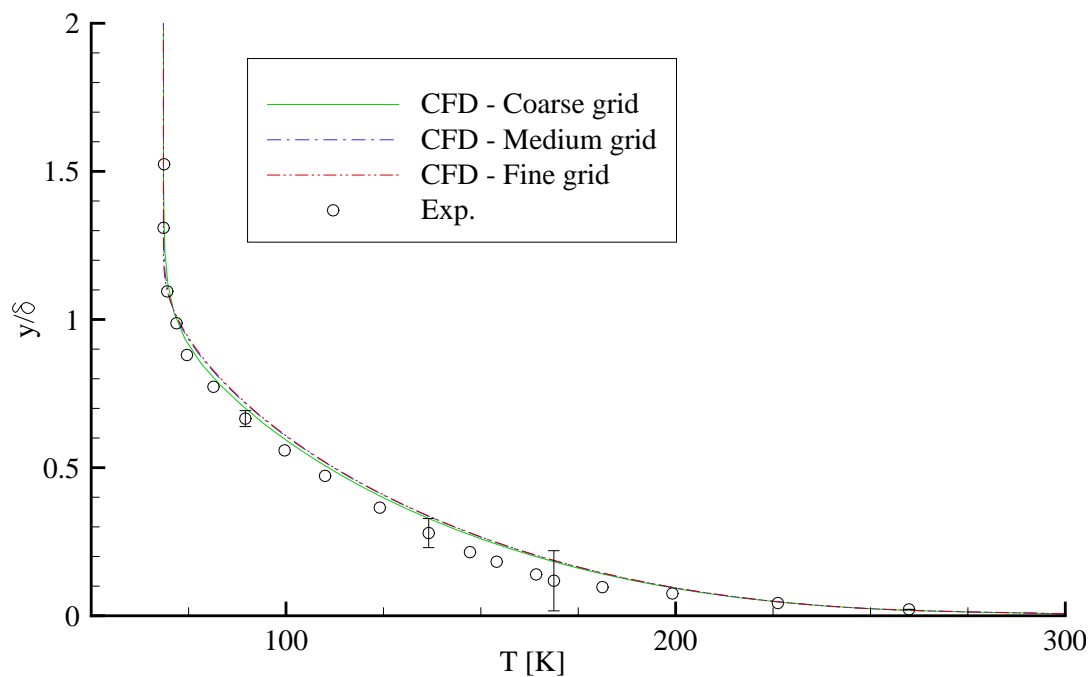


Figure 11. Temperature profile for the G0 undisturbed boundary layer case.

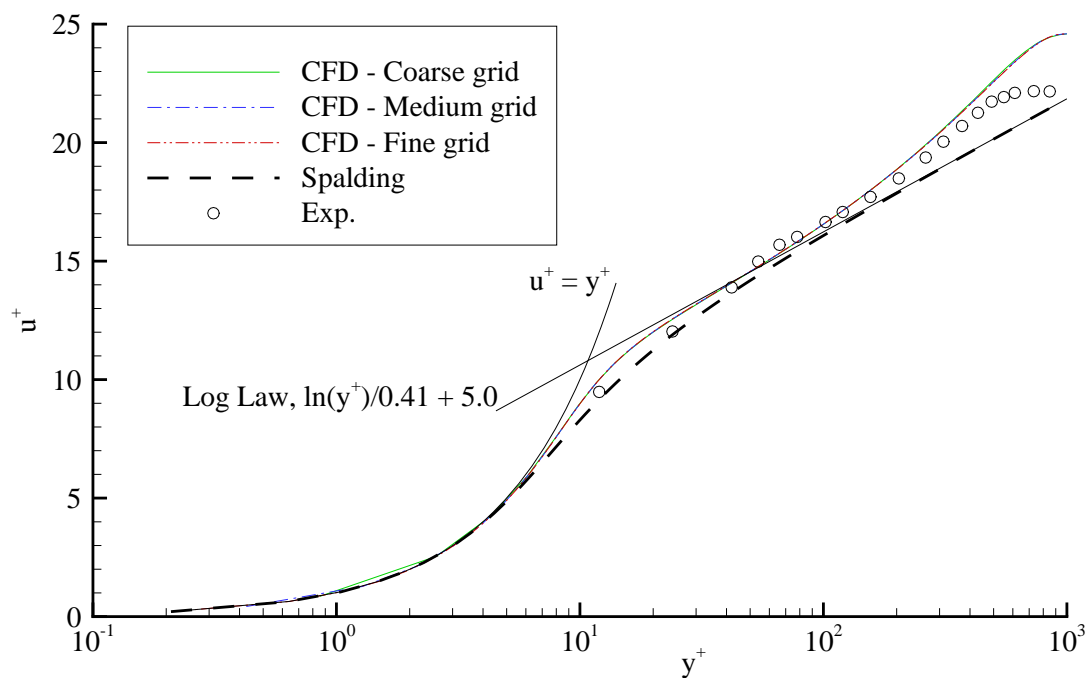


Figure 12. Van Driest profile for the G0 undisturbed boundary layer case.

The ratio of wall pressure to freestream pressure is plotted in figure 13, with the results from all three grids having converged to the same solution, except for a slight difference in trip intensity/strength between the coarse grid and the medium and fine grids. The simulation also agrees well within the scatter of the experimental data.

Skin friction along the wall is plotted in figure 14. From this plot, it can be seen that the boundary layer becomes turbulent at the trip location and remains so for the rest of the flat plate. While the strength/intensity of the trip in the computational simulations is weaker than measured in the experiment, the skin friction before and after the trip are in very close agreement between the computational grids. Once again, there is a slight difference in trip intensity/strength noticeable between the coarse grid and the medium and fine grids.

Heat transfer along the wall is shown in figure 15. Once again, the medium and fine grids have converged to the same solution. The coarse grid solution varies from the medium and fine grid solutions, both before and at the trip location. All three solutions over predict the wall heating by roughly 10%.

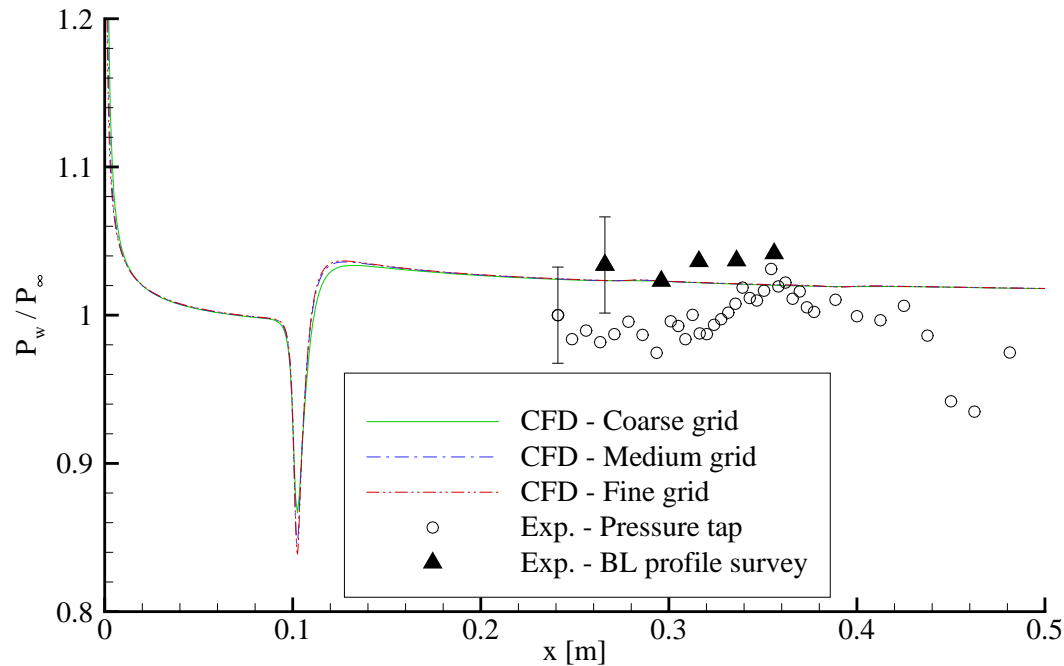


Figure 13. Wall pressure ratios for the G0 undisturbed boundary layer case.

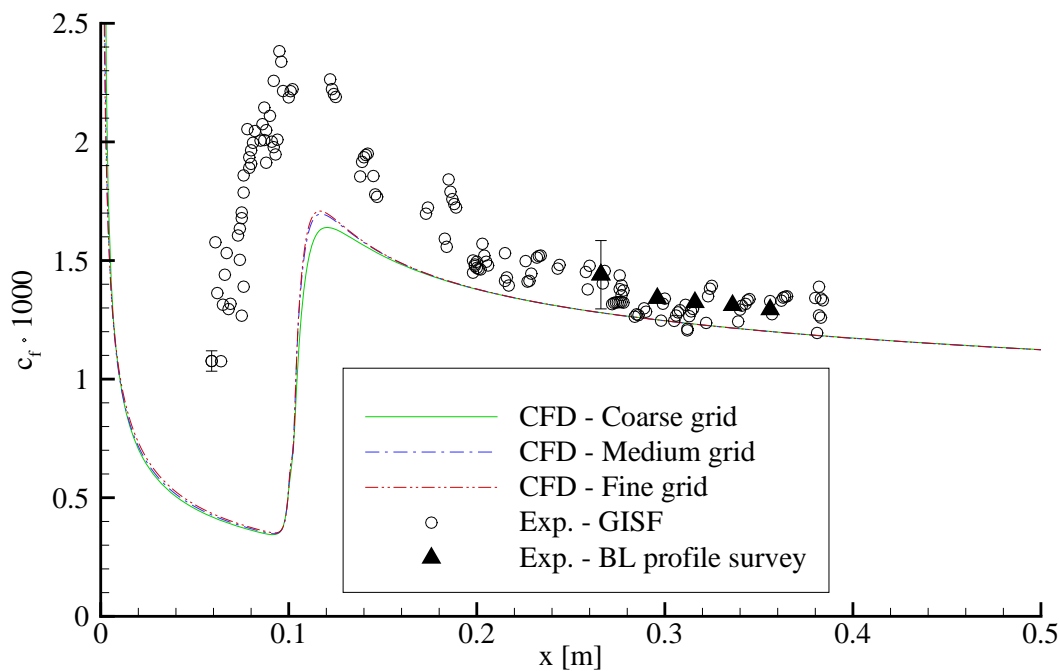


Figure 14. Skin friction for the G0 undisturbed boundary layer case.

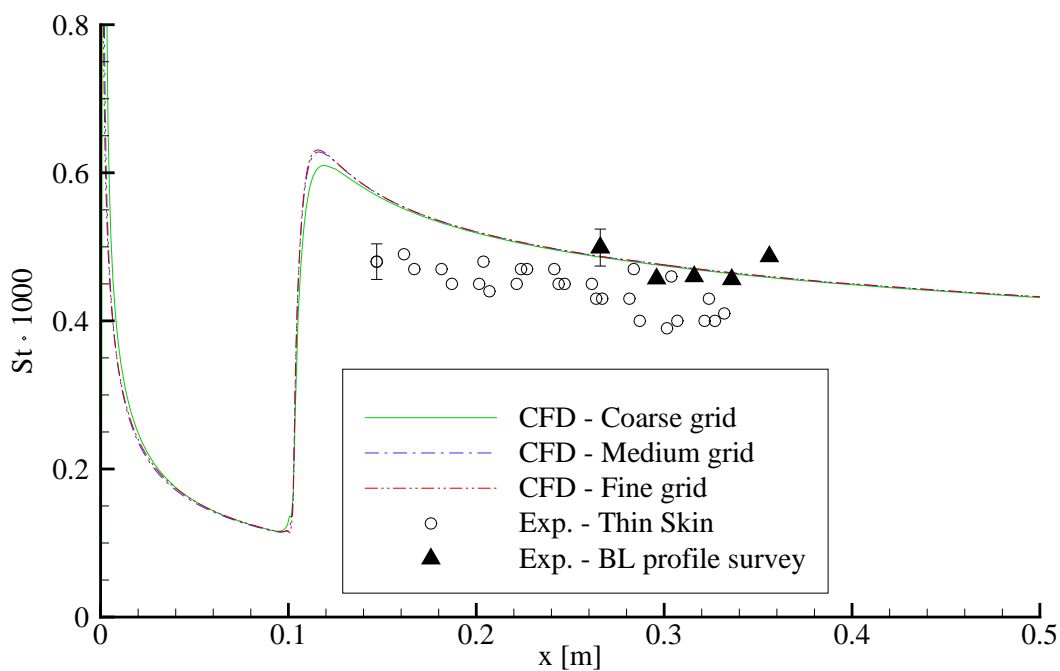


Figure 15. Heat transfer for the G0 undisturbed boundary layer case.

B. G6 Case, Weak 2-D Interaction with Fully Attached Flow

The G6 case involves the shock generator at a deflection angle β of 6° , which results in a weak interaction with fully attached flow. A pressure contour plot of this case is shown figure 16 to give a general overview of the flow involved. In this figure, the turbulence trip, turbulent boundary layer, oblique shock created by the shock generator, reflected shock, and the expansion fan at the end of the shock generator are identified.

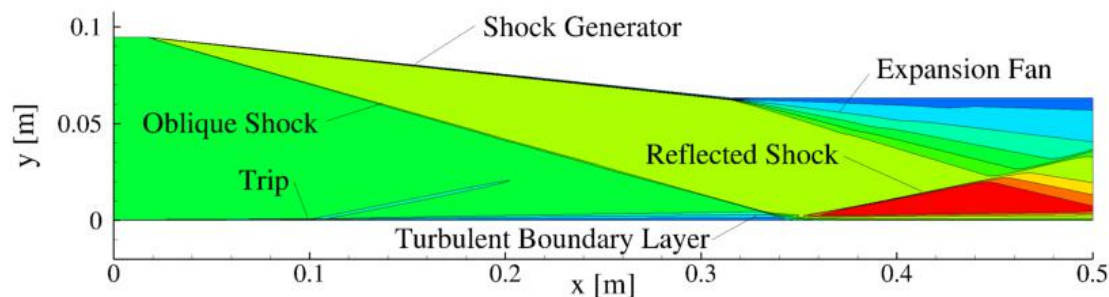


Figure 16. Pressure contour of the G6 case.

The ratio of wall pressure to freestream pressure is given figure 17. Again, the medium and fine grids show convergence to the same solution. The coarse grid solution shows a slightly earlier jump in pressure at the impingement point along with a dip in the pressure ratio at the outlet. Overall, the agreement between the computational results and the experimental data is good.

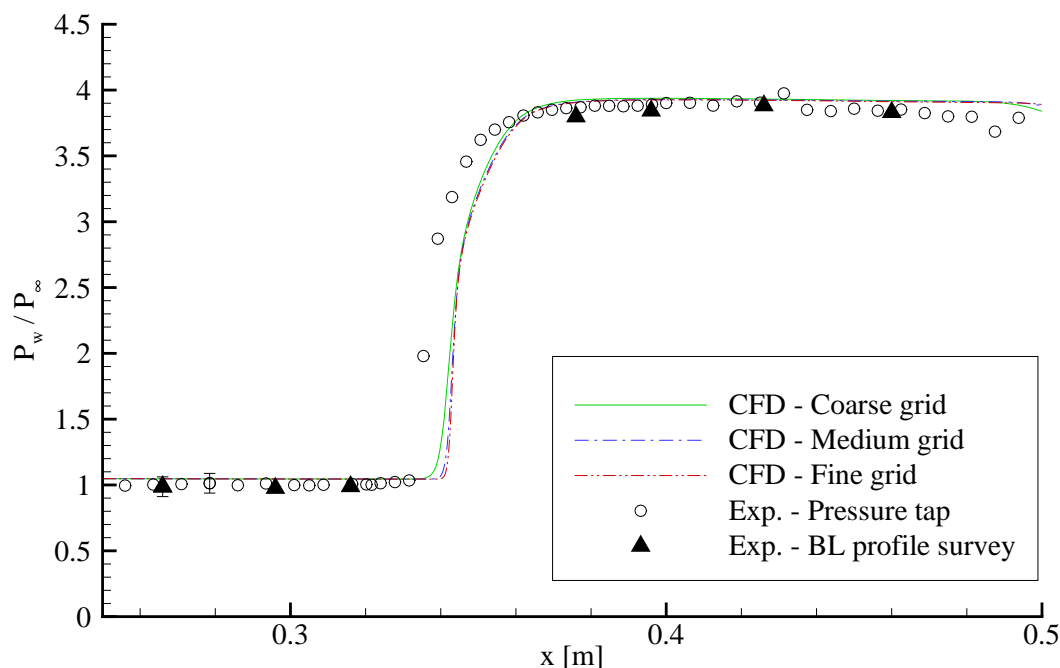


Figure 17. Wall pressure ratios for the G6 case.

Wall skin friction along the flat plate is given in figure 18. All three grids have converged to the same solution, with the exception of the coarse grid at the impingement point. At the impingement point, the coarse grid solution shows less of a drop in skin friction and slightly higher over prediction afterwards. The solutions show good agreement with the experimental data up to the last profile measurement. This is in the region past the shock

generator in which the expansion fan, formed at the end of the shock generator, weakens the reflected shock. One possible explanation for the mismatch is that the strength of the expansion shock in the simulations is not properly captured, as a result of not modeling the full aft region of the shock generator.

The predicted heat transfer for this case is given in figure 19. As with the wall pressure ratios, all three grids have converged to the same solution, with the exception of the coarse grid at the impingement point and near the outlet. The simulation significantly over predicts the heat transfer, compared with the experimental data, by nearly 30% and in addition shows a drop off after the impingement while the experimental data roughly shows a plateau in this region.

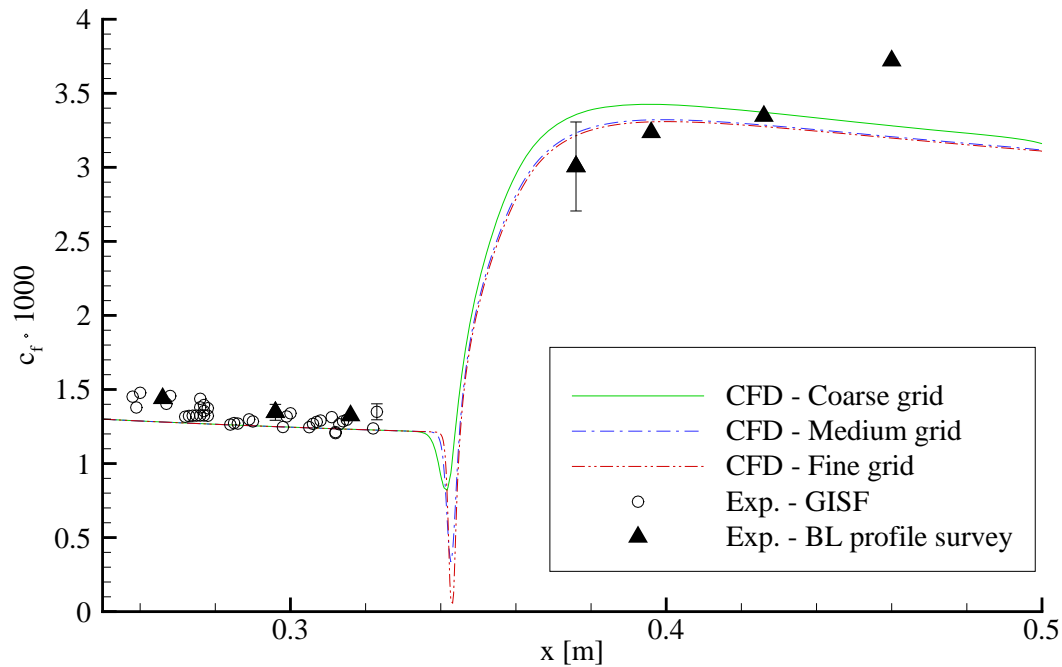


Figure 18. Skin friction for the G6 case.

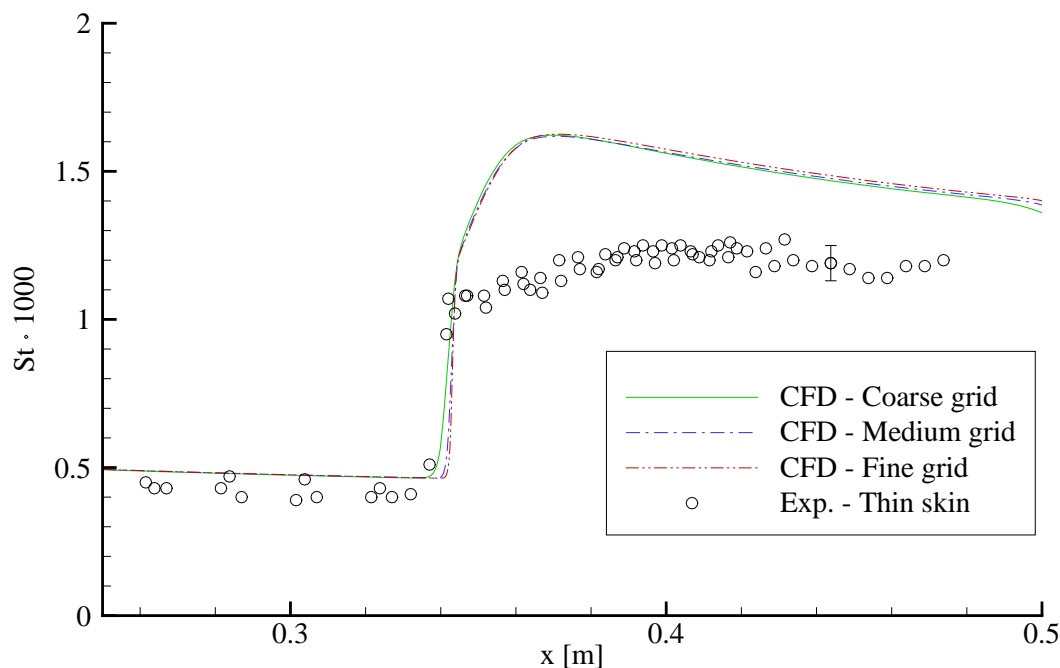


Figure 19. Heat transfer for the G6 case.

C. G10 Case, Critical 2-D Interaction with Incipient Separated Flow

For the G10 case, the shock generator is set at a deflection angle β of 10° , which results in a critical interaction with incipient separated flow. A pressure contour plot of the interaction region from the medium grid solution is given in figure 20, with features of the separation structure highlighted and streamlines in the boundary layer to help define the separation bubble. In figure 20, S and R denote the point of flow separation and reattachment respectively. In the experiment, the flow separates at $x \sim 0.334$ m and reattaches at $x \sim 0.345$ m, while in the computational simulations, the flow separates further downstream at $x \sim 0.341$ m and reattaches at $x \sim 0.347$ m.

The ratio of wall pressure to freestream pressure is given figure 21. All three grids have converged to the same solution with the exception of the coarse grid in the drop off region after the plateau in the interaction region. Interestingly enough, the coarse grid solution matches the other two grid solution at the outlet. Comparison with the experimental data shows excellent agreement, though there is slight mismatch in the initial rise of the pressure ratio. In addition, the pressure ratio drop off from the simulation is not as steep as in the experimental data.

Wall skin friction is plotted in figure 22. Unlike the previous cases, the solutions for the three grids diverge after the impingement point but converge back together at the outlet. The drop in skin friction about the impingement point is much more abrupt in the simulation results than the experimental data. In addition, the experimental data shows a peak in skin friction following the initial jump after the impingement. The difference in the simulation results and the experimental data at this point reaches roughly 25%. However, the computational simulations begin to agree with the experimental data (profile measurements) in the plateau region following this peak.

The heat transfer for this case is shown in figure 23. From this figure, the medium and fine grid solutions have converged together. The coarse grid solution shows a larger over prediction of the skin friction following the impingement, but also a quicker drop off after the plateau. All three grid solutions match back up at the outlet. The computational simulations once again show a more abrupt increase in skin friction following the impingement than the experimental data, and over predict the skin friction by roughly 30%. Both the computational results and experimental data show a sloped plateau following the rise in skin friction, with the coarse grid having a sharper slope than the medium or fine grids.

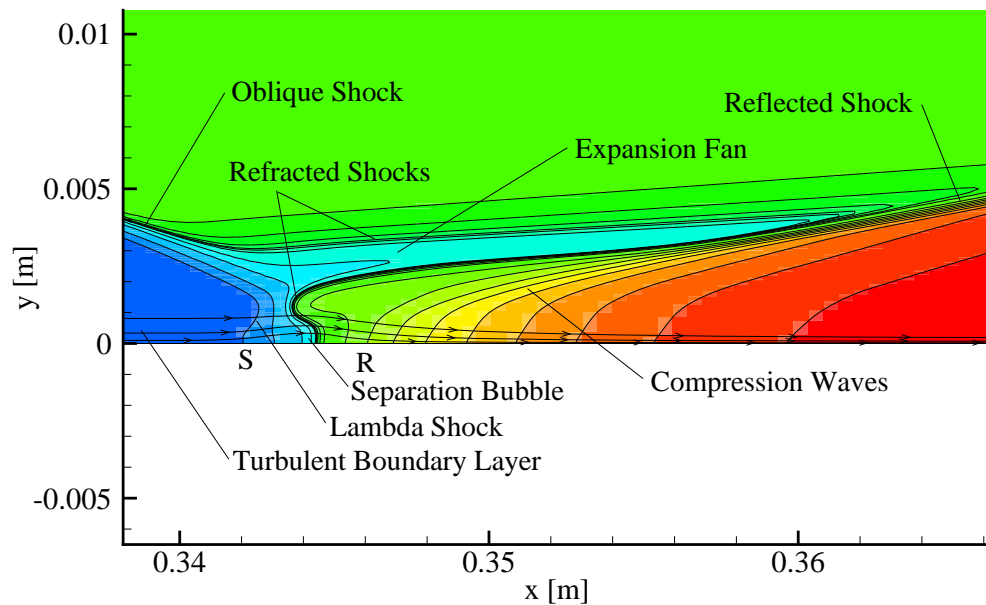


Figure 20. Pressure contour of interaction region for the G10 case, with features of the separation structure highlighted and streamlines in the boundary layer to help define the separation bubble.

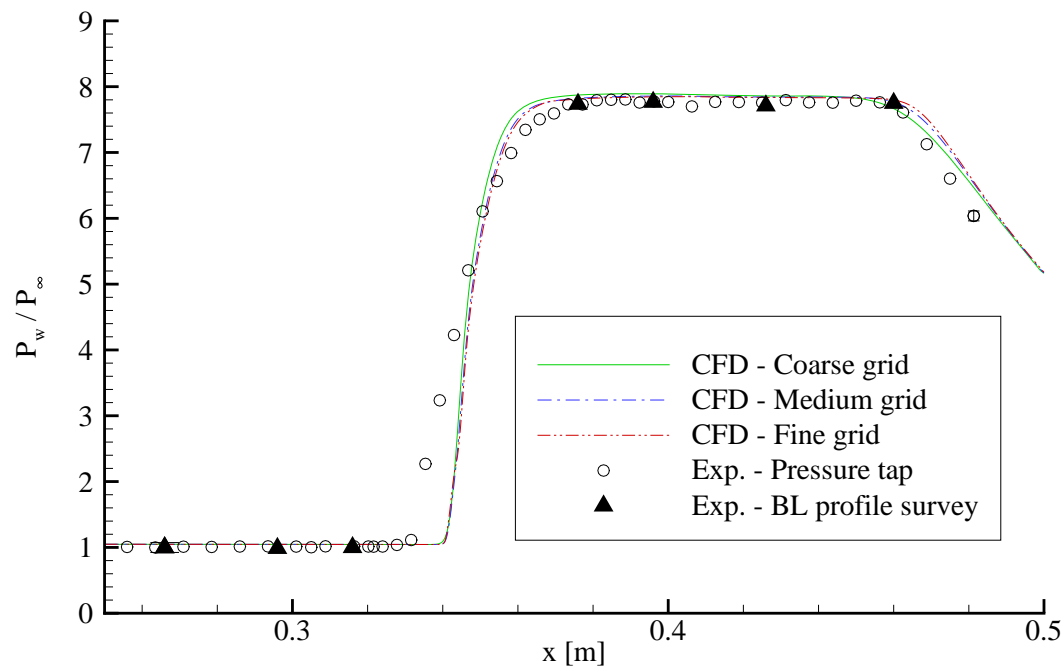


Figure 21. Wall pressure ratios for the G10 case.

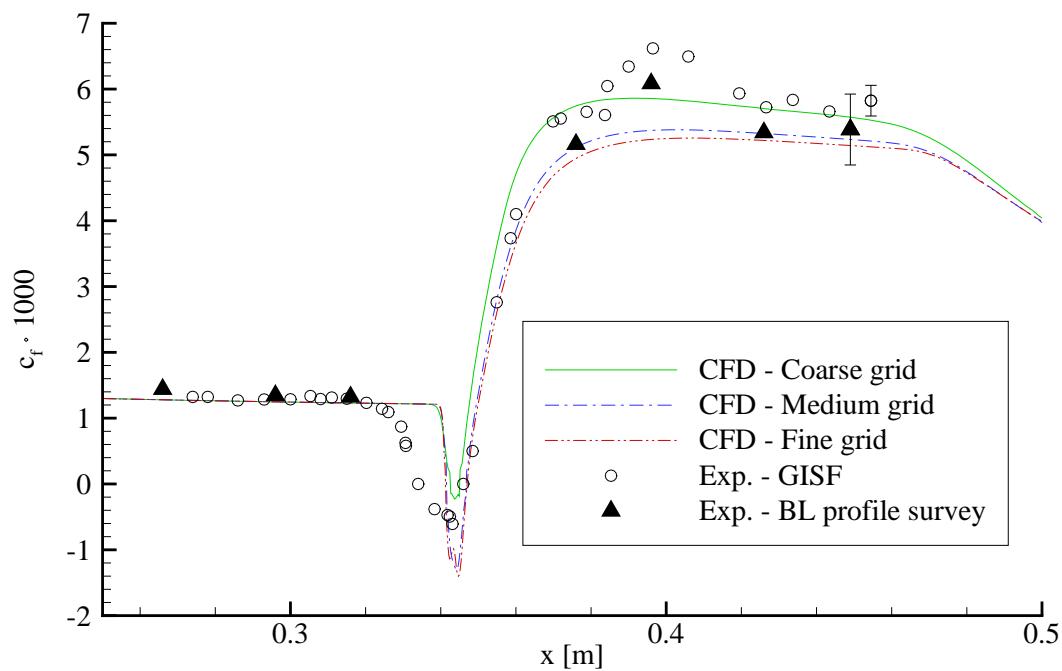


Figure 22. Skin friction for the G10 case.

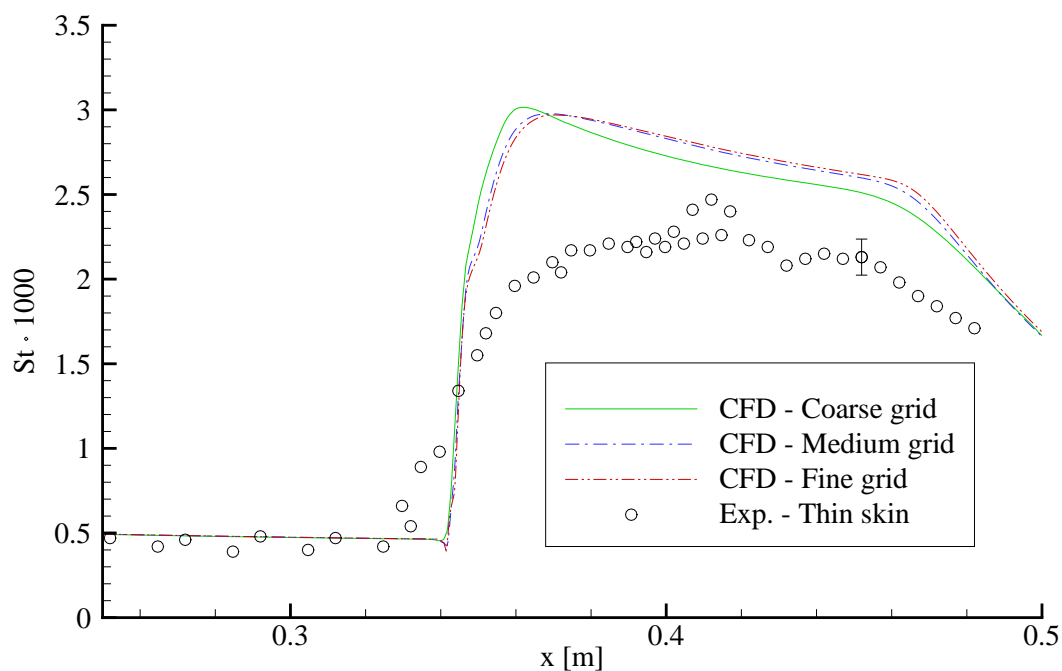


Figure 23. Heat transfer for the G10 case.

D. G14 Case, Strong 2-D Interaction with Fully Separated Flow

In the G14 case, the shock generator is set at a deflection angle β of 14° , which results in strong interaction and fully separated flow. A pressure contour plot of the interaction region from the medium grid solution is given in figure 24, with features of the separation structure highlighted and streamlines in the boundary layer to help define the separation bubble. In figure 24, the S and R denote the point of flow separation and reattachment respectively. For the computational results, separation occurs at $x \sim 0.333$ m and reattaches at $x \sim 0.350$ m, compared to the experimental data, where separation occurs earlier at $x \sim 0.314$ m and reattaches at $x \sim 0.347$ m.

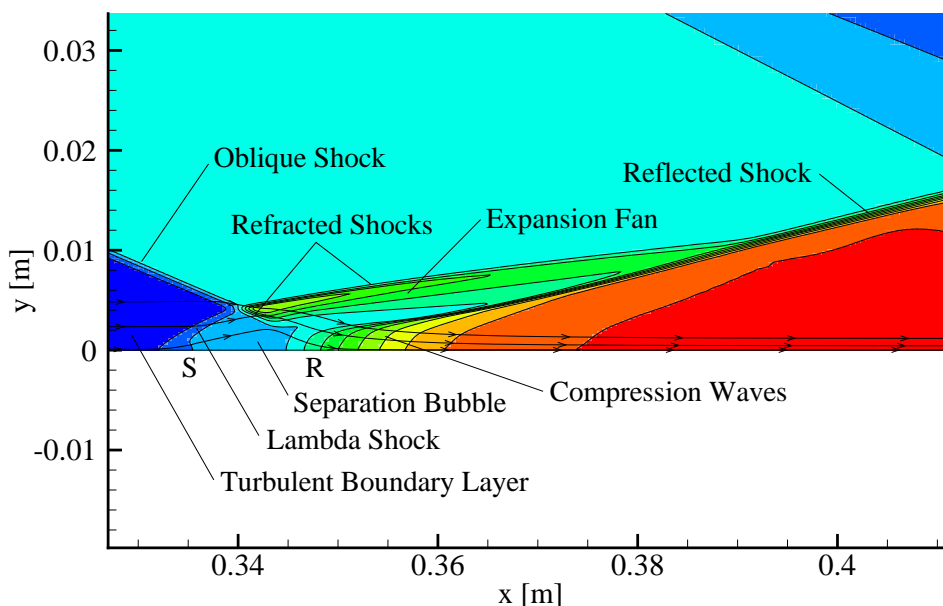


Figure 24. Pressure contour of interaction region for the G14 case, with features of the separation structure highlighted and streamlines in the boundary layer to help define the separation bubble.

The ratio of static wall pressure to static freestream pressure is given in figure 25. While the separation bubble is visible in the CFD solutions, its' effect on the initial rise in wall static pressure at the impingement point is not as strong or spread out as in the experimental data, which is likely due to the difference in location for the onset of separation. Unlike the previous cases, the coarse grid solution varies a fair amount from the medium and fine grid solutions. In addition, the pressure at the wall is slightly over predicted in comparison with the experimental data. Once again, all three grids converge to the same solution at the outlet.

Figure 26 shows the wall skin friction for this case. The coarse grid solution divergences significantly from the other two solutions starting just before flow reattachment, but begins to trend towards the other two solutions near the exit. Additionally, the medium and fine grid solutions also show significant diverge from one another shortly after the flow reattaches, but converge together near the exit. This divergence between the solutions, which was also observed in the G10 case, is most likely due to the inability of the turbulence model to handle the strong non-equilibrium boundary layer which results from the interaction. In comparison with the experimental data, the computational results show a delayed, but stronger drop in skin friction near the separation bubble. For the interaction region, the computational results trend away from the increased skin friction. It was also noted that in the interaction region, the GISF experimental results are significantly higher than even the values calculated from the profile survey measurements. From the report on the GISF measurements of the experiment,⁸ it is believed that the oil film used in the GISF method may be exhibiting instabilities from waves in the oil film as a consequence of the higher shear stress for the viscosity of oil. Thus a greater weight is given to the skin friction calculated from profile survey measurements. As in the previous cases, the skin friction is under predicted by roughly 20%.

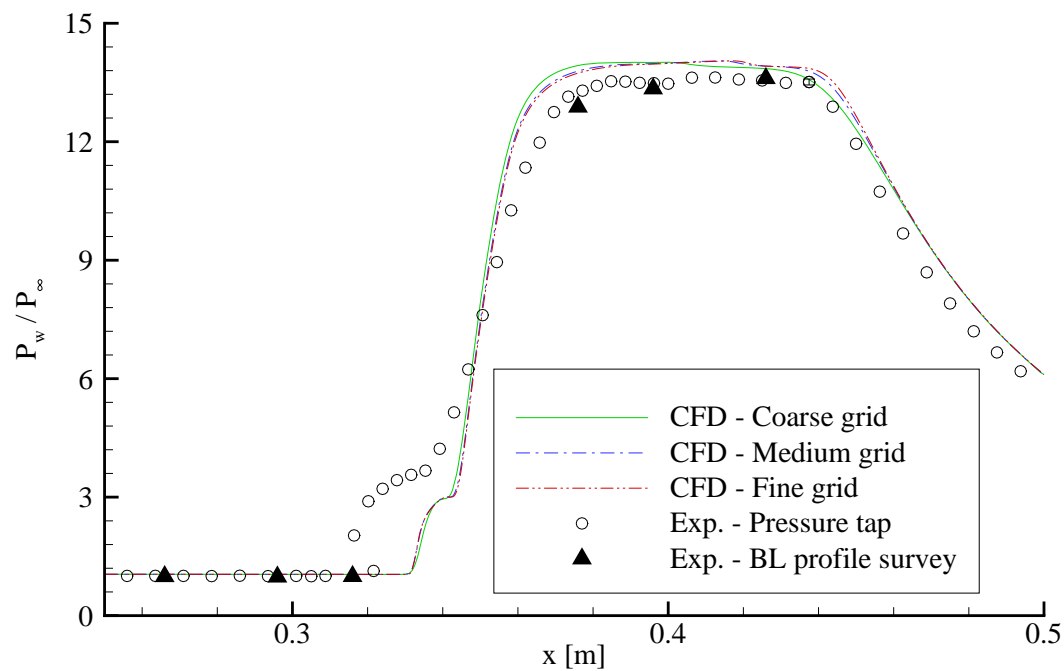


Figure 25. Wall pressure ratios for the G14 case.

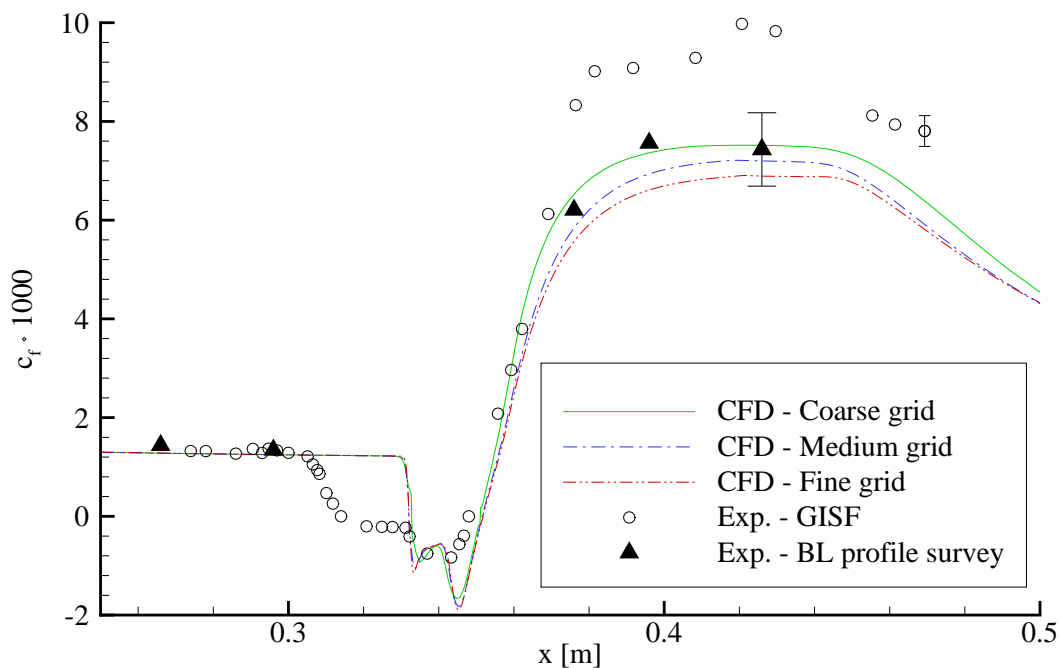


Figure 26. Skin friction for the G14 case.

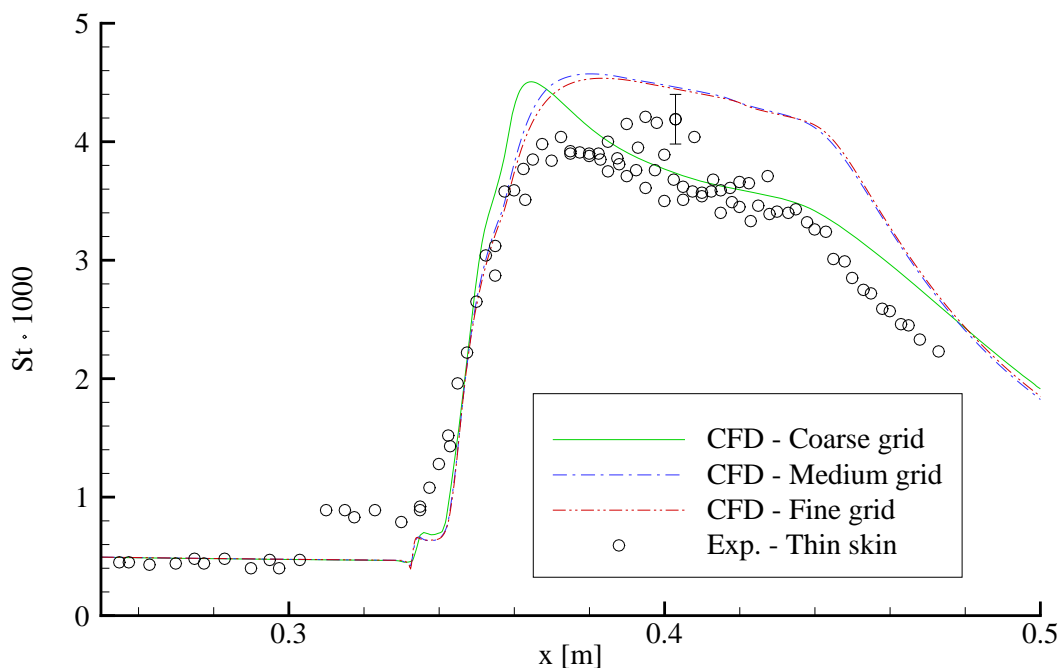


Figure 27. Heat transfer for the G14 case.

The heat transfer along the wall is plotted in figure 27. As with the wall pressure and skin friction results, the computational simulations show a more abrupt rise and lack the initial spread out effects of the separation, due to the difference in location and length of the separation bubble. The medium and fine grids show convergence to the same solution. However, the coarse grid solution shows a steeper rise in overpredicting heat transfer after the flow reattaches, followed by a drop and plateau below the other two solutions. This is most likely due to a lack of grid resolution in the region following the interaction. As a result, the coarse grid is unable to handle the non-equilibrium boundary layer produced by the interaction. Compared with the experimental data scatter, the medium and fine grid simulations over predict the heat transfer by roughly 13% for this case.

E. LF12 Case, Sharp Fin at 12°

In the LF12 case, a sharp fin is set at an angle of attack to the freestream flow, β , of 12°. This results in a swept SWTBLI and associated 3-D flow. Results from the medium grid are used to highlight features of the interaction and ensure the expected structure is present. In figure 28, a density contour plot near the exit plane ($x = 250$ mm) is given, with some of the separation structure clearly identified. Figure 29 is a contour plot of heat transfer on the plate with streamlines of the flow near the surface, making the interaction footprint easier to identify. From the streamlines and density contours, it was determined that the upstream influence, primary separation, shock, and primary reattachment angles were 31.7°, 29.5°, 21.1°, and 14.9° respectively. In the experiment, a thin mixture of mineral oil and oil-based paint was used to visualize the interaction footprint. The reported angles for upstream influence, primary separation, shock, and primary reattachment are 31.7°, 29.2°, 21.3°, and 15.2° respectively.

The ratio of pressure on the plate to freestream pressure at streamwise locations of 98 mm and 168 mm from the fin LE are given in figures 30 and 31 respectively. In these figures, the primary reattachment ($z/x \sim 0.275$), shock ($z/x \sim 0.375$), and primary separation ($z/x \sim 0.65$) locations are identifiable. The solutions from all three grids have converged together except at the primary reattachment and separation locations, indicating that the separation vortex is not properly resolved. In general, the predicted wall pressure is in good agreement with the experimentally measured values.

Figure 32 gives a comparison of the heat transfer along the plate at $z = 74.5$ mm for all three grids with the experiment. The medium and fine grid solutions have converged almost on top of one another, while the coarse grid solution shows deviation, both before the fin LE and near the outlet. In addition, the medium and fine grids appear

to resolve the primary separation region (near $x = 140$ mm) demonstrating an “S-bend”, while the coarse grid solution smears this feature. In the simulations, the plate is treated as an isothermal surface, but the experimental measurements showed the plate did have some temperature variation leading up to the primary separation location. This explains the general flat trend of the simulations compared to the oscillation in the experimental measurements in the region upstream of the primary separation. As with the 2-D impinging interaction cases, the heat transfer rate is over predicted following the separation vortex by roughly 20%.

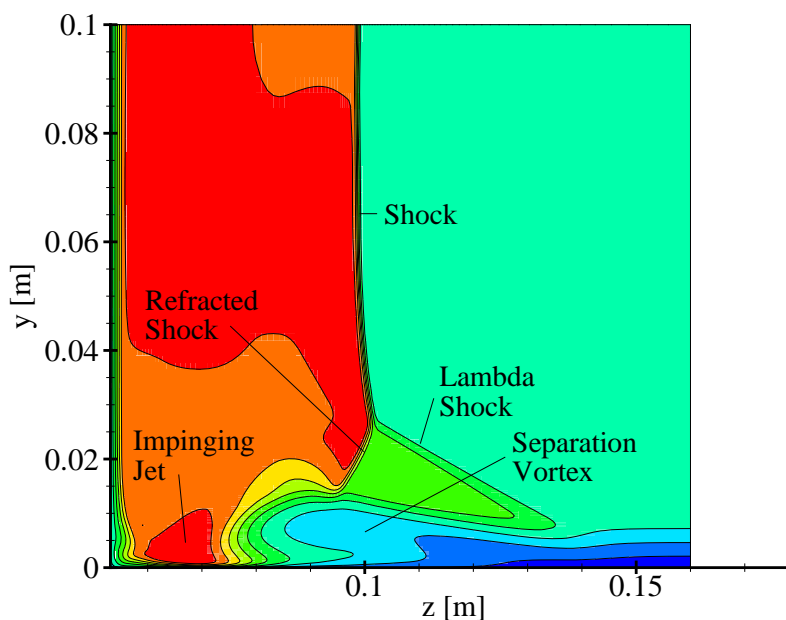


Figure 28. Density contour plot of outlet plane for the LF12 case.

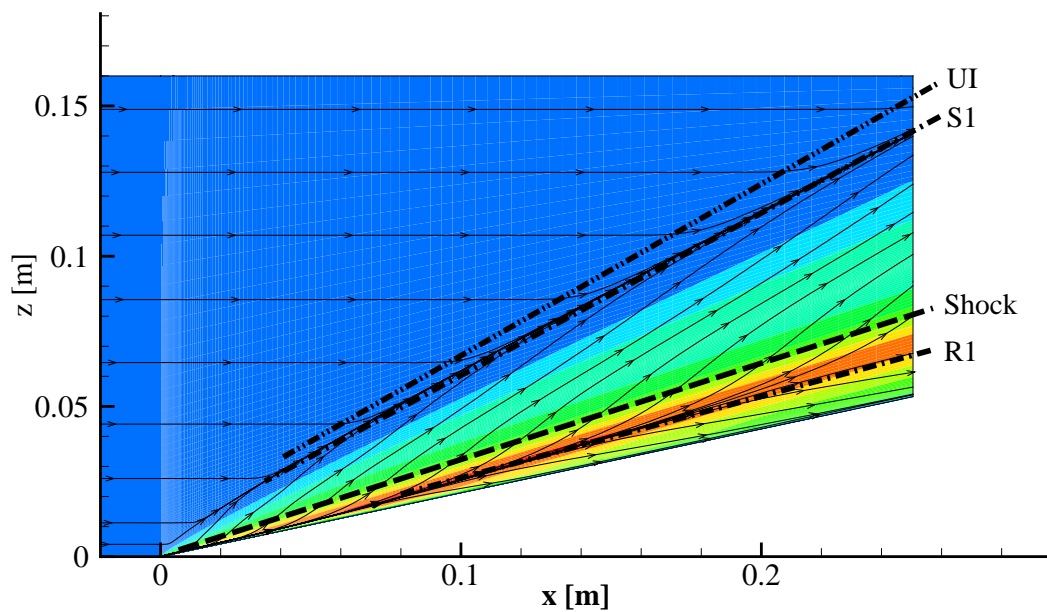


Figure 29. Contour of heat transfer on the plate for the LF12 case, with streamlines of velocity near the surface and main elements of the interaction footprint highlighted.

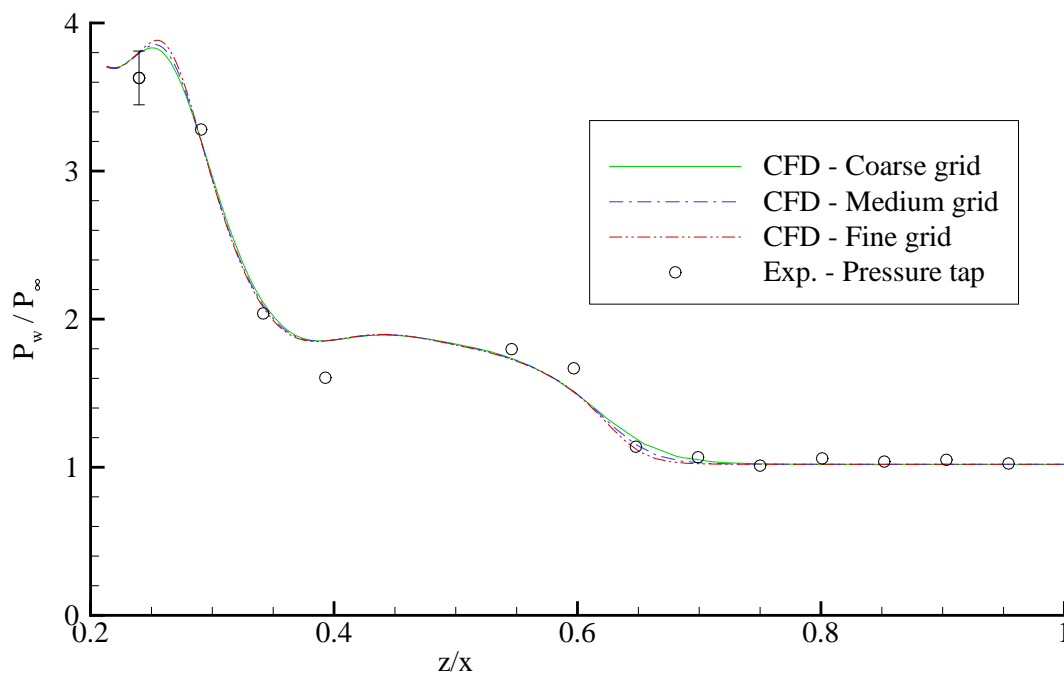


Figure 30. Wall pressure ratios along the plate at $x = 98$ mm for the LF12 case.

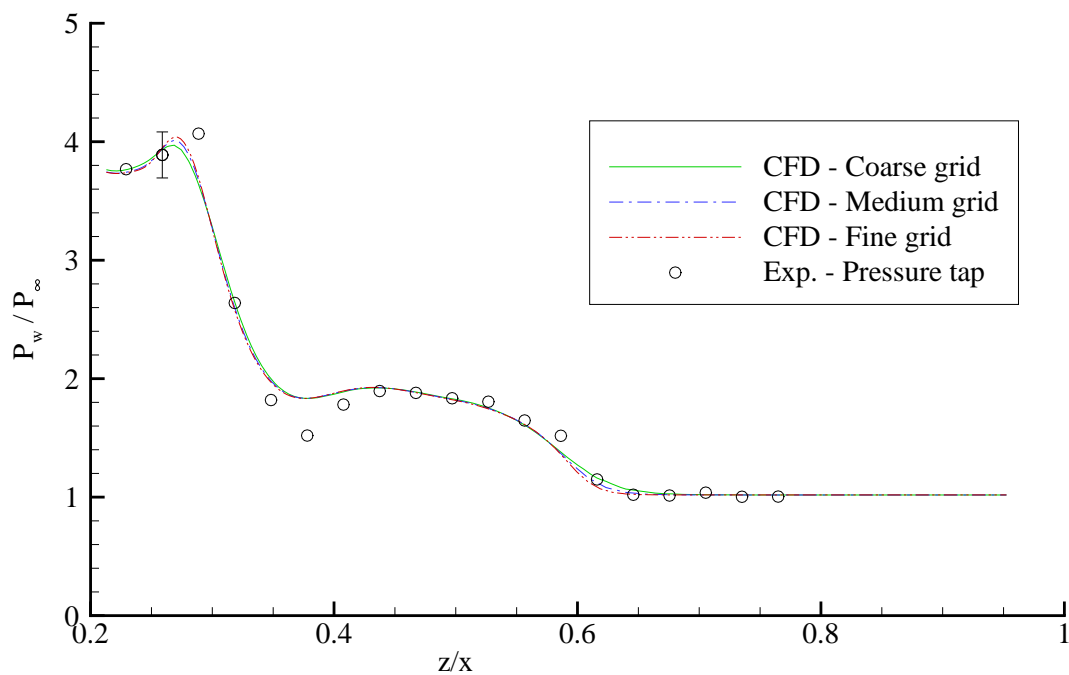


Figure 31. Wall pressure ratios along the plate at $x = 168$ mm for the LF12 case.

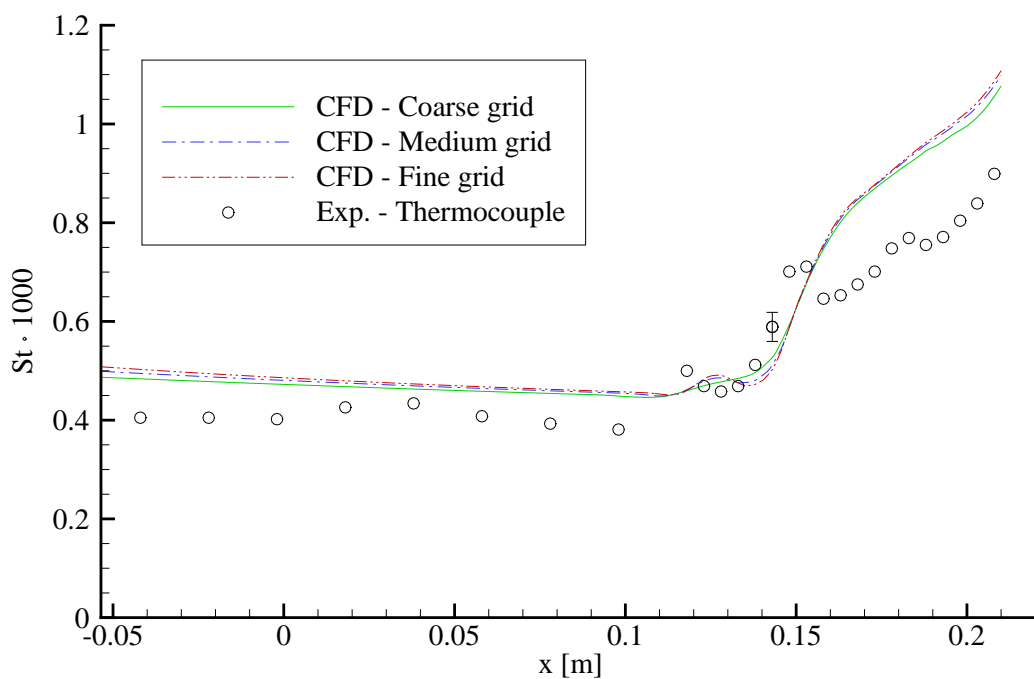


Figure 32. Heat transfer along the plate at $z = 74.5$ mm for the LF12 case.

F. LF23 Case, Sharp Fin at 23°

For the LF23 case, the sharp fin is set at an angle of attack to the freestream flow, β , of 23°, resulting in a swept SWTBLI and fully 3-D flow. Results from the medium grid are once again used to highlight features of the interaction for this case and ensure that the proper structure is present. In figure 33, a density contour plot near the exit plane ($x = 210$ mm) is given, with the main aspects of the separation structure clearly identified. Figure 34 is a contour plot of heat transfer on the plate with streamlines of the flow near the surface (making the interaction footprint clearer to see), with the main structures of the footprint identified. As with the LF12 case, streamlines and density contours were used to determine the upstream influence, primary separation, shock, and primary reattachment angles which were 50.3°, 48.2°, 33.0°, and 27.0° respectively. The reported angles for upstream influence, primary separation, shock, and primary reattachment are 49.8°, 48.82°, 33.3°, and 27.6° respectively.

The ratio of pressure on the plate to freestream pressure at streamwise locations of 83 mm, 123 mm, and 153 mm from the fin LE are given in figures 35 through 37 respectively. In these figures, the primary reattachment ($z/x \sim 0.5$), shock ($z/x \sim 0.61$), and primary separation ($z/x \sim 1.1$) locations are readily identifiable. In general, the solutions from all three grids have converged together except at the primary reattachment and separation locations, indicating that the separation vortex is not being properly resolved. Deviation of the solutions from the measured pressure are most noticeable at the shock and primary separation locations.

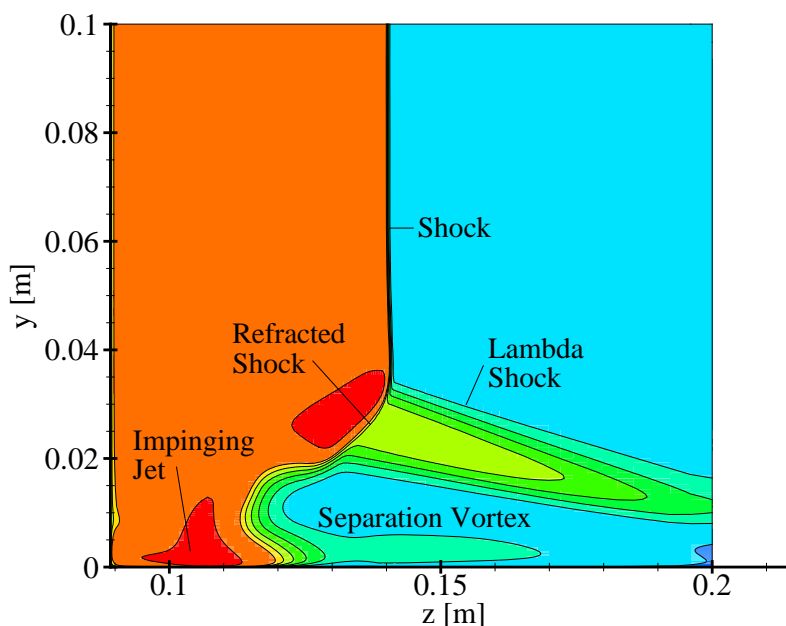


Figure 33. Density contour plot of outlet plane for the LF23 case.

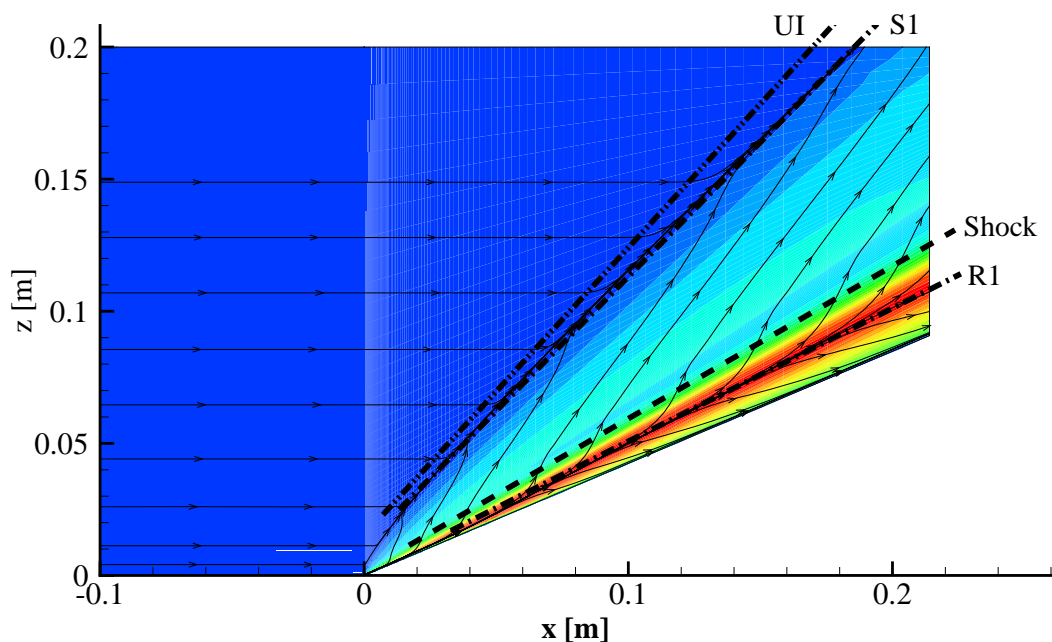


Figure 34. Contour of heat transfer on the plate for the LF23 case, with streamlines of velocity near the surface and main elements of the interaction footprint highlighted.

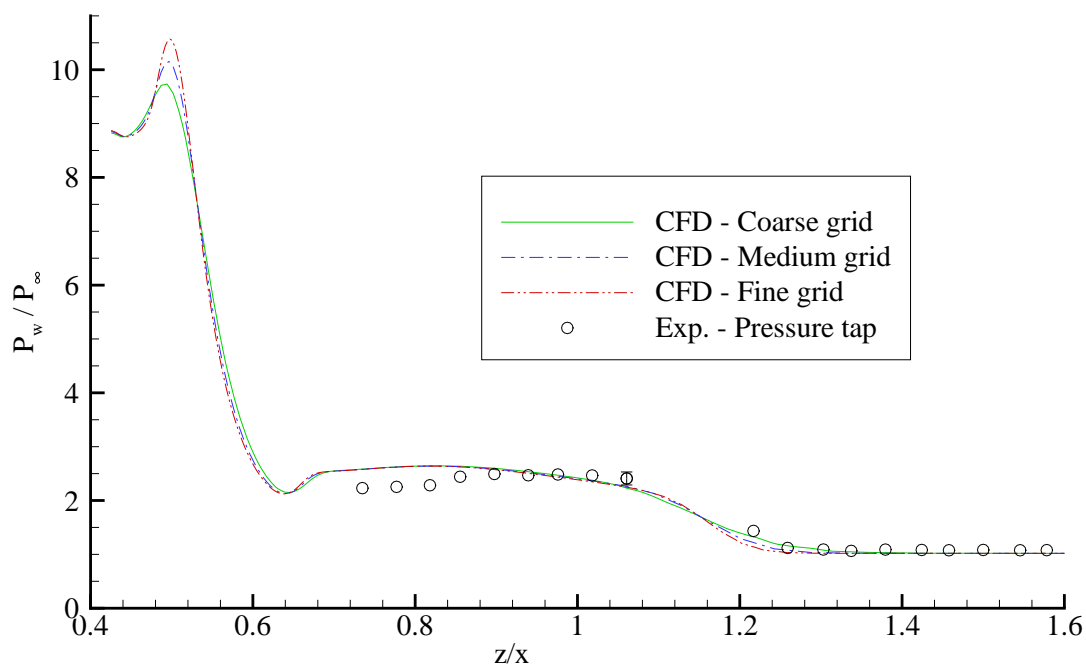


Figure 35. Wall pressure ratios along the plate at $x = 83$ mm for the LF23 case.

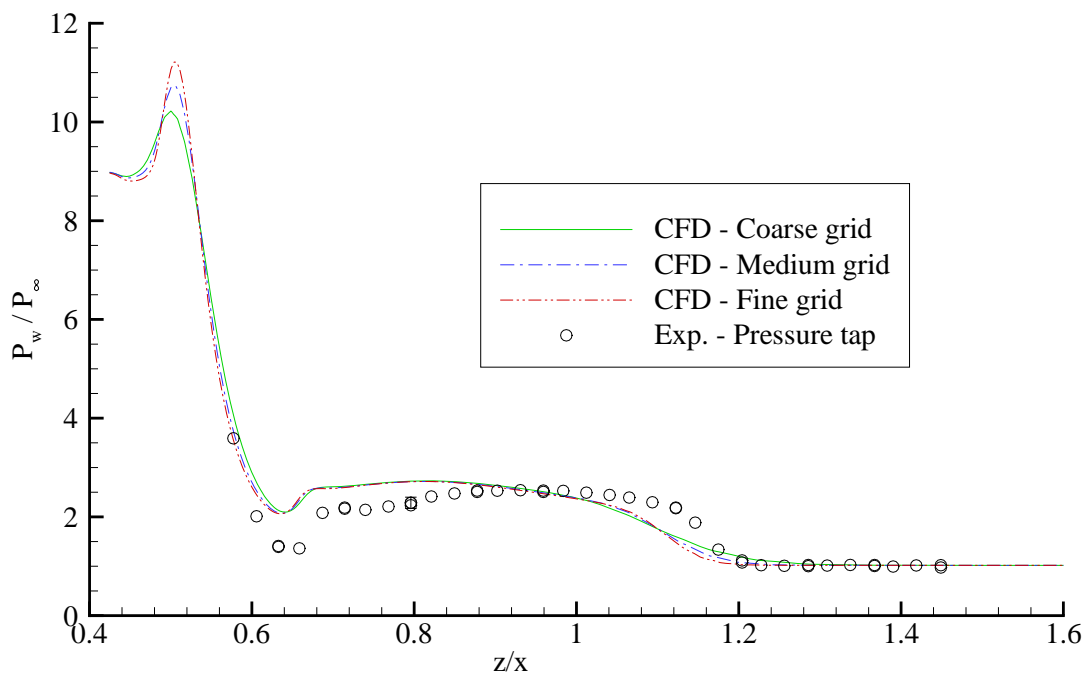


Figure 36. Wall pressure ratios along the plate at $x = 123$ mm for the LF23 case.

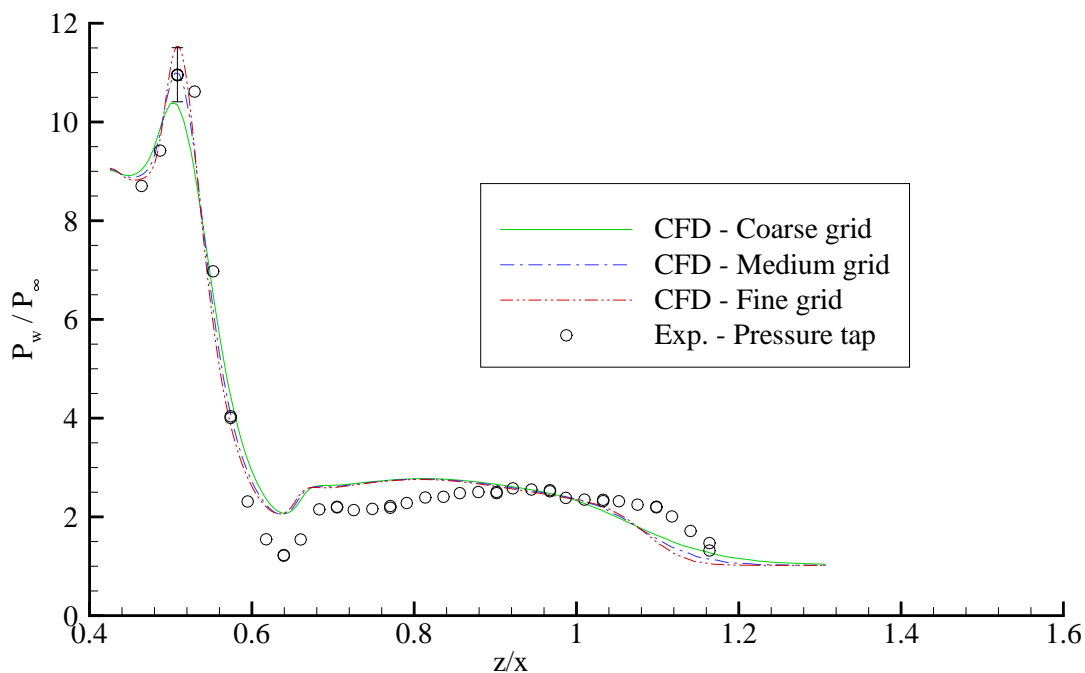


Figure 37. Wall pressure ratios along the plate at $x = 153$ mm for the LF23 case.

While not available for the LF12 case, skin friction measurements at three streamwise locations are available for the LF23 case. Figures 38 through 40 show comparisons of the measured skin friction (using the GISF method) with simulation predictions from all three grids for $x = 82$ mm, $x = 122$ mm, and $x = 162$ mm respectively. These figures show a general trend that the peak skin friction, which occurs at the reattachment location, is under predicted

the most by the coarse grid solution and predicted the closest by the fine grid solution. Despite this, all three grid solutions predict the reattachment location fairly accurately. Since the number of cells in the reattachment region increases going from the coarse to the medium grid solutions, and again from the medium to fine grid solution, the grid cell density in the reattachment region is shown to play a significant role in predicting the peak skin friction magnitude, but not location. Aside from the region of reattachment, all three grid solutions have converged on top of one another.

In figure 38, the secondary separation vortex ($z/x \sim 0.65$) is not resolved well by the simulations and they do not demonstrate the same sharp drop in skin friction as measured by the experiment. Similarly, the simulations do not capture the primary separation location ($z/x \sim 1.2$) clearly and do not show the signature “S-bend” as captured in the experimental measurements. Figures 39 and 40 show the same trends, with the secondary separation vortex and primary separation location not being well resolved.

Figure 41 gives a comparison of the heat transfer along the plate at $z = 121$ mm for all three grids to the experimental measurements. Solutions from all three grids show good convergence to each other except near the reattachment region (near $x \sim 185$ mm), where the coarse grid shows the quickest drop in heat transfer, followed by the medium grid. Upon closer inspection, the fine grid solution shows a small spike in heat transfer right before the reattachment point, which is also just noticeable in the experimental measurements. As in the LF12 case, the experimental measurements show a slight oscillation in the heat transfer along the plate leading up to the primary separation point, while the simulations used an isothermal condition for the plate, while the plate in the experiment showed slight fluctuations in surface temperature. As with the LF12 case, heat transfer is over predicted by as much as 30% following the separation location. It is also worth pointing out that the increase in heat transfer after separation is steeper in the simulations than in the experimental measurements.

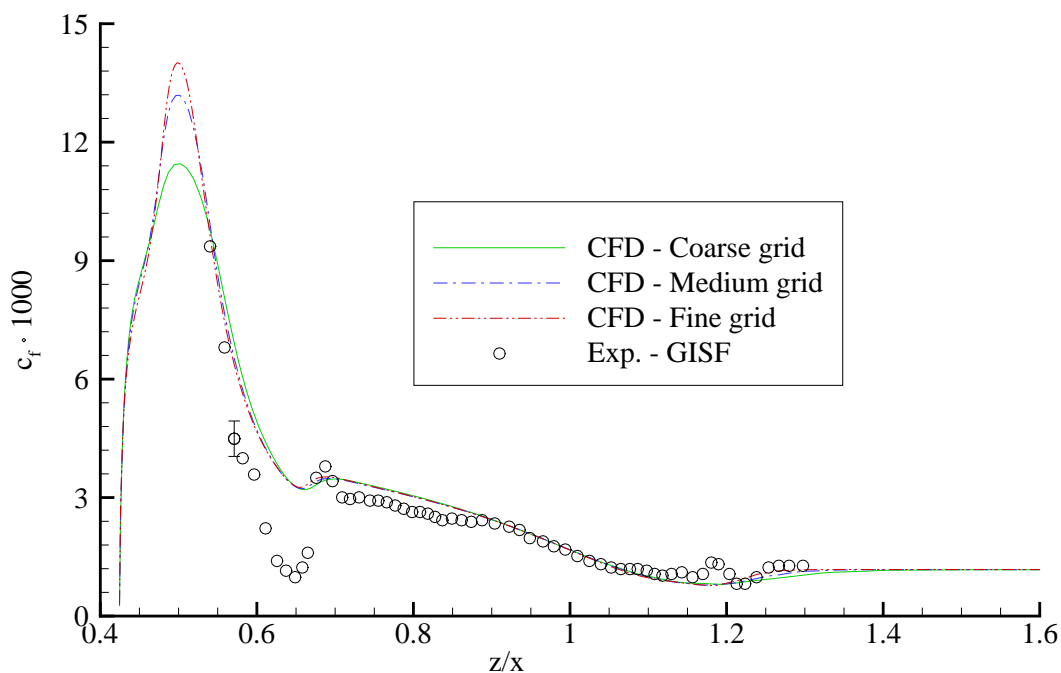


Figure 38. Skin friction along the plate at $x = 82$ mm for the LF23 case.

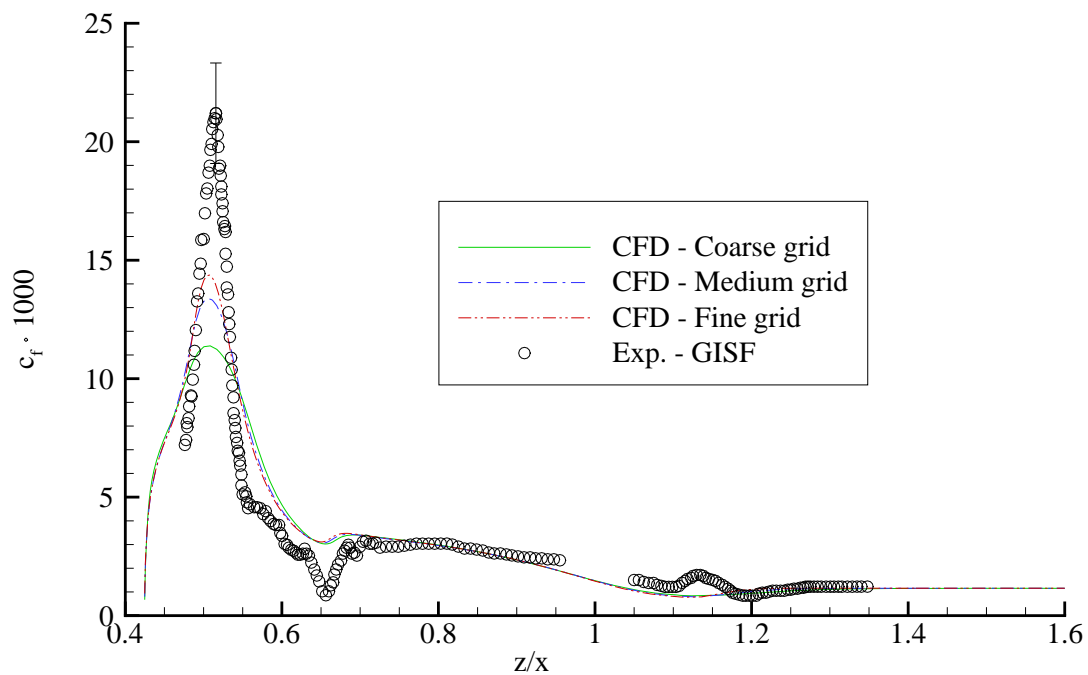


Figure 39. Skin friction along the plate at $x = 122$ mm for the LF23 case.

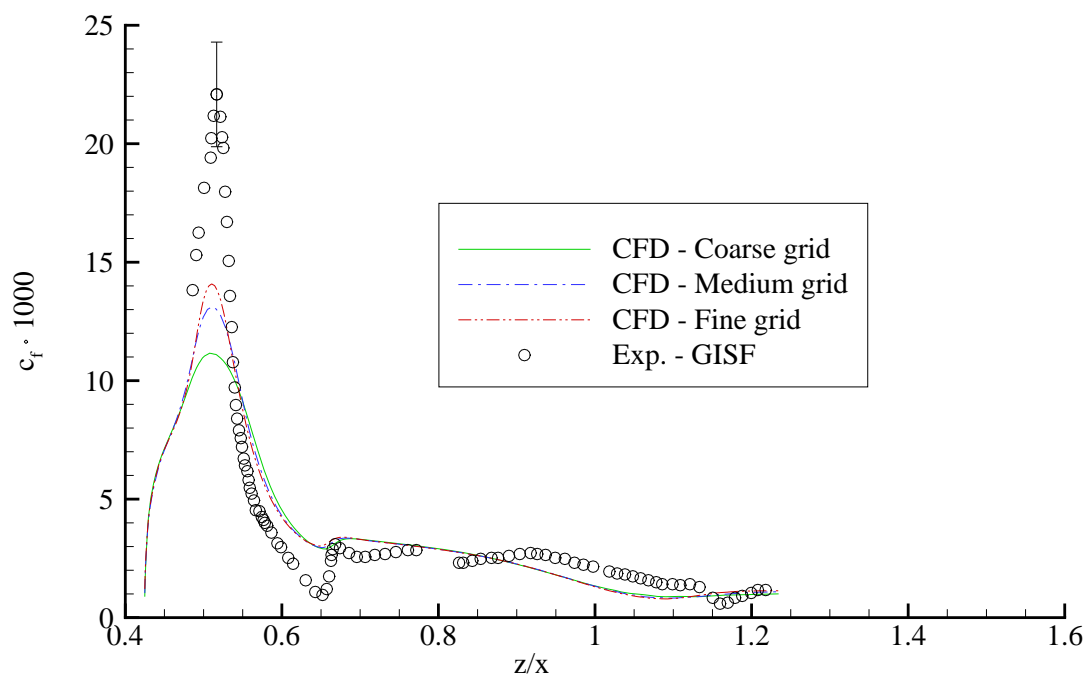


Figure 40. Skin friction along the plate at $x = 162$ mm for the LF23 case.

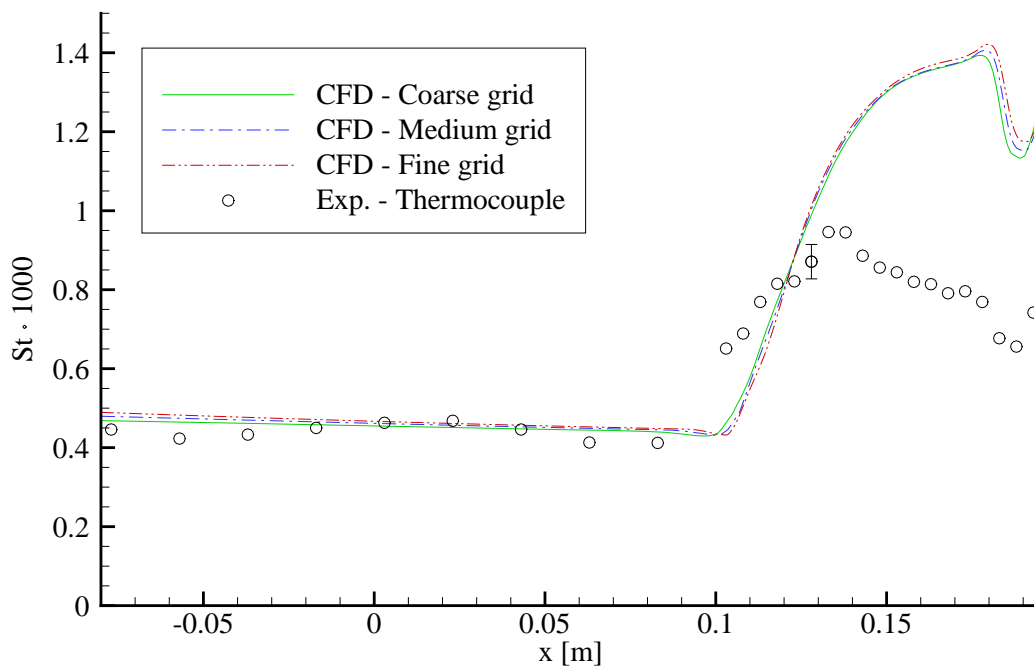


Figure 41. Heat transfer along the plate at $z = 121$ mm for the LF23 case.

VI. Conclusions

Simulations for three 2-D impinging and two 3-D swept SWTBLI cases were performed using a RANS solver, with three successively refined grids for each case. The results show that wall pressure can be predicted fairly accurately, while skin friction tends to be under predicted and heat transfer over predicted. The level of over and under prediction is increased with the strength of the interaction. This is mostly due to the limitations of the turbulence model in predicting and handling separation. In the G10 and G14 cases, the predicted separation bubble length was approximately half the length measured in the experiment. For the G14 case, the coarse grid lacked the resolution to handle the non-equilibrium boundary layer produced by the interaction, which was more apparent in the heat transfer than skin friction predictions. Additionally, the inherently unsteady nature of the separation bubble makes predicting such interaction difficult. Despite the lack of accuracy in predicting skin friction and heat transfer, the RANS simulations do show the same trends as in the measured experimental data. This ability to capture such trends in skin friction and heat transfer do make RANS simulations useful for early design work and for evaluating general configuration changes in design space.

VII. Acknowledgments

This project was funded in part by AFOSR contract LRIR12RB01COR, monitored by Dr. J. Schmisser, AFOSR/RTE. The authors wish to thank the Air Force Research Laboratory Department of Defense Supercomputing Resource Center AFRL/DSRC for computer time and Prof. G. Candler for the use of the US3D solver. The authors also thank Dr. R. Gosse and Dr. N. Bisek for their helpful and insightful discussions in performing these calculations.

VIII. References

- ¹ Knight, D. and Yan, H., "RTO WG 10: CFD Validation for Shock Wave Turbulent Boundary Layer Interactions," AIAA Paper No. 2002-0437
- ² Maicke, B. A., and Majdalani, J., "Evaluation of CFD Codes for Hypersonic Flow Modeling," AIAA Paper No. 2010-7184
- ³ Blottner, F. G., "Accurate Navier Stokes Results for the Hypersonic Flow Over a Spherical Nostetip," Journal of Spacecraft and Rockets, Vol. 27, No. 2, pp. 113-122, March, 1990
- ⁴ Reed, H. L., "Computational Fluid Dynamics Validation Issues in Transition Modeling," AIAA Journal, Vol. 36, No. 5, pp. 742-751, May, 1998
- ⁵ Christopher, R. J., and Blottner, F. G., "Review and Assessment of Turbulence Models for Hypersonic Flows: 2D/Axisymmetric Cases," AIAA Paper No. 2006-0713
- ⁶ Zheltovodov, A., "Shock Waves/ Turbulent Boundary Layer Interactions - Fundamental Studies and Applications," AIAA Paper No. 1996-1977
- ⁷ Knight, D., Yan, H., Panaras, A. G., and Zheltovodoc, A., "Advances in CFD Prediction of Shock Wave Turbulent Boundary Layer Interaction," Progress in Aerospace Sciences, Vol. 39, 2003, pp. 121-184
- ⁸ Schülein, E., Krogmann, P., and Stanewsky, E., "Documentation of Two-Dimensional Impinging Shock /Turbulent Boundary Layer Interaction Flow," DLR, German Aerospace Center, Report IB 223-96A49, Gottingen, Germany, Oct. 1996
- ⁹ Delery, J. and Marvin, J.G., "Shock-Wave Boundary Layer Interactions," AGARD-AG-280, 1986
- ¹⁰ Dolling D. S., Brusniak L., "Separation Shock Motion in Fin, Cylinder, and Compression Ramp-Induced Turbulent Interactions," AIAA Journal, Vol. 27, 1989, pp. 734-742
- ¹¹ Brown, J. L., "Hypersonic Shock Wave Impingement on Turbulence Boundary Layers: Computational Analysis and Uncertainty," Journal of Spacecraft and Rockets, Vol. 50, No. 1, Jan, 2013
- ¹² Brown, J. L., Kussoy, M. I., and Coakley, T. J., "Turbulent Properties of Axisymmetric Shock-Wave/Boundary-Layer Interaction Flows," Turbulent Shear-Layer/Shock-Wave Interactions, edited by J. Delery, Springer-Verlag, Berlin, 1986, pp. 137-148
- ¹³ Fedorova, N. N., and Fedorchenko, I. A., "Computation of Interaction of an Incident Oblique Shock Wave with a Turbulent Boundary Layer on a Flat Plate," Journal of Applied Mechanics and Technical Physics, Vol. 45, No. 3, 2004, pp. 358-336
- ¹⁴ Bisek, N. J., Rizzetta, D. P., and Poggie, J., "Plasma Control of a Turbulent Shock Boundary-Layer Interaction," AIAA Journal, Vol. 51, No. 8, 2013, pp. 1789-1804
- ¹⁵ Panaras, A. G., "Review of the Physics of Swept Shock/Boundary Layer Interaction," Progress in Aerospace Sciences, Vol. 32, 1996, pp. 173-244
- ¹⁶ Zheltovodov, A.A., "Shock Waves/Turbulent Boundary-Layer Interactions – Fundamental Studies and Applications," AIAA Paper No. 96-1977
- ¹⁷ Knight, D., Yan, H., Panaras, A. G., and Zheltovodov, A., "Advances in CFD Prediction of Shock Wave Turbulent Boundary Layer Interactions," Progress in Aerospace Sciences, Vol. 39, 2003, pp. 121-184
- ¹⁸ Schülein, E. and Zheltovodov, A. A., "Documentation of Experimental Data for Hypersonic 3-D Shock Waves/Turbulent Boundary Layer Interaction Flows," DLR, German Aerospace Center, Report IB 223-99A26, Gottingen, Germany, Mar. 2001
- ¹⁹ Rodi, P. E., Dolling, D. S., and Knight, D. D., "An Experimental/Computational Study of Heat Transfer in Sharp Fin Induced Turbulent Interactions at Mach 5," AIAA Paper No. 91-1764
- ²⁰ Schmisser, J. D., and Dolling, D. S., "Fluctuating Wall Pressures Near Separation in Highly Swept Interactions," AIAA Journal, Vol. 32, No. 6, 1994, pp. 1151-1157
- ²¹ Schülein E., "Skin Friction and Heat Flux Measurements in Shock Boundary Layer Interaction Flows," AIAA-Journal, Vol.44, No.8, Aug. 2006, pp.1732-1741
- ²² Steelant, J., "Effect of a Compressibility Correction on Different Turbulence Models," Engineering Turbulence Modeling and Experiments 5, edited by W. Rodi and N. Fueyo, Elsevier, New York, 2002, pp. 207-216
- ²³ Lenahan, K. "Mach 5 Shock Wave Boundary Layer Interaction," NPARC Alliance Validation Archive, NASA Glenn Research Center, Ohio, Nov., 2011 [<http://www.grc.nasa.gov/WWW/wind/valid/M5SWBLI/M5SWBLI.html> Accesses 5/7/2013]
- ²⁴ Lindblad, I. A. A., Wallin, S., Johansson, A. V., Friedrich, R., Lechner, R., Krogmann, P., Schulein, E., Courty, J. C., Ravachol, M., and Giordano, D., "A Prediction Method for High Speed Turbulent Separated Flows with Experimental Verification," AIAA Paper No. 1998-2547

- ²⁵ Nompelis, I., Dryna, T., and Candler, G., "Development of a Hybrid Unstructured Implicit Solver for the Simulation of Reacting Flows over Complex Geometries," AIAA Paper 2004-2227
- ²⁶ MacCormack, R., and Candler, G., "The Solution of the Navier-Stokes Equations Using Gauss-Seidel Line Relaxation," *Computers and Fluids Journal*, Vol. 17, No. 1, 1989, pp. 135-150
- ²⁷ Hirsch, C., *Numerical Computations of Internal and External Flows*, Wiley, New York, 1991
- ²⁸ Nompelis, I., Dryna, T., and Candler, G., "A Parallel Unstructured Implicit Solver for the Simulation of Reacting Flow Simulation," AIAA Paper 2005-4867
- ²⁹ Nompelis, I., *Computational Study of Hypersonic Double-Cone Experiments for Code Validation*, Ph.D. Thesis, Univ. of Minnesota, 2004
- ³⁰ MacCormack, R., and Candler, G., "The Solution of the Navier-Stokes Equations Using Gauss-Seidel Line Relaxation," *Computers and Fluids Journal*, Vol. 17, No. 1, 1989, pp. 135-150
- ³¹ Candler, G., and MacCormack, R., "The Computation of Hypersonic Ionized Flows in Chemical and Thermal Nonequilibrium," *Journal of Thermophysics and Heat Transfer*, Vol. 5, No. 3, 1991, pp. 266-273
- ³² Kim, S.-E., Makaroy, B., and Caraeni, D., "A Multi-Dimensional Linear Reconstruction Scheme for Arbitrary Unstructured Grids," AIAA Paper 2003-3990
- ³³ MacCormack, R., "Current Status of the Numerical Solutions of the Navier-Stokes Equations," AIAA Paper 1985-0032
- ³⁴ Wright, M., Candler, G., and Bose, D., "Data-Parallel Line Relaxation Method for the Navier-Stokes Equations," AIAA Journal, Vol. 36, No. 9, 1998, pp. 1603-1609
- ³⁵ Yoder, D. A., "Wind-US User's Guide," The NPARC Alliance, NASA Glenn Research Center, Ohio, Mar., 2012, pp. 314
- ³⁶ Allmaras, S. R., Johnson, F. T., Spalart, P. R., "Modification and Clarifications for the implementation of the Spalart-Allmaras Turbulence Model," ICCFD7 Paper 1902
- ³⁷ Huang, P. G., Bradshaw, P., and Coakley, T. J., "Skin Friction and Velocity Profile Family of Compressible Turbulent Boundary Layers," AIAA Journal, Vol. 31, No. 9, Sep., 1993, pp. 1600-1604
- ³⁸ Spalding, D. B., "A Single Formula for the Law of the Wall," *Journal of Applied Mechanics*, Vol. 28, pp. 455-457

Appendix C

Transitional / Turbulent Boundary Layers

Implicit Large-Eddy Simulation of a Supersonic Turbulent Boundary Layer: Code Comparison

Jonathan Poggie,^{*} Nicholas J. Bisek,[†] Timothy Leger,[‡] and Ricky Tang[§]

Air Force Research Laboratory, Wright-Patterson AFB, Ohio 45433-7512 USA

High-fidelity, implicit large-eddy simulations of a Mach 2.9 turbulent boundary layer flow have been carried out using three different computational fluid dynamics codes. The three codes (FDL3DI, HOPS, and US3D) employ the same formal order of spatial and temporal accuracy. The aim of the work was to compare code performance and accuracy, and to identify best practices for large-eddy simulations with the three codes. The simulations were carried out using the same boundary conditions, body force trip mechanism, grids, and time-step. Additional calculations were carried out to compare the results obtained with different numerical algorithms, and to explore correlations characterizing large-scale structures in the flow turbulence. All three codes were able to produce plausible turbulent boundary layers, and showed good agreement in the region where the boundary layer was well developed. The details of the transition process, however, varied with the numerical method and the details of its execution. In particular, coarser grids and more dissipative numerical schemes led to delayed transition to turbulence in the calculations. The body-force trip method was employed successfully in each case, and should be suitable for general application. Many of the features of the large-scale structures were found to match between computation and experiment, but additional work is warranted to explore the use of such comparisons to validate large-eddy simulation codes.

I. Introduction

Large-eddy simulation (LES) is becoming a useful engineering tool for the design of high-speed air vehicles. While Reynolds-averaged Navier-Stokes (RANS) simulations can be effective for flows with weak boundary layer effects, they generally perform poorly for flows with strong three-dimensionality, and very poorly for separated flows. Large-eddy simulation may be able to fill this gap in the portfolio of computational tools for aircraft design. It is thus important to assess the accuracy of large-eddy simulation as an engineering tool, in particular to investigate how the omission of the small scales affects the structure of the flow turbulence, and how the choice of numerical algorithm and code implementation affects the computational results.

In the present project, high-fidelity, implicit large-eddy simulations (HFILES) of a supersonic, turbulent boundary layer flow were performed using three different high-order computational fluid dynamics codes: FDL3DI^{1,2} and HOPS,³⁻⁶ developed at the Air Force Research Laboratory, and US3D,^{7,8} developed at the University of Minnesota. The FDL3DI code has been extensively validated for large-eddy simulation, and a growing body of work is being produced with US3D. The HOPS code was developed for plasma simulations, but has been recently been adapted for large-eddy simulation.

Both FDL3DI and HOPS are finite-difference, structured-grid codes, whereas US3D is an unstructured, finite-volume code. All three codes can employ sixth-order accurate spatial discretization and second-order accurate, implicit time advancement. The simulations were performed using the same grids, time-step, and numerical trip. With three different, independent code implementations, the comparison of numerical results helps to identify errors in coding and procedure, and assess the relative merits of the numerical algorithms. This project has also proved to be a useful exercise for identifying best practices for carrying out large-eddy simulations with the three codes.

^{*}Senior Aerospace Engineer, Aerospace Systems Directorate. Associate Fellow AIAA.

[†]Research Aerospace Engineer, Aerospace Systems Directorate. Senior Member AIAA.

[‡]Research Scientist, Ohio Aerospace Institute. Member AIAA.

[§]Research Scientist, Universal Technology Corporation. Presently at Sandia National Laboratory. Member AIAA.

II. Numerical Methods

High-fidelity, implicit large-eddy simulations were carried out with three, independently implemented computer codes. The baseline numerical scheme for all three solvers included nominally sixth-order accurate spatial differencing, and implicit, second-order accurate time integration. All three codes include the option of switching to a lower-order, upwind scheme in the vicinity of a shock. For a general review of higher order numerical methods for high-speed flows, see Pirozzoli.⁹

A. US3D

The US3D code is an unstructured, finite volume solver developed by G. Candler's group at the University of Minnesota.⁷ The code solves the compressible Navier-Stokes equations using a cell-centered, finite-volume formulation. For the calculations of both the inviscid and viscous fluxes, gradients of flow variables are computed using a weighted least squares method.¹⁰

In the present work, the inviscid fluxes were evaluated using the low-dissipation, kinetic energy preserving scheme of Subbareddy and Candler.⁸ In this formulation, the inviscid fluxes F are computed as the combination of a non-dissipative symmetric component F_s and an upwinded dissipative component F_d multiplied by a shock detecting switch α :

$$F = F_s + \alpha F_d \quad (1)$$

The parameter $\alpha \in [0, 1]$ is chosen so that the dissipative portion of the flux evaluation is only used in regions near discontinuities. The present work employed the Ducros¹¹ switch:

$$\alpha = \frac{(\vec{\nabla} \cdot \vec{u})^2}{(\vec{\nabla} \cdot \vec{u})^2 + \|\vec{\omega}\|^2} \quad (2)$$

where \vec{u} and $\vec{\omega}$ are the velocity and vorticity vectors, respectively.

Spatial derivatives of the inviscid fluxes were evaluated using a sixth-order accurate, gradient-based interpolation scheme¹² with the following form:

$$\phi_{i+\frac{1}{2}} = \frac{\phi_i + \phi_{i+1}}{2} + \frac{8(\delta\phi_i + \delta\phi_{i+1})}{15} - \frac{\delta\phi_{i-1} + \delta\phi_{i+2}}{45} \quad (3)$$

Here $\delta\phi_i$ is the scalar (dot) product of the gradient of ϕ in Cell i and the vector from the center of Cell i to the center of Face $i + \frac{1}{2}$. The viscous fluxes were evaluated using a second-order accurate central difference scheme.

The current computations were carried out using the perfect gas assumption. Second-order accurate, implicit time integration was employed.¹³

B. HOPS and FDL3DI

Two codes developed at the Air Force Research Laboratory (AFRL) were also used in this study. The FDL3DI code^{1,2} was named for the Flight Dynamics Laboratory, a precursor organization to AFRL. This code is a high-order accurate, structured-grid, finite-difference solver for the perfect-gas, compressible-flow Navier-Stokes equations. The HOPS (Higher Order Plasma Solver) code³⁻⁶ is a multi-fluid code developed for plasma computations. The code includes several physical models, but here it is employed as a single-fluid gasdynamics code. Employed in this way, the two codes represent independent implementations of essentially the same numerical approach.

Time integration of the conservation equations was carried out in the baseline approach using a second-order implicit scheme, based on a three-point backward difference of the time terms. The general formulation is similar to the standard technique of Beam and Warming.¹⁴ Approximate factoring and quasi-Newton subiterations were employed, with three applications of the flow solver per time step. The implicit terms were evaluated using the scalar pentadiagonal formulation of Pulliam and Chaussee.¹⁵ For comparison, a fourth-order, explicit Runge-Kutta method was employed for some of the calculations.

The baseline spatial differencing scheme was based on compact differencing and filtering.^{1,16} In one dimension, the finite difference approximation to the first derivative ϕ'_i at Node i is evaluated by solving a

Parameter	Value
δ_0	5.375 mm
U_∞	604.5 m/s
p_∞	2.303 kPa
T_∞	108.1 K
T_w	269.5 K
M_∞	2.9
U_∞/ν_∞	$6.0 \times 10^6 \text{ m}^{-1}$

Table 1. Flow conditions for Mach 2.9 turbulent boundary layer.

tridiagonal system of the form:

$$\alpha\phi'_{i-1} + \phi'_i + \alpha\phi'_{i+1} = a \frac{\phi_{i+1} - \phi_{i-1}}{2} + b \frac{\phi_{i+2} - \phi_{i-2}}{4} \quad (4)$$

where α , a , and b are constants chosen to give a certain order of accuracy and set of spectral properties for the scheme.

Numerical stability was enforced using a low-pass, Padé-type, non-dispersive spatial filter. The filtering approach replaces the computed value ϕ_i at a particular node with a filtered value $\bar{\phi}_i$:

$$\alpha_f \bar{\phi}_{i-1} + \bar{\phi}_i + \alpha_f \bar{\phi}_{i+1} = \sum_{n=0}^N \frac{a_n}{2} (\phi_{i+n} + \phi_{i-n}) \quad (5)$$

where the constants α_f , a_0 , ... a_N are chosen to give appropriate filter properties. The filter was applied to the solution vector, sequentially, in each of the three computational directions, following each sub-iteration for implicit time integration, or each time-step for explicit integration. The order of the filtering operation was permuted at each time step.

The hybrid compact-Roe shock capturing scheme of Visbal and Gaitonde² is employed for flows containing strong shocks, but this was not necessary in the present work. For comparison to the compact difference computations, an additional set of conventional upwind calculations was carried out with a third-order, upwind-biased Roe scheme,¹⁷⁻²⁰ and fourth-order explicit spatial differencing of the viscous and metric terms. These computations did not employ a limiter or filter.

The metrics were evaluated using the method of Thomas and Lombard.²¹

III. Results

The baseline flow investigated here consists of a Mach 2.9, flat-plate turbulent boundary layer. The flow conditions are listed in Table 1, and correspond to those reported for the experiments of Bookey et al.,²² and studied in a number of previous computations.²³ The conditions in the experiments of Spina²⁴ are similar, but correspond to an order of magnitude higher Reynolds number.

The calculation procedure was the same for each of the three computer codes. The inflow boundary condition was provided by a similarity solution of the compressible, laminar boundary layer equations. The boundary layer was tripped to turbulence using the body-force trip method of Mullenix et al.²⁵ No-slip conditions were imposed on the flat-plate surface, with zero normal pressure gradient enforced to third-order accuracy. Periodic boundary conditions were imposed in the spanwise direction. Grid stretching and extrapolation were used to provide outflow boundary conditions.

Two different computational meshes were employed: a coarse grid of 1.1×10^7 points and a fine grid of 7.7×10^7 points. The streamwise extent of the resolved region was $100\delta_0$ and the spanwise extent was $5\delta_0$. Some details of the two grids are listed in Table 2, and the fine mesh is illustrated in Fig. 1.

Table 2 also provides the grid spacing nondimensionalized in inner coordinates using reference conditions at the station $x/\delta_0 = 100$. For flat plate configurations, Georgiadis et al.²⁶ recommend $50 \leq \Delta x^+ \leq 150$, $\Delta y_{\text{wall}}^+ < 1$, and $15 \leq \Delta z^+ \leq 40$ for well-resolved large-eddy simulations, and $10 \leq \Delta x^+ \leq 20$, $\Delta y_{\text{wall}}^+ < 1$,

Quantity	Coarse Mesh	Fine Mesh
N_x	677	1161
N_y	131	261
N_z	130	255
$\Delta x/\delta_0$	2.0×10^{-1}	1.0×10^{-1}
$\Delta y_{\text{wall}}/\delta_0$	4.0×10^{-3}	2.0×10^{-3}
$\Delta z/\delta_0$	4.0×10^{-2}	2.0×10^{-2}
Δx^+	50	28
Δy_{wall}^+	1.0	0.55
Δz^+	10	5.5
$U_\infty \Delta t/\delta_0$	1.0×10^{-3}	1.0×10^{-3}
Δt^+	1.1×10^{-2}	1.2×10^{-2}
Re_θ	5.3×10^3	5.7×10^3

Table 2. Properties of the computational mesh, nondimensionalized using conditions in the vicinity of the reference station $x/\delta_0 = 100$ (HOPS code, C6/F8 scheme).

and $5 \leq \Delta z^+ \leq 10$ for direct numerical simulations. They recommend time steps in the range $\Delta t^+ < 1$. Both grids meet the criteria for well-resolved large-eddy simulation, but not the criteria for direct numerical simulation. In particular, the spacing is relatively coarse in the streamwise direction (x), about a factor of 2.5 too large to meet the recommendations for DNS.

Laminar flow calculations were carried out as a basic check of the codes (Fig. 2). These calculations were carried out on the coarse mesh, in the absence of a boundary layer trip. The similarity solution was provided as the inflow profile at $x = 0$, and a laminar boundary layer developed along the plate in the computations. Boundary layer profiles are shown in Fig. 2a for the $x/\delta_0 = 100$ station, corresponding to the end of the well-resolved region of the computational mesh. The computational results are seen to be in close agreement with the boundary layer similarity solution (marked “Theory”). The normalized skin friction coefficient $C_f \text{Re}_x^{1/2}$ is shown as a function of streamwise distance x/δ_0 along the plate center in Fig. 2b. Again, the agreement between the calculations and the similarity solution is very close.

A. Basic Results

Figure 3 shows an example of an instantaneous flow solution obtained with the HOPS code on the fine grid for the turbulent boundary layer flow. The location of the boundary layer trip is apparent at $x/\delta_0 = 2.5$, both as a bump in the temperature isosurface, and as a Mach wave in the density contours. The flow is transitional in the region up to about $x/\delta_0 = 30$, but farther downstream it appears to be fully turbulent.

To illustrate the region of the flow considered in the detailed analysis presented next, cross-sections of the instantaneous flowfield are given in Fig. 4 and Fig. 5. All the plots correspond to the same instant in time.

Figure 4 shows instantaneous contours of the streamwise mass flux ρu , a quantity that can be measured experimentally with hotwire probes.²⁷ Three planes are shown: an end view in the $x/\delta_0 = 100.00$ plane, a plan view in a plane about halfway through the boundary layer ($y/\delta_0 = 1.43$ or $y/\delta = 0.55$), and a side view plane at the center of the domain ($z/\delta_0 = 2.50$). In all the plots, the highly convoluted interface between the boundary layer and the freestream is apparent. Boundary layer fluid appears to be ejected beyond the mean boundary layer edge ($\delta/\delta_0 \approx 2.6$), and freestream fluid often reaches close to the wall. Within the sectional planes, islands of freestream fluid are sometimes visible wholly surrounded by boundary layer fluid, as are disconnected islands of boundary layer fluid in the freestream. These results are qualitatively consistent with those of flow visualization experiments.²⁸

Corresponding plots of quantities at the wall ($y = 0$) are shown in Fig. 5. Wall pressure fluctuations in turbulent boundary layer flows have been the subject of extensive experimental investigation.²⁹ Figure 5a shows the instantaneous wall pressure, and Fig. 5b shows the magnitude of the wall shear stress. (Shear stress was computed in a post-processing step, using the same compact difference formulation as for the flow

solution.) Structures in the pressure field appear relatively isotropic, whereas structures in the shear stress are elongated in the streamwise direction.

Basic statistical properties of the turbulent boundary flow are given in Fig. 6 for computations employing the HOPS code on each of the two grids. These calculations were carried out using a sixth-order compact difference scheme with eighth-order filtering (C6/F8). Figure 6a shows the skin friction coefficient, averaged in time and across the spanwise direction. Transition is seen to be delayed on the coarse grid relative to the fine grid, with a lower skin friction coefficient in the fully turbulent flow. Profiles of the mean streamwise velocity are shown in van Driest transformed coordinates³⁰ in Fig. 6c for the $x/\delta_0 = 100$ station. The velocity profile for the fine grid case matches theory closely, but the coarse grid case is still transitional.

The effect of the filtering on the transition process is also of interest. The effect of using different filter coefficients in Eq. (5) is shown in Fig. 7. (The filtering method is explained in detail in Refs. 1,16.) Filtering can be carried out for values of the filter coefficient of $-0.5 < \alpha_f < 0.5$, with values closest to $\alpha_f = 0.5$ giving the sharpest cut-off. Here we see that more severe filtering delays transition somewhat, but the effect is not very strong for the typical range of filtering coefficients employed with this numerical approach.

Statistical properties of the turbulent boundary flow are given in Fig. 8 for computations carried out using three different spatial discretization schemes implemented in the HOPS code: a sixth-order compact difference scheme (labelled C6), a fourth-order scheme based on an explicit stencil (E4), and a nominally third-order, upwind-biased implementation of the Roe scheme (ROE3). An eighth-order filter (F8) was used for the sixth-order compact difference scheme, but cases with both sixth-order (F6) and eighth-order filters were examined with the explicit fourth-order spatial scheme. An additional case was run with the sixth-order compact difference scheme using fourth-order Runge-Kutta time integration (RK4) rather than the baseline implicit time integration scheme. For these explicit calculations, the nondimensional time step was reduced to $\Delta t = 5 \times 10^{-4}$. The results of all the computations are in qualitative agreement, but the more dissipative spatial discretization approaches are seen to predict a delayed transition to turbulence.

A comparison of the results obtained with the different computational fluid dynamics codes is presented in Fig. 9 for the fine grid. The sub-figures show the mean profiles of skin friction, momentum thickness, streamwise velocity, and a form of the Reynold stress. The transition process is seen to vary slightly for the different codes and numerical approaches. Nonetheless, a well-developed turbulent boundary layer profile is obtained for each case, and the profiles agree closely when cast in nondimensional coordinates.

For reference, Fig. 10 compares the velocity profiles obtained in the present study using the HOPS code on the fine grid ($x/\delta_0 = 100$, $Re_\theta = 5.7 \times 10^3$) with those published by Spina²⁴ ($Re_\theta = 8.1 \times 10^4$). The profiles are presented both in outer variables (Fig. 10a) and van Driest transformed inner variables (Fig. 10b). The results are as expected for two well-developed turbulent boundary layers with an order-of-magnitude difference in Reynolds number. The near-wall region differs in outer variables and the wake region differs in inner variables. Reasonable agreement is obtained in the logarithmic region.

B. Correlations

It is of interest to evaluate the ability of large-eddy simulation to predict the properties of δ -scale structures, which are resolved in this approach. Here we focus on cross-correlations of various flow quantities, using the results of simulations with the HOPS code that employed the sixth-order compact difference scheme, eighth-order filtering, and implicit time advancement. For all the correlation statistics, averaging was performed for at least one domain flow-through time (1×10^5 iterations).

Time series of the fluctuations of mass flux generated by the simulations were saved in order to carry out the correlation analysis. The analysis is intended to be similar to that employed in the classic hotwire studies of Kovasznay et al.³¹ in a low-speed turbulent boundary layer, and of Spina et al.^{24,32,33} in a supersonic boundary layer.

Space-time correlations are shown in Fig. 11. Both cases shown correspond to a streamwise station of $x/\delta_0 = 97.0$, with a corresponding momentum thickness Reynolds number of $Re_\theta = 5.5 \times 10^3$. If Taylor's hypothesis³⁴ is applied to convert time to an effective streamwise coordinate, Fig. 11a can be interpreted as a side-view image of the flow in the center plane ($z/\delta_0 = 2.50$). The reference point for the correlations is set at $y_{ref}/\delta = 0.55$, and the surrounding correlation contours indicate the characteristic inclination of the large-scale boundary layer structures. (Here, the boundary layer thickness is $\delta/\delta_0 \approx 2.6$.)

Figure 11b shows the corresponding plan-view correlation, for the $y/\delta = 0.55$ plane, with $z_{ref}/\delta_0 = 2.5$. Again using Taylor's hypothesis to interpret time as a surrogate spatial coordinate, we note a characteristic elongation of the correlation contours in the streamwise direction.

Figure 12 compares space-time correlations in a horizontal plane between the computations and the experiments of Spina.²⁴ The experimental data correspond to nearly the same nondimensional distance from the wall ($y/\delta = 0.51$), but a higher Reynolds number. The shape of the correlation contours differs somewhat between computation and experiment, perhaps due to issues of spatial resolution. Nonetheless, the characteristic scale of the $R = 0.3$ correlation contour is about 0.5δ in both cases.

Spatial correlations are shown in Fig. 13. (See Fig. 4 for plots of the instantaneous mass-flux in the same planes.) The similarities between Fig. 11a and Fig. 13a, and between Fig. 11b and Fig. 13b, suggest that Taylor's hypothesis is a good approximation for this flow.

The scale and orientation of the large-scale structures in the simulated boundary layer are similar to those observed in experiments.³¹ The mass flux is well-correlated over a length scale on the order of the mean boundary layer thickness δ , and the correlation contours are roughly ellipsoidal. The characteristic length in the spanwise direction is somewhat smaller than that in the wall-normal or streamwise directions, and contours in the x - y -plane are oriented at an angle of about 45 deg from the wall. These results are generally consistent with the appearance of the instantaneous mass-flux field seen in Fig. 4.

Broad-band convection velocities, derived from space-time cross-correlations of the mass flux fluctuations, are shown in Fig. 14. The convection velocity is determined by dividing the distance between two stations separated in the streamwise direction by the time delay for optimal correlation of the signals obtained at the two stations. Computational results referenced to the $x/\delta_0 = 98$ station are shown in Fig. 14a. The convection velocity profile is seen to closely match the mean velocity profile, which is included for comparison.

The corresponding results obtained by Spina et al.³³ from hotwire measurement are shown in Fig. 14b. Those results show $U_c/U_\infty = 0.9 \pm 0.1$ across the outer part of the boundary layer. (The experimental uncertainty was primarily due to temporal discretization, the sampling rate of the analog-to-digital converter.) Because of the large error bar on the experimental data, it is difficult to say whether the convection velocity is actually constant across the boundary layer, or agrees closely with the mean velocity as seen in the computations. It should also be noted that the streamwise separation of the hotwire probes ($x/\delta = 0.1$ to 0.2) is smaller than that employed in the computational analysis ($x/\delta = 0.5$ to 2.0). We plan to explore these differences carefully in future work.

Another flow variable that has been extensively studied experimentally is the fluctuating wall pressure.²⁹ Time series of the computed wall pressure fluctuations were saved for correlation analysis. Spatial correlations of the fluctuating wall pressure are shown in Fig. 15. Computational results obtained with the HOPS code are shown in Fig. 15a, and the experimental results of Spina²⁴ are shown in Fig. 15b. (The experimental data were obtained with four Kulite pressure transducers, mounted in a line at the wall with a spacing of 0.18δ .) For the computations, the correlation contours are roughly circular, with a characteristic diameter of about 0.1δ . These results are qualitatively consistent with the features of the instantaneous wall pressure field shown in Fig. 5a. In contrast, the experimental correlation contours are elongated in the spanwise direction, and the characteristic length scale in the streamwise direction is about twice that obtained computationally. This discrepancy is also a topic of ongoing investigation, focusing in particular on issues of spatial resolution in the measurements.

Convection velocities were also computed for the wall pressure data, again by taking data from two stations separated in the streamwise direction, and dividing the distance between the stations by the time delay for optimal correlation. The results are shown in Fig. 16 as a function of the streamwise separation, and compared to several experimental data sets.^{24, 35–37} For all data sets, the convection velocity lies in the range $0.60 \leq U_c/U_\infty = 0.90$. The computational results fall in the middle of the range spanned by the experimental measurements.

IV. Summary and Conclusions

We seek to demonstrate that large-eddy simulation can take a productive place in the portfolio of tools for high-speed aircraft design, in particular replacing Reynolds-averaged Navier-Stokes methods for the simulation of highly three-dimensional flows. As a first step in this process, we have undertaken a verification and validation project for large-eddy simulation of compressible, turbulent flow. This paper has presented an initial progress report.

High-fidelity, implicit large-eddy simulations of a Mach 2.9 turbulent boundary layer flow were carried out using three different computational fluid dynamics codes (FDL3DI, HOPS, and US3D) with the same formal order of spatial and temporal accuracy. The codes FDL3DI and HOPS are finite-difference, structured-grid

solvers, developed at the Air Force Research Laboratory, whereas US3D is an unstructured, finite-volume code, developed at the University of Minnesota. The aim of the work was to compare their performance and numerical accuracy. The simulations were carried out using the same boundary conditions, body force trip mechanism, grids, and time-step. Additional calculations were carried out to compare the results obtained with different numerical algorithms.

All three codes were able to produce plausible turbulent boundary layers, and showed good agreement in the region where the boundary layer was well developed. General agreement was also obtained with experimental turbulent boundary layer profiles. The details of the transition process, however, varied with the numerical method and the details of its execution. In particular, coarser grids and more dissipative numerical schemes led to delayed transition to turbulence in the calculations. The body-force trip method was employed successfully in each case, and should be suitable for general application with different codes and numerical approaches.

Calculations were also carried out to explore correlations characterizing large-scale structures in the flow turbulence. Many of the features of the large-scale structures were found to match between computation and experiment, but additional work is warranted to explore the use of such comparisons to validate large-eddy simulation codes.

Acknowledgments

This project is sponsored in part by the Air Force Office of Scientific Research, under tasks monitored by F. Fahroo and J. Schmisser, and by grants of High Performance Computing time from the Air Force Research Laboratory (AFRL), Army Research Laboratory (ARL), and Army Engineer Research and Development Center (ERDC) Defense Supercomputing Resource Centers (DSRC).

The authors would like to acknowledge helpful discussions with D. Gaitonde, D. Garmann, R. Gosse, M. Visbal, and M. White.

References

- ¹Visbal, M. R. and Gaitonde, D. V., "On the Use of Higher-Order Finite-Difference Schemes on Curvilinear and Deforming Meshes," *Journal of Computational Physics*, Vol. 181, 2002, pp. 155–185.
- ²Visbal, M. R. and Gaitonde, D. V., "Shock Capturing Using Compact-Differencing-Based Methods," AIAA Paper 2005-1265.
- ³Poggie, J., "High-Order Compact Difference Methods for Glow Discharge Modeling," AIAA Paper 2009-1047.
- ⁴Poggie, J., "Compact Difference Methods for Discharge Modeling in Aerodynamics," AIAA Paper 2009-3908.
- ⁵Poggie, J., "Role of Charged Particle Inertia in Pulsed Electrical Discharges," AIAA Paper 2010-1195.
- ⁶Poggie, J., "High-Order Numerical Methods for Electrical Discharge Modeling," AIAA Paper 2010-4632.
- ⁷Nompelis, I., Drayna, T. W., and Candler, G. V., "A Parallel Unstructured Implicit Solver for Hypersonic Reacting Flow Simulation," AIAA Paper 2005-4867.
- ⁸Subbareddy, P. K. and Candler, G. V., "A Fully Discrete, Kinetic Energy Consistent Finite-Volume Scheme for Compressible Flows," *Journal of Computational Physics*, Vol. 228, 2009, pp. 1347–1364.
- ⁹Pirozzoli, S., "Numerical Methods for High-Speed Flows," *Annual Review of Fluid Mechanics*, Vol. 43, 2011, pp. 163–194.
- ¹⁰Mavriplis, D. J., "Revisiting the Least-Squares Procedure for Gradient Reconstruction on Unstructured Meshes," NASA/CR 2003-212683, National Aeronautics and Space Administration, Hampton, VA, December 2003.
- ¹¹Ducros, F., Ferrand, V., Nicoud, F., Weber, C., Darracq, D., Gacherieu, C., and Poinsot, T., "Large-Eddy Simulation of the Shock/Turbulence Interaction," *Journal of Computational Physics*, Vol. 152, No. 1, 1999, pp. 199–238.
- ¹²Bartkiewicz, M. D., Subbareddy, P. K., and Candler, G. V., "Numerical Simulations of Roughness Induced Instability in the Purdue Mach 6 Wind Tunnel," AIAA Paper 2010-4723.
- ¹³Wright, M. J., Candler, G. V., and Prampolini, M., "Data-Parallel Lower-Upper Relaxation Method for the Navier-Stokes Equations," *AIAA Journal*, Vol. 34, No. 7, 1996, pp. 1371–1377.
- ¹⁴Beam, R. and Warming, R., "An Implicit Factored Scheme for the Compressible Navier-Stokes Equations," *AIAA Journal*, Vol. 16, No. 4, 1978, pp. 393–402.
- ¹⁵Pulliam, T. H. and Chaussee, D. S., "A Diagonal Form of an Implicit Approximate-Factorization Algorithm," *Journal of Computational Physics*, Vol. 39, 1981, pp. 347–363.
- ¹⁶Gaitonde, D. V. and Visbal, M. R., "High-Order Schemes for Navier-Stokes Equations: Algorithm Implementation into FDL3DI," Technical Report AFRL-VA-WP-TR-1998-3060, Air Force Research Laboratory, Wright-Patterson Air Force Base, Ohio, August 1998.
- ¹⁷Roe, P. L., "Approximate Riemann Solvers, Parameter Vectors, and Difference Schemes," *Journal of Computational Physics*, Vol. 43, 1981, pp. 357–372.
- ¹⁸Anderson, W. K., Thomas, J. L., and van Leer, B., "Comparison of Finite Volume Flux Vector Splittings for the Euler Equations," *AIAA Journal*, Vol. 24, No. 9, 1986, pp. 1453–1460.

- ¹⁹Morrison, J., "Flux Difference Split Scheme for Turbulent Transport Equations," AIAA Paper 90-5251, 1990.
- ²⁰Gaitonde, D. and Shang, J. S., "Accuracy of Flux-Split Algorithms in High-Speed Viscous Flows," *AIAA Journal*, Vol. 31, No. 7, 1993, pp. 1215–1221.
- ²¹Thomas, P. D. and Lombard, C. K., "Geometric Conservation Law and Its Application to Flow Computations on Moving Grids," *AIAA Journal*, Vol. 17, No. 10, 1979, pp. 1030–1037.
- ²²Bookey, P., Wyckham, C., Smits, A., and Martin, M. P., "New Experimental Data of STBLI at DNS/LES Accessible Reynolds Numbers," AIAA Paper 2005-309.
- ²³Wu, M. and Martin, M. P., "Direct Numerical Simulation of Supersonic Turbulent Boundary Layer over a Compression Ramp," *AIAA Journal*, Vol. 45, No. 4, 2007, pp. 879–889.
- ²⁴Spina, E. F., *Organized Structures in a Supersonic Turbulent Boundary Layer*, Ph.D. Dissertation, Princeton University, Princeton NJ, October 1988.
- ²⁵Mullenix, N. J., Gaitonde, D. V., and Visbal, M. R., "Spatially Developing Supersonic Turbulent Boundary Layer with a Body-Force Based Method," *AIAA Journal*, Vol. 51, No. 8, 2013, pp. 1805–1819.
- ²⁶Georgiadis, N. J., Rizzetta, D. P., and Fureby, C., "Large-Eddy Simulation: Current Capabilities, Recommended Practices, and Future Research," *AIAA Journal*, Vol. 48, No. 8, 2010, pp. 1772–1784.
- ²⁷Smits, A. J., Hayakawa, K., and Muck, K. C., "Constant Temperature Hotwire Anemometry Practice in Supersonic Flows, Part I: The Normal Wire," *Experiments in Fluids*, Vol. 1, No. 2, 1983, pp. 83–92.
- ²⁸Poggie, J., Erbland, P. J., Smits, A. J., and Miles, R. B., "Quantitative Visualization of Compressible Turbulent Shear Flows using Condensate-Enhanced Rayleigh Scattering," *Experiments in Fluids*, Vol. 37, 2004, pp. 438–454.
- ²⁹Beresh, S. J., Henfling, J. F., Spillers, R. W., and Pruett, B. O. M., "Fluctuating Wall Pressures Measured Beneath a Supersonic Turbulent Boundary Layer," *Physics of Fluids*, Vol. 23, 2011, pp. 075110.
- ³⁰van Driest, E. R., "On the Turbulent Flow Near a Wall," *Journal of the Aeronautical Sciences*, Vol. 23, 1956, pp. 1007–1011.
- ³¹Kovaszny, L. S. G., Kibens, V., and Blackwelder, R. F., "Large-Scale Motion in the Intermittent Region of a Turbulent Boundary Layer," *Journal of Fluid Mechanics*, Vol. 41, 1970, pp. 283–325.
- ³²Spina, E. F. and Smits, A. J., "Organized Structures in a Compressible, Turbulent Boundary Layer," *Journal of Fluid Mechanics*, Vol. 182, 1987, pp. 85–109.
- ³³Spina, E. F., Donovan, J. F., and Smits, A. J., "On the Structure of High-Reynolds-Number Supersonic Turbulent Boundary Layers," *Journal of Fluid Mechanics*, Vol. 222, 1991, pp. 293–327.
- ³⁴Taylor, G. I., "The Spectrum of Turbulence," *Proceedings of the Royal Society of London A*, Vol. 164, 1938, pp. 476–490.
- ³⁵Bull, M. K., "Wall-Pressure Fluctuations Associated with Subsonic Turbulent Boundary Layer Flow," *Journal of Fluid Mechanics*, Vol. 28, 1967, pp. 719–754.
- ³⁶Chyu, W. J. and Hanly, R. D., "Power and Cross-Spectra and Space-Time Correlations of Surface Fluctuating Pressures at Mach Numbers Between 1.6 and 2.5," AIAA Paper 68-77.
- ³⁷Tan, D. K. M., Tran, T. T., and Bogdonoff, S. M., "Surface Pressure Fluctuations in a Three-Dimensional Shock Wave / Turbulent Boundary Layer Interaction," AIAA Paper 85-0125.

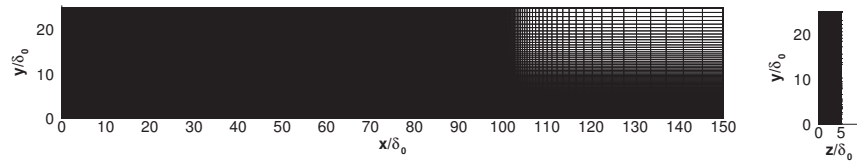
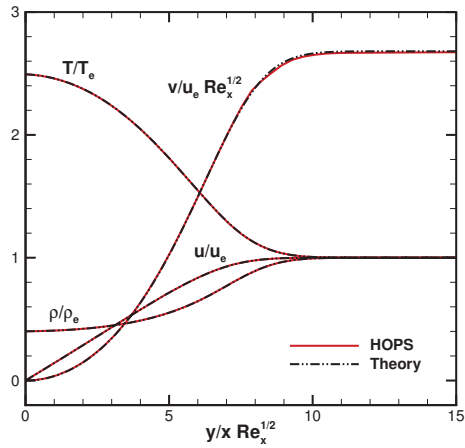
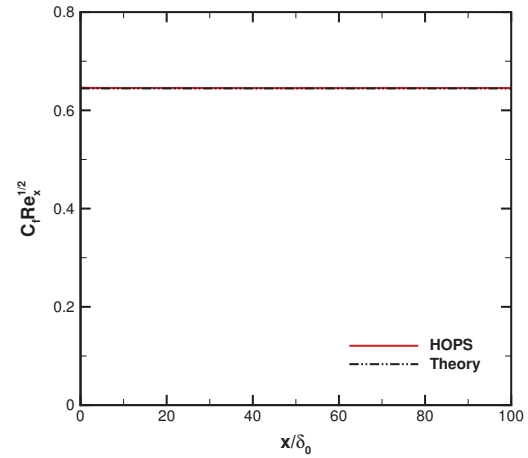


Figure 1. Computational mesh for Mach 2.9 turbulent boundary layer computations (fine grid case).

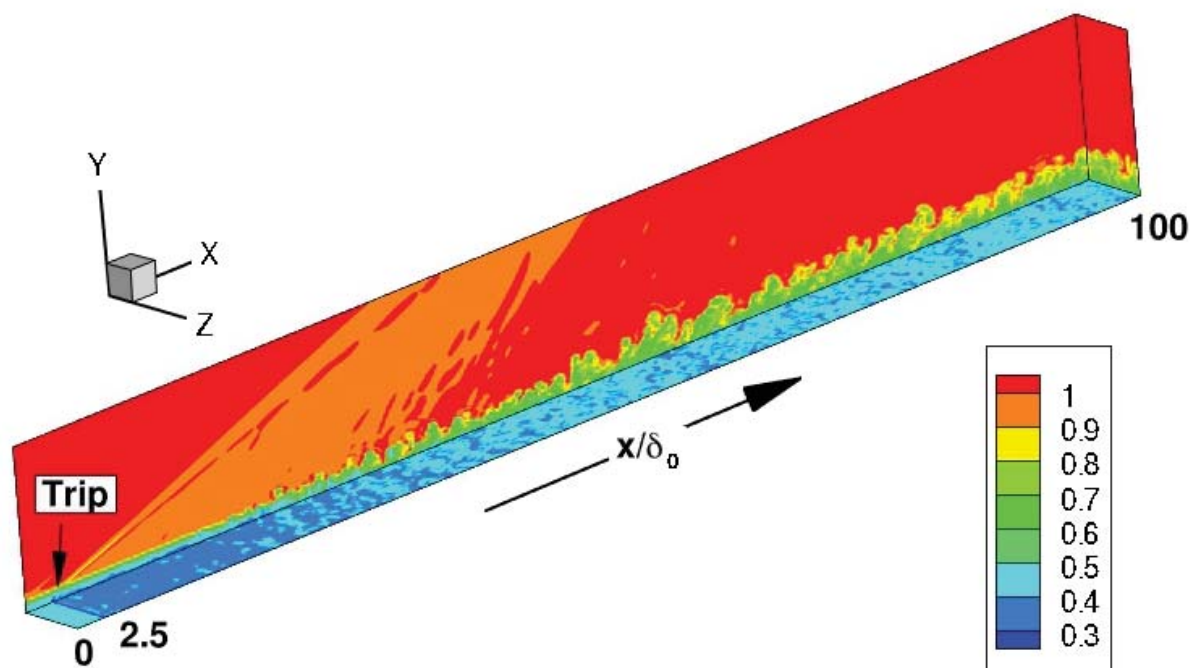


(a) Boundary layer profiles at $x/\delta_0 = 100$.

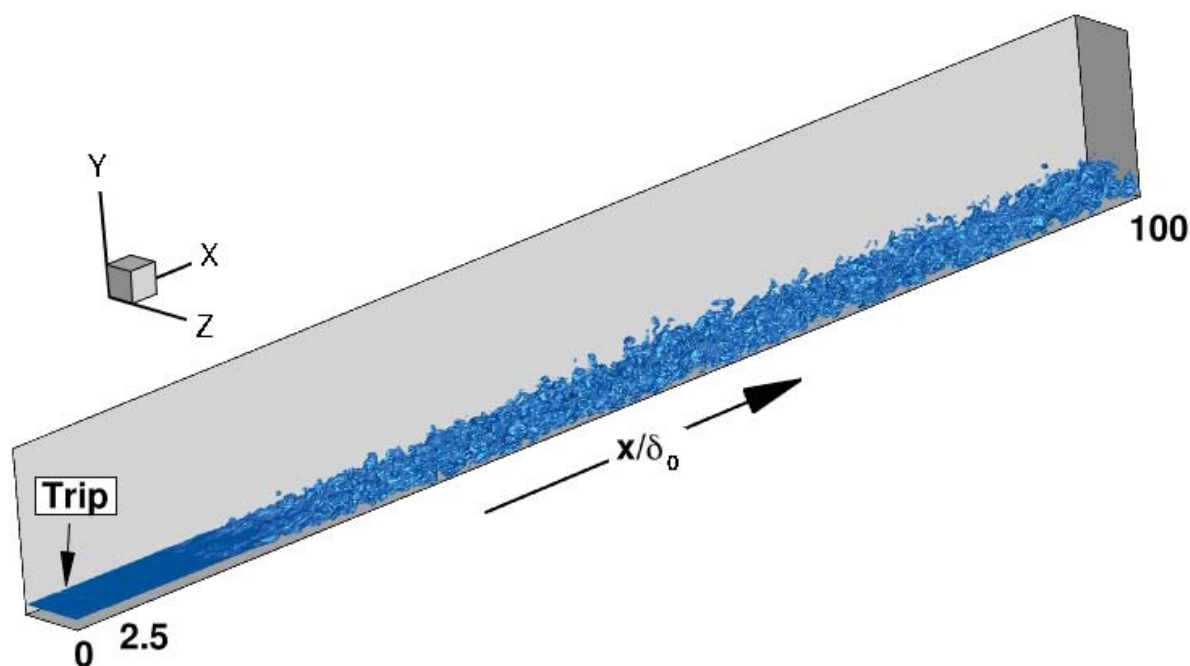


(b) Skin friction profile.

Figure 2. Mach 2.9 laminar boundary layer flow (HOPS code, coarse grid, C6/F8 scheme).



(a) Density contours, ρ/ρ_∞ .



(b) Temperature isosurface, $T/T_\infty = 1.0$.

Figure 3. Overview of Mach 2.9 turbulent boundary layer flow (HOPS code, fine grid, C6/F8 scheme).

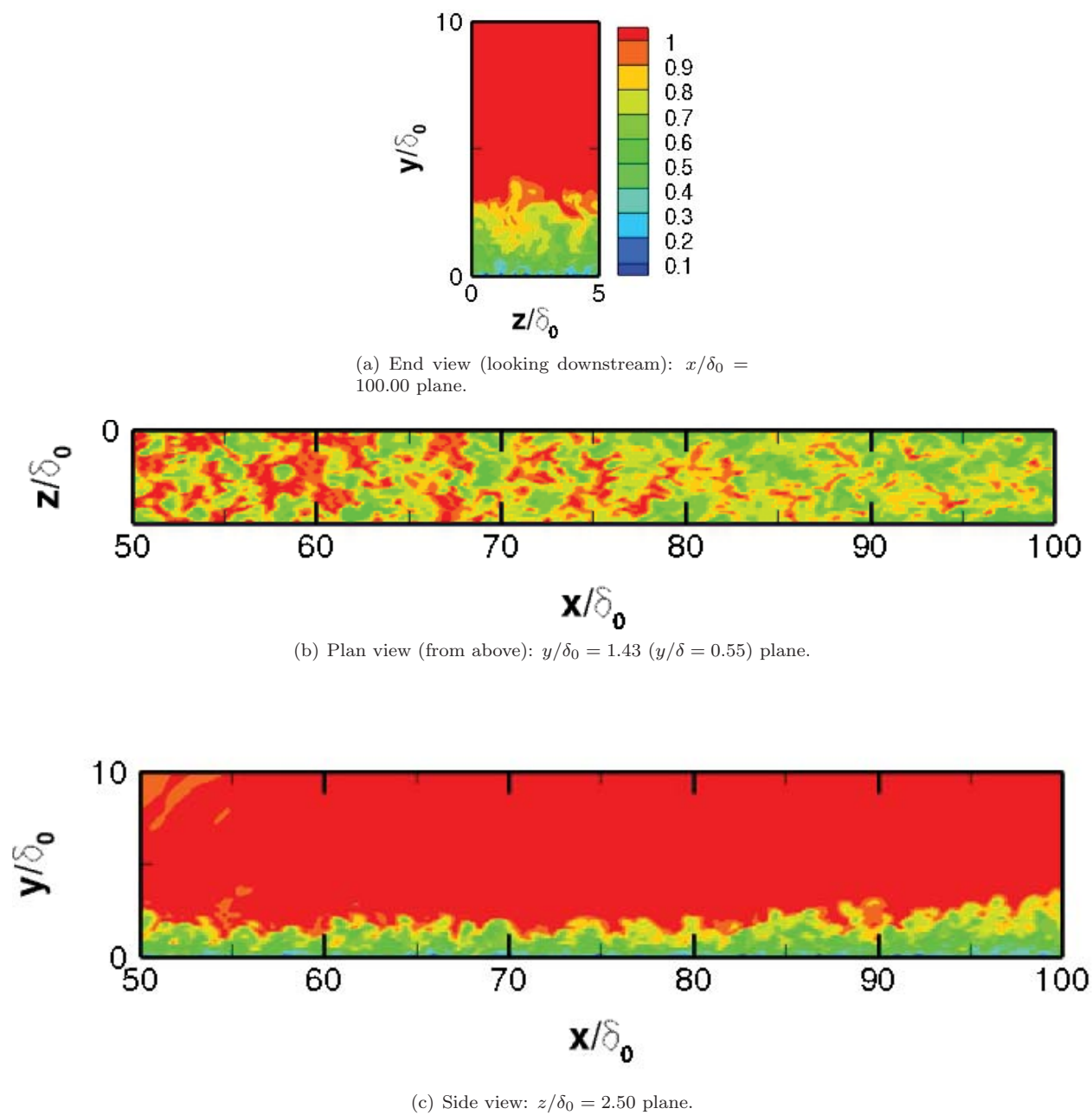


Figure 4. Contour plots of the instantaneous, streamwise component of mass flux, $\rho u / (\rho_\infty u_\infty)$ (HOPS code, fine grid, C6/F8 scheme).

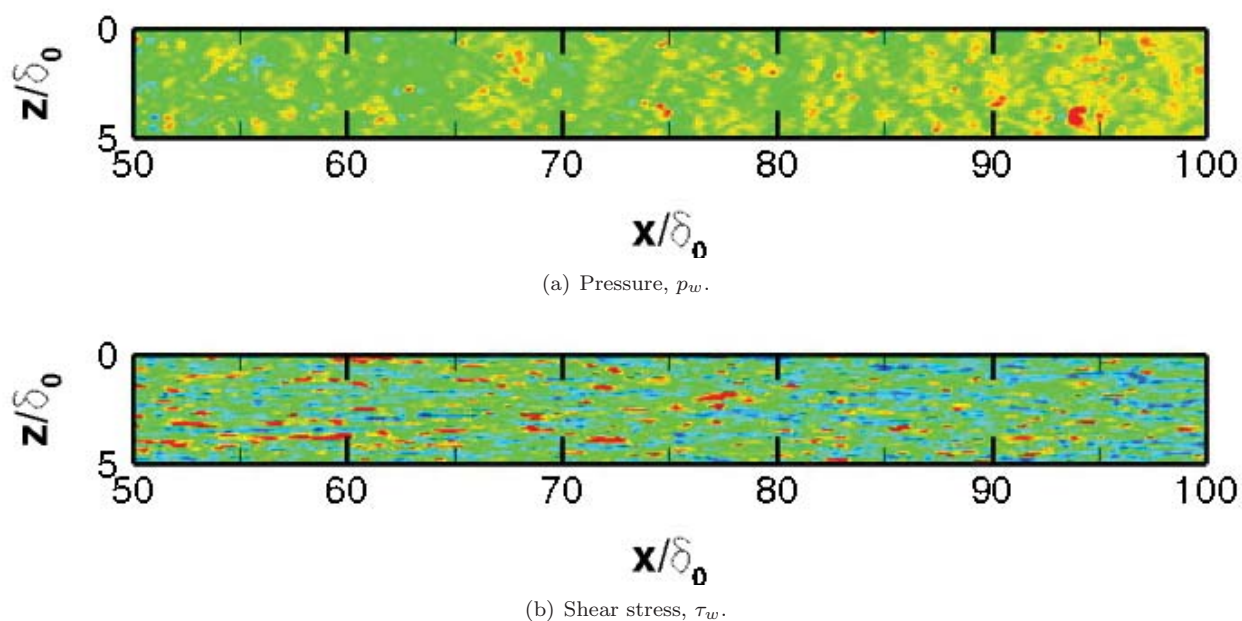


Figure 5. Instantaneous contours of flow properties at the wall (plan view from above, $y = 0$, HOPS code, fine grid, C6/F8 scheme).

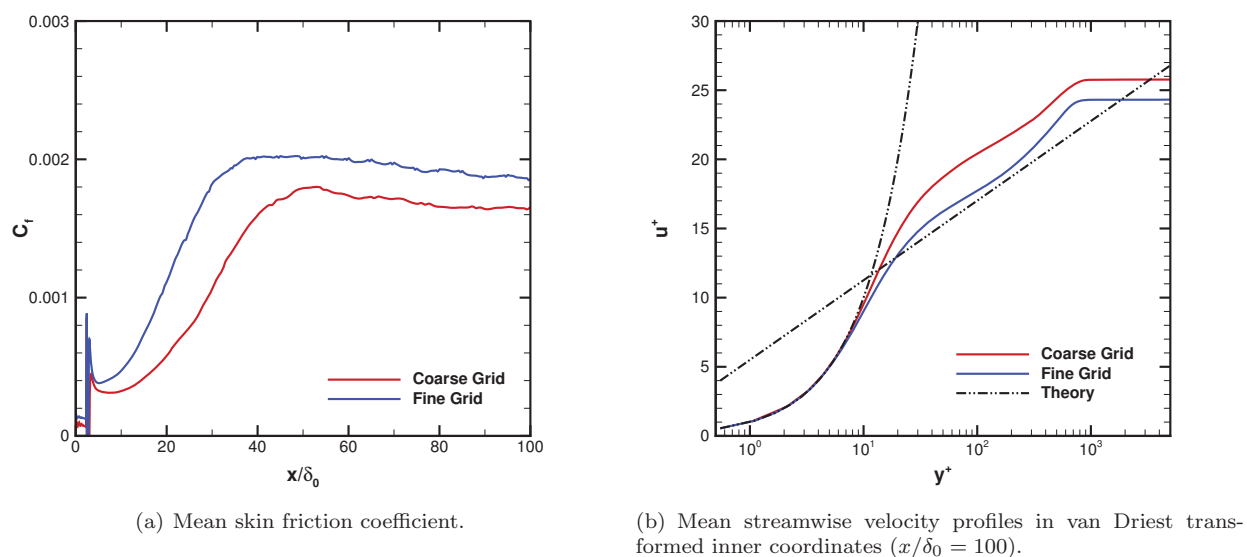
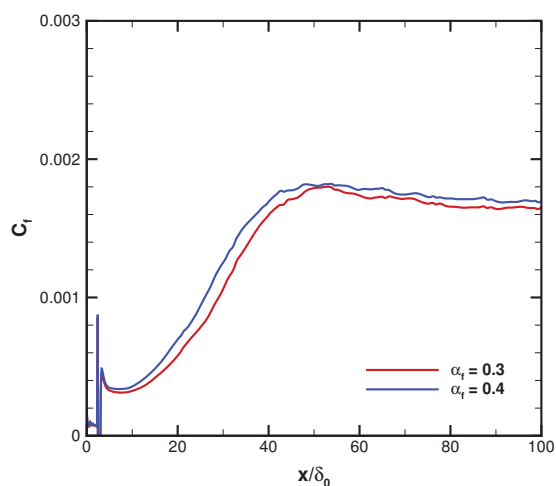
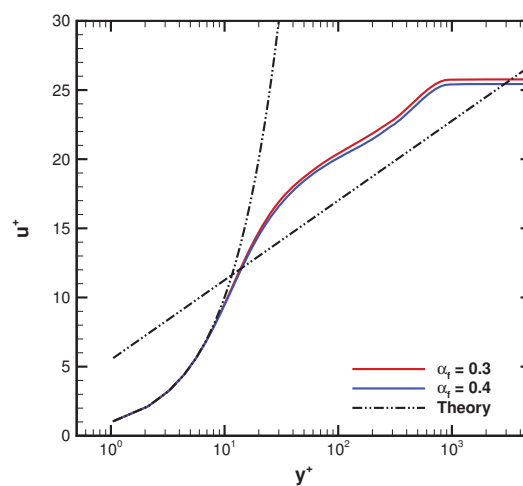


Figure 6. Mean flow properties of Mach 2.9 turbulent boundary layer for different grids (HOPS code, C6/F8 scheme).

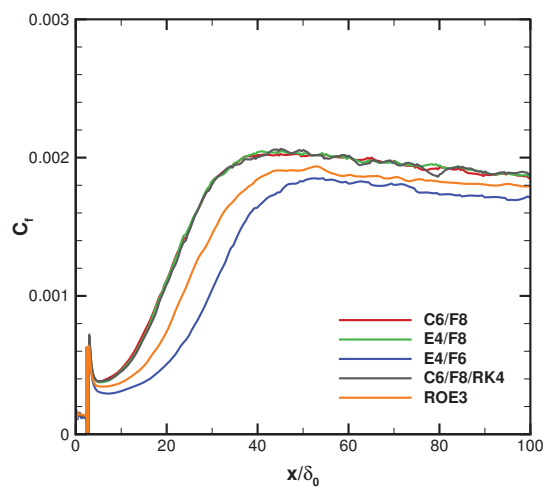


(a) Mean skin friction coefficient.

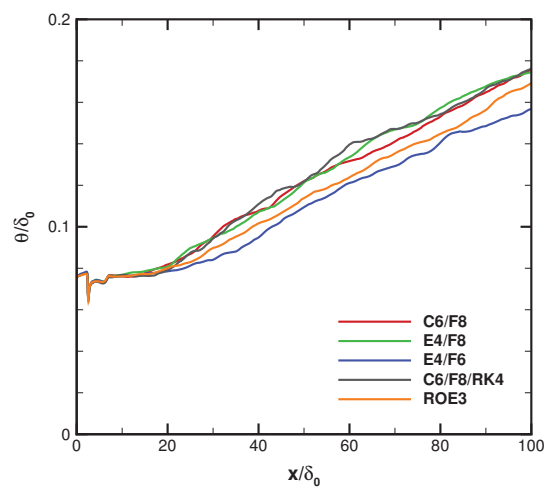


(b) Mean streamwise velocity profiles in van Driest transformed inner coordinates ($x/\delta_0 = 100$).

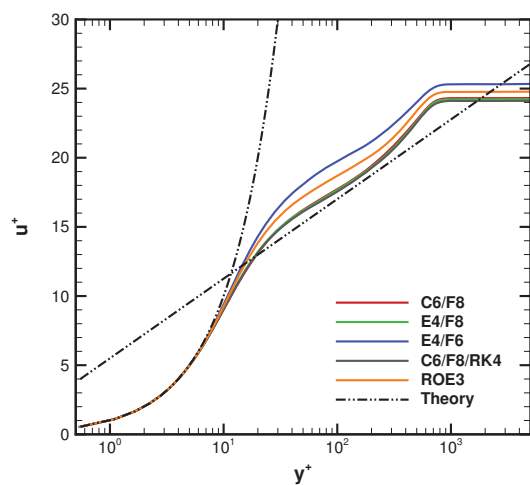
Figure 7. Mean flow properties of Mach 2.9 turbulent boundary layer for different filter coefficients (HOPS code, coarse grid, C6/F8 scheme).



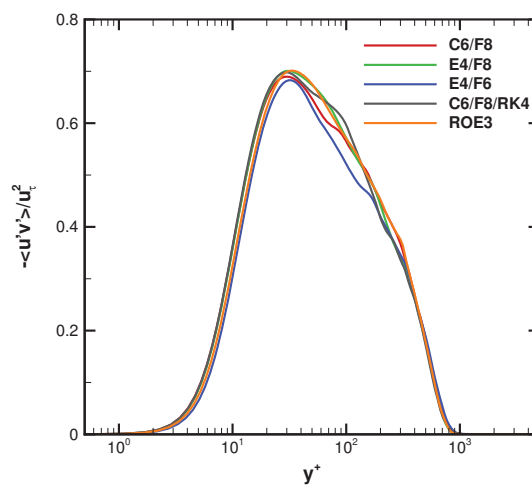
(a) Mean skin friction coefficient.



(b) Mean momentum thickness.

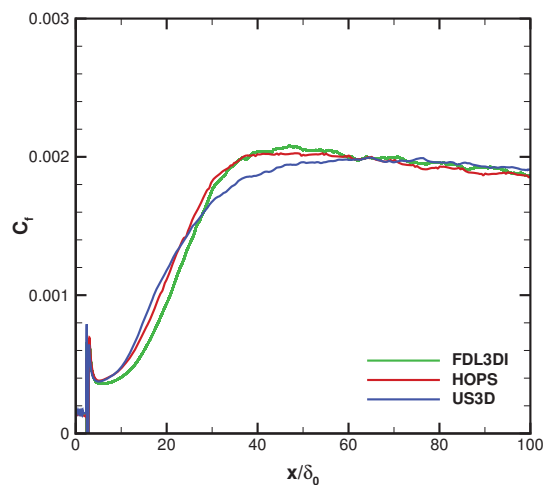


(c) Mean streamwise velocity profiles in van Driest transformed inner coordinates ($x/\delta_0 = 100$).

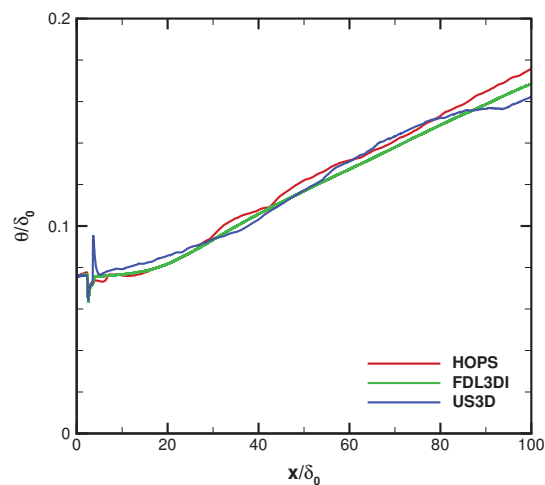


(d) Mean Reynolds stress in inner coordinates ($x/\delta_0 = 100$).

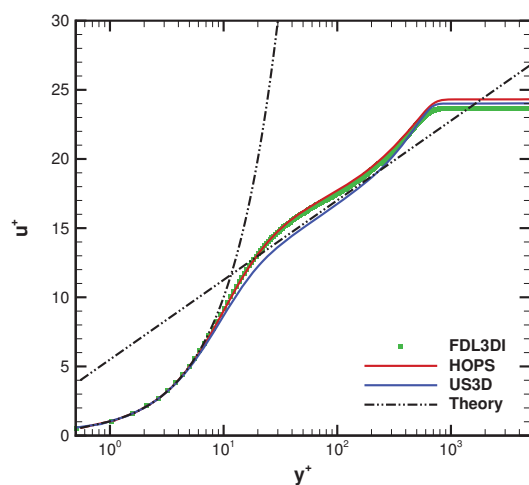
Figure 8. Mean flow properties of Mach 2.9 turbulent boundary layer for different numerical schemes (HOPS code, fine grid).



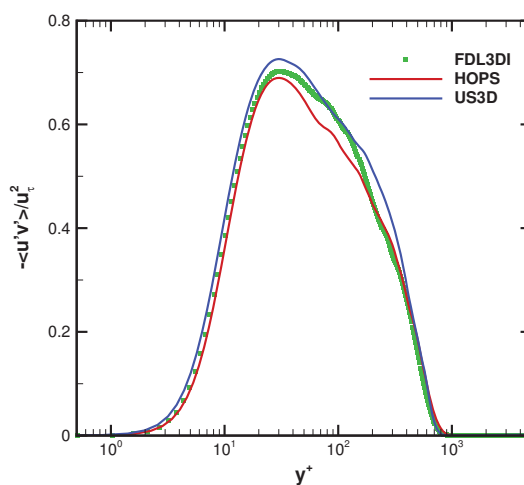
(a) Mean skin friction coefficient.



(b) Mean momentum thickness.



(c) Mean streamwise velocity profiles in van Driest transformed inner coordinates ($x/\delta_0 = 100$).



(d) Mean Reynolds stress in inner coordinates ($x/\delta_0 = 100$).

Figure 9. Mean flow properties of Mach 2.9 turbulent boundary layer for computations on fine grid with different codes.

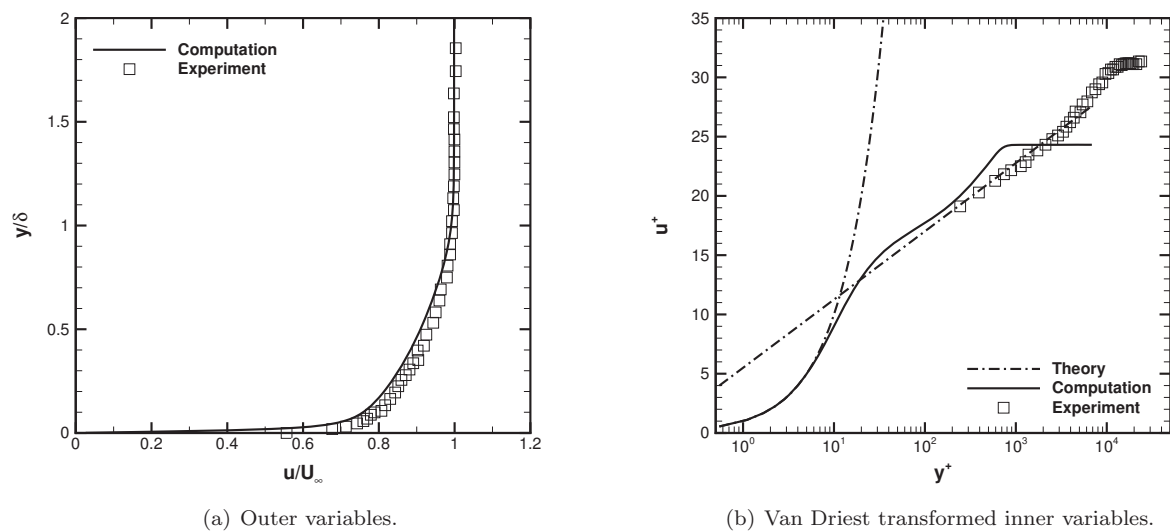


Figure 10. Mean velocity profiles obtained with HOPS code ($Re_\theta = 5.7 \times 10^3$) compared to experimental data of Figure 3-5 of Spina²⁴ ($Re_\theta = 8.1 \times 10^4$).

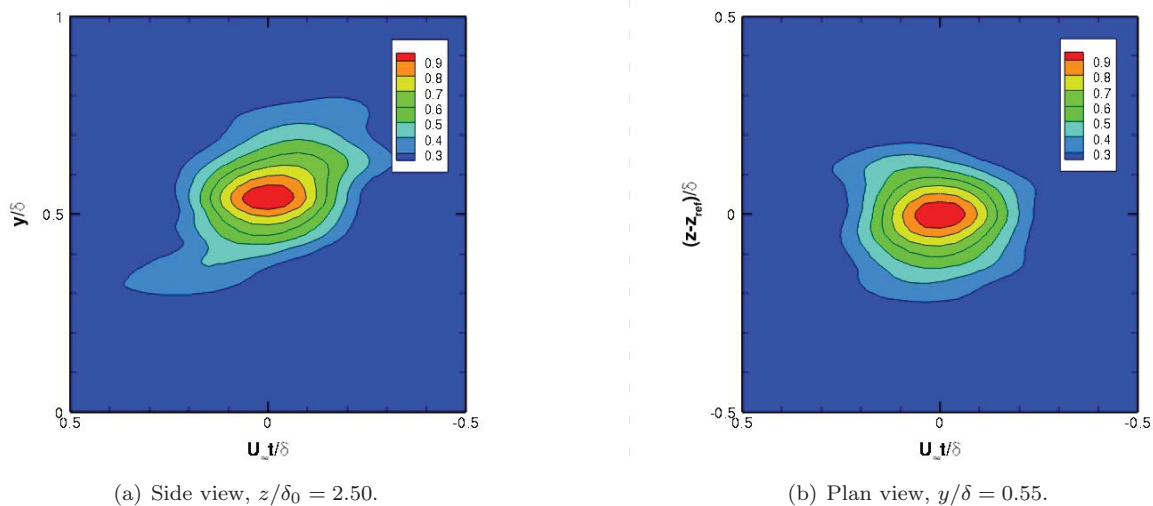
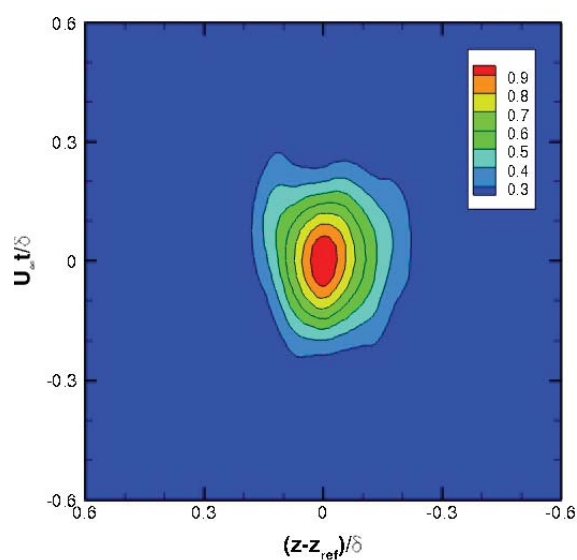
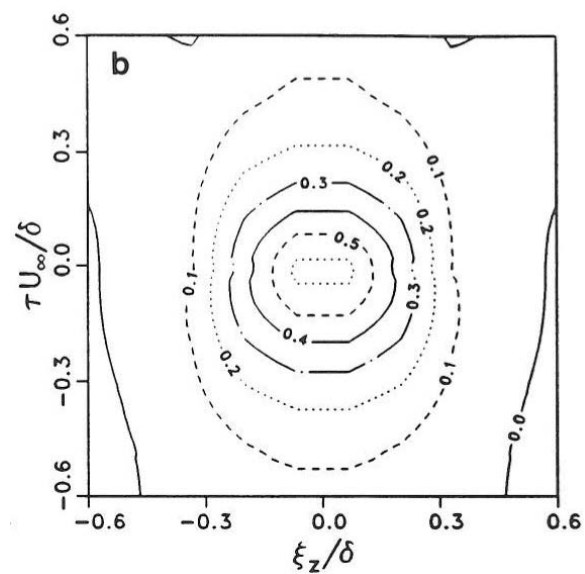


Figure 11. Space-time correlations of streamwise component of mass flux $(\rho u)'$.



(a) Computation, $y/\delta = 0.55$, $Re_\theta = 5.7 \times 10^3$.



(b) Experiment, $y/\delta = 0.51$, $Re_\theta = 8.1 \times 10^4$. Figure 4-29 of Spina.²⁴

Figure 12. Space-time correlations of streamwise component of mass flux $(\rho u)'$ for a plane parallel to the wall.

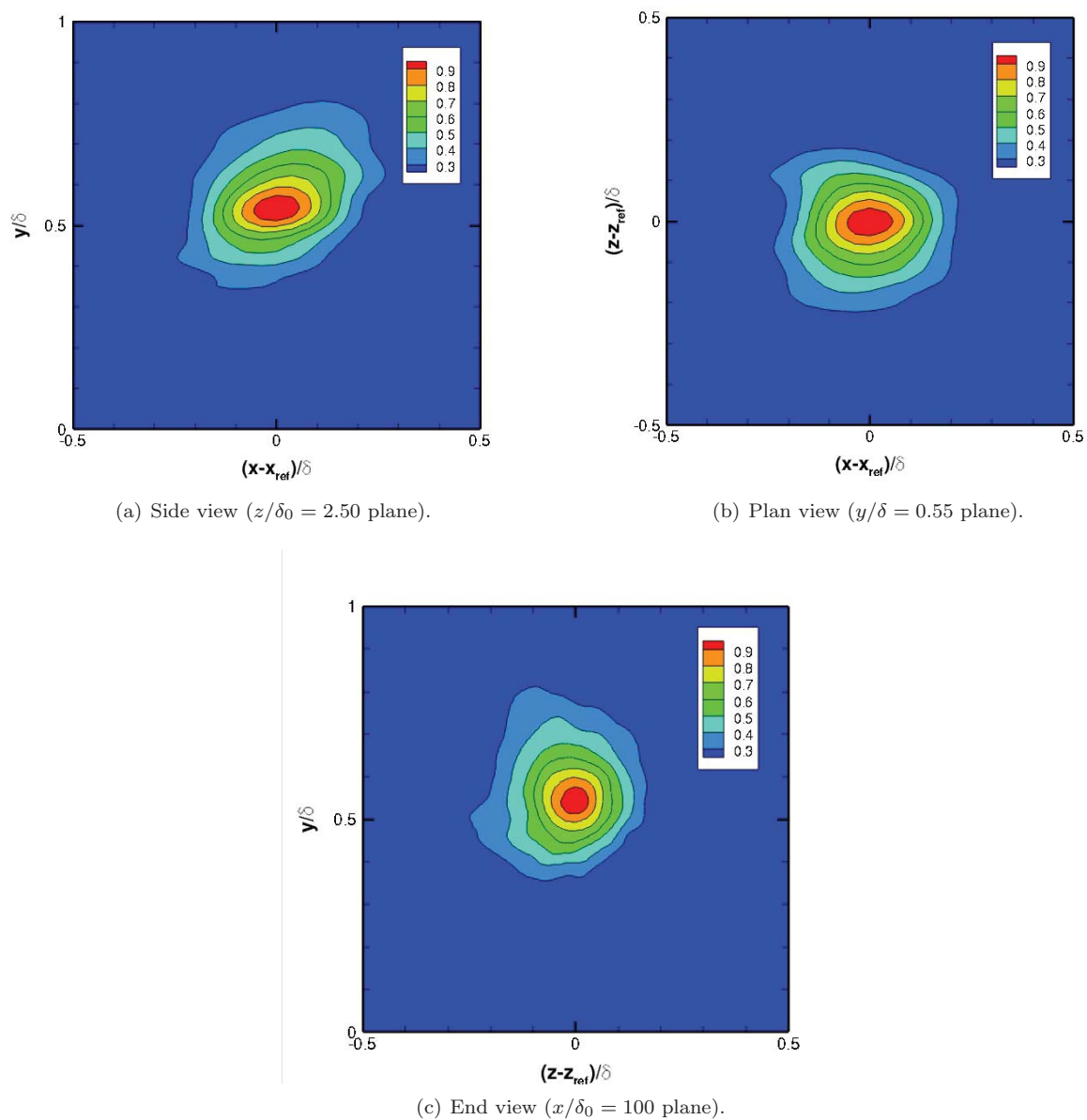
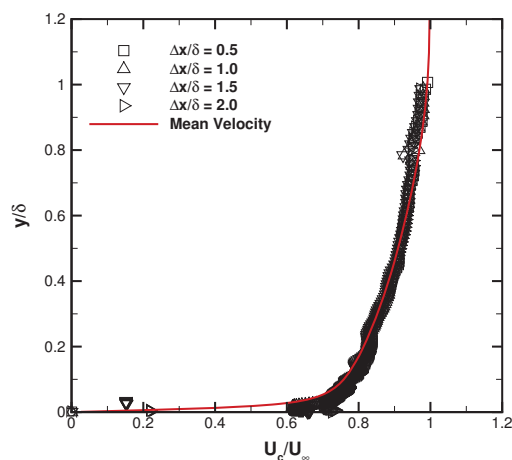
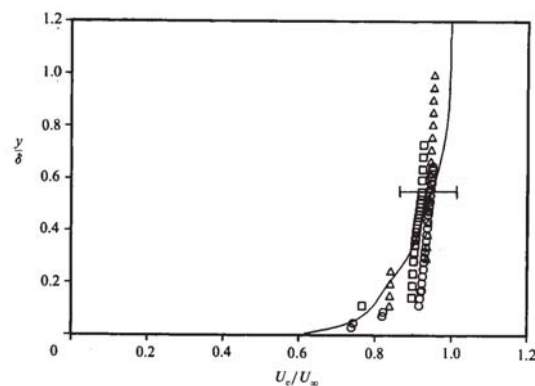


Figure 13. Two-point, spatial correlations of streamwise component of mass flux $(\rho u)'$. Reference station: $x_{ref}/\delta_0 = 97.0$, $y_{ref}/\delta = 0.55$, $z_{ref}/\delta_0 = 2.5$.

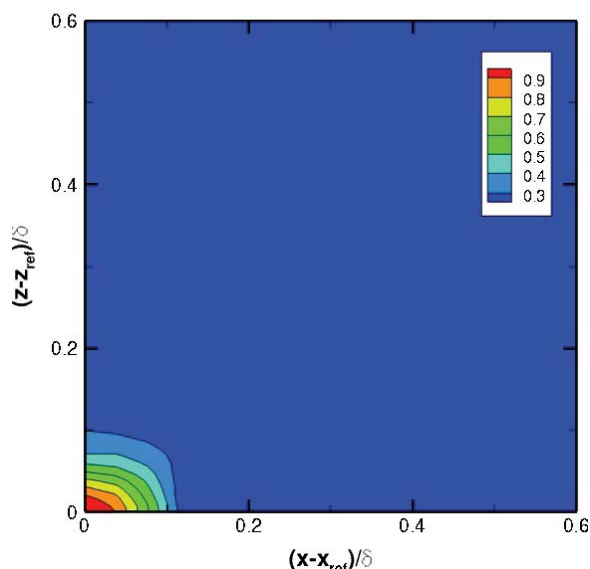


(a) Computations, $x_{\text{ref}}/\delta_0 = 98.0$, $Re_\theta = 5.6 \times 10^3$.

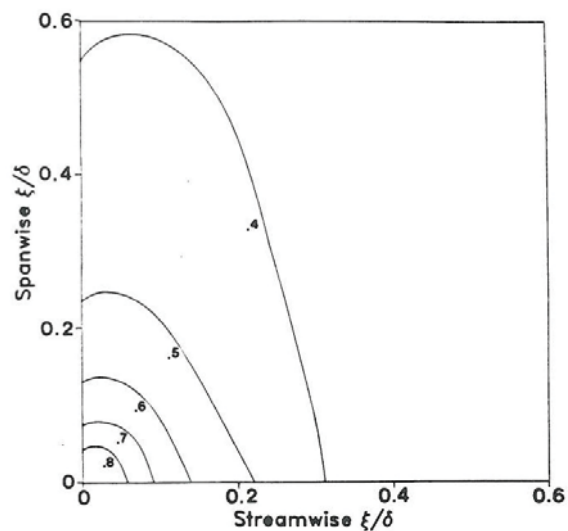


(b) Experiment, $Re_\theta = 8.1 \times 10^4$. Symbols: \square , $\Delta x/\delta = 0.11$; \circ , $\Delta x/\delta = 0.16$; \triangle , $\Delta x/\delta = 0.18$; line, mean velocity. (Figure 3 of Spina et al.,³³ used under the terms of the Cambridge University Press for the reproduction of a single figure.)

Figure 14. Broad-band convection velocity, based on mass flux fluctuations $(\rho u)'$.



(a) Computations, $Re_\theta = 5.7 \times 10^3$. Reference station: $x_{\text{ref}}/\delta_0 = 97.0$, $z_{\text{ref}}/\delta_0 = 2.5$.



(b) Experiment, $Re_\theta = 8.1 \times 10^4$. Figure 4-4 of Spina.²⁴

Figure 15. Two-point spatial correlations of wall pressure fluctuations p'_w .

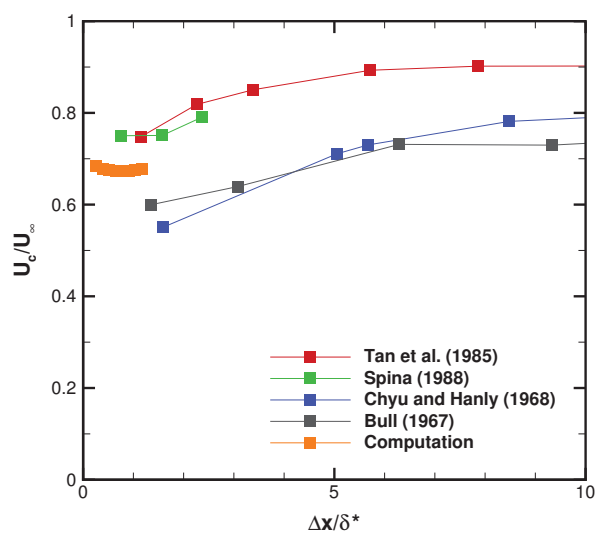


Figure 16. Broad-band convection velocity, based on wall pressure fluctuations p'_w . Reference station: $x_{\text{ref}}/\delta_0 = 98.0$. Experimental data of Bull,³⁵ Chyu and Hanley,³⁶ Tan et al.,³⁷ and Spina.²⁴

High Fidelity Computational Study of the HIFiRE-1 Boundary Layer Trip

Joel E. Gronvall*, Nicholas J. Bisek† and Jonathan Poggie‡

Air Force Research Laboratory, Wright-Patterson AFB, OH, 45433-7512, USA

A computational study of the effects of a discrete roughness element on high-speed boundary layers is investigated. Four cases are studied with one set based on the flow conditions during the ascent phase of the Hypersonic International Flight Research Experimentation Flight 1. Results that are presented include a two-dimensional stability analysis of the cone geometry without roughness and four high fidelity simulations with the diamond-shaped roughness element. Reynolds number effects on the wake pattern are compared in addition to a preliminary comparison between second-order accurate and sixth-order accurate computational results.

I. Introduction

Laminar to turbulent transition in high speed boundary layers continues to be a critical field of study. It is well known that hypersonic vehicle design is especially influenced by the effects of transition. Of these effects, two in particular provide the greatest challenge to engineers. First, a nearly five-fold increase in surface heating may occur due to the enhanced mixing within the turbulent boundary layer. Second, increased skin friction results from the increased generation of shear stresses. Therefore, gaining a deeper understanding of the physics involved will provide an improved ability to predict the onset of transition and possibly delay it.

Numerous factors have been identified in the literature as those that can directly or indirectly affect the complex process of transition. Some of these include freestream disturbances, distributed roughness, isolated roughness, surface temperature, nose bluntness, etc. Much work has been done toward gaining greater knowledge of the underlying physics of boundary layer transition. However, to a large extent our understanding of transition in high-speed flows remains incomplete¹ due to a number of factors,² including the limited availability of flight data. In part, the Hypersonic International Flight Research and Experimentation (HIFiRE) program was designed to address this issue by providing high quality boundary layer transition data in free flight conditions. The first from this series of experiments, HIFiRE-1,³⁻¹⁰ has indeed produced a great amount of work to date, including parallel ground tests¹¹⁻¹⁴ and computational analyses.¹⁵⁻²⁰ Of particular interest was the boundary layer trip on the HIFiRE-1 flight vehicle, however only a limited amount of analysis has been put forth on this portion of the experiment and has mainly focused on evaluating engineering type roughness correlations¹⁶ using ground test data. Therefore it is the intent of this paper to examine effects from the roughness element on boundary layer transition at an instant during the ascent and also over a range of freestream unit Reynolds numbers.

As has been observed, the general effect of roughness on the boundary layer is to move the transition front upstream.²¹ As such, roughness elements are generally classified in terms of the degree of impact on boundary layer transition. Any surface roughness that produces no appreciable influence on the onset of transition can necessarily be neglected. Roughness heights that begin to influence, but do not immediately cause transition in the boundary layer are often referred to as ‘critical’ or ‘incipient.’ Roughness magnitudes that are larger and result in immediate boundary layer transition are referred to as ‘effective.’ Depending on the three-dimensional shape of the roughness and overall height, the precise mechanisms that lead to transition still

*Senior Researcher, Ohio Aerospace Institute. Currently Aerospace Engineer, Southern Research Institute. Member AIAA.

†Research Aerospace Engineer, AFRL/RQHF. Senior Member AIAA.

‡Senior Aerospace Engineer, AFRL/RQHF. Associate Fellow AIAA.

remain unclear. For effective roughness heights, it is believed that the presence of flow reversal introduces an absolute instability. For incipient boundary layer trips, a transient or non-modal growth mechanism has been proposed.

A two-dimensional computational analysis has been completed for a selected instant during the ascent phase of the experiment. The mean flow solution was generated using the two-dimensional/axisymmetric CFD solver included in the STABL²² software suite. A subsequent stability analysis was conducted using the PSE-Chem code and the results are presented herein as verification that the boundary layer upstream of the trip was laminar under flight conditions. Additionally, four cases were studied using three-dimensional high fidelity grids and a second-order accurate scheme. The freestream unit Reynolds number was varied over these four cases from low to high, with high Reynolds number case representing the selected flight condition. A preliminary comparison with direct numerical simulations using the sixth-order low dissipation scheme are made.

II. HIFiRE-1 Flight Experiment

The primary focus for the current investigation is the boundary layer trip portion of the HIFiRE-1 flight experiment, specifically during the ascent. The experimental model was nominally a 7.0° half angle cone with a 2.5 mm nose radius and a total length of 1.100 m. The diamond-shaped roughness element was installed at an axial location of 0.5236 m on the cone surface and oriented in such a way that a radiused corner was aligned with the flow direction. A schematic showing the overall dimensions of the cone and the relative location of the roughness element is shown in Figure 1. The dimensions of the element were 10 mm length on each side and a 2 mm height. Figure 2 shows the element as used in the three-dimensional computation.

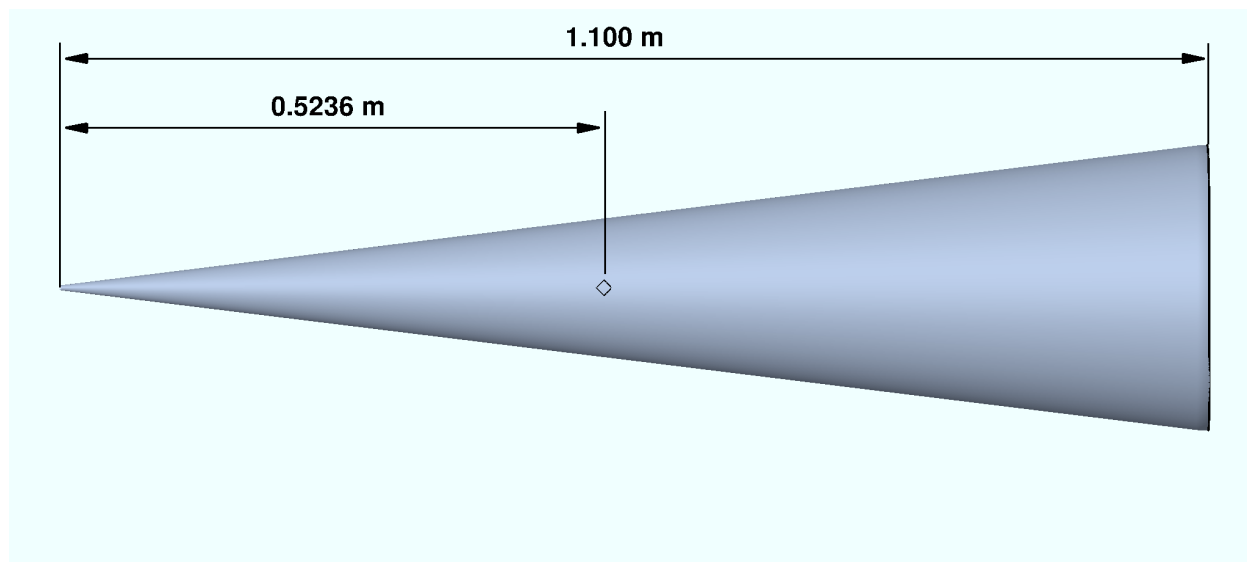


Figure 1: HIFiRE-1 Roughness Element Configuration.

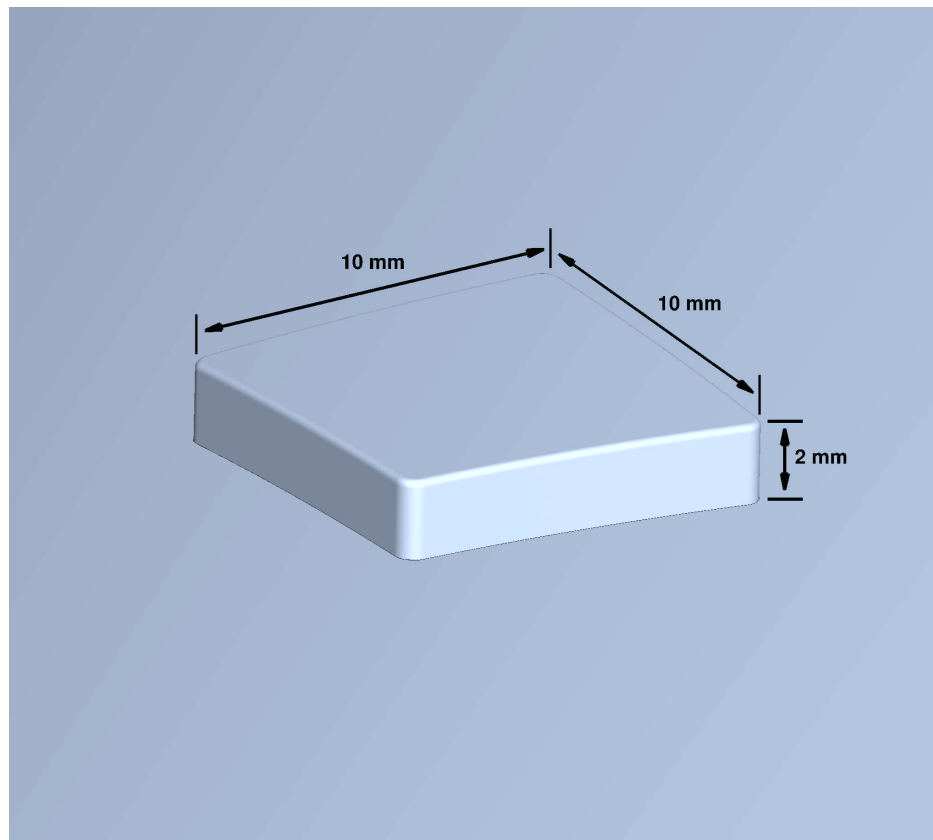


Figure 2: HIFiRE-1 Roughness Element Dimensions.

Installed on the flight vehicle were an array of pressure transducers, heat flux gauges, and thermocouples. The instrumentation was arranged along two rays of the cone with one set aligned along the smooth side of the cone and the other set aligned along the roughness element side of the cone. During the experiment, the HIFiRE-1 vehicle transmitted data on three telemetry streams. Unfortunately, the data collected from the rough side stream contained high amounts of noise which make direct comparisons relatively difficult. Lastly, due to a failure in the exoatmospheric pointing maneuver, the flight vehicle reentered the atmosphere at a high angle of attack. However, the ascent phase produced nearly axisymmetric flow conditions and thus provides the basis for this study.

III. Computational Methodology

III.A. Numerical Setup

For the two-dimensional analysis, the Stability and Transition Analysis for Hypersonic Boundary Layers (STABL)²² suite of software was used. The tools provided with this software include grid generation tools, a two-dimensional/axisymmetric CFD solver, and the stability analysis code, PSE-chem. The flow solver is a two-dimensional/axisymmetric, second order accurate mean flow solver based on the implicit data-parallel line relaxation (DPLR)²³ method. The PSE-Chem code solves the parabolized stability equations for high speed flows and includes the effects from finite-rate chemistry and translation-vibrational energy exchanges. One particularly useful quantity is the N factor from the e^N method. Briefly, this method provides a means to measure the integrated amplitude growth of constant frequency disturbances in the boundary layer as they propagate downstream. Following Jaffe *et al.*²⁴ this quantity can then be compared to experimental transition data to determine a particular value of N factor which correlates to transition. The N factor is defined as follows

$$N(\omega, s) = \int_{s_0}^s \sigma ds$$

Approved for public release; distribution unlimited.

3 of 17

where s is the distance along the surface, s_0 is the location of the first critical point, ω is the disturbance frequency, and σ is the disturbance growth rate. For more details on the PSE-Chem solver, see Johnson and Candler.²²

The three-dimensional calculations carried out for this work were conducted using the unstructured solver, US3D.²⁵ Developed and maintained by Professor Candler's research group at the University of Minnesota, US3D solves the compressible Navier-Stokes equations using a cell-centered finite volume formulation. For all calculations, the viscous fluxes were evaluated using gradients reconstructed from weighted least squares approximation with deferred correction to the cell faces. For the steady flow calculations, the inviscid fluxes were computed using the second-order-accurate modified Steger-Warming²⁶ flux vector splitting scheme. For the unsteady calculations, the inviscid fluxes were computed using a low dissipation, hybrid central/upwind scheme as described by Subbareddy and Candler.²⁷ In this form the flux, F_f , is computed as the combination of a non-dissipative symmetric component and an upwinded dissipative component multiplied by a shock detecting switch.

$$F_f = F_{sym} + \alpha_{sw} F_{diss}$$

The switch, α_{sw} , ensures that the dissipative portion of the flux evaluation is only used in regions near discontinuities. A commonly used switch for this framework is the switch due to Ducros *et al*²⁸ which is given by

$$\alpha = \frac{(\vec{\nabla} \cdot \vec{u})^2}{(\vec{\nabla} \cdot \vec{u})^2 + \|\vec{\omega}\|^2}$$

where u is the velocity and ω is vorticity. This switch provided adequate operation for the work presented herein. The symmetric component of the inviscid flux was computed using a nominally sixth order accurate gradient reconstruction. Time advancement was accomplished using second-order implicit time integration.

III.B. Grid Construction

To reproduce the experiment, the computational model consisted of a 7.0° half angle sharp cone with a 2.5 mm blunted nose and a total axial length of 1100 mm. Due to the location of the roughness element and the angle of attack of the flow, symmetry planes could not be used and therefore a grid of the full cone model was used.

By carefully constructing a grid of very high quality, the sources of grid-related errors in the computed solution can be minimized. This is especially important considering the small amplitudes of some of the quantities that are of interest to this investigation. As such, the three-dimensional unstructured grid, consisting entirely of hexahedral cells, was generated using the commercially available software package Pointwise. The grid was constructed by first generating a solution on a coarse grid where the outer domain was conservatively placed such that it would capture the shock shape. The shock position was extracted from the initial solution and used to position the outer domain surface by closely following the shock shape with minimal buffer zone. This ensured the efficient use of grid points within the domain by minimizing the number of points in the freestream and by helping to accurately capture the shock in the refined grid. Using the outer domain surface and the cone model surface, the grid topology was created with careful attention to the cone surface grid densities. It should be noted that using a grid topology paradigm, one can avoid creating a grid singularity in the nose region as would be encountered in structured grid generated by revolution. This singularity, due to its location near the stagnation region, can be troublesome for finite volume solvers.

The grid described above also utilizes the nested refinement technique. While nested refinement introduces five-cell singularities into the grid, the primary benefit of using this technique is that it provides the user the ability to tailor the shape and spacing of the cells where desired. In this case, the added complexity of meshing the roughness element is made possible by using this technique. A close-up of the grid near the roughness element is shown in Figure 3. Based on experience generating grids for similar flows, grid clustering normal to the surface and achieving a value of y^+ less than one at the first solution point away from the wall ensures that the boundary layer is appropriately resolved in the body-normal direction. The additional requirement of adequate resolution of the wake region was also obtained. After meeting all these requirements, the resulting high-quality grid consisted of 460 million cells with 300 points normal to the surface.

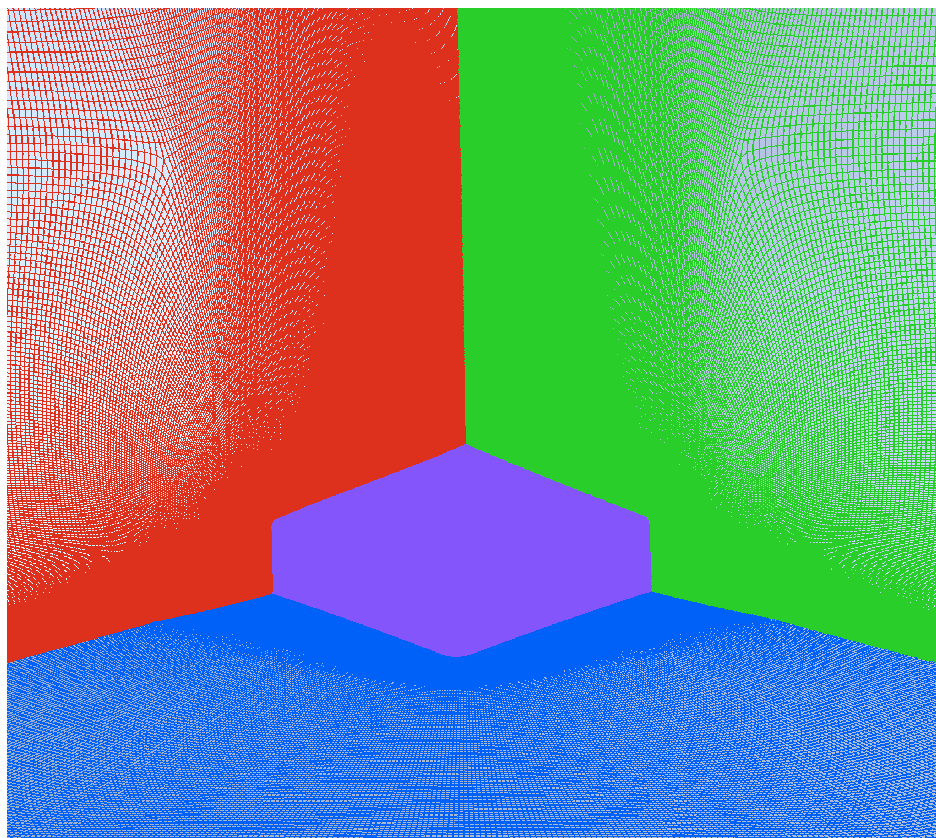


Figure 3: Close-up of mesh around roughness element.

III.C. Simulation Conditions

To anchor this computational study, one of the four hypersonic flow conditions was set to match the flight conditions at 28.4 seconds into the ascent. This is the highest Reynolds number condition and is identified as Case D. All four sets of freestream conditions are shown in Table 1. For all conditions, a specified wall temperature profile was used. This profile was based on the thermal analysis provided by AFRL's finite element code TOPAZ and combined with a smooth blending function to a laminar flow condition along the aft portion of the cone, similar to the procedure used by Li *et al.*¹⁸ A plot of the surface temperature as a function of axial distance is shown in Figure 4. Due to the relatively low stagnation temperatures, it was determined that a perfect gas assumption would be used. At 28.4 seconds into the flight, the HIFiRE-1 vehicle was calculated to be at 1.5° angle of attack which was used in the three-dimensional computations by inclining the freestream velocity vector.

	M	$R_\infty [1/m]$	$T_0 [K]$	$P_0 [kPa]$	$\rho_\infty [kg/m^3]$	$T_\infty [K]$	$u_\infty [m/s]$	$T_{wall} [K]$
Case A	5.52	1.08×10^6	568	131	0.0060	80.0	990.3	Varying
Case B	5.52	1.84×10^6	1277	737	0.0150	180.0	1484.6	Varying
Case C	5.52	2.16×10^6	1454	1035	0.0185	205.0	1584.4	Varying
Case D	5.52	2.49×10^6	1618	1373	0.0221	227.9	1671.4	Varying

Table 1: Simulation Freestream Conditions.

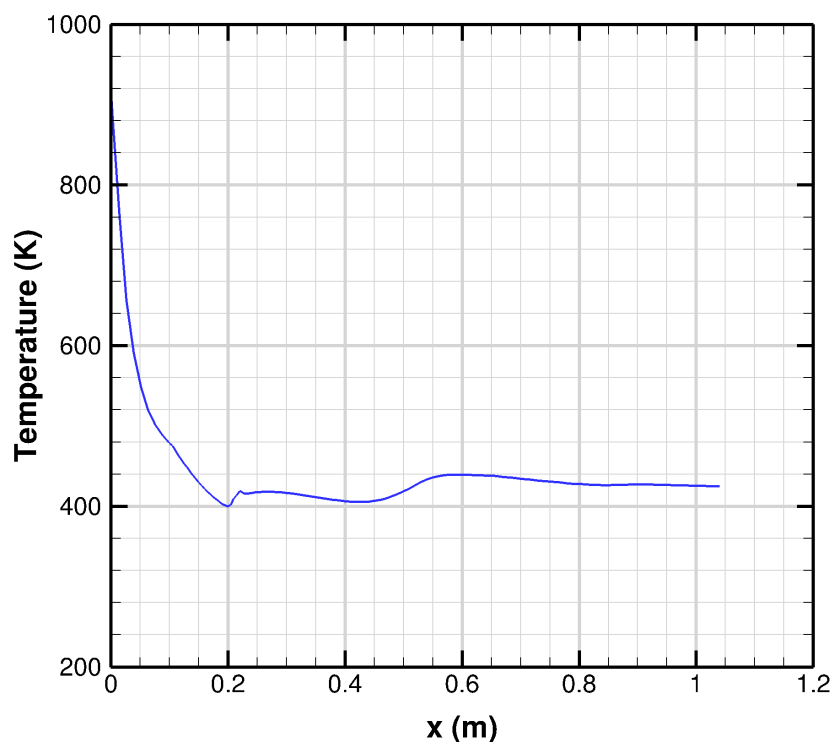
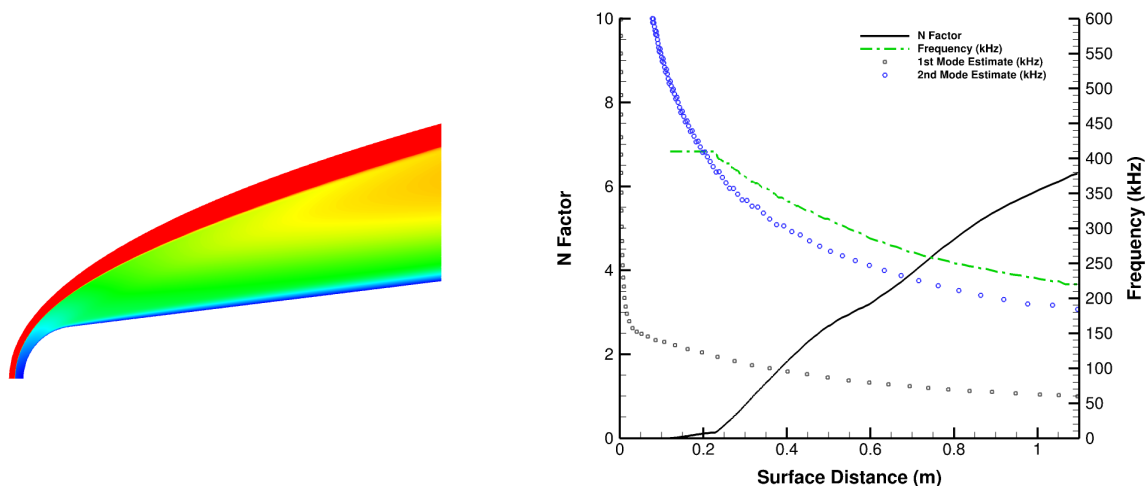


Figure 4: Surface temperature profile.

IV. Results

The two-dimensional mean flow solution was generated using DPLR as implemented in STABL. This methodology permits the use of large time steps to converge the calculation to steady state using fewer iterations. For the three-dimensional steady and unsteady calculations, however, additional restrictions were placed on maximum allowable time step due to the high grid resolution at the nose and around the boundary layer trip leading to significant increases in computational demands.

For the two-dimensional analysis, the mean flow calculation is shown in Figure 5(a) as Mach contours near the nose. A stability analysis was conducted using this mean flow and N factor results are shown in Figure 5(b). Looking at this plot, one can see that the maximum N factor reaches a value just over 6 at a frequency of 230 kHz. This matches well with analysis provided by Li *et al.*¹⁸ where it was observed that the N factor reaches a maximum of 21.2 at 20.0 seconds into the ascent and falls to 7.6 by 27.0 seconds. For free flight conditions, an N factor greater than 10 may indicate the onset of transition. It can therefore be expected that at 28.4 seconds it is unlikely that natural transition is occurring anywhere on the cone. Based on a visual comparison between the computed maximum N factor envelope frequencies and the estimates for Mack's first and second modes shown in Figure 5(b), it is reasonable to conclude that for these conditions Mack's second mode is the dominant instability absent surface roughness.



(a) Mach contours at 28.4 seconds into ascent.

(b) N factor analysis for 28.4 seconds into ascent.

Figure 5: Two-dimensional analysis of 28.4 seconds into the ascent.

Whereas the analysis discussed above examined axisymmetric flow, the high-fidelity computations used a 1.5° angle of attack to match the flight conditions at 28.4 seconds into the ascent. In this case, the roughness element was aligned along the windward ray, which will be defined as the 0° ray. When considering the effects of an isolated roughness element on boundary layer flows, two parameters are commonly referenced. The first is the k/δ parameter, which gives the relationship between roughness height and boundary layer thickness. Since no computations were completed for these cases without the roughness element, estimates are made based on boundary layer thickness values in the vicinity just upstream and to the sides of the element. These values were taken from areas that were relatively unperturbed by the presence of the roughness element. It was found that k/δ was approximately 0.7 for Case A, 1.0 for Case B, 1.1 for Case C, and 1.2 for Case D. The second parameter, Re_k or roughness Reynolds number, is used as an engineering correlation to predict whether the roughness element will affect boundary layer transition or not. Above some critical value it is considered that a boundary layer will be sufficiently perturbed such that natural transition is altered. This value is calculated using the following relation:

$$Re_k = \frac{\rho_k U_k k}{\mu_k}$$

where k is the roughness height and the subscript k denotes that the values were obtained at that same roughness height from a simulation that excluded the roughness element. Again, absent such a computation, estimates are provided and were obtained in a similar fashion as the k/δ parameter. For the lowest Reynolds number case, Case A, it is estimated that $Re_k \approx 250$. For Case B Re_k was approximately 1450, for Case C $Re_k \approx 6050$, and for Case D $Re_k \approx 7150$.

In Figure 6, four slices centered along the windward ray show pressure contours normalized by the freestream pressure. In all cases a shock can be observed emanating from the leading corner of the roughness element followed by an expansion wave attached to the trailing corner. As the freestream unit Reynolds number increases from Cases A to D, the incoming boundary layer that the roughness element sees decreases in thickness. This results in a rise in the incoming Mach number that interacts with the element and a subsequent gain in shock strength, as indicated by the increased intensity in the normalized pressure contours shown in Figure 6. It is noted that the increase from Case B through D is quite subtle, which is expected given the relatively small increases in k/δ for those cases. This is in contrast to the more significant increase in k/δ when comparing Case A to Case B. It will be shown in following examination of results that the flow over and around the roughness element in Case A is in many ways fundamentally different than Cases B, C, and D.

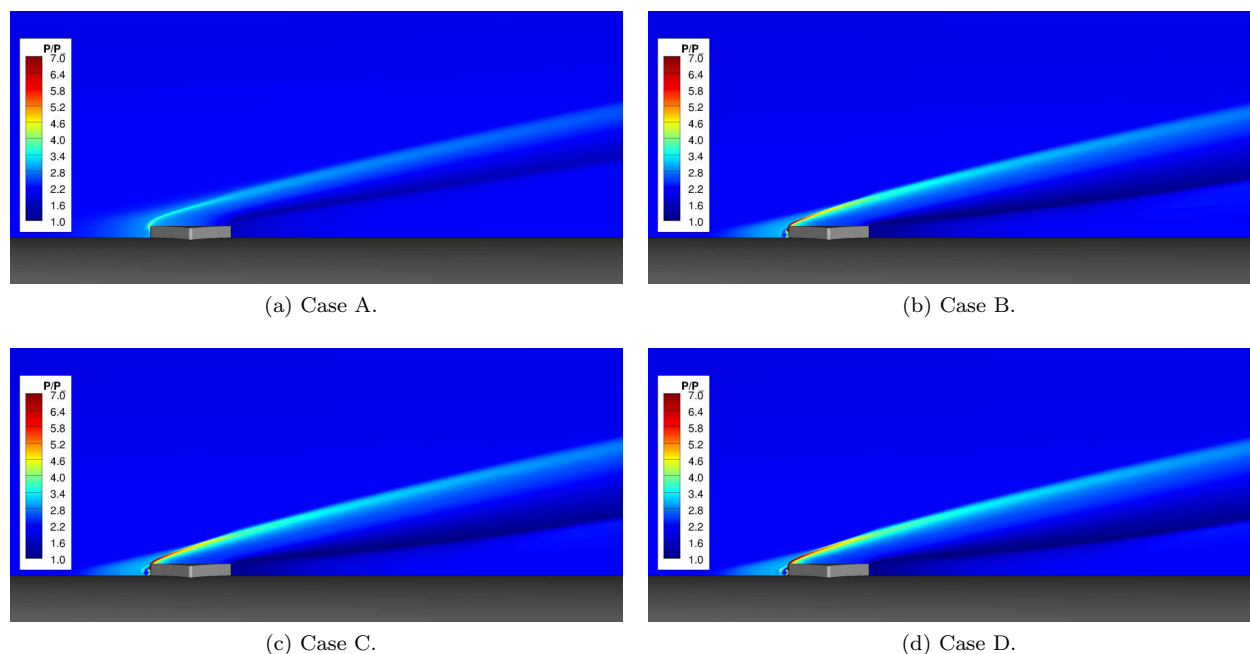


Figure 6: Centerline pressure contours normalize by freestream static pressure, P_∞ .

One of the more well-known published results with respect to boundary layer trips in high-speed flows is that of Whitehead.²⁹ In his work, several boundary layer trip configurations and trip shapes were examined on an inclined wedge. Of particular note and relevance to this work was the comparison between the flow pattern produced by an isolated cylindrical trip and a triangular prism trip. These results can be found in Figure 4 of Whitehead²⁹ and are reproduced here in Figure 7(a) and 7(b) along with a comparison with the current computations in Figure 7(c). Focusing on the oil flow results, the flow pattern immediately upstream of both trips are markedly different. In the cylindrical trip case several of the horseshoe vortices are fully visible in the oil flow as they wrap completely around the trip. In the case of the triangular prism, only one vortex footprint is visible just upstream of the element, but as the flow turns laterally around the element other vortical structures begin to appear. In both cases, the region of relatively unperturbed oil splashes indicate a large separated region. Based on the other results presented by Whitehead, it would be expected that upstream of the separated region the oil flow would exhibit patterns consistent with laminar boundary layer flow.

With these observations in mind, a comparison can be made with the computational results shown in Figure 7(c). In this case, two contour colors are shown for wall shear stress along with surface limiting streamlines. While the contours were arbitrarily selected, the lighter regions represent a significant increase over the darker regions. In the case of oil-flow visualization, it would be expected that these regions of higher shear stress would provide sufficient force to smear the oil to produce flow patterns. As can be seen, the square shaped roughness element oriented as a diamond with respect to the flow produces flow patterns qualitatively similar to the triangular prism trip as compared to the cylindrical trip. This in spite of the fact that both experimental trips had values of $k/\delta = 2$ and the triangular prism was slightly wider at 23.8 mm (corner-to-corner) versus the 14.1 mm (corner-to-corner) found on the HIFiRE-1 geometry. Instead of an easily identifiable radius of influence as in the cylindrical trip case, for a protuberance that has a leading corner pointing into the flow there appears a broad, square shouldered pattern that will be seen in subsequent plots.

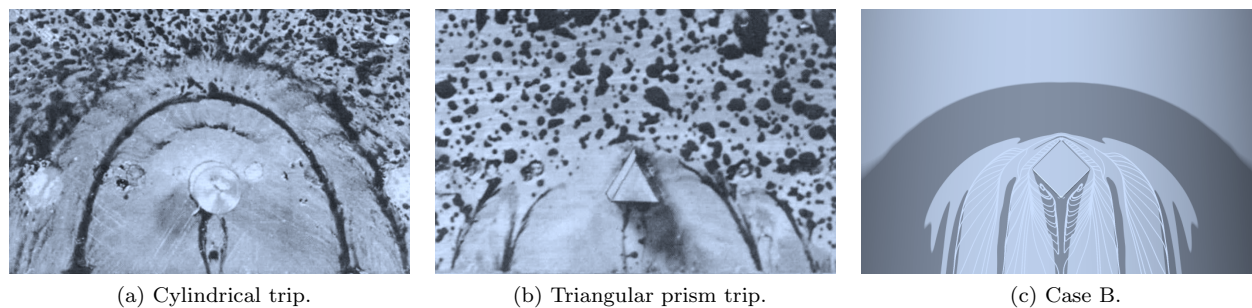


Figure 7: Comparison of oil flow visualization from (a) cylindrical and (b) triangular prism trips with (c) shear stress contours from computations. Experimental results taken from Whitehead, Figure 4.²⁹

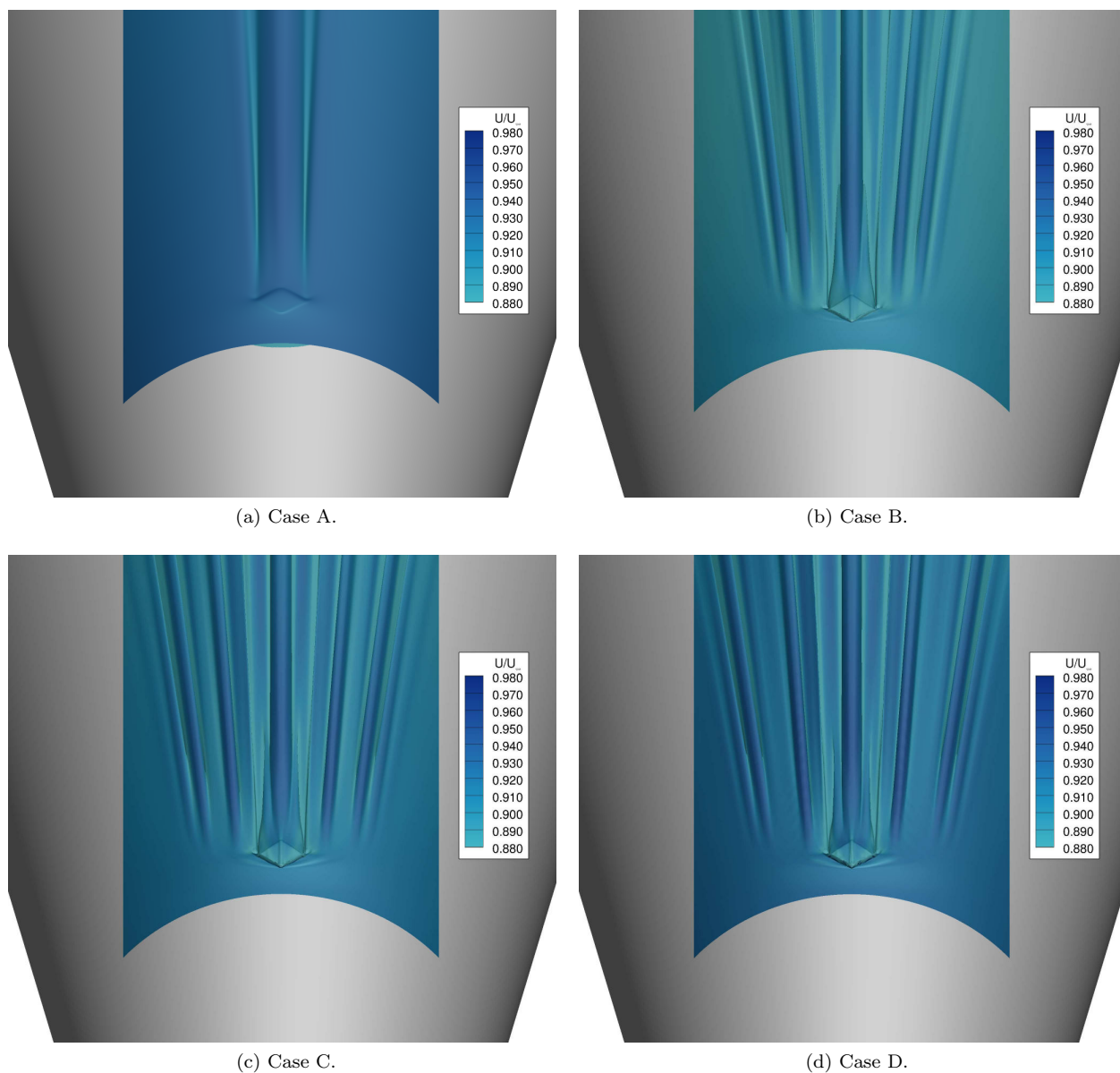
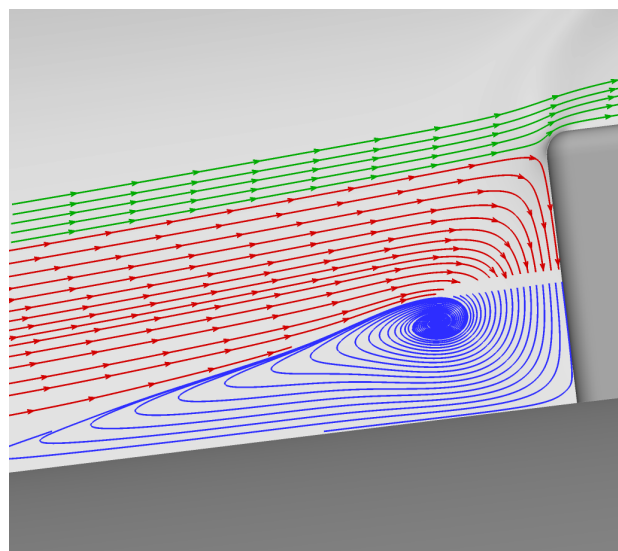


Figure 8: Isosurfaces of Vorticity Magnitude in the near vicinity of the roughness element. Surfaces are colored by the normalized velocity U .

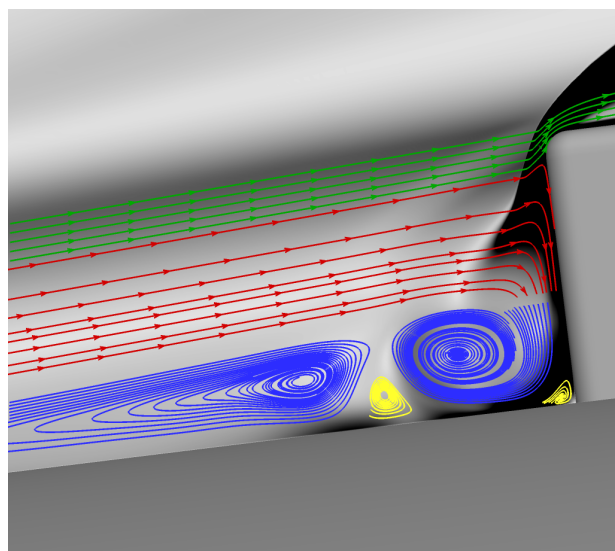
In order to compare the differences between the four Reynolds number cases and to aid in visualizing the flow patterns produced by the roughness element, isosurfaces of vorticity magnitude are shown in Figures 8(a), 8(b), 8(c), and 8(d). Each corresponds with Case A, B, C, and D, respectively. The isosurfaces are colored by the streamwise velocity U which has been normalized by the freestream value, U_∞ . Very clearly, the flow pattern produced in Case A differs significantly compared with Cases B, C, and D. Case A shows two streaks indicating a simple horseshoe vortex system. In contrast, Cases B, C, and D display a multiple vortex system that propagates downstream. As was seen in the oil-flow and shear stress visualization, the vortex pattern appears at the roughness element in a broad, squared shoulder like fashion. The most obvious difference between Cases B, C, and D is that with increasing freestream unit Reynolds number, the vortex pattern broadens and produces vortex structures that develop to a greater degree.

Digging into the details of the flow structures produced by the roughness element, four plots showing close-up views just upstream of the roughness element are shown in Figure 9. For each plot the centerline slice is shown as a numerical shadowgraph. Plotted over the numerical shadowgraph are streamlines of various colors. This color scheme groups together related streamlines and will be used in subsequent figures. A short description of each color group follows. The green streamlines represent boundary layer flow lines which do not get entrained in the separated region and the horseshoe vortex system but are at minimum deflected to some extent. The red streamlines represent boundary layer flow that originates from the upstream, unperturbed flow, but which enter the roughness element vortex system. Blue streamlines are used to show vortex structures that rotate clockwise with respect to the reader's perspective of Figure 9. Yellow streamlines are used to visualize vortex structures with a counter-clockwise rotation. Both the yellow and blue streamlines lack direction arrows for clarity. As has been previously observed, Case A displays a very simple vortex system compared with the other cases. There is only a single clockwise rotating recirculation zone upstream of the element. The extent of this separated region is the shortest of all the cases. Moving to Case B, the separation region moves upstream and a much more complex flow system can be seen. In this case a counter-clockwise rotating vortex (yellow) sits immediately adjacent to the roughness element. Moving upstream, a larger clockwise rotating vortex (blue) sits adjacent to another small counter-clockwise rotating (yellow) which in turn is adjacent to the furthest upstream and largest vortex. For Case C in Figure 9(c), the flow structure looks quite similar to Case B. However, there begins to appear a second clockwise rotating vortex core in the furthest upstream recirculation zone. This further develops in Case D, where the twin co-rotating vortices are readily visible. Between and just below the pair, the streamlines begin to lift, indicating that a further increase in Reynolds number would produce an additional counter-clockwise vortex near the surface.

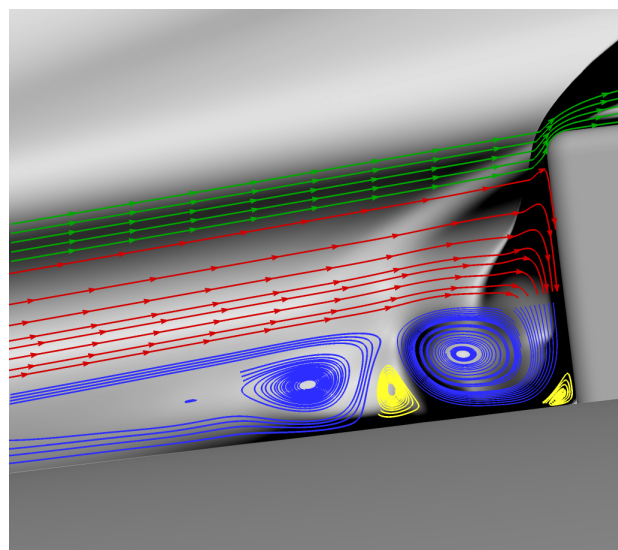
Using the same color grouping, streamlines on the centerline plane along with surface limiting streamlines are shown in Figures 10(a), 10(b), 10(c), and 10(d). One additional color group for streamlines is used: the color black representing roughness wake streamlines. Here again the centerline slice is a numerical shadowgraph, and the cone surface is shown with grayscale contours of wall shear stress. In this perspective view, the effect of the protuberance can be seen on incoming green streamlines on the surface. In Case A, these streamlines travel the closest to the roughness element of all the cases and are displaced the least. On the roughness element side that is visible, the incoming red streamlines are directed downward and swept back along the side. These streamlines are either incorporated into the horseshoe vortex (blue), or are directed into the wake region (black). Note again the simple flow structure as compared to the higher Reynolds number cases. In Case B, the streamline structure becomes much more complex. The side of the roughness element now shows two zones. One with the incoming red streamlines and the other, a separated region associated with the counter-clockwise rotating vortex (yellow). Moving away from the roughness element, the alternating pattern of clockwise and counter-clockwise rotating vortices that was seen previously is visible here as well and indicate a series of alternating separation lines and re-attachment lines. Additionally, the number of counter-rotating vortices that are visible has increased from that observed in Figures 9(b)-(d). This trend continues in Cases C and D and in some sense matches the observation in Whitehead's triangular prism trip results where vortices become visible on the surface to the sides of the roughness element.



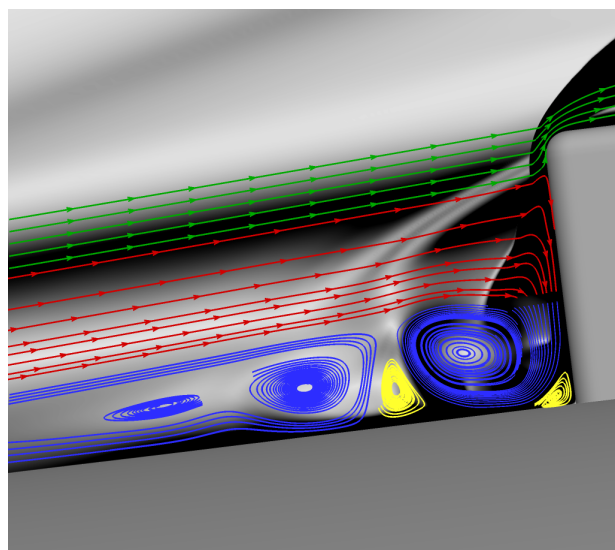
(a) Case A.



(b) Case B.



(c) Case C.



(d) Case D.

Figure 9: Centerline shadowgraph upstream of roughness element.

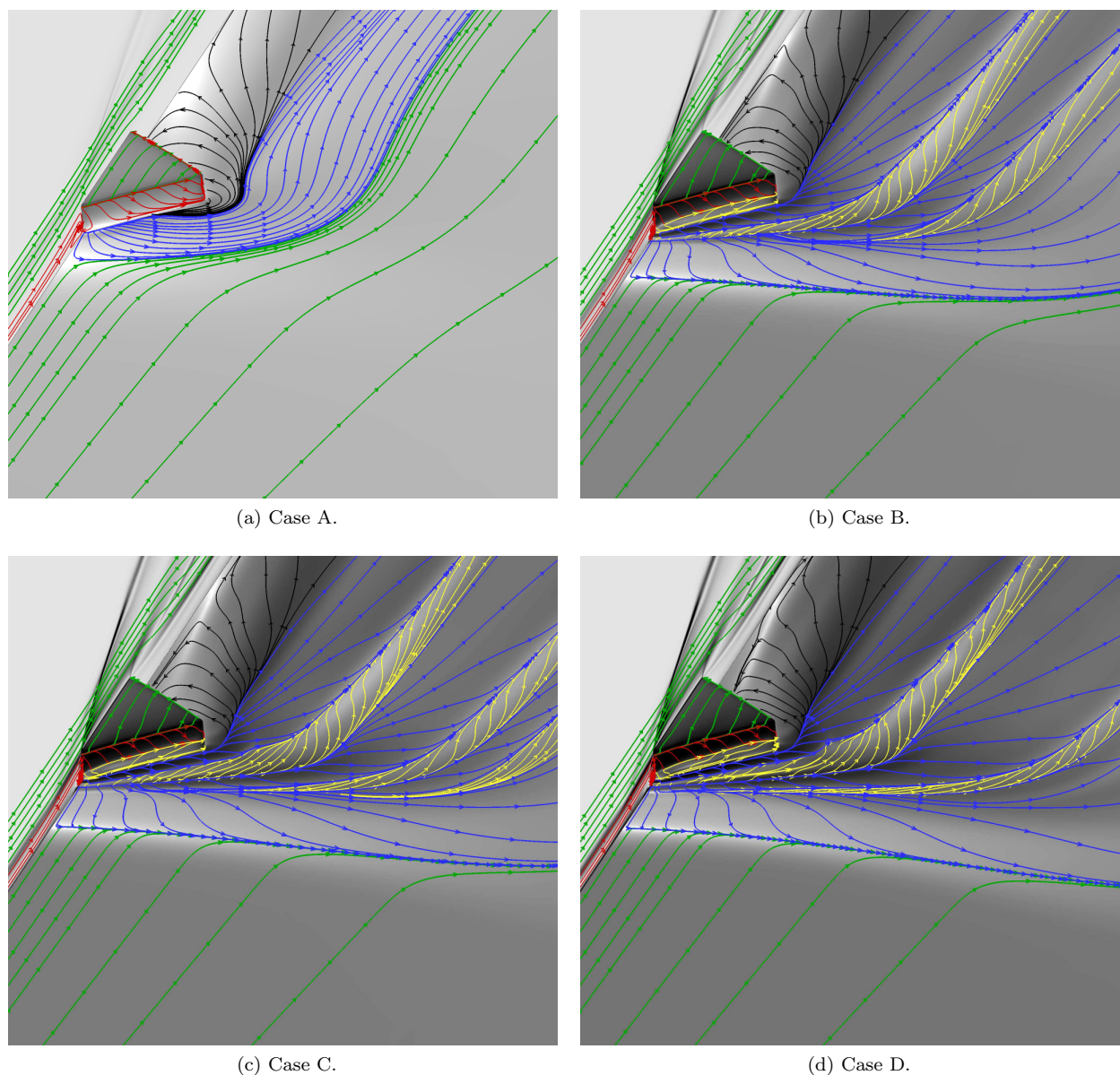


Figure 10: Surface pressure with limiting streamlines.

In order to examine the profiles produced by the roughness element wake, four axial slices showing contours of vorticity magnitude are shown for each case in Figure 11. The axial stations used were $x=0.60$ m, $x=0.75$ m, $x=0.90$ m, and $x=1.05$ m. In order to improve clarity, the x axis shows values of the cone ray angle, where the 0° ray is centered along the windward ray, which have been displayed in a normal Cartesian layout. The y axis represents the surface distance normal to the surface and are scaled appropriately for each case. Note that all vorticity magnitude contours are displayed at identical levels, except for Case A where the range of levels has been reduced. The fundamental difference between Case A and all other Cases is readily observed. The flow exhibits two regions of increased vorticity corresponding to the simple horseshoe vortex system. It is interesting to note the differences between Cases B, C, and D at the furthest upstream axial location ($x=0.60$ m). In Case B, there is the central “mushroom” shaped lobe with four off-center lobes to each side. In Cases C and D, the center line “mushroom” is flanked by five off-center lobes. When comparing Cases C and D, besides observing a general broadening in Case D, there appears to be a system of pairs of vortices. It is between these pairs that the general broadening sees the greatest increase. It is possible that

this effect is related to the crossflow velocity component produced by the small angle of attack. Generally for all cases, when viewing axial slices from upstream toward downstream, there is a general dissipation of the flow structures indicated by the reduction in vorticity magnitude.

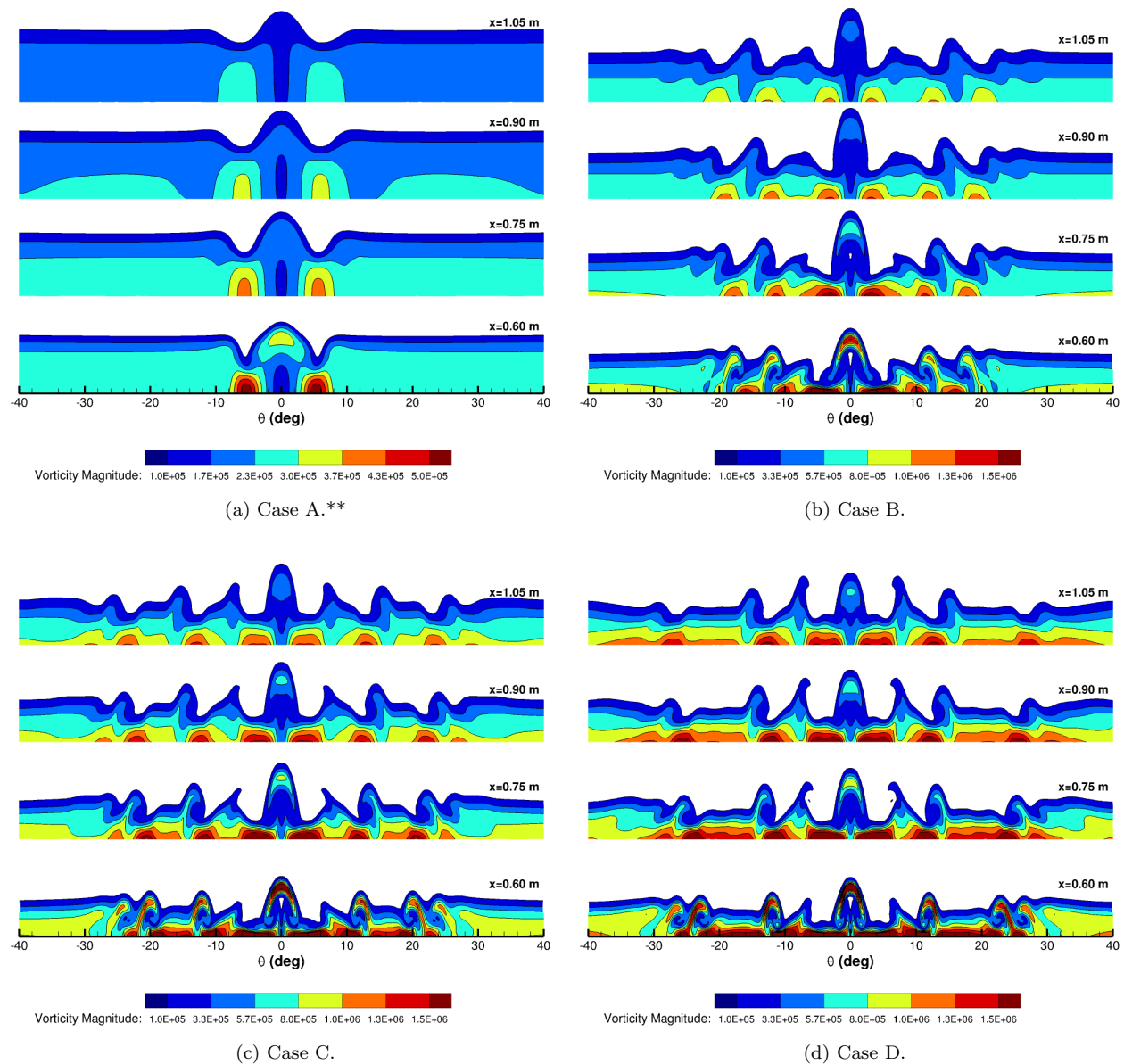


Figure 11: Surface heat flux and boundary layer velocity slices. **(Note: A different contour scale was used for clarity in Case A only)

In addition to the four cases simulated using second-order numerics, preliminary work has been completed using the sixth-order low-dissipation scheme implemented in US3D. The purpose of this is to observe any unsteady behavior associated with the tripped boundary layer. Two cases will be presented here, Case A and Case B. To illustrate any immediate differences in the results, plots showing surface heat flux are shown and compared in Figure 12. For Case A, the standard numerics are shown in Figure 12(a) while the high order, low dissipation calculation is shown in Figure 12(b). One can observe that these two figures are identical, indicating that absent freestream disturbances the flow remains laminar. However, for Case B there is a noticeable difference between Figure 12(c), the standard calculation, and Figure 12(d), the low-dissipation

calculation. Indeed, Figure 12(d) represents a time averaged heat flux. The increased heating near the aft portion of the cone indicates that transition is occurring. Upstream of the increased heating zone, it can be observed that the vortex structures appear more intense and remain coherent for a longer extent in the low-dissipation calculation as compared with the standard calculation.

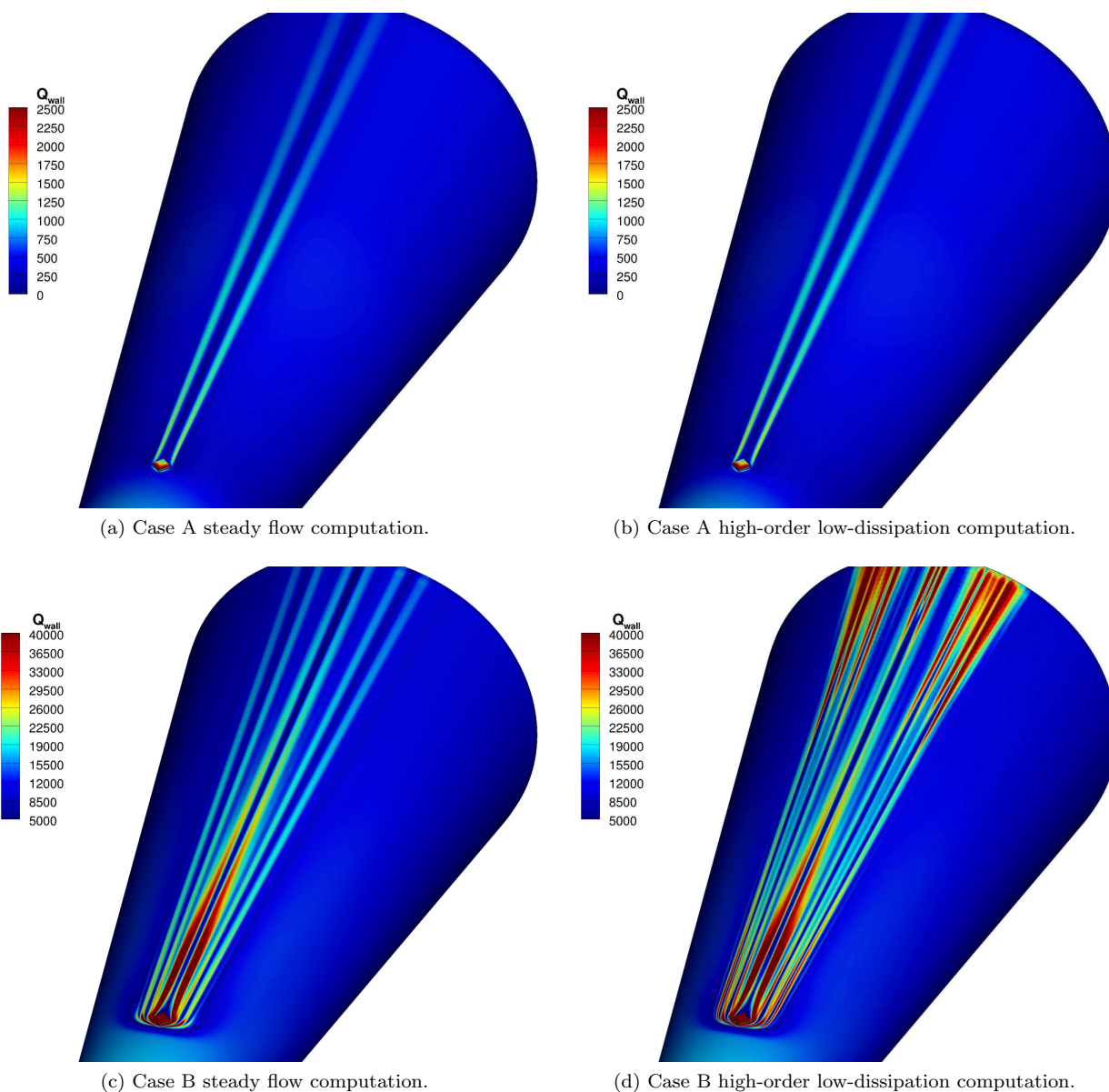


Figure 12: Surface heat flux comparison between steady flow computations and high-order, low-dissipation computations.

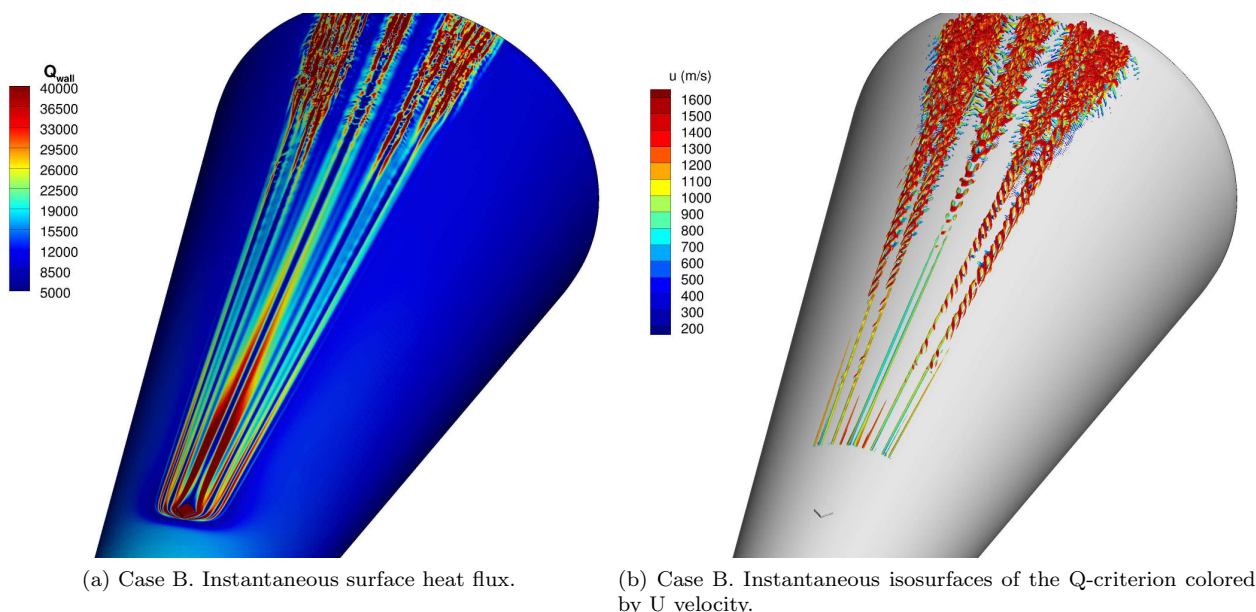


Figure 13: Case B. High-order, low dissipation simulation.

To help illustrate the unsteady vortex structure that is observed in the low-dissipation calculation for Case B, a plot showing the instantaneous surface heat flux is shown in Figure 13(a) and isosurfaces of the Q-criterion colored by contours of the streamwise velocity, U , are shown in Figure 13(b). The Q-criterion is defined as $Q = \frac{1}{2} (|\Omega|^2 - |S|^2) > 0$ where S is the rate of strain tensor and Ω is the rate of rotation tensor. In the surface heat flux, waves can be seen in the off-center vortex structures which ultimately result in transition. The same observation can be made in the centerline wake vortices, however these transition further aft, resulting in a three-pronged transition pattern. Examining the isosurfaces of the Q-criterion, the off-center vortices exhibit a rope-like pattern which grow in intensity as they travel downstream ultimately leading to the onset of transition.

V. Conclusions

In this work, a series of four different Reynolds number conditions were examined for an isolated, diamond-shaped roughness element. The geometry was based on the HIFiRE-1 flight vehicle and one of the four conditions was derived from the conditions at 28.4 seconds into the ascent. This was chosen largely due to the fact the flow was nearly axisymmetric at roughly 1.5° angle of attack. A preliminary investigation was conducted using two-dimensional computational analysis. This consisted of a stability analysis which confirmed that transition was not occurring upstream of the roughness element. Four steady state three-dimensional computations were run on a high-fidelity grid. These computations were used to evaluate the effect of Reynolds number on an isolated boundary layer trip. It was observed for the lowest Reynolds number case resulted in the least complex flow with a single horseshoe vortex system resulting in a pair of streaks of increased heating downstream of the element. With the increase in Reynolds number, the incoming boundary layer, as seen by the roughness element, decreased in thickness which resulted in increased shock strength produced by the protuberance. It also increased the number of vortex pairs observed upstream of the element which subsequently wrapped around the element producing multiple streaks of increased heating. A brief comparison between the steady flow computations and ongoing high-order, low-dissipation computations. The lowest Reynolds number case showed very little difference between the two numerical schemes. For Case B it was observed that the streaks in the wake retained their intensity to a much greater extent in the low-dissipation calculations and instabilities in both the off-center vortex systems and centerline wake region lead to the onset of transition. Future work will include further investigation of unsteady calculations using the high-order, low-dissipation numerics with the intent of observing wake instabilities.

Acknowledgments

I would personally like to acknowledge Dr. Roger Kimmel and Dr. Scott Stanfield for sharing data and insights on the HIFiRE-1 flight. The material presented herein is based on research completed by OAI and the Air Force Research Laboratory under agreement number FA8650-04-2-3445. This work was sponsored by the Air Force Office of Scientific Research under grant number LRIR 12RB01COR monitored by Dr. John Schmisser, AFOSR/RTE. Computations were performed at the U.S. Department of Defense Supercomputing Resource Center at the U.S. Army Engineer Research and Development Center, Vicksburg, MS and the Air Force Research Laboratory, Wright-Patterson Air Force Base, OH.

The views and conclusions contained herein are those of the authors and should not be interpreted as necessarily representing the official policies or endorsements, either expressed or implied, of Air Force Research Laboratory or the U.S. Government. The U.S. Government is authorized to reproduce and distribute reprints for Governmental purposes notwithstanding any copyright notation thereon.

References

- ¹Bertin, J. and Cummings, R., "Fifty Years of Hypersonics: Where We've Been, Where We're Going," *Progress in Aerospace Sciences*, Vol. 39, August-October 2003, pp. 511-536.
- ²Schneider, S., "Hypersonic laminar-turbulent transition on circular cones and scramjet forebodies," *Progress in Aerospace Sciences*, Vol. 40, January-February 2004, pp. 1-50.
- ³Kimmel, R., Adamczak, D., Gaitonde, D., Rougeux, A., and Hayes, J., "HIFiRE-1 Boundary Layer Transition Experiment Design," Paper 2007-0534, AIAA, January 2007.
- ⁴Kimmel, R., "Aerothermal Design for the HIFiRE-1 Flight Vehicle," Paper 2008-4034, AIAA, June 2008.
- ⁵Kimmel, R., "Roughness Considerations for the HIFiRE-1 Vehicle," Paper 2008-4293, AIAA, June 2008.
- ⁶Adamczak, D., Alesi, H., and Frost, M., "HIFiRE-1: Payload Design, Manufacture, Ground Test, and Lessons Learned," Paper 2009-7294, AIAA, October 2009.
- ⁷Adamczak, D. and Kimmel, R., "HIFiRE-1 Flight Trajectory Estimation and Initial Experimental Results," Paper 2011-2358, AIAA, April 2011.
- ⁸Kimmel, R. and Adamczak, D., "HIFiRE-1 Preliminary Aerothermodynamic Measurements," Paper 2011-3413, AIAA, June 2011.
- ⁹Stanfield, S., Kimmel, R., and Adamczak, D., "HIFiRE-1 Flight Data Analysis: Boundary Layer Transition Experiment During Reentry," Paper 2012-1087, AIAA, January 2012.
- ¹⁰Kimmel, R. and Adamczak, D., "HIFiRE-1 Background and Lessons Learned," Paper 2012-1088, AIAA, January 2012.
- ¹¹Wadhams, T., MacLean, M., Holden, M., and Mundy, E., "Pre-Flight Ground Testing of the FRESH FX-1 at Flight Duplicated Conditions," Paper 2007-4488, AIAA, June 2007.
- ¹²Wadhams, T., Mundy, E., MacLean, M., and Holden, M., "Pre-Flight Ground Testing of the Full Scale HIFiRE-1 Vehicle at Fully Duplicated Flight Conditions: Part II," Paper 2008-0639, AIAA, January 2008.
- ¹³Berger, K. and Kimmel, R., "Aerothermodynamic Testing and Boundary Layer Trip Sizing of the HIFiRE Flight 1 Vehicle," Paper 2008-0640, AIAA, January 2008.
- ¹⁴Casper, K., Wheaton, B., Johnson, H., and Schneider, S., "Effect of Freestream Noise on Roughness-Induced Transition at Mach 6," Paper 2008-4291, AIAA, June 2008.
- ¹⁵Johnson, H., Alba, C., Candler, G., MacLean, M., Wadhams, T., and Holden, M., "Boundary Layer Stability Analysis to Support the HIFiRE Transition Experiment," Paper 2007-311, AIAA, January 2007.
- ¹⁶Alba, C., Johnson, H., Bartkiewicz, M., and Candler, G., "Boundary Layer Stability Calculations of the HIFiRE Flight 1 Vehicle in the LaRC 20-Inch Mach 6 Air Tunnel," Paper 2008-0505, AIAA, January 2008.
- ¹⁷MacLean, M., Wadhams, T., Holden, M., and Johnson, H., "A Computational Analysis of Ground Test Studies of the HIFiRE-1 Transition Experiment," Paper 2008-0641, AIAA, January 2008.
- ¹⁸Li, F., Choudhari, M., Chang, C., Kimmel, R., Adamczak, D., and Smith, M., "Transition Analysis for the HIFiRE-1 Flight Experiment," Paper 2011-3414, AIAA, June 2011.
- ¹⁹Marek, L., "Assessing Uncertainties in Boundary Layer Transition Predictions for HIFiRE-1 at Non-zero Angles of Attack," Paper 2012-1015, AIAA, January 2012.
- ²⁰Li, F., Choudhari, M., Chang, C., White, J., Kimmel, R., Adamczak, D., Borg, M., Stanfield, S., and Smith, M., "Stability Analysis for HIFiRE Experiments," Paper 2012-2961, AIAA, June 2012.
- ²¹Schneider, S., "Effects of Roughness on Hypersonic Boundary-Layer Transition," Paper 2007-0305, AIAA, January 2007.
- ²²Johnson, H. and Candler, G., "Hypersonic Boundary Layer Stability Analysis Using PSE-Chem," Paper 2005-5023, AIAA, June 2005.
- ²³Wright, M., Candler, G., and Bose, D., "A Data-Parallel Line-Relaxation Method for the Navier-Stokes Equations," Paper 1997-2046, AIAA, June 1997.
- ²⁴Jaffe, N., Okamura, T., and Smith, A., "Determination of Spatial Amplification Factors and Their Application to Predicting Transition," *AIAA Journal*, Vol. 8, No. 2, February 1970, pp. 301-308.
- ²⁵Nompelis, I., Drayna, T., and Candler, G., "A Parallel Unstructured Implicit Solver for Hypersonic Reacting Flow Simulation," Paper 2005-4867, AIAA, June 2005.

- ²⁶MacCormack, R. and Candler, G., "The Solution of the Navier-Stokes Equations Using Gauss-Seidel Line Relaxation," *Computers and Fluids*, Vol. 17, No. 1, 1989, pp. 135–150.
- ²⁷Subbareddy, P. and Candler, G., "A fully discrete, kinetic energy consistent finite-volume scheme for compressible flows," *Journal of Computational Physics*, Vol. 228, No. 5, 2009, pp. 1347–1364.
- ²⁸Ducros, F., Ferrand, V., Nicoud, F., Weber, C., Darracq, D., Gacherieu, C., and Poinso, T., "Large-Eddy Simulation of the Shock/Turbulence Interaction," *Journal of Computational Physics*, Vol. 152, No. 1, 1999, pp. 199–238.
- ²⁹Whitehead, Jr., A., "Flow-Field and Drag Characteristics of Several Boundary-Layer Tripping Elements in Hypersonic Flow," Technical Note TN-D-5454, NASA, October 1969.